


8-2019

QUANTIFYING UNCERTAINTY IN A MEASUREMENT-BASED ASSESSMENT OF RELATIVE BIOLOGICAL EFFECTIVENESS IN CARBON ION RADIOTHERAPY

Shannon Hartzell

Follow this and additional works at: https://digitalcommons.library.tmc.edu/utgsbs_dissertations

 Part of the [Biological and Chemical Physics Commons](#), [Medicine and Health Sciences Commons](#), and
the [Other Physics Commons](#)

Recommended Citation

Hartzell, Shannon, "QUANTIFYING UNCERTAINTY IN A MEASUREMENT-BASED ASSESSMENT OF RELATIVE BIOLOGICAL EFFECTIVENESS IN CARBON ION RADIOTHERAPY" (2019). *The University of Texas MD Anderson Cancer Center UTHealth Graduate School of Biomedical Sciences Dissertations and Theses (Open Access)*. 968.

https://digitalcommons.library.tmc.edu/utgsbs_dissertations/968

This Thesis (MS) is brought to you for free and open access by the The University of Texas MD Anderson Cancer Center UTHealth Graduate School of Biomedical Sciences at DigitalCommons@TMC. It has been accepted for inclusion in The University of Texas MD Anderson Cancer Center UTHealth Graduate School of Biomedical Sciences Dissertations and Theses (Open Access) by an authorized administrator of DigitalCommons@TMC. For more information, please contact digitalcommons@library.tmc.edu.

QUANTIFYING UNCERTAINTY IN A MEASUREMENT-BASED
ASSESSMENT OF RELATIVE BIOLOGICAL EFFECTIVENESS
IN CARBON ION RADIOTHERAPY

A

THESIS

Presented to the Faculty of
The University of Texas

MD Anderson Cancer Center UTHealth

Graduate School of Biomedical Sciences
in Partial Fulfillment

of the Requirements

for the Degree of

MASTER OF SCIENCE

by

Shannon Hartzell, B.S., B.A.
Houston, Texas

August 2019

Dedication

To my parents, Andy and Karen, for their endless support, and for forcing me to take physics classes instead of art in high school.

Acknowledgements

I would like to thank my advisor, Dr. Stephen Kry, for introducing me to an exciting subject within medical physics and for providing guidance along the way.

I would also like to both acknowledge and thank my committee members for their valuable feedback and time throughout this process: Dr. Fada Guan, Dr. Oleg Vassiliev, Dr. Christine Peterson, and Ms. Paige Taylor.

Finally, I would like to express my gratitude to all of my family and friends for their continuous support.

QUANTIFYING UNCERTAINTY IN A MEASUREMENT-BASED ASSESSMENT OF RELATIVE BIOLOGICAL EFFECTIVENESS IN CARBON ION RADIOTHERAPY

Shannon Hartzell, B.S., B.A.

Advisory Professor: Stephen Kry, Ph.D.

One of the largest inconsistencies in dose delivered during carbon ion therapy is due to uncertainties in relative biological effectiveness (RBE), a value that is calculated via one of several clinically implemented algorithms. This study investigates the uncertainty in measured microdosimetric parameters for RBE calculation by the Microdosimetric Kinetic Model (MKM), Repair Misrepair Fixation model (RMF), and Local Effect Model I (LEM) using a Tissue Equivalent Proportional Counter (TEPC).

Microdosimetric spectra, kinetic energy spectra, and dose fragment contributions were calculated using Monte Carlo (GEANT IV) for monoenergetic and SOBP carbon beams of clinical energy. From microdosimetric spectra, lineal energy values were calculated as functions of beam energy and depth and used to calculate RBE based on MKM and RMF. From kinetic energy spectra and dose fragment contributions, RBE was calculated with LEM. To allow the assessment of RBE by RMF and LEM using microdosimetry, a method of estimating RBE from microdosimetric input values was then created with less than 5% error, on average, across all clinical energies and SOBPs.

The impact on the RBE from eight unique random or systematic sources of uncertainty associated with TEPC measurements were then simulated including electronic uncertainty, gas pressure, W-value, energy calibration, low energy cut-off, counting statistics, wall effects and pulse pile-up. These sources were quantified by statistically introducing uncertainty into the simulated measurements 200 times and sampling the resultant RBE associated with each of the 200 perturbations. The uncertainty introduced by the sources of physical noise varied depending on the model used, measurement depth, and beam energy.

The largest source of uncertainty was associated with the W-value (i.e., detector calibration), which had an uncertainty of typically 2% (1σ). Overall, the total 1σ uncertainty in the MKM based on uncertainty in TEPC measurements ranged from 2-4%. Uncertainty ranging from 2-12% was seen for RMF and LEM, incorporating error due to microdosimetric estimation. While the true RBE has extensive uncertainty associated with it, the modeled RBE can be measured with good accuracy, within a 5% deviation for MKM, which meets the reasonable tolerance goal for assessing delivered dose. For RMF and LEM, this threshold is exceeded in several individual cases (i.e. certain depths within specific beams),

but is met on average. The number of cases in which this threshold is met can be increased by applying a common correction factor for both measurement and estimation based bias.

Table of Contents

Dedication	i
Acknowledgements.....	ii
1 Introduction and Background.....	1
1.1 Statement of Problem	1
1.1.1 General Problem	1
1.1.2 Specific Problem.....	2
1.2 Carbon Ion Radiotherapy.....	2
1.2.1 Introduction	2
1.2.2 Beam Delivery	7
1.3 Microdosimetry	9
1.3.1 Introduction	9
1.3.2 Lineal Energy.....	12
1.3.3 Tissue Equivalent Proportional Counter (TEPC).....	14
1.4 Relative Biological Effectiveness	16
1.4.1 Introduction	16
1.4.2 Microdosimetric-Kinetic Model	20
1.4.3 Repair-Misrepair Fixation Model	24
1.4.4 Local Effect Model	27
1.4.5 Comparison	31

1.5	Consistency in Radiotherapy	32
1.5.1	IROC Houston	34
1.5.2	Carbon Radiotherapy	34
1.6	Hypothesis	35
1.6.1	Specific Aims	35
2	Specific Aim 1.....	36
2.1	Introduction	36
2.1.1	LET-1/2	36
2.1.2	Uncertainty Analysis	40
2.2	Materials and Methods.....	47
2.2.1	Clinical Beam	48
2.2.2	Monte Carlo	49
2.2.3	Uncertainty Analysis	51
2.3	Results	65
2.3.1	Monte Carlo	65
2.3.2	Uncertainty Analysis	71
2.4	Discussion	99
3	Specific Aim 2.....	99
3.1	Introduction	99
3.2	Materials and Methods.....	100

3.2.1	Monte Carlo	100
3.2.2	MKM.....	101
3.2.3	RMF	102
3.2.4	LEM.....	105
3.2.5	Adding Uncertainty	130
3.3	Results	131
3.3.1	Monte Carlo	132
3.3.2	MKM.....	138
3.3.3	RMF	148
3.3.4	LEM.....	169
3.4	Discussion	196
3.4.1	MKM.....	196
3.4.2	RMF	196
3.4.3	LEM.....	197
4	Conclusions	198
5	Appendix.....	200
5.1	Microdosimetry	200
5.1.1	146 MeV/u Monoenergetic Beam	200
5.1.2	218 MeV/u Monoenergetic Beam	203
5.1.3	276 MeV/u Monoenergetic Beam	206

5.1.4	330 MeV/u Monoenergetic Beam	209
5.1.5	424 MeV/u Monoenergetic Beam	212
5.1.6	5 cm SOBP	215
5.1.7	7 cm SOBP	218
5.1.8	10 cm SOBP	221
5.2	Alpha and Beta values of Each Model	224
5.2.1	Alpha Values	224
5.2.2	Beta Values	228
5.3	RBE.....	232
5.4	Biological Dose.....	236
5.5	Kinetic Energy	240
5.5.1	146 MeV/u.....	240
5.5.2	424 MeV/u.....	244
5.5.3	7 cm SOBP	248
5.6	Energy Deposition	252
6	References	255
7	Vita.....	261

List of Figures

Figure 1. Example of a carbon Bragg peak, located at a depth of 30 cm, for a 424 MeV/u monoenergetic beam. The dose is normalized to 1 Gy at the entrance. ...	4
Figure 2. Example of a carbon SOBPs weighted to deliver 2 Gy to a 7 cm target.	6
Figure 3. LEM α as a function of kinetic energy for primary carbons and all relevant fragments.	29
Figure 4. LEM β as a function of kinetic energy for primary carbons and all relevant fragments.	30
Figure 5. Diagram of the LET-1/2 manufactured by Far West Technologies. Figure adapted from the user manual [11].	38
Figure 6. Displays the electronic interconnection components of the LET-1/2 as described in the operation manual [11].	39
Figure 7. Example of one iteration of the frequency spectra shifted to a higher lineal energy bin (spectra shifts right), applied to all spectra (i.e., all depths) for a single initial carbon energy.	54
Figure 8. Example of one iteration of the dose spectra shifted to a higher lineal energy bin (spectra shifts right), applied to all spectra (i.e., all depths) for a single initial carbon energy.	54
Figure 9. Example of one iteration of the frequency spectra shifted to a higher number of counts per bin (spectra shifts up), applied to all spectra (i.e., all depths) for a single initial carbon energy.	55

Figure 10. Example of one iteration of the dose spectra shifted to a higher number of counts per bin (spectra shifts up), applied to all spectra (i.e., all depths) for a single initial carbon energy.	55
Figure 11. Displays the W-value of substantial dose contributing ion species as a function of kinetic energy in water. Data points are taken from [11].	59
Figure 12. Frequency spectra for a 146 MeV/u monoenergetic beam. The red dotted line is located at 0.5 keV/ μ m on a log scale to localize the threshold of the low energy cutoff.	61
Figure 13. Frequency distribution measured with walled and wall-less TEPC. Monte Carlo calculated distribution presented for comparison [28].	64
Figure 14. Monte Carlo calculated microdosimetric frequency spectra for 146 MeV/u monoenergetic beam. Curves show the spectra for different depths, ranging from 0 to 40 cm at 0.1 cm intervals.	66
Figure 15. Monte Carlo calculated microdosimetric frequency spectra for 424 MeV/u monoenergetic beam. Curves show the spectra for different depths, ranging from 0 to 40 cm at 0.1 cm intervals.	67
Figure 16. Monte Carlo calculated microdosimetric frequency spectra for 7 cm SOBP. Curves show the spectra for different depths, ranging from 0 to 40 cm at 0.1 cm intervals.	67
Figure 17. Monte Carlo calculated microdosimetric dose spectra at 146 MeV/u beam energy. Curves show the spectra for different depths, ranging from 0 to 40 cm at 0.1 cm intervals.	68

Figure 18. Monte Carlo calculated microdosimetric dose spectra at 424 MeV/u beam energy. Curves show the spectra for different depths, ranging from 0 to 40 cm at 0.1 cm intervals.....	68
Figure 19. Monte Carlo calculated microdosimetric dose spectra for 7 cm SOBP. Curves show the spectra for different depths, ranging from 0 to 40 cm at 0.1 cm intervals.	69
Figure 20. Frequency mean lineal energy values calculated as a function of depth for 146 MeV/u monoenergetic, 424 MeV/u monoenergetic, and 7 cm SOBP beams.....	70
Figure 21. Dose mean lineal energy values calculated as a function of depth for 146 MeV/u monoenergetic, 424 MeV/u monoenergetic, and 7 cm SOBP beams.	70
Figure 22. Saturation corrected dose mean lineal energy values calculated as a function of depth for 146 MeV/u monoenergetic, 424 MeV/u monoenergetic, and 7 cm SOBP beams.	71
Figure 23. The large figure on the top shows the original frequency weighted spectra on a linear x-axis for scale reference. The middle left figure displays the original microdosimetric spectra below 0.5 keV/ μ m zoomed in. The other three figures display each of three simulated tails appended to the microdosimetric spectrum at 0.5 keV/ μ m.....	79
Figure 24. Probability of pulse pile-up as a function of count rate (pps). Note that the scale for count rate is $\times 10^6$	83

Figure 25. Average bias introduced to MKM RBE by pulse pile-up as a function of count rate.	84
Figure 26. Average bias introduced to RBE_{RMF} by pulse pile-up as a function of count rate.	84
Figure 27. Average bias introduced to RBE_{LEM} by pulse pile-up as a function of count rate. Both entrance regions and Bragg peak are shown.....	85
Figure 28. Example of the dose weighted microdosimetric spectra for both original and pile-up situations at a dose rate of $2.5E5$ pps.	86
Figure 29. Example of the dose weighted microdosimetric spectra for both original and pile-up situations at a dose rate of $2.5E5$ pps.	86
Figure 30. Example of the dose weighted microdosimetric spectra for both original and pile-up situations at a dose rate of $2.5E5$ pps.	87
Figure 31. Example of the dose weighted microdosimetric spectra for both original and pile-up situations at a dose rate of $4E5$ pps, the count rate at which uncertainty began to drastically increase through the RBE models. This example is for a 146 MeV/u beam.	87
Figure 32. Example of the frequency weighted microdosimetric spectra for both original and wall effect simulations. Note the log scale on both the x- and y-axis.	91
Figure 33. Frequency mean lineal energy with added bias and uncertainty as a function of depth for 146 MeV/u monoenergetic beam.	93
Figure 34. Dose mean lineal energy with added bias and uncertainty as a function of depth for 146 MeV/u monoenergetic beam.	94

Figure 35. Saturation corrected dose mean lineal energy with added bias and uncertainty as a function of depth for 146 MeV/u monoenergetic beam.	94
Figure 36. Frequency mean lineal energy with added bias and uncertainty as a function of depth for 424 MeV/u monoenergetic beam.	95
Figure 37. Dose mean lineal energy with added bias and uncertainty as a function of depth for 424 MeV/u monoenergetic beam.	95
Figure 38. Saturation corrected dose mean lineal energy with added bias and uncertainty as a function of depth for 424 MeV/u monoenergetic beam.	96
Figure 39. RMF α values calculated by Monte Carlo and estimated by fit (solid line).	104
Figure 40. RMF β values calculated by Monte Carlo and estimated by fit (solid line).	104
Figure 41. LEM α values calculated by Monte Carlo and estimated by fit (solid line).	107
Figure 42. True LEM β values (based on Monte Carlo calculations and the definition of LEM), and those estimated by a polynomial fit based on y^* (solid line).	107
Figure 43. Microdosimetric spectra of a 300 MeV/u carbon beam subdivided by fragment using MCHIT calculations [32].	109
Figure 44. Frequency weighted microdosimetric spectra at entrance, Bragg peak, and tail regions for 146 MeV/u monoenergetic beam.	111
Figure 45. Frequency weighted microdosimetric spectra at entrance, Bragg peak, and tail regions for 424 MeV/u monoenergetic beam.	112

Figure 46. Frequency weighted microdosimetric spectra at entrance, SOBP, and tail regions for 7 cm SOBP.	112
Figure 47. Frequency weighted microdosimetric spectra cut into primary and secondary peaks for 146 MeV/u monoenergetic beam.....	114
Figure 48. Dose weighted microdosimetric spectra cut into primary and secondary peaks for 146 MeV/u monoenergetic beam.....	114
Figure 49. Frequency weighted microdosimetric spectra cut into primary and secondary peaks for 424 MeV/u monoenergetic beam.....	115
Figure 50. Dose weighted microdosimetric spectra cut into primary and secondary peaks for 424 MeV/u monoenergetic beam.....	115
Figure 51. Frequency weighted microdosimetric spectra cut into primary and secondary peaks for 7 cm SOBP.	116
Figure 52. Dose weighted microdosimetric spectra cut into primary and secondary peaks for 7 cm SOBP.	117
Figure 53. Shows the primary α values as a function of $y * Primary$ calculated by Monte Carlo for 146 MeV/u and 424 MeV/u monoenergetic beams and fit with the polynomial described in Table 22. Primary carbon α values are shown in blue, while boron α values are shown in yellow. The solid lines represent the fit polynomials.	118
Figure 54. Shows the primary β values as functions of $y * Primary$ calculated by Monte Carlo for 146 MeV/u and 424 MeV/u monoenergetic beams and fit with the polynomial described in Table 20. Primary carbon β values are shown in blue,	

while boron β values are shown in yellow. The solid lines represent the fit polynomials. 119

Figure 55. Shows the primary alpha values as a function of $y * Primary$ calculated by Monte Carlo for the 7 cm SOBP and fit with the polynomial described in Table 23. Primary carbon α values are shown in blue, while boron α values are shown in yellow. The solid lines represent the fit polynomials..... 120

Figure 56. Shows the primary β values as functions of $y * Primary$ calculated by Monte Carlo for a 7 cm SOBP and fit with the polynomial described in Table 23. Primary carbon β values are shown in blue, while boron β values are shown in yellow. The solid lines represent the fit polynomials. 120

Figure 57. Shows the secondary alpha values as a function of $y * Secondary$ calculated by Monte Carlo for 146 MeV/u and 424 MeV/u monoenergetic beams and fit with the polynomial described in Table 24. Helium α values are shown in purple, while proton α values are shown in orange. The solid lines represent the fit polynomials. 122

Figure 58. Shows the secondary β values as a function of $y * Secondary$ calculated by Monte Carlo for 146 MeV/u and 424 MeV/u monoenergetic beams and fit with the polynomial described in Table 24. Helium β values are shown in purple, while proton β values are shown in orange. The solid lines represent the fit polynomials. 122

Figure 59. Shows the secondary alpha values as a function of $y * Secondary$ calculated by Monte Carlo for a 7 cm SOBP and fit with the polynomial described

in Table 26. Helium α values are shown in purple, while proton α values are shown in orange. The solid lines represent the fit polynomials.....	123
Figure 60. Shows the secondary β values as a function of $y * Secondary$ calculated by Monte Carlo for a 7 cm SOBP and fit with the polynomial described in Table 25. Helium β values are shown in purple, while proton β values are shown in orange. The solid lines represent the fit polynomials.....	124
Figure 61. Contribution of carbon and boron calculated with Monte Carlo (solid lines) and that estimated by the cut spectra (dashed lines) for 146 MeV/u monoenergetic beam. Carbon contribution is shown in blue and boron contribution is shown in yellow.....	127
Figure 62. Contribution of helium and protons calculated with Monte Carlo (solid lines) and that estimated by the cut spectra (dashed lines) for 146 MeV/u monoenergetic beam. Helium contribution is shown in purple and boron contribution is shown in orange.....	128
Figure 63. Contribution of carbon and boron calculated with Monte Carlo (solid lines) and that estimated by the cut spectra (dashed lines) for a 424 MeV/u monoenergetic beam. Carbon contribution is shown in blue and boron contribution is shown in yellow.....	128
Figure 64. Contribution of helium and protons calculated with Monte Carlo (solid lines) and that estimated by the cut spectra (dashed lines) for a 424 MeV/u monoenergetic beam. Helium contribution is shown in purple and boron contribution is shown in orange.....	129

Figure 65. Contribution of carbon and boron calculated with Monte Carlo (solid lines) and that estimated by the cut spectra (dashed lines) for a 7 cm SOBP. Carbon contribution is shown in blue and boron contribution is shown in yellow.	129
Figure 66. Contribution of helium and protons calculated with Monte Carlo (solid lines) and that estimated by the cut spectra (dashed lines) for a 7 cm SOBP. Helium contribution is shown in purple and boron contribution is shown in orange.	130
Figure 67. Energy deposition by each fragment as a function of depth for 146 MeV/u monoenergetic beam.	133
Figure 68. Energy deposition by each fragment as a function of depth for 424 MeV/u monoenergetic beam.	133
Figure 69. Energy deposition by each fragment as a function of depth for 7 cm SOBP.	134
Figure 70. Kinetic energy distribution of primary carbon at five different depths between the entrance and Bragg peak for a 146 MeV/u monoenergetic beam.	135
Figure 71. Average kinetic energy as a function of depth for primary carbons and secondary fragments for a 146 MeV/u monoenergetic beam.	136
Figure 72. Kinetic energy distribution of primary carbon at five different depths between the entrance and Bragg peak for a 424 MeV/u monoenergetic beam.	136
Figure 73. Average kinetic energy as a function of depth for primary carbons and secondary fragments for a 424 MeV/u monoenergetic beam.	137

Figure 74. Kinetic energy distribution of primary carbon at five different depths between the entrance and Bragg peak for a 7 cm SOBP.	137
Figure 75. Average kinetic energy as a function of depth for primary carbons and secondary fragments for a 7 cm SOBP.	138
Figure 76. RBE and biological dose calculated with MKM for 146 MeV/u monoenergetic beam.	139
Figure 77. RBE and biological dose calculated with MKM for 424 MeV/u monoenergetic beam.	139
Figure 78. RBE and biological dose calculated with MKM for 7 cm SOBP.	140
Table 27 and is broken down by bias introduced by each source, as well as total bias. The bias was low in the entrance and Bragg peak regions, and did not exceed 2.8%. The bias introduced in the 424 MeV/u monoenergetic beam was, on average, roughly 1% higher than the bias introduced to 146 MeV/u or 7 cm SOBP beam. The pulse pile-up was the greatest contributor to the overall bias for this model. The RBE with bias is shown against purely Monte Carlo calculated RBE in Table 27 for reference. The variance is similarly presented in Table 28. The variance in MKM due to all of the noise sources summed in quadrature was, at most, 2.2%. The variance in the 146 MeV/u monoenergetic beam was typically 25% higher than that of the other beams. Error bars corresponding to the 1σ standard deviation about the perturbed RBE are shown in Figure 79 - Figure 80, with the true RBE plotted in orange for reference.	140

Figure 81. RBE_{MKM} with added bias (blue line) and uncertainty (error bars) as a function of depth for 146 MeV/u monoenergetic beam. Monte Carlo calculated RBE shown in orange.....	143
Figure 82. RBE_{MKM} with added bias (blue line) and uncertainty (error bars) as a function of depth for 218 MeV/u monoenergetic beam. Monte Carlo calculated RBE shown in orange.	144
Figure 83. RBE_{MKM} with added bias (blue line) and uncertainty (error bars) as a function of depth for 276 MeV/u monoenergetic beam. Monte Carlo calculated RBE shown in orange.....	144
Figure 84. RBE_{MKM} with added bias (blue line) and uncertainty (error bars) as a function of depth for 330 MeV/u monoenergetic beam. Monte Carlo calculated RBE shown in orange.....	145
Figure 85. RBE_{MKM} with added bias (blue line) and uncertainty (error bars) as a function of depth for 424 MeV/u monoenergetic beam. Monte Carlo calculated RBE shown in orange.....	145
Figure 86. RBE_{MKM} with added bias (blue line) and uncertainty (error bars) as a function of depth for a 5 cm SOBP. Monte Carlo calculated RBE shown in orange.	146
Figure 87. RBE_{MKM} with added bias (blue line) and uncertainty (error bars) as a function of depth for a 7 cm SOBP. Monte Carlo calculated RBE shown in orange.	146

Figure 88. RBE_{MKM} with added bias (blue line) and uncertainty (error bars) as a function of depth for a 10 cm SOBP. Monte Carlo calculated RBE shown in orange.	147
Figure 89. RBE (right axis) and biological dose (left axis) calculated with RMF for 146 MeV/u monoenergetic beam. Physical dose normalized to 1 Gy at the entrance is plotted in the dotted line for reference.	149
Figure 90. RBE (right axis) and biological dose (left axis) calculated with RMF for 424 MeV/u monoenergetic beam. Physical dose normalized to 1 Gy at the entrance is plotted in the dotted line for reference.	149
Figure 91. RBE (right axis) and biological dose (left axis) calculated with RMF for 7 cm SOBP. Physical dose normalized to 2 Gy throughout the SOBP is plotted in the dotted line for reference.	150
Figure 92. Estimated and Monte Carlo calculated RBE_{RMF} values for a 146 MeV/u monoenergetic beam. Percent difference between the two values is shown on the right axis.	152
Figure 93. Estimated and Monte Carlo calculated RBE_{RMF} values for a 218 MeV/u monoenergetic beam. Percent difference between the two values is shown on the right axis.	152
Figure 94. Estimated and Monte Carlo calculated RBE_{RMF} values for a 276 MeV/u monoenergetic beam. Percent difference between the two values is shown on the right axis.	153

Figure 95. Estimated and Monte Carlo calculated RBE_{RMF} values for a 330 MeV/u monoenergetic beam. Percent difference between the two values is shown on the right axis.	153
Figure 96. Estimated and Monte Carlo calculated RBE_{RMF} values for a 424 MeV/u monoenergetic beam. Percent difference between the two values is shown on the right axis.	154
Figure 97. Estimated and Monte Carlo calculated RBE_{LEM} values for a 5 cm SOBP. Percent difference between the two values is shown on the right axis.	154
Figure 98. Estimated and Monte Carlo calculated RBE_{LEM} values for a 7 cm SOBP. Percent difference between the two values is shown on the right axis.	155
Figure 99. Estimated and Monte Carlo calculated RBE_{LEM} values for a 10 cm SOBP.	155
Figure 100. Estimated RBE_{RMF} with added bias (blue line) and uncertainty (error bars) as a function of depth for 146 MeV/u monoenergetic beam. Monte Carlo calculated RBE shown in orange.	162
Figure 101. Estimated RBE_{RMF} with added bias (blue line) and uncertainty (error bars) as a function of depth for 218 MeV/u monoenergetic beam. Monte Carlo calculated RBE shown in orange.	162
Figure 102. Estimated RBE_{RMF} with added bias (blue line) and uncertainty (error bars) as a function of depth for 276 MeV/u monoenergetic beam. Monte Carlo calculated RBE shown in orange.	163

Figure 103. Estimated RBE_{RMF} with added bias (blue line) and uncertainty (error bars) as a function of depth for 330 MeV/u monoenergetic beam. Monte Carlo calculated RBE shown in orange.	163
Figure 104. Estimated RBE_{RMF} with added bias (blue line) and uncertainty (error bars) as a function of depth for 424 MeV/u monoenergetic beam. Monte Carlo calculated RBE shown in orange.	164
Figure 105. Estimated RBE_{RMF} with added bias (blue line) and uncertainty (error bars) as a function of depth for 5 cm SOBP. Monte Carlo calculated RBE shown in orange.	164
Figure 106. Estimated RBE_{RMF} with added bias (blue line) and uncertainty (error bars) as a function of depth for 7 cm SOBP. Monte Carlo calculated RBE shown in orange.	165
Figure 107. Estimated RBE_{RMF} with added bias (blue line) and uncertainty (error bars) as a function of depth for 10 cm SOBP. Monte Carlo calculated RBE shown in orange.	165
Figure 108. RBE (right axis) and biological dose (left axis) calculated with LEM for 146 MeV/u monoenergetic beam. Physical dose normalized to 1 Gy at the entrance plotted for reference.	169
Figure 109. RBE (right axis) and biological dose (left axis) calculated with LEM for 424 MeV/u monoenergetic beam. Physical dose normalized to 1 Gy at the entrance plotted for reference.	170

Figure 110. RBE (right axis) and biological dose (left axis) calculated with LEM for a 7 cm SOBP. Physical dose normalized to 2 Gy across the SOBP plotted for reference.	170
Figure 111. Estimated and Monte Carlo calculated RBE_{LEM} values for a 146 MeV/u monoenergetic beam. Percent difference shown on the y-axis to the right.	172
Figure 112. Estimated and Monte Carlo calculated RBE_{LEM} values for a 218 MeV/u monoenergetic beam. Percent difference shown on the y-axis to the right.	172
Figure 113. Estimated and Monte Carlo calculated RBE_{LEM} values for a 276 MeV/u monoenergetic beam. Percent difference shown on the y-axis to the right.	173
Figure 114. Estimated and Monte Carlo calculated RBE_{LEM} values for a 330 MeV/u monoenergetic beam. Percent difference shown on the y-axis to the right.	173
Figure 115. Estimated and Monte Carlo calculated RBE_{LEM} values for a 424 MeV/u monoenergetic beam. Percent difference shown on the y-axis to the right.	174
Figure 116. Estimated and Monte Carlo calculated RBE_{LEM} values for a 5 cm SOBP. Percent difference shown on the y-axis to the right.	174
Figure 117. Estimated and Monte Carlo calculated RBE_{LEM} values for a 7 cm SOBP. Percent difference shown on the y-axis to the right.	175

Figure 118. Estimated and Monte Carlo calculated RBE_{LEM} values for a 10 cm SOBP. Percent difference shown on the y-axis to the right.	175
Figure 119. Estimated and Monte Carlo calculated RBE_{LEM} values for a 146 MeV/u monoenergetic beam. Percent difference shown on the right axis for reference.	178
Figure 120. Estimated and Monte Carlo calculated RBE_{LEM} values for a 218 MeV/u monoenergetic beam. Percent difference shown on the right axis for reference.	178
Figure 121. Estimated and Monte Carlo calculated RBE_{LEM} values for a 276 MeV/u monoenergetic beam. Percent difference shown on the right axis for reference.	179
Figure 122. Estimated and Monte Carlo calculated RBE_{LEM} values for a 330 MeV/u monoenergetic beam. Percent difference shown on the right axis for reference.	179
Figure 123. Estimated and Monte Carlo calculated RBE_{LEM} values for a 424 MeV/u monoenergetic beam. Percent difference shown on the right axis for reference.	180
Figure 124. Estimated and Monte Carlo calculated RBE_{LEM} values for a 5 cm SOBP. Percent difference shown on the right axis for reference.	180
Figure 125. Estimated and Monte Carlo calculated RBE_{LEM} values for a 7 cm SOBP. Percent difference shown on the right axis for reference.	181
Figure 126. Estimated and Monte Carlo calculated RBE_{LEM} values for a 10 cm SOBP. Percent difference shown on the right axis for reference.	181

Figure 127. Estimated RBE_{LEM} with added bias (blue line) and uncertainty (error bars) as a function of depth for 146 MeV/u monoenergetic beam. Monte Carlo calculated RBE shown in orange.	189
Figure 128. Estimated RBE_{LEM} with added bias (blue line) and uncertainty (error bars) as a function of depth for 218 MeV/u monoenergetic beam. Monte Carlo calculated RBE shown in orange.	189
Figure 129. Estimated RBE_{LEM} with added bias (blue line) and uncertainty (error bars) as a function of depth for 276 MeV/u monoenergetic beam. Monte Carlo calculated RBE shown in orange.	190
Figure 130. Estimated RBE_{LEM} with added bias (blue line) and uncertainty (error bars) as a function of depth for 330 MeV/u monoenergetic beam. Monte Carlo calculated RBE shown in orange.	190
Figure 131. Estimated RBE_{LEM} with added bias (blue line) and uncertainty (error bars) as a function of depth for 424 MeV/u monoenergetic beam. Monte Carlo calculated RBE shown in orange.	191
Figure 132. Estimated RBE_{LEM} with added bias (blue line) and uncertainty (error bars) as a function of depth for a 5 cm SOBP. Monte Carlo calculated RBE shown in orange. Estimated RBE reached values of -5 in the tail, and were cutoff to maintain an appropriate scale in the entrance and Bragg peak region.	191
Figure 133. Estimated RBE_{LEM} with added bias (blue line) and uncertainty (error bars) as a function of depth for a 7 cm SOBP. Monte Carlo calculated RBE shown in orange. Estimated RBE reached values of -5 in the tail, and were cutoff to maintain an appropriate scale in the entrance and Bragg peak region.	192

Figure 134. Estimated RBE_{LEM} with added bias (blue line) and uncertainty (error bars) as a function of depth for a 10 cm SOBP. Monte Carlo calculated RBE shown in orange. Estimated RBE reached values of -2 in the tail, and were cutoff to maintain an appropriate scale in the entrance and Bragg peak region.	192
Figure 135. Alpha calculated with all RBE models for 146 MeV/u monoenergetic beam.	224
Figure 136. Alpha calculated with all RBE models for 146 MeV/u monoenergetic beam.	224
Figure 137. Alpha calculated with all RBE models for 146 MeV/u monoenergetic beam.	225
Figure 138. Alpha calculated with all RBE models for 146 MeV/u monoenergetic beam.	225
Figure 139. Alpha calculated with all RBE models for 424 MeV/u monoenergetic beam.	226
Figure 140. Alpha calculated with all RBE models for 5 cm SOBP.	226
Figure 141. Alpha calculated with all RBE models for 7 cm SOBP.	227
Figure 142 Alpha calculated with all RBE models for 10 cm SOBP.	227
Figure 143. Beta calculated with all RBE models for 146 MeV/u monoenergetic beam.	228
Figure 144. Beta calculated with all RBE models for 218 MeV/u monoenergetic beam.	228
Figure 145. Beta calculated with all RBE models for 276 MeV/u monoenergetic beam.	229

Figure 146. Beta calculated with all RBE models for 330 MeV/u monoenergetic beam.	229
Figure 147. Beta calculated with all RBE models for 424 MeV/u monoenergetic beam.	230
Figure 148. Beta calculated with all RBE models for 5 cm SOBP.	230
Figure 149. Beta calculated with all RBE models for a 7 cm SOBP.	231
Figure 150. Beta calculated with all RBE models for a 10 cm SOBP.	231
Figure 151. RBE calculated with each model for 146 MeV/u monoenergetic beam.	232
Figure 152. RBE calculated with each model for 218 MeV/u monoenergetic beam.	232
Figure 153. RBE calculated with each model for 276 MeV/u monoenergetic beam.	233
Figure 154. RBE calculated with each model for 330 MeV/u monoenergetic beam.	233
Figure 155. RBE calculated with each model for 424 MeV/u monoenergetic beam.	234
Figure 156. RBE calculated with each model for a 5 cm SOBP.	234
Figure 157. RBE calculated with each model for a 7 cm SOBP.	235
Figure 158. RBE calculated with each model for a 10 cm SOBP.	235
Figure 159. Biological dose calculated with each model for 146 MeV/u monoenergetic beam. Physical dose showed by the dotted line for reference.	236

Figure 160. Biological dose calculated with each model for 218 MeV/u monoenergetic beam. Physical dose showed by the dotted line for reference.	236
Figure 161. Biological dose calculated with each model for 276 MeV/u monoenergetic beam. Physical dose showed by the dotted line for reference.	237
Figure 162. Biological dose calculated with each model for 330 MeV/u monoenergetic beam. Physical dose showed by the dotted line for reference.	237
Figure 163. Biological dose calculated with each model for 424 MeV/u monoenergetic beam. Physical dose showed by the dotted line for reference.	238
Figure 164. Biological dose calculated with each model for a 5 cm SOBP. Physical dose showed by the dotted line for reference.	238
Figure 165. Biological dose calculated with each model for a 7 cm SOBP. Physical dose showed by the dotted line for reference.	239
Figure 166. Biological dose calculated with each model for a 10 cm SOBP. Physical dose showed by the dotted line for reference.	239
Figure 167. Average kinetic energy of each fragment for a 146 MeV/u monoenergetic beam.	240
Figure 168. Kinetic energy distribution of primary carbons at the following depths for a 146 MeV/u monoenergetic beam: 10 mm, 20 mm, 30 mm, 40 mm, and 50 mm.	240
Figure 169. Kinetic energy distribution of secondary H at the following depths for a 146 MeV/u monoenergetic beam: 10 mm, 20 mm, 30 mm, 40 mm, and 50 mm.	241

Figure 170. Kinetic energy distribution of secondary He at the following depths for a 146 MeV/u monoenergetic beam: 10 mm, 20 mm, 30 mm, 40 mm, and 50 mm.....	241
Figure 171. Kinetic energy distribution of secondary Li at the following depths for a 146 MeV/u monoenergetic beam: 10 mm, 20 mm, 30 mm, 40 mm, and 50 mm.	242
Figure 172. Kinetic energy distribution of secondary Be at the following depths for a 146 MeV/u monoenergetic beam: 10 mm, 20 mm, 30 mm, 40 mm, and 50 mm.	242
Figure 173. Kinetic energy distribution of secondary B at the following depths for a 146 MeV/u monoenergetic beam: 10 mm, 20 mm, 30 mm, 40 mm, and 50 mm.	243
Figure 174. Kinetic energy distribution of secondary carbons at the following depths for a 146 MeV/u monoenergetic beam: 10 mm, 20 mm, 30 mm, 40 mm, and 50 mm.	243
Figure 175. Kinetic energy distribution of primary carbons at the following depths for a 424 MeV/u monoenergetic beam: 5 mm, 50 mm, 100 mm, 150 mm, 200 mm, 250 mm, 300 mm, 350 mm, 400 mm.	244
Figure 176. Kinetic energy distribution of secondary H at the following depths for a 424 MeV/u monoenergetic beam: 5 mm, 50 mm, 100 mm, 150 mm, 200 mm, 250 mm, 300 mm, 350 mm, 400 mm.	245

Figure 177. Kinetic energy distribution of secondary He at the following depths for a 424 MeV/u monoenergetic beam: 5 mm, 50 mm, 100 mm, 150 mm, 200 mm, 250 mm, 300 mm, 350 mm, 400 mm.	245
Figure 178. Kinetic energy distribution of secondary Li at the following depths for a 424 MeV/u monoenergetic beam: 5 mm, 50 mm, 100 mm, 150 mm, 200 mm, 250 mm, 300 mm, 350 mm, 400 mm.	246
Figure 179. Kinetic energy distribution of secondary Be at the following depths for a 424 MeV/u monoenergetic beam: 5 mm, 50 mm, 100 mm, 150 mm, 200 mm, 250 mm, 300 mm, 350 mm, 400 mm.	246
Figure 180. Kinetic energy distribution of secondary B at the following depths for a 424 MeV/u monoenergetic beam: 5 mm, 50 mm, 100 mm, 150 mm, 200 mm, 250 mm, 300 mm, 350 mm, 400 mm.	247
Figure 181. Kinetic energy distribution of secondary carbons at the following depths for a 424 MeV/u monoenergetic beam: 5 mm, 50 mm, 100 mm, 150 mm, 200 mm, 250 mm, 300 mm, 350 mm, 400 mm.	247
Figure 182. Average kinetic energy as a function of depth by each fragment in a 7 cm SOBP.	248
Figure 183. Kinetic energy distribution of primary carbons at the following depths for a 7 cm SOBP: 5 mm, 25 mm, 50 mm, 75 mm, 100 mm, 125 mm, 150 mm.	248
<i>Figure 184. Kinetic energy distribution of secondary H at the following depths for a 7 cm SOBP: 5 mm, 25 mm, 50 mm, 75 mm, 100 mm, 125 mm, 150 mm.</i>	<i>249</i>
Figure 185. Kinetic energy distribution of secondary He at the following depths for a 7 cm SOBP: 5 mm, 25 mm, 50 mm, 75 mm, 100 mm, 125 mm, 150 mm.	249

Figure 186. Kinetic energy distribution of secondary Li at the following depths for a 424 MeV/u monoenergetic beam: 5 mm, 25 mm, 50 mm, 75 mm, 100 mm, 125 mm, 150 mm.	250
Figure 187. Kinetic energy distribution of secondary Be at the following depths for a 7 cm SOBP: 5 mm, 25 mm, 50 mm, 75 mm, 100 mm, 125 mm, 150 mm.....	250
Figure 188. Kinetic energy distribution of secondary B at the following depths for a 7 cm SOBP: 5 mm, 25 mm, 50 mm, 75 mm, 100 mm, 125 mm, 150 mm.....	251
Figure 189. Kinetic energy distribution of secondary C at the following depths for a 7 cm SOBP: 5 mm, 25 mm, 50 mm, 75 mm, 100 mm, 125 mm, 150 mm.....	251
Figure 190. Energy deposition by fragment for a 218 MeV/u monoenergetic beam.	252
Figure 191. Energy deposition by fragment for a 276 MeV/u monoenergetic beam.	252
Figure 192. Energy deposition by fragment for a 330 MeV/u monoenergetic beam.	253
Figure 193. Energy deposition by fragment for a 5 cm SOBP.	253
Figure 194. Energy deposition by fragment for a 10 cm SOBP.	254

List of Tables

Table 1. Values for parameters used in each RBE model, where the subscript c indicates parameters specific to a carbon beam. The starred cell lines are the values used in these RBE calculations.	20
Table 2. Recommended operating specifications for the LET-1/2 for specific simulated diameters as a function of tissue equivalent gas used (methane vs. propane based) [11].....	37
Table 3. Parameters of clinical beams as indicated by each of 5 surveyed institutions.	48
Table 4. Depth of the Bragg peak for a range of monoenergetic beams, and both start and end depths of the SOBP.	51
Table 5. Percent standard deviation, at the 1σ level, introduced in lineal energy values by counting statistics.	73
Table 6. Percent standard deviation, at the 1σ level, introduced in lineal energy values by gas pressure and mean chord length.....	74
Table 7. Percent standard deviation, at the 1σ level, introduced in lineal energy values by electronic uncertainty.	75
Table 8. Percent standard deviation, at the 1σ level, introduced in lineal energy values by gain instability.	76
Table 9. Bias introduced to lineal energy values by W-value calibration. Expressed as a percent difference between the perturbed values and true lineal energy values.....	77

Table 10. Percent standard deviation, at the 1σ level, introduced in lineal energy values by W-value calibration.....	78
Table 11. Percent difference in RBE between the Monte Carlo spectra and spectra where the cutoff model replace Monte Carlo below 0.5 keV/ μ m.	80
Table 12. Bias introduced to lineal energy values by low energy cutoff. Expressed as a percent difference between the perturbed values and true lineal energy values.....	81
Table 13. Percent standard deviation, at the 1σ level, introduced in lineal energy values by low energy cutoff.	82
Table 14. Shows the bias introduced to lineal energy values by pulse pile-up in the entrance and Bragg peak regions with a particle rate of 2.5E5 particles per second. Bias is expressed as a percent difference between the perturbed values and true lineal energy values.	89
Table 15. Displays the percent standard deviation, at the 1σ level, introduced in lineal energy values by pulse pile-up for the entrance and Bragg peak regions with a particle rate of 2.5E5 particles per second.....	90
Table 16. Average bias introduced to lineal energy values by wall effects in the entrance and Bragg peak regions, expressed as a percent difference between the perturbed values and true lineal energy values.....	92
Table 17. Percent standard deviation, at the 1σ level, introduced in lineal energy values by wall effects for the entrance and Bragg peak regions.	92

Table 18. Average bias introduced to lineal energy values by systematic sources of error (W-value calibration, low energy cutoff, pulse pile-up, and wall effects) in the entrance and Bragg peak regions.....	98
Table 19. Average variance introduced to lineal energy values by systematic sources of error (W-value calibration, low energy cutoff, pulse pile-up, and wall effects) in the entrance and Bragg peak regions.....	98
Table 20. Polynomial variables used to estimate RMF β values.	105
Table 21. Polynomial variables used to estimate LEM α and β values.	108
Table 22. Polynomial variables used to estimate α and β values of the primary peak of monoenergetic beams.	119
Table 23. Polynomial variables used to estimate α and β values of the primary peak of SOBP spectra.	121
Table 24. Polynomial variables used to estimate α and β values of the secondary peak of monoenergetic beams.	123
Figure 60. Shows the secondary β values as a function of $y * \textit{Secondary}$ calculated by Monte Carlo for a 7 cm SOBP and fit with the polynomial described in Table 25. Helium β values are shown in purple, while proton β values are shown in orange. The solid lines represent the fit polynomials.....	124
Table 26. Polynomial variables used to estimate α and β values of the secondary peak of SOBP spectra.	124
Table 27. Displays the bias introduced into calculated RBE_{MKM} by each source of uncertainty.....	141

Table 28. Variance introduced into calculated RBE_{MKM} by each source of uncertainty.....	142
Table 29. Total uncertainty introduced in RBE_{MKM} by physical measurement based noise.....	148
Table 30. Percent difference between RBE calculated by Monte Carlo and RBE calculated by estimation. Results are compared for test data sets (146 MeV/u, 424 MeV/u, 7 cm SOBP) to validation data sets (218 MeV/u, 276 MeV/u, 330 MeV/u, 5 cm SOBP, 10 cm SOBP).	151
Table 31. Bias introduced into calculated RBE_{RMF} by each source of uncertainty, expressed as a percent difference between the shifted and true RBE. Results are compared for test data sets (146 MeV/u, 424 MeV/u, 7 cm SOBP) to validation data sets (218 MeV/u, 276 MeV/u, 330 MeV/u, 5 cm SOBP, 10 cm SOBP). ...	157
Table 32. Variance introduced into calculated RBE_{RMF} by each source of uncertainty, expressed as a percent standard deviation at the 1σ level. Results are compared for test data sets (146 MeV/u, 424 MeV/u, 7 cm SOBP) to validation data sets (218 MeV/u, 276 MeV/u, 330 MeV/u, 5 cm SOBP, 10 cm SOBP).	159
Table 33. Total uncertainty in estimated RBE_{RMF} by each source assessed. ...	167
Table 34. Percent difference between RBE calculated by Monte Carlo simulations and estimated RBE. Results are compared for test data sets (146 MeV/u, 424 MeV/u, 7 cm SOBP) to validation data sets (218 MeV/u, 276 MeV/u, 330 MeV/u, 5 cm SOBP, 10 cm SOBP).....	176

Table 35. Percent difference between RBE calculated by Monte Carlo simulations and RBE calculated by cutting the microdosimetric spectra at select points in both the entrance region and Bragg peak. Results are compared for test data sets (146 MeV/u, 424 MeV/u, 7 cm SOBP) to validation data sets (218 MeV/u, 276 MeV/u, 330 MeV/u, 5 cm SOBP, 10 cm SOBP).	182
Table 36. Bias introduced into estimated RBE_{LEM} by each source of uncertainty, expressed as a percent difference between shifted and true RBE. Results are compared for test data sets (146 MeV/u, 424 MeV/u, 7 cm SOBP) to validation data sets (218 MeV/u, 276 MeV/u, 330 MeV/u, 5 cm SOBP, 10 cm SOBP). ...	184
Table 37. Variance introduced into estimated RBE_{LEM} by each source of uncertainty, expressed as percent uncertainty at the 1σ standard deviation level. Results are compared for test data sets (146 MeV/u, 424 MeV/u, 7 cm SOBP) to validation data sets (218 MeV/u, 276 MeV/u, 330 MeV/u, 5 cm SOBP, 10 cm SOBP).	186
Table 38. Total uncertainty in estimated RBE_{LEM} by each source assessed. ...	194
Table 40. Displays lineal energy values and RBE calculated by each model for 146 MeV/u monoenergetic beam.	200
Table 41. Displays lineal energy values and RBE calculated by each model for 218 MeV/u monoenergetic beam.	203
Table 42. Displays lineal energy values and RBE calculated by each model for 276 MeV/u monoenergetic beam.	206
Table 43. Displays lineal energy values and RBE calculated by each model for 330 MeV/u monoenergetic beam.	209

Table 44. Displays lineal energy values and RBE calculated by each model for a 424 MeV/u monoenergetic beam.	212
Table 45. Displays lineal energy values and RBE calculated by each model for a 5 cm SOBP.	215
Table 46. Shows the lineal energy values and RBE calculated by each model as a function of depth for a 7 cm SOBP.	218
Table 47. Shows the lineal energy values and RBE calculated by each model as a function of depth for a 10 cm SOBP.	221

1 Introduction and Background

1.1 Statement of Problem

1.1.1 General Problem

Carbon ion therapy is a novel modality used for the treatment of tumors that are unresectable, close to critical structures, or resistant to standard radiotherapy. This includes treatment of pancreatic cancer, which is largely untreatable with current radiotherapy (i.e., x-rays), and is the 3rd leading cause of cancer related death in the US. However, this potential is, at present, untested. There are currently 12 carbon centers operating clinically throughout the world, with 6 located in Japan, 2 in Germany, 2 in China, and 1 each in Italy and Austria. There are several other carbon centers also under construction (China, Japan, South Korea, and Taiwan), but there are no confirmed plans to date for carbon centers to be built in the United States. However, there are clinical trials in the United States that are collaborating with these facilities, raising a need for radiotherapy credentialing as required by the NCI. As part of this credentialing, IROC Houston QA Center would like to develop a means of evaluating the consistency of carbon treatment plan delivery.

A particularly important aspect of carbon therapy is the relative biological effectiveness (RBE) of the beam (i.e., how biologically potent are carbon ions compared to x-rays), a value that is calculated via one of several recognized algorithms. Currently, however, there exist no established processes with which the accuracy and consistency of these RBE estimates may be uniformly

assessed across models, which means that results from one institution cannot be reasonably compared to results from another institution and cannot effectively guide clinical practice at any other institution.

1.1.2 Specific Problem

While there are several RBE models currently employed in carbon ion research, only two are used clinically. This includes the Microdosimetric Kinetic Model (MKM) used in Japanese facilities, and the Local Effect Model (LEM) used primarily in European facilities. A large area of concern within carbon ion therapy lies with consistency in clinical RBE, particularly between the values presented in treatment planning systems as compared to those calculated using model specific parameters.

For consistent outcomes in radiation therapy, the dose must be delivered within 5% of the desired value. According to AAPM Report 85, a 5% change in dose may result in a 10%-20% change in tumor control probability and a 20%-30% impact on normal tissue complication rate [1]. Therefore to conduct clinical trials and compare patient outcomes, uncertainties, including in RBE, should be less than 5%.

1.2 Carbon Ion Radiotherapy

1.2.1 Introduction

Clinically used for the first time in 1995 at the Heavy Ion Medical Accelerator in Japan, carbon ion radiotherapy is presently garnering interest due to a wide range of recognized benefits. Particularly, carbons are useful for

targeting tumors that are unrespectable or resistant to standard radiotherapy techniques. Similar to standard radiation, carbon ions in radiotherapy are effective in initiating tumor cell death through DNA damage in the cell nucleus. Unlike standard radiation, however, carbon ions deposit enough energy to cause direct double strand breaks within the DNA, resulting in dramatically greater biological effects than typical radiation, which relies heavily on the creation of free radicals to result in DNA damage [2]. Carbon ions accomplish the direct double stand breaks due to the property of linear energy transfer (LET), defined as the amount of energy deposited per unit length. When carbon ions travel through matter, they begin to lose energy and slow down. As this happens, the ions start to lose energy at a greater rate, therefore increasing their LET. At the end of their range, the LET increases substantially, as does the dose distributed by the ions. This phenomenon, where the vast majority of the dose is deposited at a targeted depth within the patient, is known as the Bragg peak and is pictured in Figure 1. The dose escalation in this peak allows for the general sparing of healthy tissue, and reduction in overall patient dose.

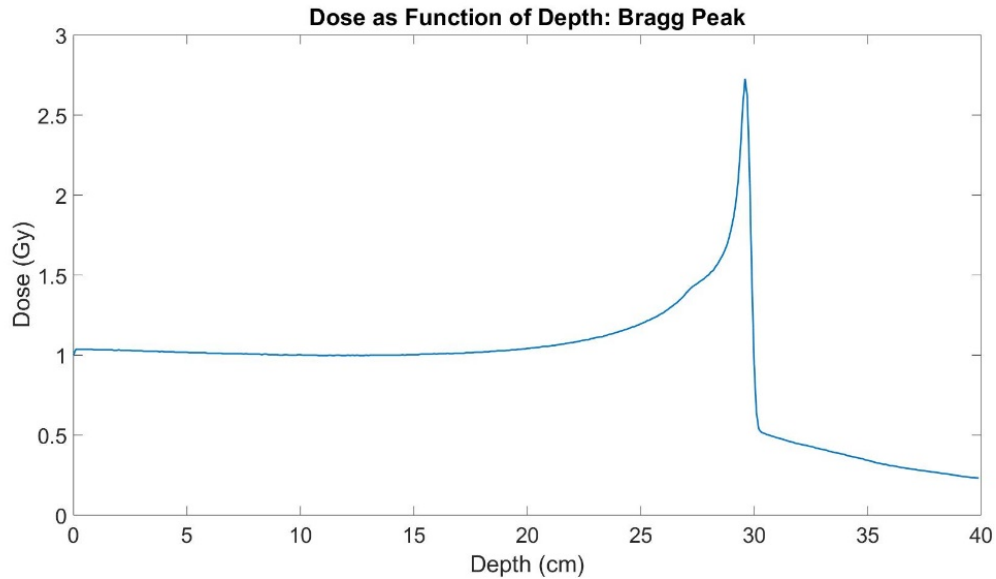


Figure 1. Example of a carbon Bragg peak, located at a depth of 30 cm, for a 424 MeV/u monoenergetic beam. The dose is normalized to 1 Gy at the entrance.

Due to nuclear interactions that cause fragmentation of the projectile nucleus into lighter nuclei, the therapeutic carbon beam is subject to high levels of contamination by other particles. At any given depth within a medium, there will be substantial dose contributions from a range of secondary particles within the beam, including H, He, Li, Be, B, secondary C, N, O and F, ordered on average from highest to lowest dose contribution. In addition to complicating the assessment of the carbon beam, this fragmentation results in a minor tail distal to the Bragg peak that causes a small amount of dose to be distributed beyond the region of interest, as can be seen in the range of 30 to 40 cm in Figure 1. This fragmentation is typically a disadvantage of the carbon beam in that it results in extra dose distributed beyond the Bragg peak, the total contribution of which increases with particle range. Proton therapy, a lighter particle therapy technique that has been clinically used since 1990, experiences a few times less nuclear

interactions than carbon as a result of its reduced size and has a subsequently negligible tail beyond the fall-off of the Bragg peak [3]. However, the distance required for the dose to fall from 100% at the Bragg peak to 20% or less is in the tail is on the order of several millimeters greater for proton than for carbon beams. Similarly, in the buildup region proximal to the Bragg peak, the relative physical dose contribution is roughly 20% to 30% less in carbon than proton beams for equivalent maximum dose levels [4].

In order to cover tumors of varying sizes, different energy carbon beams are weighted and superimposed to create a spread out Bragg peak (SOBP), an example of which is shown in Figure 2. This allows the delivery of a consistent dose across a larger area, as the pristine Bragg peak of a carbon beam is only a few millimeters wide [3]. However, the summation of multiple beams results in both a higher entrance dose and a larger tail due to the increased dose contribution by fragments.

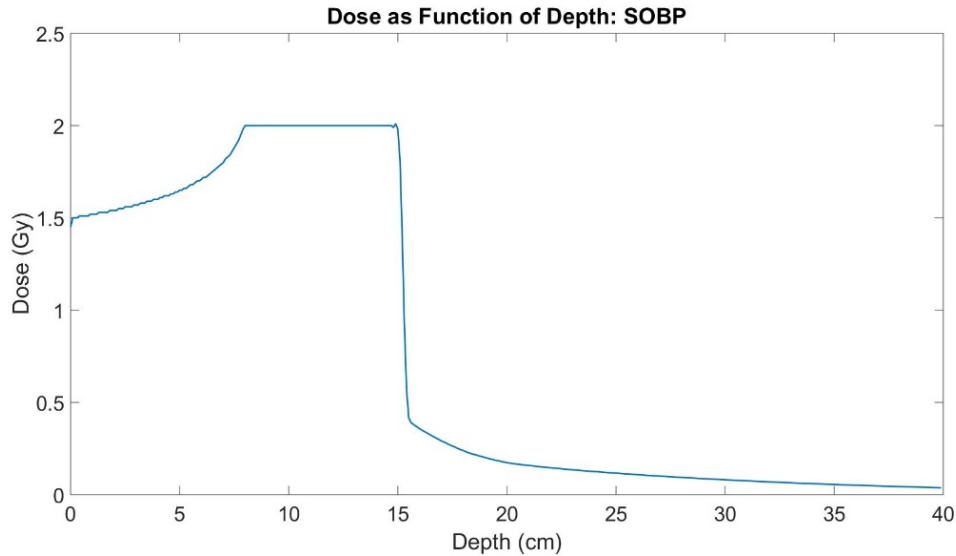


Figure 2. Example of a carbon SOBP weighted to deliver 2 Gy to a 7 cm target.

The penumbra, or lateral dose fall off, of the Bragg peak of carbon ions is superior to that even in proton therapy, with sharper and better defined margins. The carbon ion has 12 times the mass of a proton, and therefore has an LET of 36 times higher at the same velocity [3]. However, due to the same atomic properties, the carbon ions also have 12 times the kinetic energy under similar conditions, and therefore have a range that is just 1/3 that of protons [3]. Resultantly, carbon beams produce markedly less lateral scattering than protons, at just 1.5 mm compared to 6.5 mm at 20 cm depth in water [3]. This results in a sharper penumbra, which is beneficial in reducing dose to surrounding tissue. Furthermore, due to the properties described above, this sharp penumbra is typically constant at depths ranging from 0.4 cm - 24 cm, whereas the penumbra of protons increases markedly with depth [5].

1.2.2 Beam Delivery

1.2.2.1 Synchrotron

In order to be suitable for radiotherapy, carbon ions must be accelerated to roughly 70% the speed of light, or $210 \times 10^6 \text{ m/s}$. This is presently accomplished through the use of an accelerator known as a synchrotron. There are three ion sources in a synchrotron, including a linear-accelerator cascade and two synchrotron rings. An ion source is used to produce C^{2+} carbon ions, which are transported to and subsequently injected into the linear-accelerator cascade [3]. The linear-accelerator cascade accelerates the ions up to energies of 6 MeV/u, which are then injected into the synchrotron rings. The ions are accelerated by radiofrequency cavities in a circular path, maintained with strong bending magnets, until they reach the desired energy for clinical applications. At this time, the beam is slowly extracted by an RF-knockout method [3]. This method uses RF excitation to modulate and improve beam stability. Manipulation of the RF excitation amplitude allows dynamic control of the extraction rate, which allows the beam to be fully turned on or off in just 1 ms. Furthermore, this technique allows the extraction efficiency to reach between 80% and 90% [6].

1.2.2.2 Beam Delivery

After extraction, the high energy beam is sent to the delivery system, which adapts the beam for therapeutic use and provides the actual patient treatment. In order to cover a range of tumor sizes with the resultant beam, two

beam delivery techniques were established. The first, known as passive scattering, is a method in which the beam is perturbed by a pair of magnets (wobbler magnets) into a circular orbit about the axis of the original beam [3]. Simultaneously, the beam is scattered through thin foil placed beyond the wobbler magnets to increase the cross sectional area of the beam. With appropriate parameters selected for the wobbler magnets and the scattering foil thickness, a homogenous dose can be achieved. A multi-leaf collimator is then used to shape the beam laterally to match the target. The active scanning method was developed more recently, and uses a three-dimensional scanning technique with the original pencil beam. This method uses a pair of dipole scanning magnets along with a sophisticated beam control mechanism to paint spots onto a target, by actively modulating the beam energy and particle fluence [3].

In addition to passive scattering and active scanning methods, there are several ways in which a carbon beam can be modulated, including the use of ridge filters, ripple filters, and range shifters. The ridge filter consists of a series of parallel aluminum ridges, whose height corresponds to the shift of the peak and whose width is proportional to the contribution in the total SOBPs [3]. The ridge filter is typically used to create larger SOBPs, on the order of several centimeters or more. In order to achieve a pristine Bragg peak that is widened on the order of millimeters, a ripple filter may be used. The ripple filter, consisting of a 2 mm plexiglass plate with uniformly spaced grooves, is designed to widen a Bragg peak into a Gaussian peak [7]. This allows the use of fewer energy steps to

create a homogenous dose distribution and can result in a reduction in overall irradiation time.

1.3 Microdosimetry

1.3.1 Introduction

Standard dosimetry techniques provide dose through the assessment of average quantities of energy deposition. However, the nature of energy deposition throughout a volume by ionizing radiation is non-uniform. In addition to measuring absorbed dose, it is therefore useful to measure the number, magnitude, and spatial deposition of individual energy deposits as these characteristics impact the effect of radiation of cellular structures. Microdosimetry is a technique which allows the systematic analysis of energy deposition patterns on a microscopic platform to provide track information that is essential in understanding beam characteristics [8]. This is of particular interest in carbon therapy, where the beam incident on a medium becomes highly fragmented.

Traditional dosimetry utilizes the linear energy transfer (LET) as a measure of the energy transferred by a primary particle to surrounding material along the length of its track. Microdosimetry, however, employs the analogous quantity of lineal energy. Lineal energy is the sum of all energy deposits in a microscopic volume, and therefore takes into account the secondary particles in addition to the primary particles. This is an important component in dosimetry for carbon therapy, as the beam incident on a surface quickly becomes highly fragmented. Each fragment, in turn, has a unique LET that varies, along with

kinetic energy, as a function of depth. Rather than focusing individually on each particle, which quickly becomes complex in assessment, microdosimetry and lineal energy values simplify this assessment by quantifying the energy deposited by all ions within a sub volume. LET and lineal energy approach equivalence at large volumes, but are very different under small (i.e. micro- or nano-) volumes [9]. The dosimetric assessment of energy deposition within sites of this magnitude are crucial as this is the scale at which biological effects occur, such as the volume of the cell nucleus where double strand DNA breaks may occur [9].

A fundamental quantity in microdosimetry is a single event or deposit, denoted ε_s , which is the energy deposited by a single primary particle and all correlated secondary particles, including delta rays and fragments. A multi-event subsequently refers to the energy deposited by uncorrelated particles along with their secondaries. These energy deposits are important as they lead to the quantity of imparted energy, ε_i , which refers to the sum of all single events, or deposits, within a user-specified volume. The specific energy, z , is then the imparted energy divided by the mass of that volume, as shown in Equation 1.

Equation 1
$$z = \frac{\varepsilon_i}{m}$$

Due to the inherent properties of radiation interactions within a medium, specific energy is stochastic in nature and is applicable over a range of event sizes. The average absorbed dose, D , is the simplest deterministic

microdosimetric quantity and refers to the average energy imparted in a volume. The units of absorbed dose are in J/kg, or gray (Gy).

Equation 2
$$D = \frac{d\bar{\varepsilon}}{dm} = \bar{z}$$

Another important microdosimetric parameter is the random chord length, l , which describes the length of the path taken by a charged particle through a volume. The track of the charged particle is random, able to take any value between zero and the diameter of the volume (if spherical), so the length must be described by a probability density function. The mean chord length, \bar{l} , is the expectation value of this distribution and represents the average path length, which can be calculated using Equation 3 for a spherical target of volume V and surface area S . The number of collisions that a charged particle undergoes as it traverses a distance is given by a Poisson distribution that is proportional to stopping power and mean chord length, and inversely proportional to particle energy [9].

Equation 3
$$\bar{l} = \frac{4V}{S}$$

For a spherical target volume of diameter d , the mean chord length is simply calculated using Equation 4.

Equation 4

$$\bar{l} = \frac{2d}{3}$$

1.3.2 Lineal Energy

After an overview of the fundamental microdosimetric quantities, the lineal energy concepts may be introduced. Lineal energy, y , is the energy due to a single energy deposition event divided by the mean chord length of that volume. Lineal energy, a stochastic quantity, is typically characterized by its distribution in terms of frequency and dose. The frequency distribution, $yf(y)$, is representative of the number of events that occur as a function of event size. More precisely, this distribution returns the likelihood of observing an event within a specified interval.

In the dose distribution, $yd(y)$, the likelihood of observing a fraction of absorbed dose within specific lineal energy values is assessed. Accordingly, the size interval is multiplied by the event size to create the probability density function [9]. The distinction between these distributions is clear, where high lineal energy values carry a greater weight than low lineal energy events in the dose distribution. The expectation value of these distributions, respectively, return the frequency- and dose-mean lineal energies which are denoted \bar{y}_F and \bar{y}_D . These values allow the deterministic quantification of the probability distributions.

Equation 5
$$\bar{y}_F = \int_0^{\infty} y f(y) dy$$

Equation 6
$$\bar{y}_D = \int_0^{\infty} y d(y) dy$$

The relationship between $d(y)$ and $f(y)$ is given in Equation 7.

Equation 7
$$d(y) = \frac{y}{\bar{y}} f(y)$$

Along with the \bar{y}_F and \bar{y}_D parameters, a third value known as the saturation-corrected dose mean lineal energy (y^*) is used. Though biological effect increases with increasing energy deposition, there exists a maximum effect beyond which energy deposition has no proliferating impact. This results in a reduction of effect per unit energy deposited, or a diminished biological effect [9]. This particular situation is described by the saturation, or over-kill, effect and is corrected for with the y^* value. The saturation effect is responsible for the decrease in RBE with lineal energy beyond the peak of maximum effect. This correction is typically small with low LET radiation and with low doses, and increases correspondingly to become obligatory for high LET charged particles [8].

Equation 8
$$y^* = \frac{y_0^2 \int \left(1 - e^{-\frac{y^2}{y_0^2}} \right) f(y) dy}{\int y f(y) dy}$$

The saturation parameter, y_0 , is calculated as follows in Equation 9, where ρ is the domain density, r_d is the radius of the domain, R_n is the radius of the nucleus of

the particular cell line studied, and β is quadratic component of the linear-quadratic cell survival theory.

Equation 9

$$y_0 = \frac{\rho\pi r_d R_n^2}{\sqrt{\beta(r_d^2 + R_n^2)}}$$

The saturation parameter has been established for use within the MKM model based on a spherical nucleus of an HSG cell in the G₁ phase [10]. In microdosimetry, the value of y_0 typically falls between 125 keV/μm and 150 keV/μm and is dependent on radiation type, with the latter endpoint employed in carbon therapy [9].

1.3.3 Tissue Equivalent Proportional Counter (TEPC)

1.3.3.1 Detector

While there are several types of detectors capable of making microdosimetric measurements, the most established of which is the tissue-equivalent proportional counter (TEPC). A TEPC utilizes the properties of the ideal gas laws to simulate a small diameter with a reduced pressure. Using low enough pressures, a detector with a physical volume on the order of centimeters can approximate a simulated volume on the order of micrometers. Commercial TEPCs typically follow the designs of Dr. H. H. Rossi of Columbia University, and as such are often referred to as Rossi counters [11].

This physical quantity that is actually measured by the TEPC is a charge that is proportional to the number of ion pairs created by particles crossing the

active volume [8]. From this charge, the energy imparted can be calculated with the application of a W-value. This value is defined by the amount of energy required for a particle to form a single ion pair, and is used here to relate the energy imparted (signal) with the number of ion pairs created. While the W-value is dependent on both particle species and energy, a constant W-value is typically used for the entire spectrum. This is a recognized limitation of the detector [8].

The principle requirement of a TEPC is that both the fill gas and the counter wall materials consist of the same number and composition of atoms as that found in tissue [12]. However, this becomes difficult in practicality, where the density difference between cavity and wall introduce energy deposition effects, which will be explained in detail in a later section.

1.3.3.2 Uncertainty

Measurements made by the TEPC are, as any physical measurements, subject to inherent sources of uncertainty. The ICRU Report 36, on microdosimetry, identifies eight unique sources of noise that are anticipated to affect and perturb TEPC measurements [8]. These sources are categorized as either random or both random and systematic sources of uncertainty based on their anticipated affect, and are listed as such below. Random sources of uncertainty introduce variance in physical measurements, but do not cause an overall shift in mean measured values. Systematic sources, however, drive a shift of the mean value. Sources that are quantified here as both random and systematic introduce both an inherent bias and a variance into the final measured

values. Each of these sources will be introduced independently, in detail, in Section 4.1.2.

- a. Random:
 - a. Counting statistics
 - b. Gas pressure and mean chord length
 - c. Electronic uncertainty
 - d. Gain instability and energy calibration
- b. Random and systematic:
 - a. W-value
 - b. Low energy cutoff
 - c. Pulse pile-up
 - d. Wall effects

1.4 Relative Biological Effectiveness

1.4.1 Introduction

1.4.1.1 RBE

Relative biological effectiveness is defined as the dose of reference radiation, D_{ref} , required to create the same biological endpoint as that of experimental radiation, D_{exp} , as shown in Equation 10.

Equation 10

$$RBE = \frac{D_{ref}}{D_{exp}}$$

Currently, both low LET radiation and light particle radiation employ constant RBE values, of 1 and 1.1 respectively. Carbon ions, however, employ RBE values that vary as a function of many parameters and may reach values of up to 5-6 at the distal edge of the Bragg peak where the LET is highest. RBE is typically proportional to dose up to an LET of around 100 keV/μm, after which the RBE plateaus or declines [13].

1.4.1.2 RBE Models

RBE is a complex parameter to measure as it is dependent on a range of factors including, but not limited to, biological endpoint, physical dose, LET, and cellular oxygenation. Consequently, RBE is particularly difficult to measure in vivo and necessitates predictive models for given treatment setups when it comes to patient treatments.

While several models have been proposed to assess the relative biological effectiveness (RBE) of carbon beams, only two are currently implemented clinically. The first, the Local Effect Model (LEM), has been employed in treatment planning systems throughout many European facilities for nearly 20 years. Though this model has had several variations throughout time (LEM I through LEM IV), the initial model (LEM I) currently dominates clinically. The second, microdosimetric kinetic model (MKM), was developed around the same time and is currently implemented in the treatment planning system of most

clinically active carbon centers within Asia. The principle difference between the two models are in the cell survival curve derivations. LEM uses a theoretical track structure model to estimate cell survival, while MKM uses a microdosimetric energy deposition approach. A third model, the Repair Misrepair Fixation (RMF) model, is introduced and assessed here along with the clinical models in order to provide independent comparison. While the RMF model has not been used clinically, to date, it is available in one commercial clinical treatment planning system and several research based treatment planning systems [2] and the potential for clinical implementation in the near future is high. Typically, the physical dose is the only parameter needed to determine RBE clinically, as the complexities of RBE modelling are hidden within the treatment planning systems [3].

Though there are unique derivations and modification of each, the foundation of surviving fraction are based on the linear-quadratic model for all three RBE models. The surviving fraction, S , is described with Equation 11, in which α and β represent the linear and quadratic portions of the curve, respectively, and D the absorbed dose.

Equation 11
$$-\ln(S) = \alpha D + \beta D^2$$

Combining this equation with the definition of RBE, the surviving fraction of reference and experimental radiation can be equated to give the following equation that describes the foundation of each model.

$$\text{Equation 12 } RBE = \frac{-\alpha_{ref} + \sqrt{\alpha_{ref}^2 + 4\beta_{ref}(\alpha_{exp}D_{exp} + \beta_{exp}D_{exp}^2)}}{2\beta_{ref}D_{exp}}$$

While x-rays are typically the reference radiation used in these models, the other reference parameters (biological endpoint, and cell line) used to derive survival curves vary across models. This causes the reference alpha/beta ratio, α_x/β_x , to fluctuate and becomes a contributor to inhomogeneity in RBE across models. Table 1 displays typical reference values that are used by each model.

Table 1. Values for parameters used in each RBE model, where the subscript c indicates parameters specific to a carbon beam. The starred cell lines are the values used in these RBE calculations.

RBE Model	Cell Line	$\alpha_x (\text{Gy}^{-1})$	$\beta_x (\text{Gy}^{-2})$	$\alpha_c (\text{Gy}^{-1})$	$\beta_c (\text{Gy}^{-2})$	Source
MKM	HSG Tumor*	0.19	0.05	Variable	0.05	[14]
LEM	Chordoma*	0.1	0.05	Variable	Variable	[14]
LEM	Skin	0.0172	0.0029	Variable	Variable	[14]
LEM	CHO-K1	0.2	0.019	Variable	Variable	[14]
LEM	Lung	0.0684	0.0167	Variable	Variable	[14]
RMF	NSCLC H460*	0.29	0.083	Variable	Variable	[2]

1.4.2 Microdosimetric-Kinetic Model

1.4.2.1 Introduction

The MKM employs the dual radiation action (TDRA) theory, which postulates that the number of lethal hits in a cell nucleus is proportional to the square of the specific energy (z) deposited in that volume. As a result, a linear-quadratic correlation of specific energy to average number of lethal lesions can be made within a domain.

Equation 13
$$L = Az + Bz^2$$

The number of domains in a nucleus, N , can be combined with this statement to estimate the average number of lethal lesions in a nucleus, L_n .

Equation 14

$$L_n = N(A\bar{z} + B\bar{z}^2)$$

The surviving fraction of cells is then approximated by assuming a Poisson distribution of lethal lesions for low-LET radiation.

Equation 15

$$-\ln(s) = \alpha\bar{z} + \beta\bar{z}^2$$

Equation 16

$$-\ln(s) = (\alpha_0 + \beta z_{1D})D + \beta D^2$$

In this equation, NA is represented by α_0 and $N\beta$ is represented by β . The term z_{1D} refers to the dose mean specific energy due to a single energy deposition within a domain, and can be directly measured using a TEPC. The parameter D refers to the absorbed dose, in Gy, and can similarly be measured by a TEPC [8]. It is typically assumed that D and \bar{z} are equal.

Equation 17

$$z_{1D} = \frac{l}{m} y_D = \frac{y_D}{\rho\pi r_d^2}$$

The non-Poisson distribution of high-LET radiation is corrected for using the saturation correction employed by the TDRA. To employ this correction, z_{1D} is replaced with z_{1D}^* .

Equation 18

$$Z_{1Dn}^* = \frac{l}{m} y^* = \frac{y^*}{\rho \pi r_d^2}$$

Here, y^* is the dose mean lineal energy corrected for saturation, and is calculated according to Equation 8, as introduced previously. The saturation parameter (y_0), introduced in Equation 9, is an essential part of this calculation and is determined by three parameters established for MKM specifically. The first two parameters, the domain radius and the quadratic portion of the LQ model, were selected based on survival curves and \bar{y}_D values for reference radiation of 200 kVp x-rays. The third value, R_n , was selected to represent the radius of an HSG cell nucleus in G₁ phase [15]. MKM employs a high saturation parameter of 150 keV/ μ m, which was calculated using the following factors: $r_d = 0.42 \pm 0.04 \mu$ m, $\beta = 0.05 Gy^{-2}$, $R_n = 4.1 \mu$ m, and $\rho = 1.0 g/cm^3$. The model specific parameters (domain size, α_0 , β) used to make these corrections and calculations were selected based on the survival curve and y_D values for a reference radiation of 200 kVp X rays, and for human salivary gland (HSG) tumor cells [15].

1.4.2.2 Calculating RBE_{MKM}

In order to calculate RBE_{MKM} , a frequency-weighted microdosimetric spectra is needed. The expectation value of this spectra, \bar{y}_F , is then calculated as a function of both depth and initial beam energy. Using the formalism described above, y^* is then calculated from these parameters by correcting \bar{y}_D for saturation. The y^* then provides the direct input to calculate the α value of the

carbon beam using the first term of the linear-quadratic equation of surviving fraction, as shown in Equation 19.

$$\text{Equation 19} \quad \alpha^* = \alpha_0 + \beta z_{1D}^* = \alpha_0 + \beta \left(\frac{y^*}{\rho \pi r_d^2} \right)$$

$$\text{Equation 20} \quad \alpha^* = 0.13 + 0.01446 y^* = \alpha_C$$

For clinical carbon beams, published values of $\beta = 0.05 \text{ Gy}^{-2}$ and $r_d = 0.42 \mu\text{m}$ are used in this equation, to provide an equation for α_C that varies only as a parameter of y^* .

Once α_C is obtained as a function of beam energy and depth, the only other outstanding parameter in the linear-quadratic formulation for calculating RBE is the physical dose. The remaining parameters involved in the equation are fixed as a function of depth at the following values, which were obtained using LQ survival curves of the reference radiation: $\beta_C = 0.05 \text{ Gy}^{-2}$, $\alpha_X = 0.19 \text{ Gy}^{-1}$, and $\beta_X = 0.05 \text{ Gy}^{-2}$ [10].

1.4.3 Repair-Misrepair Fixation Model

1.4.3.1 Introduction

The foundation of the RMF model is that reproductive cell death is correlated directly with DNA double-strand break (DSB) induction. When multiple double strand breaks occur, DNA damage can arise through the incorrect rejoining of chromosome ends in a pairwise manner. This can be caused by energy deposits formed by one radiation track, more commonly, or by multiple radiation tracks through the cell [16]. With energy deposition by multiple tracks, rejoining may occur in one DSB before another is even created. The RMF model takes into account five different mechanisms for which DSBs may result in cell death, as described by Carlson and colleagues [16]. While DSB yield is typically generated directly using Monte Carlo Damage Simulation software, the calculations are shown below for reference. The DSB yield, Σ_i , may be calculated using Equation 21 for each contributing fragment with atomic numbers one through five [2].

Equation 21
$$\Sigma_i = \Sigma_x \left\{ \alpha + b - [b^{(1-d)} + cx(d-1)]^{\left(\frac{1}{1-d}\right)} \right\}$$

In this equation, Σ_x represents the DSB yield for reference radiation. The coefficients are derived as part of the original model development and are as follows: $a = 0.9902$, $b = 2.411$, $c = 7.32\text{E-}4$, and $d = 1.539$ [2]. The physical parameter x is calculated as a function of particle type, and is broken down by component in Equation 22.

Equation 22

$$x = \left(\frac{Z_{Eff}}{\sqrt{1 - \frac{1}{\left(1 + \frac{T}{m_0 c^2}\right)^2}}} \right)^2$$

Within this series of equations, Z_{Eff} represents effective particle charge and is calculated using Equation 23 where Z is the atomic number, T the kinetic energy, and $m_0 c^2$ the rest mass.

Equation 23

$$Z_{Eff} = Z \left(1 - e^{-125 \sqrt{1 - \frac{1}{\left(1 + \frac{T}{m_0 c^2}\right)^2}} Z^{-2/3}} \right)$$

1.4.3.2 Calculating RBE_{RMF}

Typically, Monte Carlo Damage Simulation software is used to quantify DSB yields from track structure simulations as functions of ion and beam energy to serve as input to the RMF calculations. Once the DSB yield is calculated, only two other variable parameters are required to calculate RBE, including both specific energy, z_F , and physical dose. The specific energy is a microdosimetric quantity that may be calculated using and the diameter of the simulated volume, d , equal to $5 \mu m$ in RMF calculations, and \bar{y}_F . As noted, \bar{y}_F can be calculated directly from the frequency distribution of a microdosimetric measurement.

Equation 24

$$Z_{F,i} = \frac{0.204 * \bar{y}_F}{d^2}$$

Once specific energy is calculated, it can be combined with the DSB yield and two fixed biophysical parameters to calculate fragment specific α_i , using Equation 25.

Equation 25

$$\alpha_i = \theta \Sigma_i + \kappa Z_{F,i} \Sigma_i^2$$

These constant parameters are specific to the cell line of the reference radiation. The term κ describes the fraction of initial DSBs that undergo damage interaction in a pairwise fashion. For this cell line, it is fixed at a value of 2.407E-03 (DSB/Gbp)⁻² for H460 cells, as are used in this study [2]. The term θ is defined by the fraction of DSBs that submit to lethal first order misrepair and damage fixation, and is fixed at 3.487E-2 (DSB/Gbp)⁻¹ for this study [16] [2].

The calculation of the linear quadratic parameter β_i requires no additional parameters, and is simply described by Equation 26.

Equation 26

$$\beta_i = \left(\frac{\kappa}{2}\right) \Sigma_i^2$$

Once alpha and beta are calculated for each particle, they are weighted according to the fragment dose contribution based on the following equations, where the subscript i indicates the fragment.

Equation 27

$$\bar{\alpha}_C = \frac{\sum_{i=1}^n \alpha_i * D_i}{\sum_{i=1}^n D_i}$$

Equation 28

$$\bar{\beta}_C = \left(\frac{\sum_{i=1}^n \sqrt{\beta_i} * D_i}{\sum_{i=1}^n D_i} \right)^2$$

Finally, the weighted alpha and beta values are used in calculation with both reference alpha and beta values and physical dose to calculate RBE according to the LQ formulation shown in Equation 12. The reference parameters, α_X and β_X , were selected from a study by Guan and colleagues, in which the cell survival data was amassed for H460 cells irradiated by Cs-137 photons [2].

1.4.4 Local Effect Model

1.4.4.1 Introduction

LEM I assumes that local biological damage is determined entirely by the expectation value of the energy deposited within a volume and is, consequently, independent of the radiation type that deposits that energy. This means that differences in biological effect are due to the spatial deposition pattern of energy by charged particles, which is primarily driven by secondary electrons. The pattern of average energy deposition by the secondary electrons follows the inverse square law ($\frac{1}{r^2}$) where r is the distance from the trajectory. This principle provides an upper limit of the track radius that depends only on the specific energy of the projectile and a constant. This pattern is then compared to that of a reference radiation to determine biological effect.

The cell nucleus, approximated by a cylinder lying perpendicular to the particle trajectory, is assumed to be the critical target. It is assumed that a single lethal event within the nucleus is capable of inactivating the cell. As a result, a Poisson distribution of the fraction of cells in which no lethal events occur is created around the average number of lethal events. This distribution is used to create both a standard and modified version of the linear-quadratic cell survival approach, differentiated by target dose. This modification includes a transition from linear-quadratic to exponential shape at high doses, resulting from the increase in homogeneity of energy deposition with dose.

1.4.4.2 Calculating RBE_{LEM}

LEM assesses the energy deposited by each fragment independently and, as such, requires both the kinetic energy spectra and the energy distribution of the primary particle and each substantially contributing secondary particle. The kinetic energy as a function of particle depth is needed in order to obtain appropriate alpha and beta values for charged particles (α_i and β_i), while the energy deposition is needed to properly weight the average alpha and beta values for the mixed field.

This model is implemented using prepopulated tables of alpha and beta values as functions of kinetic energy for both carbon ions and several secondary fragments. Plots of these tables are shown in Figure 3 and Figure 4, respectively. Included in the table are protons, helium, boron, beryllium, lithium and secondary carbons as these fragments contribute the majority of secondary energy

deposition within the beam line. In order to use this table, the kinetic energy spectra of each particle is needed to interpolate the corresponding alpha and beta values per fragment at any given depth.

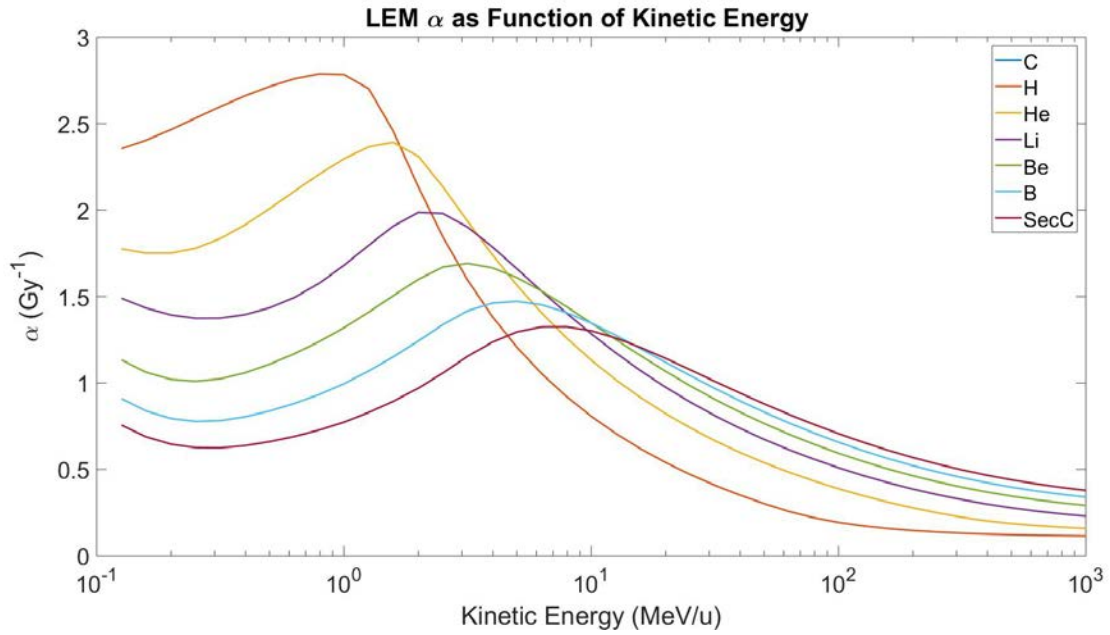


Figure 3. LEM α as a function of kinetic energy for primary carbons and all relevant fragments.

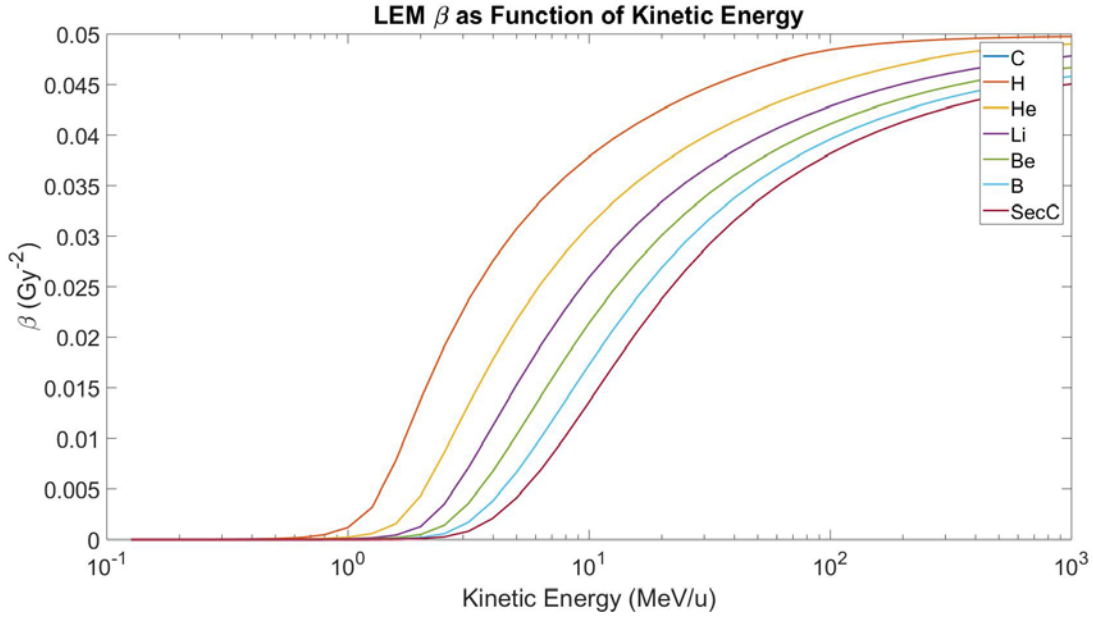


Figure 4. LEM β as a function of kinetic energy for primary carbons and all relevant fragments.

Once the values are extracted, the α_i and β_i of each fragment are weighted by dose contribution using the following formulas to produce an average mixed field alpha and beta, $\bar{\alpha}_C$ and $\bar{\beta}_C$.

Equation 29

$$\bar{\alpha}_C = \frac{\sum_{i=1}^n \alpha_i * D_i}{\sum_{i=1}^n D_i}$$

Equation 30

$$\bar{\beta}_C = \left(\frac{\sum_{i=1}^n \sqrt{\beta_i * D_i}}{\sum_{i=1}^n D_i} \right)^2$$

After the weighted alpha and beta values are obtained at a given point, the formulas established previously in Equation 11 and Equation 12 are used to calculate the surviving fraction and RBE, respectively. The reference values of α_X and β_X are variable across cell lines and biological endpoints. The α_X and β_X of

Chordoma cells, used in accordance with the α_i and β_i tables in Figure 3 and Figure 4, were derived from tumor growth characteristics reported by Battermann and colleagues [14] [17].

At doses above a certain threshold, however, the low dose approximation and corresponding linear quadratic formalism described above are no longer practical according to LEM framework. This cutoff dose, D_{cut} , is dependent on the cell line and biological endpoint used and may take on a value of either 15 Gy, for skin and pig lung tissues, or 30 Gy, for CHO-K1 and chordoma tissues. When absorbed physical dose surpasses D_{cut} , the linear quadratic model shifts to an exponential model with a slope defined by s_{max} .

Equation 31
$$s_{max} = \alpha + 2\beta D_{cut}$$

The surviving fraction at this dose can then be calculated using the following equation.

Equation 32
$$-\ln(S) = \alpha D_{cut} + \beta D_{cut}^2 + (D - D_{cut})s_{max}$$

1.4.5 Comparison

The parameters used across each model are unique, and may require values that must be calculated rather than measured. LEM considers the local dose of infinitesimal volumes, while MKM focuses on the stochastic energy deposition in a microscopic domain. Therefore, in LEM the cell survival curve can be simulated using a theoretical track structure model, while MKM uses an experimental lineal energy spectra with a microdosimetric method [10]. RMF

similarly uses a microdosimetric approach, but requires additional calculations based on DSB yield. Though these models require either direct measurements or intensive calculations, the time intensive nature associated with these are overcome by using precalculated model outputs in treatment planning systems. This compensation can lead to deviations between the RBE as seen in treatment planning systems and those specific to the individual beamline.

1.5 Consistency in Radiotherapy

It is well established within the field of medical physics that accurate dose delivery is necessary to avoid bad outcomes in radiotherapy. Long term outcome is one of the parameters assessed by Ohri and colleagues, who conducted a meta-analysis on the association between radiation therapy deviations and disease control [18]. Deviations in radiotherapy were found to be associated with both a statistically significant decrease in overall survival and a statistically significant worsening of secondary outcomes. Furthermore, this analysis found that 8% to 71% of cases deviated from radiotherapy protocol. These deviations were then associated with an increased risk of both treatment failure and mortality of approximately 75% [18]. Additional outcome studies were conducted by Peters and coworkers, who explored the impact of radiotherapy quality on treatment outcome for head and neck cancers [19]. Here, a 20% decrease in overall 2 year survival was found as a result of poor radiotherapy compliance [19].

Furthermore, uncertainties in delivered dose can put clinical trials at risk of being statistically underpowered. As described by AAPM Report 85, the number of patients required to have a statistically significant clinical trial result is dependent on the error in tumor control probability [1]. This standard error is propagated in quadrature and directly increases the number of patients required for statistically significant results. Accordingly, for a standard error in tumor control probability of 10%, the number of patients required for statistical significance between each treatment arm of the clinical trial doubles [1]. As noted in Section 3.1.1, a 10% error in tumor control probability can be achieved through just a 5% change in dose.

The effect of uncertainty in dose was also explored in 2008 by Pettersen and colleagues, who quantified the increase in the number of patients required to create an equivalent steepness in clinical response curve at different dose uncertainties [20]. It was found that increases in the dose uncertainty to 5% reduced the clinical dose response by anywhere from 10-30%, depending on the steepness of the biological dose response curve. The effect of the biological variation was also seen to decrease with increasing dose uncertainty. At a response difference between clinical arms of 5%, a 1% increase in dose uncertainty could cause between a 20% and 30% increase in required sample number [20].

1.5.1 IROC Houston

With the importance of dose consistency quantified, means of ensuring that dose uncertainty is kept below reasonable levels is needed. IROC Houston is a quality assurance center whose mission is just that; to ensure consistency of radiotherapy delivery in clinical trials and improve patient outcomes. IROC has been working towards this goal for over 50 years in x-ray therapy, and more recently has taken on the same charge in proton therapy. In x-ray therapy, IROC uses standardized tests to validate whether the machine output matches the treatment planning system calculation for both basic dosimetry and complex end-to-end tests. The need for this is great, as established in the meta-analysis by Ohri, who found the number of deviations from radiotherapy protocol to span from 8% to 75% [18]. This is evidence of a routine inconsistency between delivered dose and that implemented in the treatment planning system.

1.5.2 Carbon Radiotherapy

This need for quality assurance can be translated to carbon therapy, where one of the largest inconsistencies lies in the RBE implementation. Consequently, a system should be developed to ensure that the RBE of the therapeutic beam output matches that predicted by the treatment planning system. Current treatment planning systems implement standard tables with which to calculate RBE that are uniform across each treatment delivery. As each carbon beam and delivery setup is unique, this implementation does not meet the specificity inherent to the complex model calculations, as described in Section 3.4. This

inconsistency is currently unquantifiable without extensive Monte Carlo calculations, for RMF and LEM models, and can lead to significant uncertainties in delivered dose as it is not computationally feasible to model each unique treatment delivery setup. Therefore, it is of particular significance to establish a method by which the RBE can be directly measured and compared to the value used within the treatment planning system. It is important to note that this system will not test the validity of any one RBE model, but it will at least ensure that it has been correctly implemented within the treatment planning system.

1.6 Hypothesis

A uniform microdosimetric measurement approach can be developed that will introduce less than 5% uncertainty into the modeled RBE of an arbitrary carbon beam based on any clinical model.

1.6.1 Specific Aims

1. Quantify and introduce each of eight unique sources of noise into lineal energy spectra to evaluate their impact on calculated values.
2. Incorporate uncertainty into calculated RBE values across three models to quantify physical measurement based uncertainty.

2 Specific Aim 1

2.1 Introduction

The first component involved with Specific Aim 1 is to quantify the uncertainty introduced by each of the eight sources of physical measurement based noise listed in Section 3.3.3. In order to do this, a commercial TEPC was selected for use in this study. The TEPC and corresponding electronics are introduced below. This is followed by a detailed introduction to each of the eight sources of uncertainty, as ordered first by random sources (counting statistics, gas pressure and mean chord length, electronic uncertainty, and gain instability) followed by sources that were both random and systematic in nature (W-value and energy calibration, low energy cutoff, pulse pile-up, and wall effects).

2.1.1 LET-1/2

Although this study relied entirely on Monte Carlo calculated data, ultimately physical measurements are desired and therefore a specific model of TEPC was selected upon which estimations and evaluations could be made. The specific TEPC that was selected for this project was the LET-1/2, a model produced and sold by Far West Technologies (FWT, Goleta CA). The LET-1/2 has been used to take microdosimetric measurements within heavy ion beams in several previous studies, providing a strong indication that this model would meet the needs of this study [15]. With correct amplifier settings, the LET-1/2 allows data collection for lineal energies ranging from 0.5 to 1000 keV/ μm , roughly five orders of magnitude, which is the typical range of lineal energies in carbon

measurements [11]. Using the accompanying software, this spectra may then be converted to absorbed dose in LET, or the probability function $yd(y)$.

The LET-1/2 consists of a spherical active volume of 0.500 inches in diameter surrounded by a tissue equivalent wall of 0.05 inches thick. An accompanying gas-fill system is sold by FWT that allows the user to manipulate and maintain the fill gas of the active volume. The fill gas, tissue equivalent propane, is typically maintained at pressures ranging from 2.5 to 40 cm Hg. Respectively, this range corresponds to simulated tissue volume diameters in the range of 1 to 8 microns. The recommended operating specifications of the detector for various simulated diameters are shown in Table 2.

Table 2. Recommended operating specifications for the LET-1/2 for specific simulated diameters as a function of tissue equivalent gas used (methane vs. propane based) [11].

Simulated Diameter	Gas Pressure	Gas Composition	Density (at STP)	Operating Voltage
Methane-Based TE				
1 μm	56.3 mm Hg	29.9% CO ₂ , 2.75% N ₂ , 67.54% CH ₄	1.064 g/L	450-500 V
2 μm	112.6 mm Hg	29.9% CO ₂ , 2.75% N ₂ , 67.54% CH ₄	1.826 g/L	550-600 V
Propane-Based TE				
1 μm	33.2 mm Hg	39.6% CO ₂ , 5.4% N ₂ , 55% C ₃ H ₈	1.064 g/L	450-500 V
2 μm	66.4 mm Hg	39.6% CO ₂ , 5.4% N ₂ , 55% C ₃ H ₈	1.826 g/L	550-600 V

The wall material of the active volume is made of Shonka Type A-150 plastic with a density of 1.12 g/cm, which attaches to the stem of the detector through a connector block, transporting both high voltage and signal. The stem also holds a vacuum fitting, which maintains a vacuum evacuated space between the tissue equivalent shell and the external aluminum shell [11]. This thin external shell, at just 0.007 inches thick, is grounded to serve as an electrostatic shield. Both the external shell and stem are entirely submersible and can be used in any common tissue equivalent fluids. The recommended calibration source for the LET-1/2 is a Cf-252 source, which produces neutrons with a mean energy of 2 MeV [11].

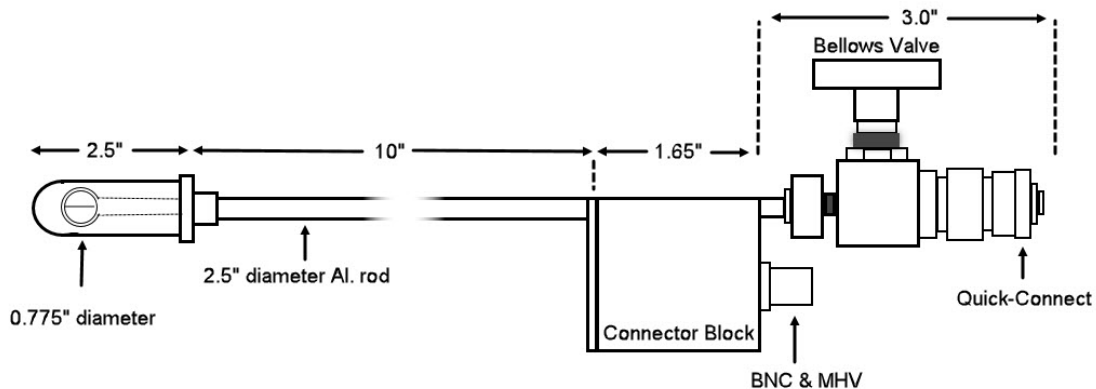


*Figure 5. Diagram of the LET-1/2 manufactured by Far West Technologies.
Figure adapted from the user manual [11].*

2.1.1.1 Electronics

The LET-1/2 proportional counter is diagramed in Figure 5, and produces an analog signal which is fed immediately into the preamplifier through a low

noise signal cable. The preamplifier extracts the signal directly from the detector, and is typically located as close as physically possible to the detector to prevent the spurious addition of noise. The preamplifier then converts the ionization charge to an output voltage, whose amplitude is proportional to the total collected charge [21]. The signal is then fed to the linear amplifier, where filters are applied to shape the pulse. Overall amplification also occurs here. Finally, the analog signal is sent to the multi-channel analyzer (MCA). The MCA contains an analog-to-digital converter (ADC) that converts the pulse to a digital value based on discrete intervals, or channels. The number of channels is unique to the converter, and determines the energy resolution of the MCA. As the pulse range is digitized over the number of channels, the resolution increases proportionally with channel number.

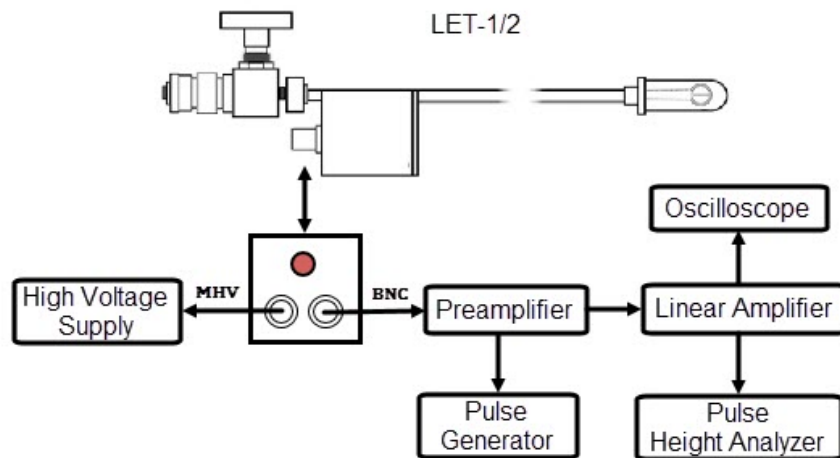


Figure 6. Displays the electronic interconnection components of the LET-1/2 as described in the operation manual [11].

2.1.2 Uncertainty Analysis

2.1.2.1 Counting Statistics

The counting statistics of a measured frequency distribution introduce an inherent source of noise into the system. This uncertainty is typically governed by the Poisson distribution, in which the probability of occurrence is characterized by the mean. The standard deviation about the mean, at the 1σ level, is characterized by $\frac{1}{\sqrt{N}}$, where N is the number of counts in each channel. As such, bins with higher count numbers are subject to less noise than those with lower count numbers. This results in higher noise levels in both the low lineal energy portion of the dose and frequency spectra and in the high lineal energy portion of the frequency weighted microdosimetric spectra.

2.1.2.2 Gas Pressure and Mean Chord Length

A TEPC uses ideal gas laws to simulate a microdosimetric volume by manipulating gas pressure in a macroscopic detector volume. The relationship is shown in Equation 34, where p and V indicate the pressure and volume of the site, respectively.

Equation 33

$$\rho_1 V_1 = \rho_2 V_2$$

At very low pressures, the active volume can simulate microdosimetric volumes on the order of $1 \mu\text{m}^3$. Consequently, the magnitude of the simulated volume and, subsequently the mean chord length, are dependent on the accuracy and

consistency of this gas pressure. Fluctuations cause over- or under-estimations of the simulated volume, which is used to calculate lineal energy.

2.1.2.3 Electronic Uncertainty

The electronic uncertainty of the detector is a function primarily of the associated electronics, consisting of a preamplifier, linear amplifier, and multichannel analyzer (MCA) as seen previously in Figure 6. As noted, the preamplifier is fed the direct signal from the detector and is the dominant source of electronic noise [8]. The preamplifier adds noise to the signal before it is processed, causing an increase or decrease in pulse amplitude and resulting in the pulse being recorded in a higher or lower lineal energy bin than it should be.

2.1.2.4 Gain Instability

The gas gain refers to the average number of electrons collected at the anode per primary ion pair created by the charged particle. Fluctuations in the gain can result in shifts in ion pair counts to shift up or down in energy bin. As a result, the effect of gain instability on lineal energy must be quantified for the LET-1/2. Microdosimetric spectra uncertainties arising from gain instability are a result of channel drift over time, a property that is unique to each detector.

2.1.2.5 W-Value and Energy Calibration

The uncertainty in measurements is due largely to the uncertainty in energy required to create an ion pair in a medium, known as the W-value [8]. As mentioned in the introduction to the TEPC, the constant W-value application is a

recognized limitation in the specifications of the detector. More properly defined, the W-value is the quotient of the initial energy of the particle and the number of ions produced [22]. As such, the W value directly relates the signal received by the detector (number of ion pairs created) and the energy of the particle.

In practice, the W value is implicitly incorporated into the relationship between TEPC signal and particle energy. This is done through a calibration of the TEPCs with a known source, most often a Cf-252 source, with a mean neutron energy of 2 MeV. This known source allows assignment of an energy to each bin, thereby relating signal to energy. When an experimental measurement is done, the same signal to energy relationship is used. The measurement error is induced through the difference between the W-value of the TEPC calibration source, a Cf-252 neutron source, and the experimental carbon beam. Furthermore, if the detector is placed below the surface, the beam is subject to heavy fragmentation and will be mixed with many other ions. While the suggested W-value for neutrons is well characterized as 31 ± 1.5 eV for neutrons of energy 1-14 MeV in tissue-equivalent ion chambers, a unique W-value for the mixed radiation field of the ion beam is not identical and therefore introduces uncertainty [23]. It is recommended by Lindborg and Walker that the energy dependence of the W-value be taken into account for volumes on the order of nanometers [9]. As microdosimetry begins to approach this order of magnitude, this analysis is important.

2.1.2.6 Low Energy Cutoff

The low energy cutoff of a microdosimetric spectra represents the lower threshold below which accurate measurements may not be obtained.

Uncertainties in the measured microdosimetric spectra arise when the spectra is extrapolated to zero below this threshold. The magnitude of these uncertainties vary based on the cutoff threshold, the statistics above that threshold, and the impact of noise in the low lineal energy region that is cutoff. The impact of extrapolating the spectra at lineal energy values below the cutoff value are notable in the frequency weighted spectra, with experimental error amounting to greater than 20% for \bar{y}_F of low-LET radiation [8]. As low energy events carry little weight in the $y d(y)$, however, the effect on \bar{y}_D is often negligible [8].

According to ICRU Report 36, the magnitude of the low energy cutoff is roughly 50 times the noise of the preamplifier [8]. While this estimate may be used to calculate low energy cutoff, a threshold value is directly proposed by the manufacturers of the LET-1/2 as 0.5 keV/ μm , eliminating the need for this calculation in this study. In order to mitigate the error introduced by simply cutting the spectra below this point, simulated low lineal energy values below the threshold may be appended to the spectra. It is important to then quantify the uncertainty associated with this process.

2.1.2.7 Pulse Pile-up

Pulse pile-up occurs if a second pulse arrives while the previous pulse is still being digitized, resulting in a pulse with a height of anywhere between one and two times the original pulse heights. As a result, the entire pulse is placed in a higher energy bin, causing portions of the distribution to shift toward higher lineal energy values and causing a net increase in \bar{y}_D , \bar{y}_F , and y^* . The area of the distribution that is most likely to see the spurious piled-up pulses are at a lineal energy of twice the main peak height. Pulse pile-up was anticipated to be a large problem with carbon ion beams as the count rate used clinically is quite high, ranging from 1.25E07 pps to 3E07 pps according to the survey sent out by IROC Houston. While most institutions (three out of the fives sampled) were able to mechanically tune the instantaneous dose rate of their machines below clinical levels, not all were willing and/or able.

In order to characterize the pile-up during physical measurements, the corresponding electronics were first assessed. The MCA that is most often used with the LET-1/2 is the EASY-MCA-8k by Ortec, which drives the dead time of the detection system. This MCA was chosen both because it has been used with the LET-1/2 in previous studies, and because of its excellent pulse-pileup rejection and correction features [24]. The Easy-MCA first employs an internal pulse pile-up rejecting circuit. This mechanism paralyzes the detector for a short period of time when a pulse arrives, so that a second pulse arriving during the same time period is thrown out, or eliminated. This prevents summation of the pulses, and allows the first pulse to be properly placed within its original energy

bin. This pulse pile-up rejecter, however, has no means of discriminating between pulses that arrive simultaneously, resulting in an inherent uncertainty within the rejection system.

The properties of the detection system can often change this distribution by reducing the number of counts, at an unknown rate. The live time clock, operating by the Gedcke-Hale method, is a useful feature of the MCA that allows users to correct for dead time and reduce the resulting distortion of counting statistics error [24]. The live time clock counts elapsed time only in the case when new pulses are being accepted by the system, and extends the collecting time of the system to make up for lost counts. If the collection and resulting experiment run for a preset live time, the MCA will automatically correct for dead time by dividing the observed counts by the preset live time. This yields a true count rate, and eliminates the distortion of counting statistics due to the difference in true and observed count rates. This difference is particularly relevant in detection within a carbon beam, as the high count rate introduces substantial issues related to pulse pile up and detector dead time. The uncertainty in spectra corrected by the Live Time Clock is well characterized for nuclear spectroscopy systems, quoting 1σ standard deviations of below 2% [25]. Though these characterizations are for lower count rate systems, it is anticipated that the resulting error, when propagated through to its effect on counting statistics, is negligible in this assessment.

2.1.2.8 Wall Effects

Another systemic measurement error contributing to overall uncertainty is the wall effects of the detector. Wall effects affect the production of ion pairs of particles that are associated statistically. The effects are, at a high level, due to the inhomogeneity in density between the air cavity, filled with tissue equivalent gas, and the surrounding wall of tissue equivalent plastic [22]. As a result of this difference, energy deposition events that originally would have occurred at slightly offset times are superimposed, causing a net increase in imparted energy as they appear to have been caused by a single event. These effects are primarily seen for low energy fragments as they slow down, perturbing the low lineal energy portion of the spectra.

There are four distinct effects caused by the wall. The first, known as the δ -ray effect, occurs when a heavy charged particle and one, or more, of its δ rays enter the volume simultaneously. Without the high density of the wall, the distance between the tracks of the particles would be great enough that each particle would be counted as a unique event, but instead they are measured simultaneously. This effect also incorporates situations in which the delta ray is produced after the charged particle has left the active volume. Overall, the δ -ray effect is the most important of the four with regards to heavy charged particles [8]. The second, the re-entry effect, occurs when an electron re-enters a cavity after already having traversed it. This phenomenon only applies to electrons, as they are the only particles with sufficient curvature to their path to allow for reentry to occur. The third effect, termed the V-effect, occurs when more than

one nuclear fragment produced outside the active volume traverse it [8]. Without the higher wall density, these interactions would likely originate far enough apart to count as separate events. The final effect is known as the scattering effect, and occurs when primary uncharged particles produce charged particles close enough in proximity that both may enter the cavity. Without the presence of the wall, the two particles may be far enough apart that only one of the particles would enter the volume. The scattering effect is prominent for neutrons and photons in multiple scattering events [8].

Perturbations of the microdosimetric spectra due to the walls of the detector are discussed in depth but are poorly characterized for therapeutic carbon beams. The calculated frequency of double events of protons above 5 MeV has been estimated at roughly 15% [8]. While this effect has not yet been investigated in depth for heavier ions, increases in \bar{y}_F by up to 30% have been quoted [8]. Wall-less proportional counters have been developed and studied to an extent in particle therapy with positive results [26] [27] [28]. To date, however, none are commercially available for purchase.

2.2 Materials and Methods

The process of quantifying the uncertainty and introducing it into a measurement based simulation is described here. For several of these sources, this was done first by selecting an appropriate TEPC for use in the study, and analyzing both its properties and those of the corresponding electronics. For others, this was done by assessing the parameters of a clinical carbon beam and

quantifying their effect, requiring an understanding of clinical beam parameters. In order to introduce and quantify the uncertainty, microdosimetric spectra calculated with Monte Carlo were also needed.

2.2.1 Clinical Beam

In order to understand the parameters of clinically active carbon beams beyond that detailed in literature, a survey was sent out by IROC Houston to each of twelve carbon ion centers that were either clinically active or in the building stages. Out of the twelve centers surveyed, there were five responses. Table 3 below displays the parameters surveyed along with the responses. Across institutions, the minimum beam energy ranged from 56 MeV/u to 140 MeV/u, with an average value of 102 MeV/u. The maximum beam energy ranged from 399 MeV/u to 430 MeV/u with an average value of 418 MeV/u. Reported treatment planning systems were manufactured by numerous different vendors. Each surveyed institution indicated that they either currently participated in or planned to participate in clinical trials, emphasizing the need to establish consistency across treatment delivery.

Table 3. Parameters of clinical beams as indicated by each of 5 surveyed institutions.

Question	Response
Beam delivery mode	Scanning (5) Scattered (1)
Lowest instantaneous dose rate	1.25E7 pps (1) 1.59E7 pps (1) 3E7 pps (2) Unknown (1)

Can instantaneous dose rate be mechanically tuned down?	Yes (3) No (2)
Minimum clinical beam energy	56 MeV/u (1) 80 MeV/u (1) 115 MeV/u (1) 120 MeV/u (1) 140 MeV/u (1)
Maximum clinical beam energy	400 MeV/u (2) 430 MeV/u (3)
Treatment planning system	Siemens Syngo (2) Elekta (2) RayStation (1)
RBE model used	LEM I (3) MKM (2)
Ridge/ripple filter use	Yes (5)
Sites treated	Prostate, Bone & Soft Tissue, Liver, Lung, Pancreas, Head & Neck, Nasopharynx, Rectum, Gynecological Region, Eye, etc.

2.2.2 Monte Carlo

Monte Carlo was used to calculate microdosimetric spectra, which were then perturbed based on quantified uncertainty to simulate physical measurement based values. The general-purpose Monte Carlo toolkit from Geant4 (version 10.4) was used for particle tracking. The setup used to simulate these parameters involved a pure carbon beam, free of filters, incident on a water phantom of 80 x 80 x 40 cm³. The carbon beam entered the target phantom along the z-axis using the general particle source (GPS) method. The number of events per simulation was fixed at 10⁶.

A scoring disc with a radius 40 cm and a thickness of 1 µm was used to cover the size of the beam spot and to capture particles scattered laterally. This

allowed the integral depth dose to be scored. The thickness of 1 μm was selected in order to represent the scale of the cell nucleus. This value has also been used in several published studies of Monte Carlo carbon microdosimetry, and therefore provides a strong basis for comparison [10]. The spacing of two adjacent scoring discs along the beam path was set to 1 mm. Many different physics lists in Geant4 can be used for particle therapy and the difference in simulation results was found negligible. The 'FTFP_BERT' physics list was adopted in the current study, which provides both standard electromagnetic physics processes and hadronic physics processes [29]. Different types of scorers were defined to score different physical quantities of interest such as dose, kinetic energy spectra, and microdosimetric spectra. All of the simulation results were scored in ROOT histograms and then dumped for further data analysis [30].

Each of the parameters detailed below were extracted for 161 energy groups, spanning 120 to 440 MeV/u at 2 MeV/u intervals with subsequent ranges of 4.1 cm to 33.1 cm in water [2]. In order to represent SOBP setups, a physical dose distribution for the SOBP along with a beam weighting scheme was generated for three different SOBP widths: 5 cm, 7 cm, and 10 cm. This allowed the proper weighting of each beam energy to create an SOBP, across which the physical dose was fixed at a constant 2 Gy. Although the physical dose is typically optimized to provide a flat RBE weighted dose, this method was used to provide a comparative basis across all RBE models assessed.

Table 4. Depth of the Bragg peak for a range of monoenergetic beams, and both start and end depths of the SOBP.

Beam	Peak	Start Depth	End Depth
146 MeV/u Monoenergetic	4.7 cm		
218 MeV/u Monoenergetic	9.7 cm		
276 MeV/u Monoenergetic	14.6 cm		
330 MeV/u Monoenergetic	19.7 cm		
424 MeV/u Monoenergetic	29.7 cm		
5 cm SOBP		5 cm	10 cm
7 cm SOBP		8 cm	15 cm
10 cm SOBP		20 cm	30 cm

2.2.2.1 Microdosimetric Spectra

Frequency and dose and weighted lineal energy spectra were generated for all relevant energies described above. For this simulation, the bin width of the lineal energy spectra was equal with logarithmic spacing. 700 bins spanning lineal energy values of 0.001 keV/ μm to 1000 keV/ μm were used.

2.2.3 Uncertainty Analysis

In order to assess the uncertainty introduced into the physical microdosimetric measurements, eight sources of noise were identified using ICRU Report 36 [8]. Each of these sources were quantified according to the properties of the LET-1/2 detector and respective electronics, as necessary. The uncertainty sources are typically categorized as either random uncertainties, introducing a variance about the true Monte Carlo calculated lineal energy, or

systematic uncertainties, introducing a systematic bias in the true Monte Carlo calculated lineal energy. Each of the systematic sources of uncertainty were also associated with an additional random variance about the shifted value.

- c. Random:
 - a. Counting statistics
 - b. Gas pressure and mean chord length
 - c. Electronic uncertainty
 - d. Gain instability and energy calibration
- d. Random and systematic:
 - a. W-value
 - b. Low energy cutoff
 - c. Pulse pile-up
 - d. Wall effects

The effect of the noise source on the microdosimetric spectra was also assessed, whether the source would shift the spectra up or down in energy bin (example shown in Figure 7 and Figure 8) or in number of counts per bin (example shown in Figure 9 and Figure 10). For each of the random uncertainty sources, a MatLab program was written in which noise was randomly added over 200 iterations. At each iteration, the spectra was shifted by random number distributed normally with a 1σ standard deviation equal to the quantified value of the shift. If the source was systematic and induced a shift, that shift was induced over 200 iterations with a 1σ variance distributed about the shifted mean. If the

source affected bin height, the height of each bin was independently and randomly adjusted according to the characteristics of the noise.

For each iteration, the lineal energy values were recalculated using the shifted spectrum to result in a matrix of 200 different lineal energy values. The standard deviation of these 200 values were used to form error bars for the measured lineal energy value. However, if the source was both systematic and random (W-value calibration, low energy cutoff, pulse pile-up, and wall effects), the average of the shifted values was calculated and compared with the original RBE by computing a percent difference. This percent difference indicated the shift towards the new mean, about which the standard deviation was calculated. Finally, the standard deviation for each source was calculated independently, and then summed in quadrature to form overall margins for the measured lineal energy value as a function of initial beam energy and depth. These error bars were centered about the shifted lineal energy value, which was calculated through summing and incorporating the percent difference of each systematic source. This value was then compared to the true lineal energy as calculated through the Monte Carlo microdosimetric spectra.

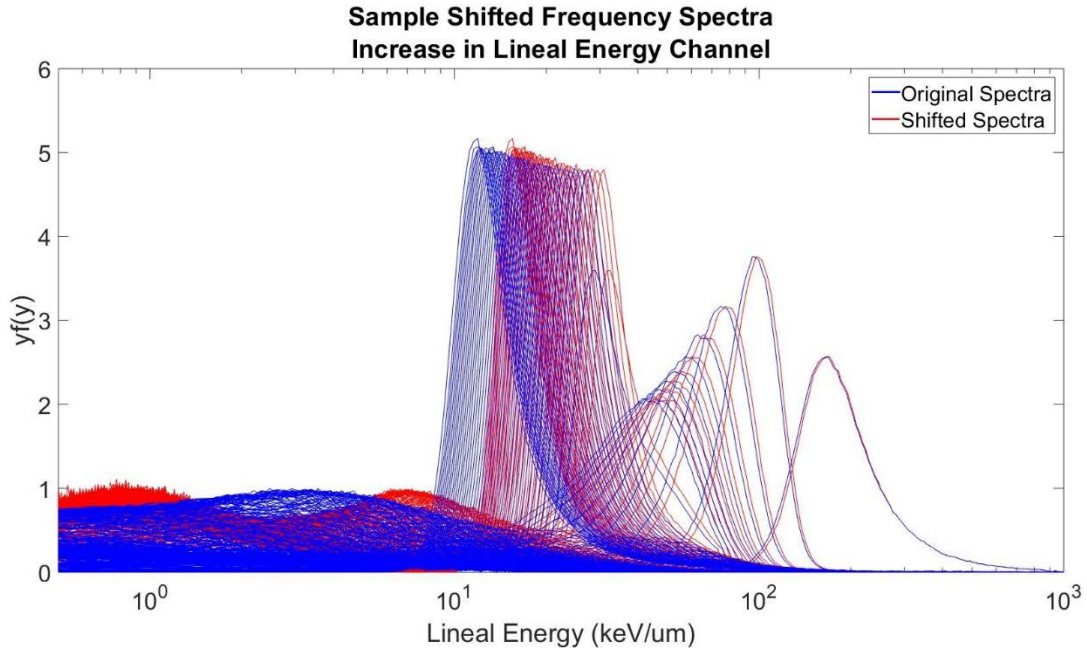


Figure 7. Example of one iteration of the frequency spectra shifted to a higher lineal energy bin (spectra shifts right), applied to all spectra (i.e., all depths) for a single initial carbon energy.

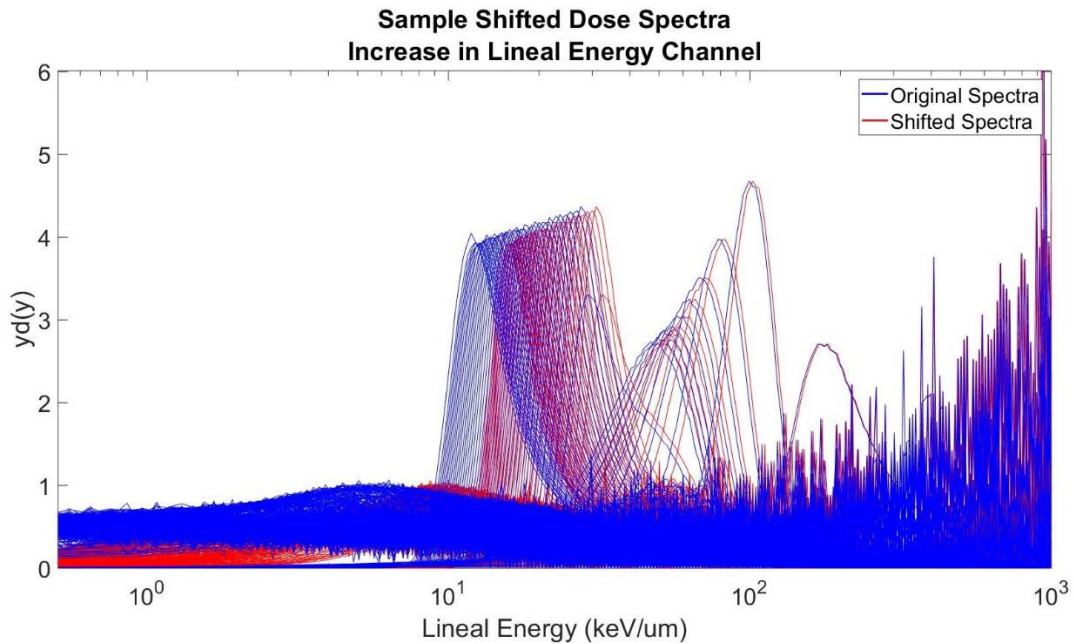


Figure 8. Example of one iteration of the dose spectra shifted to a higher lineal energy bin (spectra shifts right), applied to all spectra (i.e., all depths) for a single initial carbon energy.

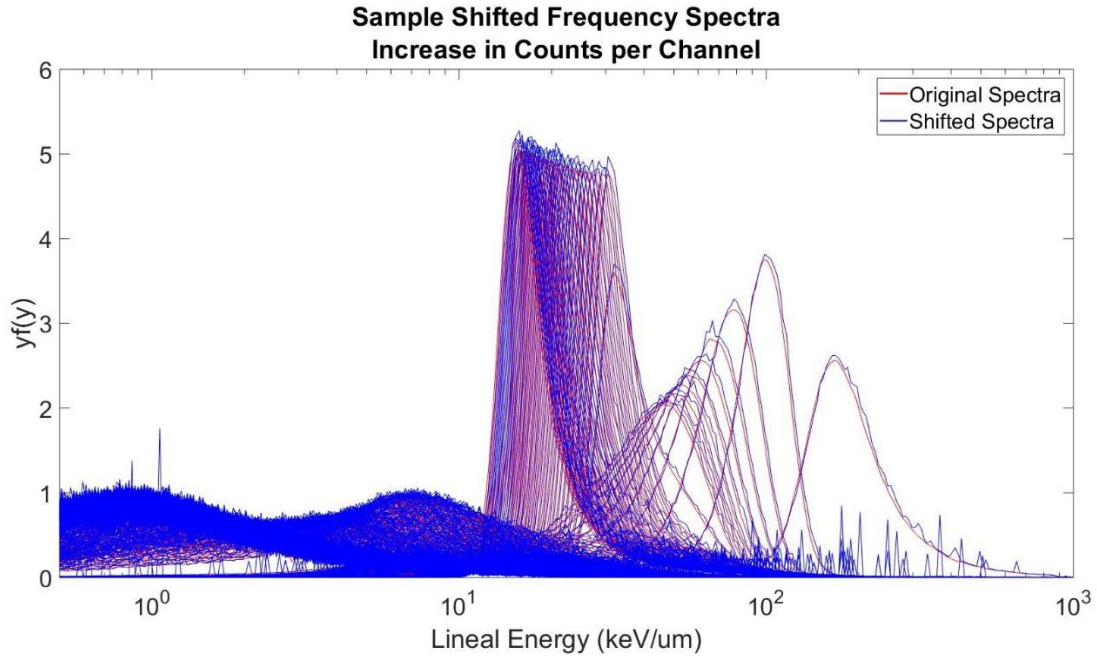


Figure 9. Example of one iteration of the frequency spectra shifted to a higher number of counts per bin (spectra shifts up), applied to all spectra (i.e., all depths) for a single initial carbon energy.

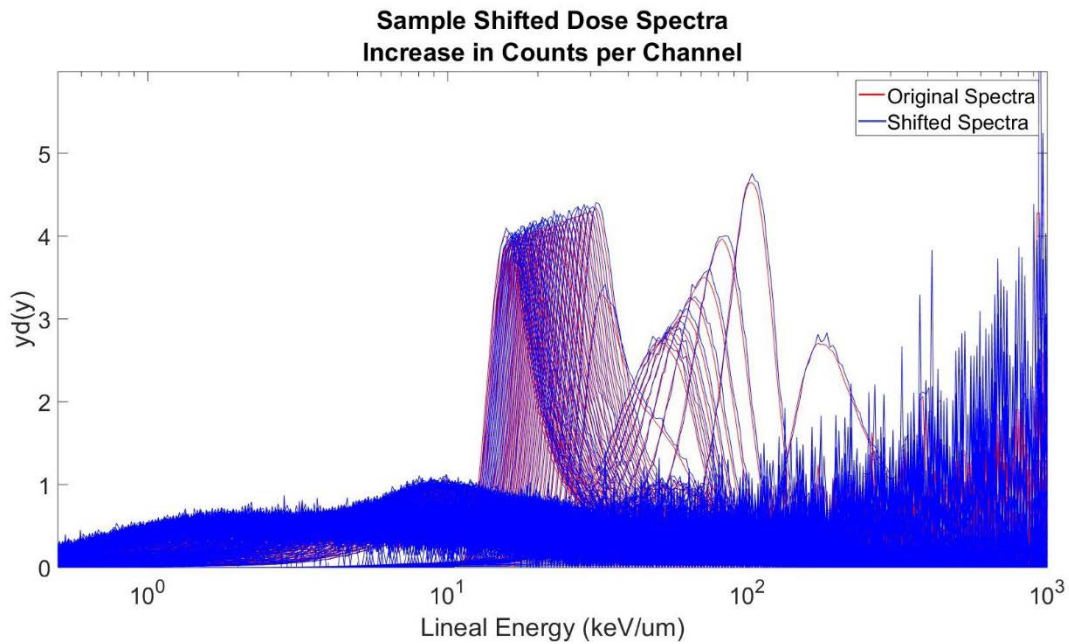


Figure 10. Example of one iteration of the dose spectra shifted to a higher number of counts per bin (spectra shifts up), applied to all spectra (i.e., all depths) for a single initial carbon energy.

2.2.3.1 Counting Statistics

As described, the microdosimetric spectra calculated with Monte Carlo are subject to uncertainty equal to $\frac{1}{\sqrt{N}}$. In order to obtain the number of counts, the normalized probability density function was multiplied by the total number of counts anticipated in the collection time. An estimate of $10E7$ particles was used for this assessment. As the count rate is typically on the order of $10E7$ pps clinically, the total number of counts will likely be much higher in practice, reducing the uncertainty introduced here.

At each lineal energy, a random number distributed about the mean, N , of the channel was added to the channel at 200 different iterations. The random numbers had a 1σ standard deviation equal to $\frac{1}{\sqrt{N}}$, resulting in wider distributions for low count channels. Once 200 different spectra were generated, new lineal energy values were calculated for each. The uncertainty was then quantified based on the variance across each of the 200 shifted values.

2.2.3.2 Gas Pressure and Mean Chord Length

The LET-1/2 detector is sold with a gas fill system that has a recorded uncertainty of 0.3% [11]. As no further analysis was available upon discussion with the manufacturer, a conservative assumption that this value correlated to 1σ standard deviation was made. This results in the channels being shifted to higher or lower lineal energy values. As such, the spectra was shifted horizontally by random numbers about a 1σ standard deviation of 0.3% of the channel energy.

2.2.3.3 Electronic Uncertainty

While there was little published data as to the uncertainty in the electronics used with the LET-1/2, it was noted that several electronic components were tested prior to being sold, and would be discarded if the uncertainty exceeded 1 keV/ μm . As this was a hard cutoff threshold, it was estimated that this value corresponded to a 3- σ standard deviation. Accordingly, the microdosimetric spectra was shifted in horizontally in lineal energy over 200 iterations with a 1 σ standard deviation of 0.33 keV/ μm . The respective lineal energy values were calculated for each model, and the standard deviation of these values was calculated.

2.2.3.4 Gain Instability

According to Far West Technologies, the LET-1/2 has a maximum channel drift of 1 in 100 channels in every eight hours [11]. Linearly extrapolating this value to a very liberal measurement time of one hour results in a channel drift of 0.125%. As this is the maximum recorded drift of this detector, 0.125% was assumed to be a 2- σ , or 97.5%, uncertainty. In order to quantify the effect of this uncertainty on microdosimetric parameters, the microdosimetric spectra was randomly shifted in energy 200 times, with a 1 σ standard deviation of 0.0625%. The spectra was shifted in this manner as channel drift can cause ion pair collection to move to either higher or lower energy bins.

2.2.3.5 W-Value and Energy Calibration

In order to quantify this value, the kinetic energy of each fragment was calculated in the entrance of the beam, at a depth of 1 mm. The W -value that corresponded to that energy and fragment in liquid water, a similar medium to tissue-equivalent gas, was obtained through literature [12]. As the TEPC utilizes tissue-equivalent material rather than water, the W -values per fragment would ideally be for tissue equivalent material. However, due to the lack of published W -values for heavy ions in TE material, the experimental data that was available (found for carbon, oxygen, and nitrogen) were compared to their corresponding W -values in water [23]. A percent difference of 3% was calculated, which was within the 1σ level uncertainty with the quoted values. As a result, it was assumed that this difference will be negligible in the overall uncertainty analysis and W -values for fragments may accurately be taken from water in this assessment.

The W -value of heavy ions is highly energy dependent, particularly at energies lower than 1 MeV, which is caused primarily by the corresponding energy dependence of the ratio of ionization to excitation cross section [23]. This energy dependence is shown in Figure 11 for carbon ions in water. The W -value of other heavy ion carbon beam fragments follow similar trends.

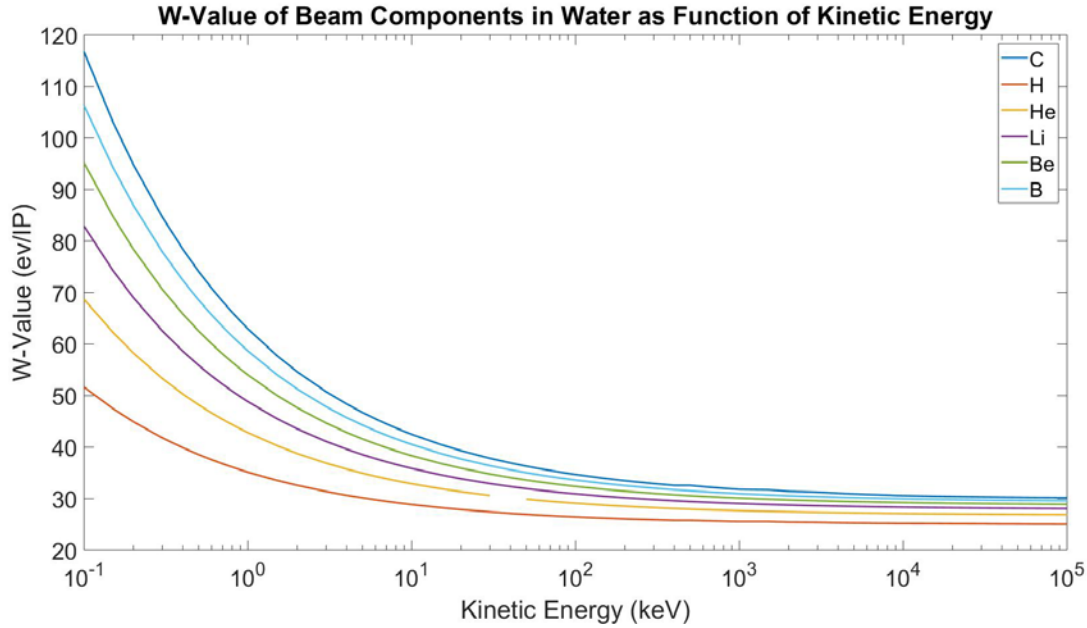


Figure 11. Displays the W -value of substantial dose contributing ion species as a function of kinetic energy in water. Data points are taken from [11].

The kinetic energy of each species at the beam entrance (depth of 1 mm) was used to interpolate the data from Figure 11 to determine the exact W -value of each fragment. Once these values were obtained, a weighted average was calculated using the percent contribution of each fragment as a function of depth. This provided an overall W -value for each unique simulated carbon beam. The percent difference between this calculated W -value and that of the neutron source, [23], then provided the basis with which to empirically shift the spectra. The standard deviation came from the uncertainty in the neutron W -value, at 4.8%, which was translated to the overall uncertainty in the shift as there were no quoted uncertainties for the W -values of the carbon beam [12]. This was assumed to correspond to a 1σ level, and was used to perturb the spectra about the shifted mean.

The perturbation of the microdosimetric spectra was repeated for 200 iterations. The mean of the perturbed values was centered at the lineal energy value plus the difference in W-value of the neutron source and that unique carbon beam, and the standard deviation corresponded to a 1σ standard deviation of 4.8%. Corresponding lineal energy values were calculated. To quantify the bias, the percent difference was taken between the mean of the 200 shifted values and the true lineal energy value. In order to incorporate the variance, the 1σ standard deviation was calculated across the 200 perturbed values.

2.2.3.6 Low Energy Cutoff

The ICRU Report recommends quantifying low energy cutoff based off of preamplifier noise; however, the LET-1/2 has a quoted cutoff value of 0.5 keV/ μm below which the signal is no longer reliable. While unconfirmed, it is likely that this value refers to the typical preamplifiers used with the system. Commonly used proportional counter preamplifiers were also investigated, with recommended cutoff values similar to 0.5 keV/ μm , affirming the decision to use this value in the uncertainty assessment.

The simulated spectra, which is not subject to low energy cutoff, is shown below in Figure 12. The red line represents the cutoff point. In a practical measurement of these spectra, the signal below this line would be unreliable. In order to compensate for this, the effect of removing the spectra entirely below 0.5 keV/ μm was quantified. This was deemed substantial in its impact on the lineal

energy values, so methods to append a modeled low lineal energy tail below the cutoff value were investigated and quantified.

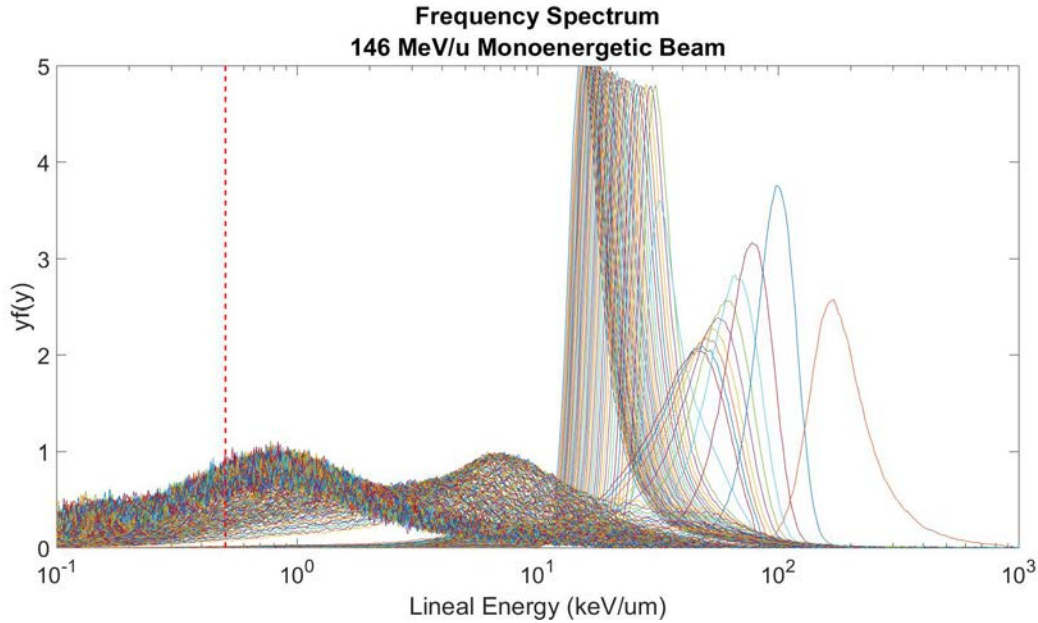


Figure 12. Frequency spectra for a 146 MeV/u monoenergetic beam. The red dotted line is located at 0.5 keV/um on a log scale to localize the threshold of the low energy cutoff.

Three models were examined, based on a linear, exponential, and log-linear fit. They were evaluated for uncertainty introduced in lineal energy and, based on this, the best fitting model was selected to extrapolate from the 0.5 keV/um cutoff down to zero energy.

Once a model was selected, it was appended to the lineal energy spectra at a count number distributed about the 0.5 keV/um cutoff value. While there was no uncertainty quoted with the cutoff value of the detector, a 1σ standard deviation of this distribution was selected at the 10% level to sample a range of appending points for the cutoff model. As this uncertainty source was anticipated

to have low impact on the calculations, small deviations from the 10% have little significance.

2.2.3.7 Pulse pile-up

A Matlab code was written to simulate pulse pileup by randomly sampling the distribution of the counts. The probability of more than one pulse, $p(>1)$, arriving simultaneously at the detector for a given count rate can be described by a Poisson distribution [31]. This probability is defined in Equation 35, in which τ represents the dead time of the detector, fixed at 2 μ s for the Ortec Easy-MCA-8k, and ρ is the count rate of the carbon beam [31] [24]. The count rate was varied across a range of counts in order to determine the highest count rate that could be used to produced reasonable measurement uncertainty.

Equation 34
$$p_n(> 1) = 1 - e^{-\rho\tau} - \rho e^{-\rho\tau}$$

For a wide range of count rates, including both clinical and mechanically tunable, the probability of more than one pulse arriving simultaneously was calculated and used to randomly sample the microdosimetric frequency distribution. At each sample, the channel within which the summed pulses would fall was calculated, and a count was then added to that channel. Counts were added spanning the pileup probability to result in unique perturbed dose and frequency-weighted spectra for an arbitrarily high dose rate. This process was repeated 200 different times, consistent with number of iterations used with other sources of noise, and resulted in 200 different lineal energy spectra. The resulting \bar{y}_D , \bar{y}_F , and y^* values were calculated with each spectra, across which

the standard deviation was calculated to determine the overall 1σ uncertainty. After a range of count rates were assessed, the highest rate that could be used with reasonable uncertainty was determined and used throughout the uncertainty calculations.

2.2.3.8 Wall Effects

A paper by Tsuda and colleagues investigates the differences between Monte Carlo calculated spectra, and measurements taken both by walled (LET-1/2) and wall-less TEPCs [28]. Based on these comparisons, the shape of the spectra as measured with walled and wall-less detectors was found to be quite similar in shape for the primary peak, around 10 keV/ μm , and above. However, the peak with the walled TEPC was roughly 0.25 keV/ μm higher in lineal energy than the peak of the wall-less detector [28]. While the primary peak is shifted slightly, it had the same shape, indicating that the walled and wall-less TEPC show similar response with regard to the primary beam corresponding to heavier particle contributions such as carbon and boron. At lineal energies around 0.2 - 3 keV/ μm , the number of counts were much lower, by about an order of magnitude, for the walled TEPC as compared to the wall-less. The authors indicated that this is likely due to the absence of delta rays produced outside the wall [28]. As little other data was found as to the direct effect on the spectra, these are the parameters that were used in the uncertainty analysis.

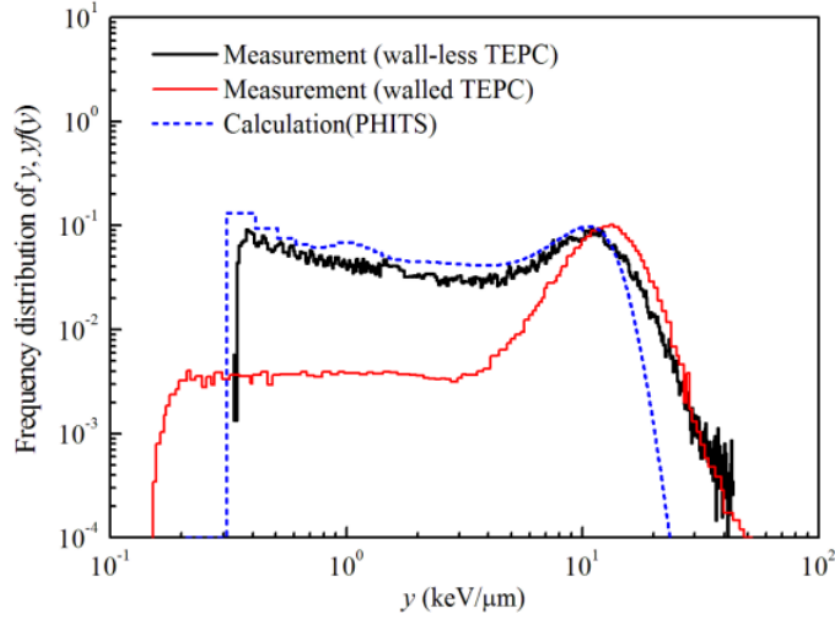


Figure 13. Frequency distribution measured with walled and wall-less TEPC. Monte Carlo calculated distribution presented for comparison [28].

In order to introduce wall effect error into the Monte Carlo simulations, the empirical spectra was manipulated following the indications by Tsuda and colleagues. In the low lineal energy region, energies below 3 keV/μm, the spectra was suppressed to between 5% and 15% of the original magnitude. These values were arbitrarily selected to sample a range about the 10% value seen in the literature. The entire spectra was also shifted up in lineal energy by 0.25 keV/μm. As per the standard procedure of introducing uncertainty, the spectra was perturbed 200 times at this threshold. The resulting uncertainty due to the spectra was then quantified through the lineal energy values.

2.2.3.9 Total Uncertainty

The bias produced by each of the systematic sources of uncertainty was calculated by averaging the shifted spectrum, and calculating a percent difference between the true lineal energy value and the perturbed average. The total bias was added for each of the four sources to present a picture of corrections that may be required for a measured spectra.

The variance introduced by each source was calculated by taking the standard deviation across the matrix of 200 perturbed values. The total uncertainty was then calculated by summing the variance due to each of the eight independent sources in quadrature. This gave an overall 1σ variance for lineal energy value as a function of beam and depth, quantified for both monoenergetic beams and for SOBP beams.

2.3 Results

2.3.1 Monte Carlo

For the first specific aim in this project, the Monte Carlo setup was used to extract microdosimetric over a range of clinical beam energies including monoenergetic beams from 120 MeV/u to 440 MeV/u and SOBPs from 5 cm to 10 cm in length. From these spectra, respective lineal energy values were calculated and perturbed using quantified uncertainty to simulate a measurement based setup. The Monte Carlo setup used to generate the microdosimetric spectra was validated through comparison of calculated lineal energy values with those published by Kase and colleagues [10].

2.3.1.1 Microdosimetric Spectra

While analysis was performed on wide range of clinical energies, microdosimetric data are shown here for a 146 MeV/u monoenergetic, a 424 MeV/u monoenergetic, and a 7 cm SOBPs beam to represent the spread. Figure 14, Figure 15, and Figure 16 give the frequency weighted microdosimetric spectra for each of these beams, respectively. Each curve in the figure corresponds to the microdosimetric spectrum at a given depth in water, ranging from the entrance to 40 cm depth. The dose weighted spectra are shown for the same set of beams in **Error! Reference source not found.**, Figure 18, and Figure 19 respectively.

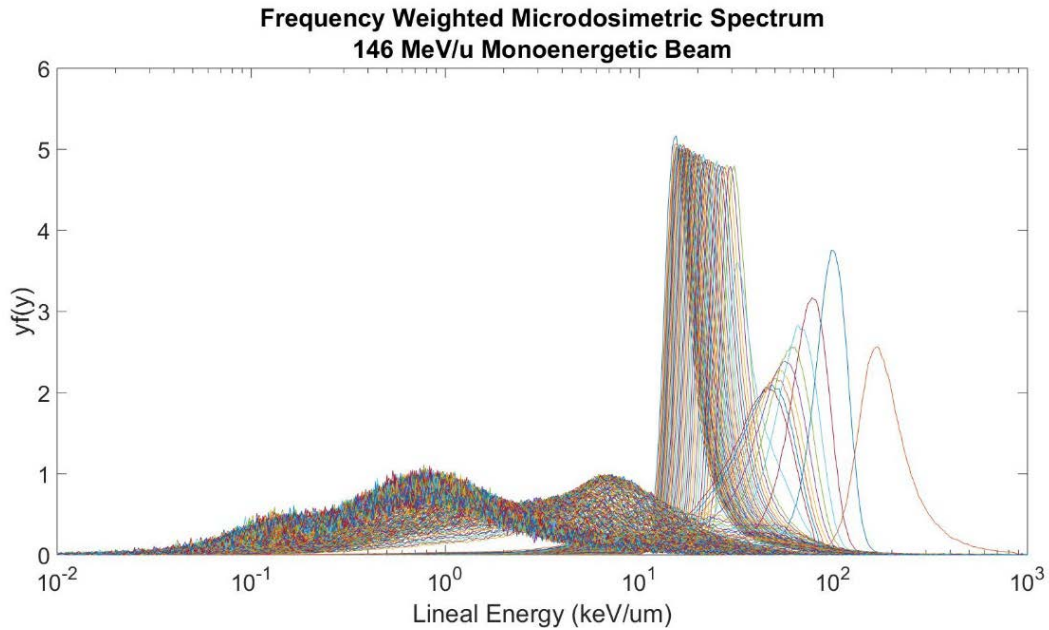


Figure 14. Monte Carlo calculated microdosimetric frequency spectra for 146 MeV/u monoenergetic beam. Curves show the spectra for different depths, ranging from 0 to 40 cm at 0.1 cm intervals.

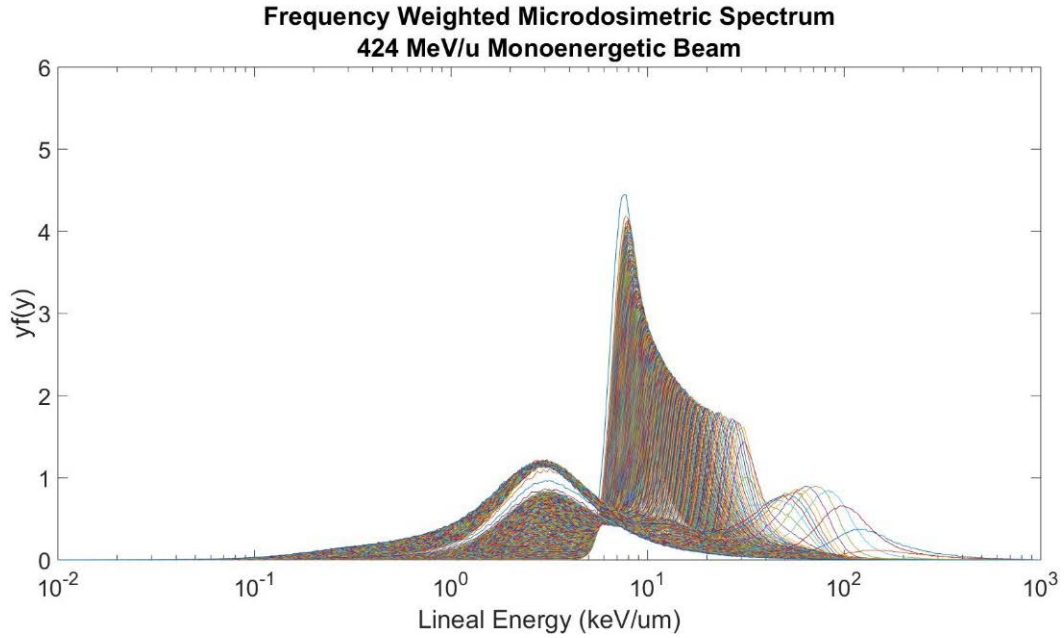


Figure 15. Monte Carlo calculated microdosimetric frequency spectra for 424 MeV/u monoenergetic beam. Curves show the spectra for different depths, ranging from 0 to 40 cm at 0.1 cm intervals.

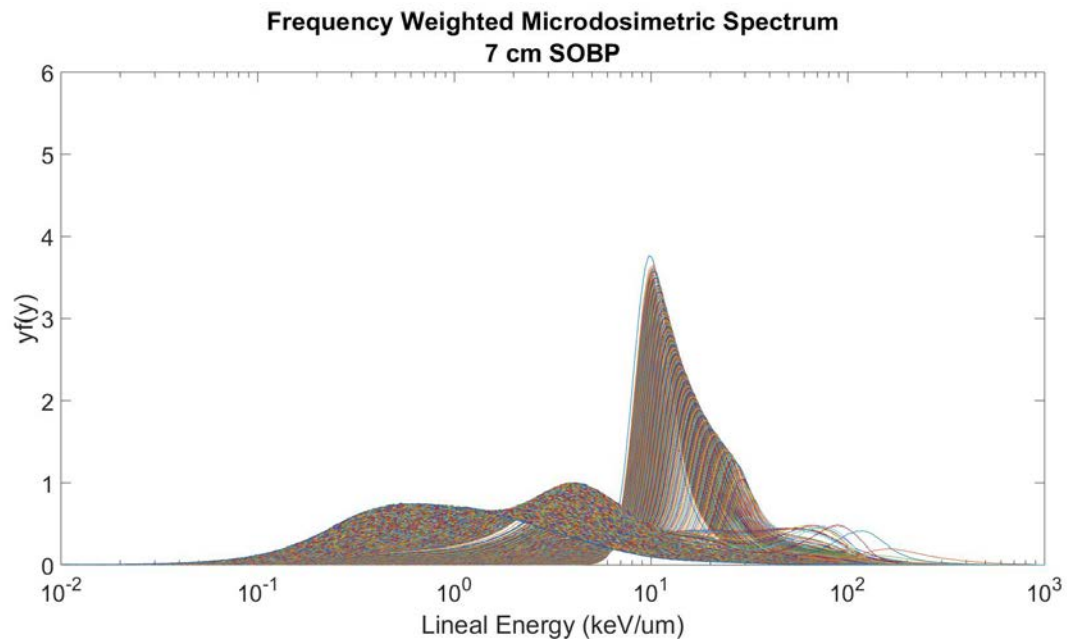


Figure 16. Monte Carlo calculated microdosimetric frequency spectra for 7 cm SOBP. Curves show the spectra for different depths, ranging from 0 to 40 cm at 0.1 cm intervals.

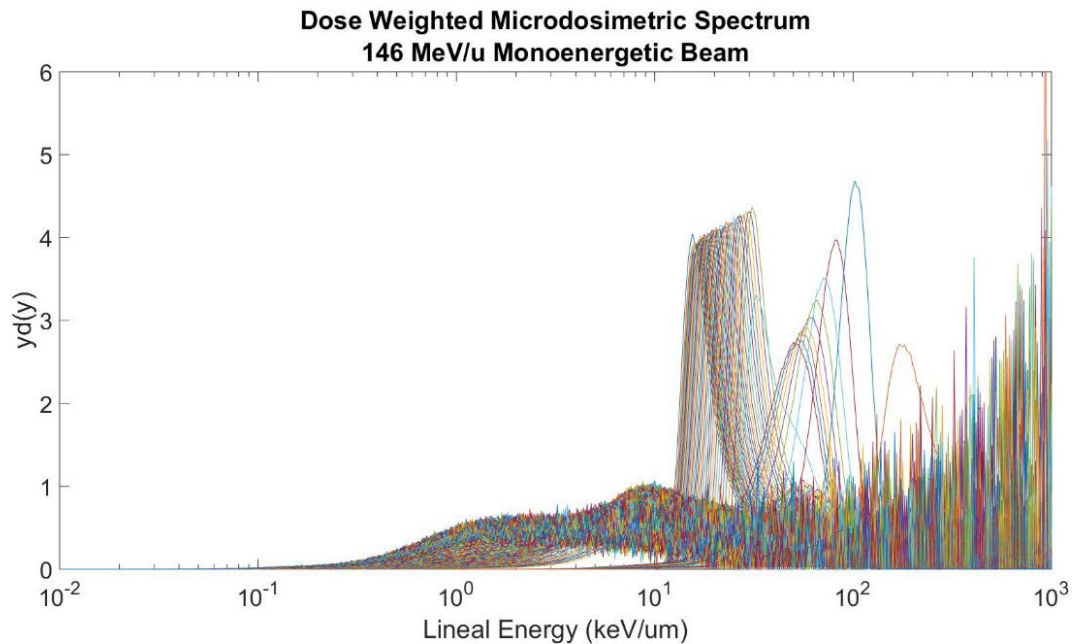


Figure 17. Monte Carlo calculated microdosimetric dose spectra at 146 MeV/u beam energy. Curves show the spectra for different depths, ranging from 0 to 40 cm at 0.1 cm intervals.

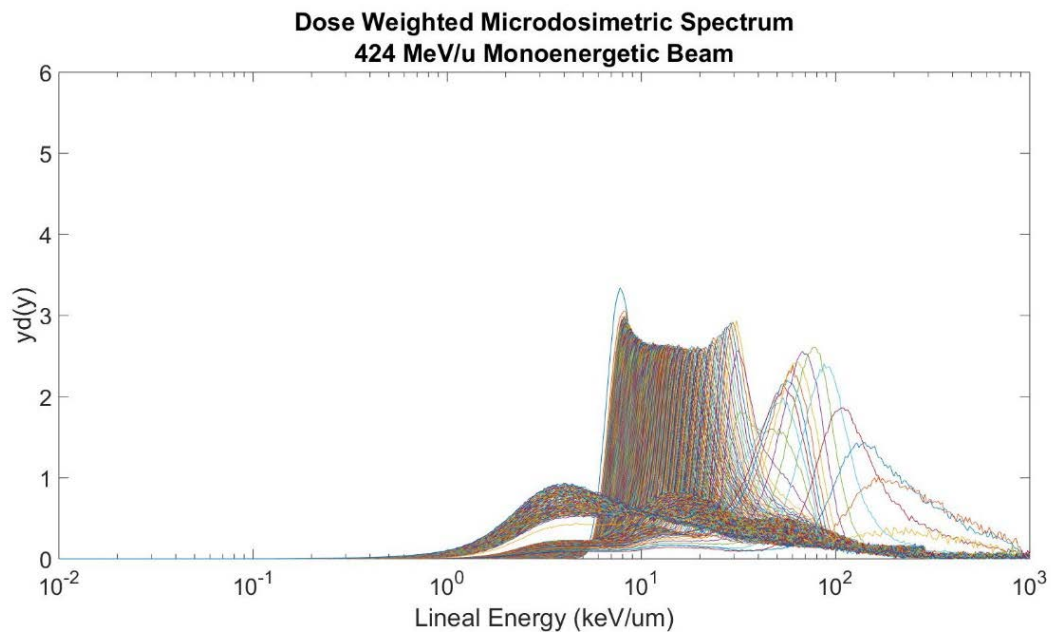


Figure 18. Monte Carlo calculated microdosimetric dose spectra at 424 MeV/u beam energy. Curves show the spectra for different depths, ranging from 0 to 40 cm at 0.1 cm intervals.

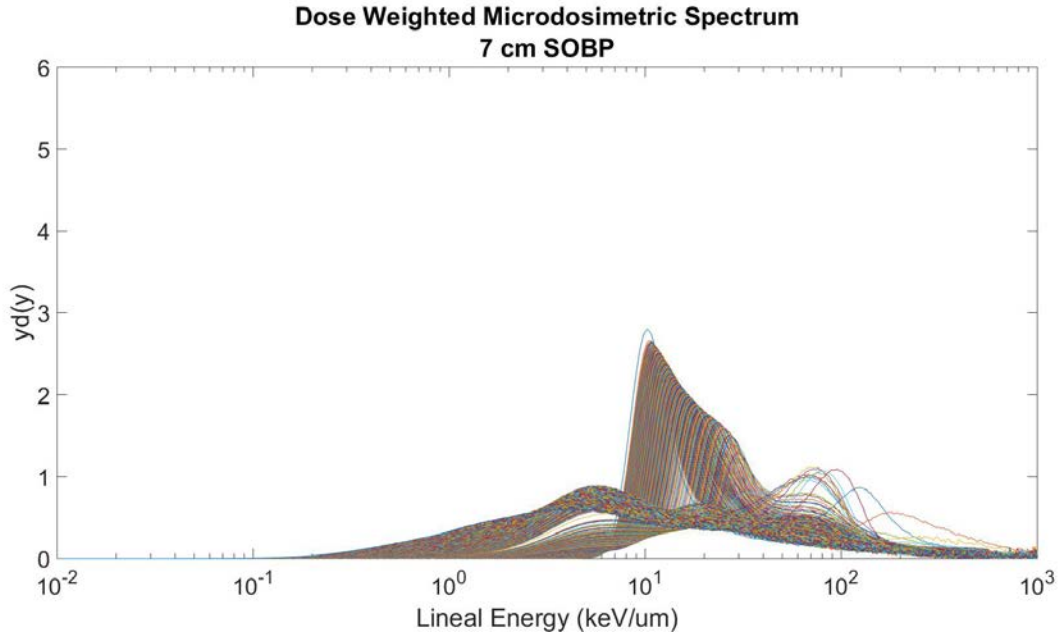


Figure 19. Monte Carlo calculated microdosimetric dose spectra for 7 cm SOBP. Curves show the spectra for different depths, ranging from 0 to 40 cm at 0.1 cm intervals.

The lineal energy values were then calculated from these spectra using Equation 5, Equation 6, and Equation 8 from Section 3.3.2. The lineal energy values are shown in Figure 20, Figure 21, and Figure 22 as a function of depth. Additionally, a full tables of lineal energy values as functions of depth as calculated in this study are presented in the Appendix. As can be seen in Figure 21, extensive noise is associated with the dose mean lineal energy.

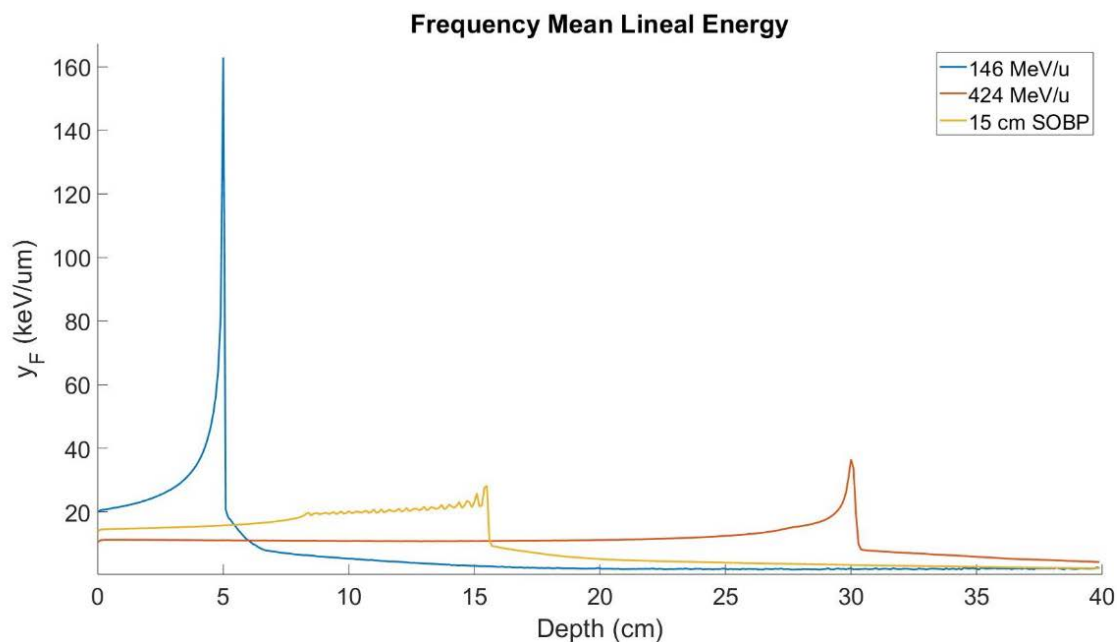


Figure 20. Frequency mean lineal energy values calculated as a function of depth for 146 MeV/u monoenergetic, 424 MeV/u monoenergetic, and 7 cm SOBP beams.

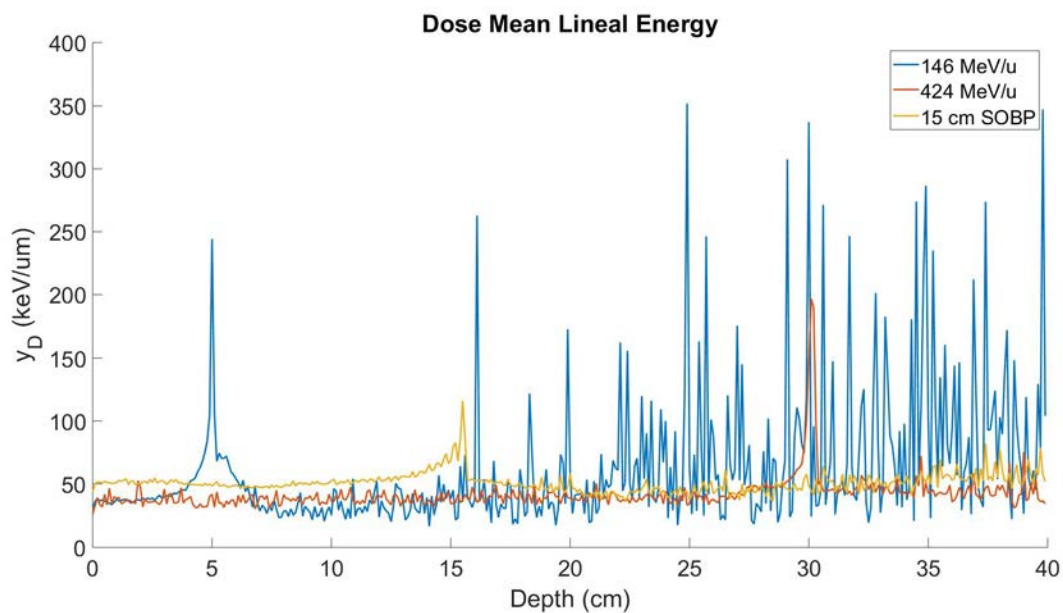


Figure 21. Dose mean lineal energy values calculated as a function of depth for 146 MeV/u monoenergetic, 424 MeV/u monoenergetic, and 7 cm SOBP beams.

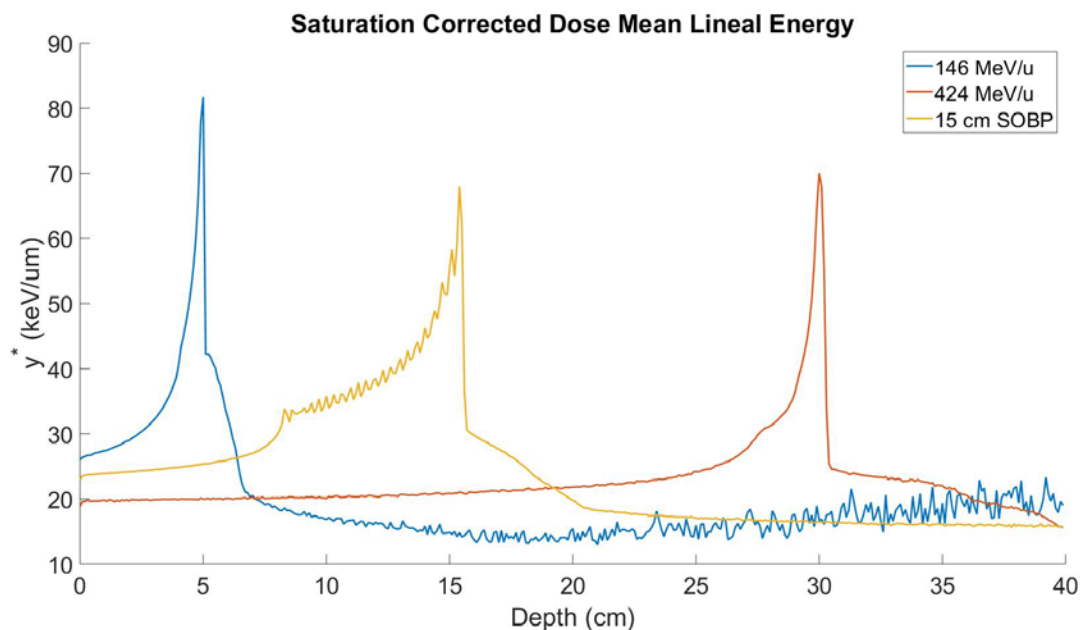


Figure 22. Saturation corrected dose mean lineal energy values calculated as a function of depth for 146 MeV/u monoenergetic, 424 MeV/u monoenergetic, and 7 cm SOBP beams.

2.3.2 Uncertainty Analysis

The results are presented below for the uncertainties propagated through to the lineal energy values by each source independently. For the random sources of uncertainty (counting statistics, gas pressure and mean chord length, electronic uncertainty, and gain instability) the variance alone was calculated. Variance is presented as the percent standard deviation, at the 1σ level, in lineal energy across the perturbed values. For the sources that were both systematic and random (W-value and energy calibration, low energy cutoff, pulse pile-up, and wall effects), both variance and bias were quantified. Bias is presented as the percent difference between the average of the perturbed values and the true lineal energy. In order to quantify total uncertainty, the variance due to each

source was added in quadrature. The bias was summed to calculate an overall percent difference. Data points are presented at a specific entrance point (2 cm), and the corresponding average and maximum values are taken from 0.1 cm to 1 cm proximal to the Bragg peak. They are also presented for the Bragg peak, and the corresponding average and maximum values are taken across the Bragg peak region, if an SOBP.

2.3.2.1 Counting Statistics

The uncertainty introduced by counting statistics into the lineal energy values was quite low, averaging 0.59% across all \bar{y}_D values and just 0.16% across all \bar{y}_F values. Slight increases in standard deviation were seen with increasing beam energy, and with the SOBP, but only changed on the order of 0.4% across the range of clinical energies. Table 5 displays the variance introduced in each of the lineal energy values in further detail.

Table 5. Percent standard deviation, at the 1σ level, introduced in lineal energy values by counting statistics.

Beam	Lineal Energy	Standard Deviation (%)					
		Entrance	Avg.	Max.	Bragg Peak	Avg.	Max.
146 MeV/u Monoenergetic	\bar{y}_F	0.07	0.12	0.36	0.07		
	\bar{y}_D	0.10	0.09	0.12	0.03		
	y^*	0.07	0.08	0.24	0.05		
424 MeV/u Monoenergetic	\bar{y}_F	0.06	0.21	2.05	0.90		
	\bar{y}_D	0.10	0.08	0.12	0.06		
	y^*	0.15	0.20	0.54	0.16		
7 cm SOBP	\bar{y}_F	0.07	0.14	2.93	0.06	0.10	1.13
	\bar{y}_D	0.26	0.20	0.72	0.07	0.15	0.37
	y^*	0.14	0.13	1.73	0.22	0.06	0.78

2.3.2.2 Gas Pressure and Mean Chord Length

Gas pressure and mean chord length introduce a variance about the lineal energy values that was, on average, 0.32%. Overall, this source did not present a variance of over 0.55%. The y^* values were most highly impacted by this source, at about 25% higher than the other values. The variance in each lineal energy value is presented in Table 6.

Table 6. Percent standard deviation, at the 1σ level, introduced in lineal energy values by gas pressure and mean chord length.

Beam	Lineal Energy	Standard Deviation (%)					
		Entrance	Avg.	Max.	Entrance	Avg.	Max.
146 MeV/u Monoenergetic	\bar{y}_F	0.32	0.32	0.32	0.32		
	\bar{y}_D	0.32	0.32	0.32	0.32		
	y^*	0.27	0.27	0.30	0.25		
424 MeV/u Monoenergetic	\bar{y}_F	0.31	0.31	0.31	0.31		
	\bar{y}_D	0.31	0.31	0.46	0.31		
	y^*	0.15	0.20	0.54	0.15		
7 cm SOBP	\bar{y}_F	0.40	0.40	0.40	0.40	0.40	0.40
	\bar{y}_D	0.40	0.39	0.40	0.40	0.40	0.40
	y^*	0.22	0.22	0.34	0.25	0.23	0.26

2.3.2.3 Electronic Uncertainty

The variance introduced by electronic uncertainty was, on average, the second highest contributing source of uncertainty, reaching values up to 3.0%. Variance in \bar{y}_F values were considerably higher than that of \bar{y}_D and y^* , by anywhere from 2-5 times greater in magnitude. This is likely a result of the distribution weighting, as the low lineal energy values have a greater impact on the frequency weighted microdosimetric spectra. These values are detailed in Table 7 for each lineal energy value and beam energy quantified.

Table 7. Percent standard deviation, at the 1σ level, introduced in lineal energy values by electronic uncertainty.

Beam	Lineal Energy	Standard Deviation (%)					
		Entrance	Avg.	Max.	Bragg Peak	Avg.	Max.
146 MeV/u Monoenergetic	\bar{y}_F	1.30	1.29	1.52	0.65		
	\bar{y}_D	0.82	0.80	0.98	0.49		
	y^*	0.68	0.66	0.69	0.34		
424 MeV/u Monoenergetic	\bar{y}_F	2.84	2.78	3.04	1.54		
	\bar{y}_D	0.61	0.84	1.23	0.52		
	y^*	0.18	0.14	0.21	0.31		
7 cm SOBP	\bar{y}_F	1.44	1.39	1.55	1.10	1.07	1.17
	\bar{y}_D	0.50	0.48	0.55	0.48	0.47	0.50
	y^*	0.17	0.21	0.23	0.21	0.18	0.26

2.3.2.4 Gain Instability

The uncertainty introduced by gain instability did not exceed 0.50% in any of the lineal energy values. The variance in the 146 MeV/u monoenergetic beam are higher than those in the 424 MeV/u monoenergetic beam and the 7 cm SOBP by around 50% on average. Dramatic changes in variance were not present across lineal energy values within each energy. The values of variance are expressed as a percent standard deviation at the 1σ level in Table 8.

Table 8. Percent standard deviation, at the 1σ level, introduced in lineal energy values by gain instability.

Beam	Lineal Energy	Standard Deviation (%)					
		Entrance	Avg.	Max.	Bragg Peak	Avg.	Max.
146 MeV/u Monoenergetic	\bar{y}_F	0.09	0.09	0.09	0.09		
	\bar{y}_D	0.09	0.09	0.09	0.09		
	y^*	0.08	0.08	0.08	0.07		
424 MeV/u Monoenergetic	\bar{y}_F	0.31	0.31	0.31	0.31		
	\bar{y}_D	0.31	0.31	0.46	0.31		
	y^*	0.06	0.06	0.06	0.07		
7 cm SOBP	\bar{y}_F	0.14	0.14	0.16	0.11	0.11	0.12
	\bar{y}_D	0.50	0.48	0.55	0.48	0.47	0.50
	y^*	0.25	0.22	0.34	0.22	0.23	0.26

2.3.2.5 W-Value and Energy Calibration

The overall shift in W-value between neutrons and the simulated carbon beam ranged from 0.03% - 0.04% in the 146 MeV/u monoenergetic beam and the 424 MeV/u monoenergetic beam, respectively. In the SOBP, the W-value shift was less than 0.01%. The variation introduced by moving from the entrance region to the Bragg peak was, at most, 0.02% percent and was typically an order of magnitude less. The difference in bias introduced into the lineal energy values was only 0.2% in comparing the lowest and highest W-value shift, so it is unlikely that the positioning of the detector will greatly affect the error.

The W-value calibration introduced a systematic shift of roughly 1.5%, on average, to higher lineal energy values. The bias was generally lowest in y^* values, and on the order of 25-40% higher for \bar{y}_D and \bar{y}_F values. These biases are shown in Table 9.

The random variation associated with the W-value calibration, and centered about the biased offset, is shown in Table 10 below. This source introduced the highest variance of all uncertainty sources in each lineal energy value, and was the only source to exceed 4%.

Table 9. Bias introduced to lineal energy values by W-value calibration. Expressed as a percent difference between the perturbed values and true lineal energy values.

Beam	Lineal Energy	Percent Difference (%)					
		Entrance	Avg.	Max.	Bragg Peak	Avg.	Max.
146 MeV/u Monoenergetic	\bar{y}_F	1.42	1.41	1.48	1.42		
	\bar{y}_D	1.45	1.39	1.47	1.42		
	y^*	1.16	1.13	1.20	1.04		
424 MeV/u Monoenergetic	\bar{y}_F	1.83	1.81	1.85	1.69		
	\bar{y}_D	1.58	1.55	1.64	1.57		
	y^*	0.96	0.93	0.97	1.07		
7 cm SOBP	\bar{y}_F	1.64	1.62	1.64	2.02	2.26	4.72
	\bar{y}_D	1.63	1.58	1.64	0.252	0.29	0.64
	y^*	0.88	0.89	0.98	2.18	0.93	1.04

Table 10. Percent standard deviation, at the 1σ level, introduced in lineal energy values by W-value calibration.

Beam	Lineal Energy	Standard Deviation (%)					
		Entrance	Avg.	Max.	Bragg Peak	Avg.	Max.
146 MeV/u Monoenergetic	\bar{y}_F	5.41	5.41	5.42	5.41		
	\bar{y}_D	5.41	5.41	5.41	5.41		
	y^*	4.55	4.54	5.32	4.26		
424 MeV/u Monoenergetic	\bar{y}_F	4.86	4.86	4.86	4.85		
	\bar{y}_D	4.85	4.85	4.85	4.85		
	y^*	3.11	3.14	4.74	3.80		
7 cm SOBP	\bar{y}_F	3.46	3.46	3.46	3.46	3.46	3.46
	\bar{y}_D	3.46	3.46	3.46	4.90	3.46	3.46
	y^*	1.86	1.94	3.29	2.18	1.99	2.22

2.3.2.6 Low Energy Cutoff

As the low energy cutoff point is low, 0.5 keV/ μm on a scale extending to 1000 keV/ μm , the impact of removing all distribution values below the 0.5 keV/ μm threshold was first assessed. This resulted in lineal energy values increasing by up to 6%, for \bar{y}_D and y^* , and up to 60% for \bar{y}_F at the lowest clinical energies. At the highest clinical energies, error did not exceed 1% and 10%, respectively. In order to mitigate this error, three different cutoff models were appended onto the microdosimetric spectra at a joining point of 5 keV/ μm . The models investigated were exponential, semilog, and linear functions of lineal

energy, and are shown in Figure 23 on a linear y-axis scale, along with the original tail for reference.

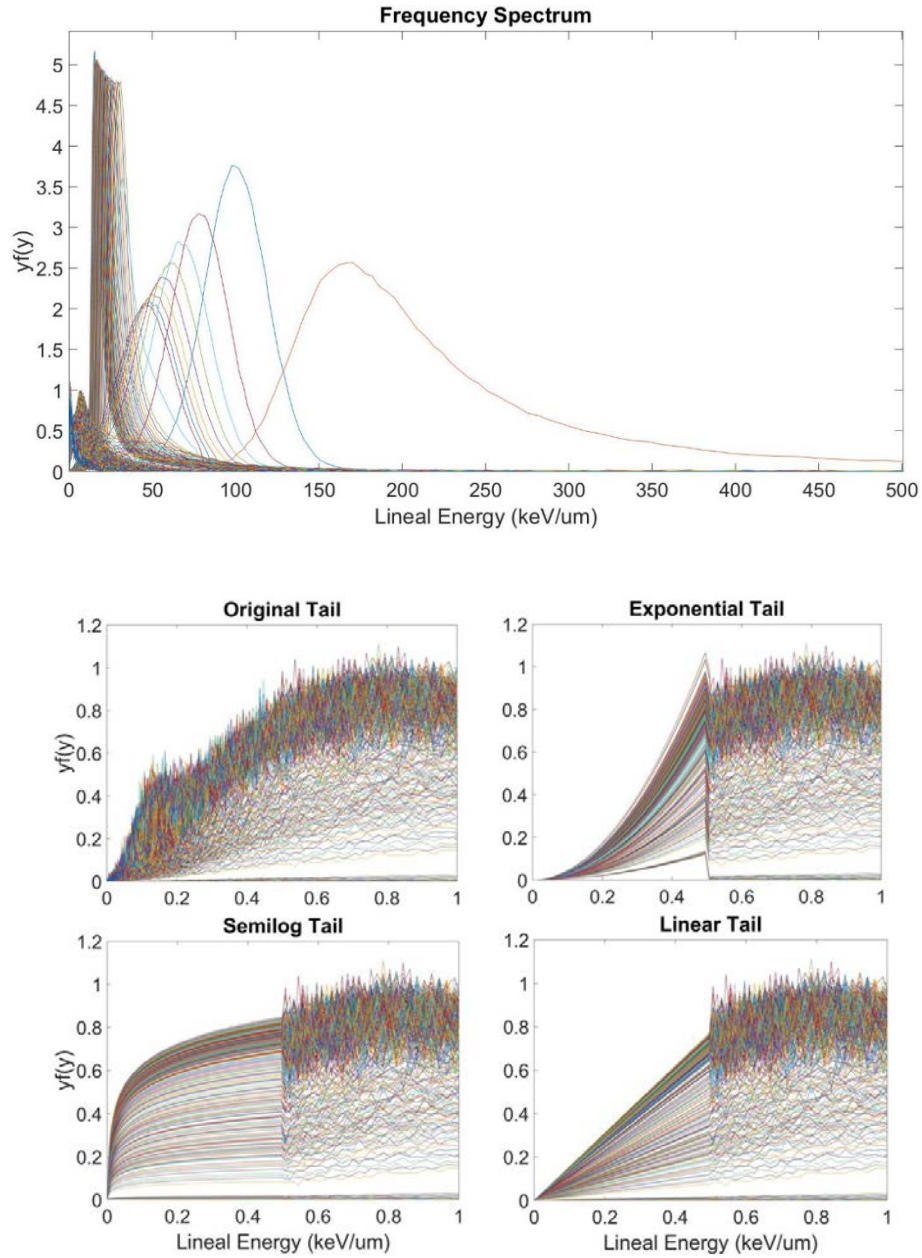


Figure 23. The large figure on the top shows the original frequency weighted spectra on a linear x-axis for scale reference. The middle left figure displays the original microdosimetric spectra below 0.5 keV/ μ m zoomed in. The other three figures display each of three simulated tails appended to the microdosimetric spectrum at 0.5 keV/ μ m.

In order to determine the best fitting model, each was appended onto frequency and dose weighted spectra of various clinical energies for comparison. The average and maximum percent difference caused by each tail model on lineal energy values and propagated through to final RBE values are shown in Table 11 below. These values represent the average percent difference between perturbed and true RBE values, averaged across all three models investigated. The linear cutoff model was found to have the lowest percent difference at all energies and was therefore selected to propagate bias through to the microdosimetric spectra in the rest of the assessment.

Table 11. Percent difference in RBE between the Monte Carlo spectra and spectra where the cutoff model replace Monte Carlo below 0.5 keV/μm.

Cutoff Model	Percent Difference in RBE	
	Average	Maximum
Exponential	0.33%	0.85%
Semilog	0.19%	0.67%
Linear	0.09%	0.39%

The linear cutoff model was used to append a tail on both the frequency and dose weighted microdosimetric spectra simulated with Monte Carlo, at a cutoff with a mean value of 0.5 keV/μm. The 1σ standard deviation of the bin height was randomly varied by 5%. The removal of the spectra resulted in both a systematic shift and random introduced uncertainty, which was propagated through to calculated lineal energy values and is displayed in Table 12 and Table 13, respectively.

The introduced bias from the systematic shift was, on average, 0.01%, and did not exceed a shift of 0.09% throughout all energies and depths. Similarly, the variance about the systematic bias was small, 0.02% on average, and not exceeding 0.33%. The uncertainty in the y^* values were typically far lower than those in \bar{y}_D and \bar{y}_F values.

Table 12. Bias introduced to lineal energy values by low energy cutoff. Expressed as a percent difference between the perturbed values and true lineal energy values.

Beam	Lineal Energy	Percent Difference (%)					
		Entrance	Avg.	Max.	Bragg Peak	Avg.	Max.
146 MeV/u Monoenergetic	\bar{y}_F	<0.01	<0.01	<0.01	-0.05		
	\bar{y}_D	<0.01	<0.01	<0.01	<0.01		
	y^*	<0.01	<0.01	<0.01	<0.01		
424 MeV/u Monoenergetic	\bar{y}_F	<0.01	-0.07	<0.01	-0.06		
	\bar{y}_D	<0.01	<0.01	<0.01	-0.02		
	y^*	<0.01	<0.01	<0.01	<0.01		
7 cm SOBP	\bar{y}_F	<0.01	<0.01	-0.01	-0.01	-0.14	-0.02
	\bar{y}_D	<0.01	<0.01	<0.01	-0.03	-0.04	-0.09
	y^*	<0.01	<0.01	<0.01	<0.01	<0.01	<0.01

Table 13. Percent standard deviation, at the 1σ level, introduced in lineal energy values by low energy cutoff.

Beam	Lineal Energy	Standard Deviation (%)					
		Entrance	Avg.	Max.	Bragg Peak	Avg.	Max.
146 MeV/u Monoenergetic	\bar{y}_F	<0.01	<0.01	<0.01	0.03		
	\bar{y}_D	<0.01	<0.01	<0.01	<0.01		
	y^*	<0.01	<0.01	<0.01	<0.01		
424 MeV/u Monoenergetic	\bar{y}_F	<0.01	0.02	0.12	0.16		
	\bar{y}_D	<0.01	<0.01	<0.01	0.20		
	y^*	<0.01	<0.01	<0.01	<0.01		
7 cm SOBP	\bar{y}_F	0.07	<0.01	<0.01	<0.01	0.12	0.33
	\bar{y}_D	<0.01	<0.01	<0.01	0.01	0.01	0.03
	y^*	<0.01	<0.01	<0.01	<0.01	<0.01	<0.01

2.3.2.7 Pulse Pile-up

According to Equation 35 described in the methods, the pile-up probability was calculated as a function of count rate and the dead time of the detector. This probability is displayed in Figure 24.

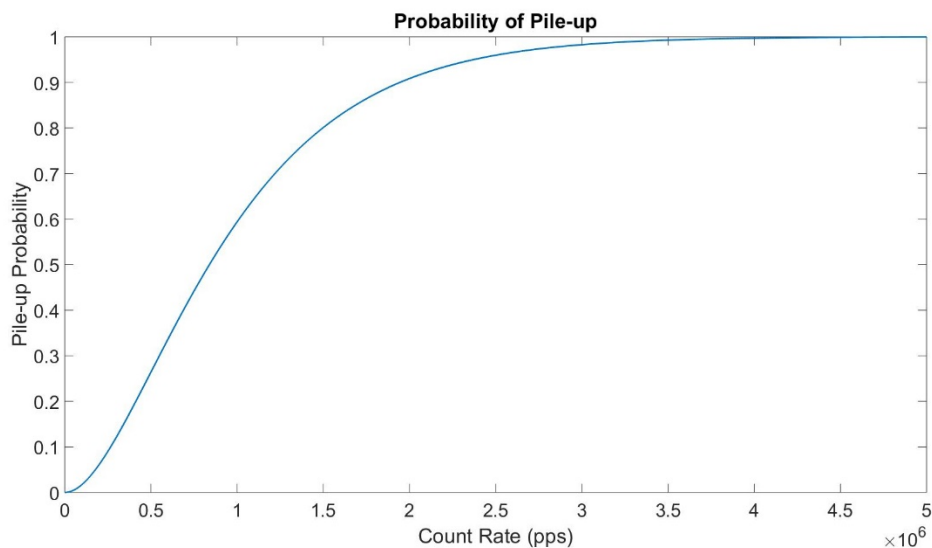


Figure 24. Probability of pulse pile-up as a function of count rate (pps). Note that the scale for count rate is $\times 10^6$.

In order to determine which dose rates produces reasonable uncertainty, this probability was used to sample a range of dose rates (1E5 to 1E6 counts per second). At each dose rate, the average percent difference between pure RBE and pile-up RBE was calculated for each RBE model for a 146 MeV/u monoenergetic beam. This was done for each model by propagating the error in the lineal energy values through to the final RBE calculations. Then, the percent difference between the true and piled-up RBE was taken. The 146 MeV/u monoenergetic beam was selected as it resulted in the highest bias as a function of count rate, as compared to both high energy monoenergetic beams and SOBPs. Percent difference in both the entrance region, 2 cm depth, and the Bragg peak, 4.7 cm depth, are shown in Figure 25 - Figure 27 below.

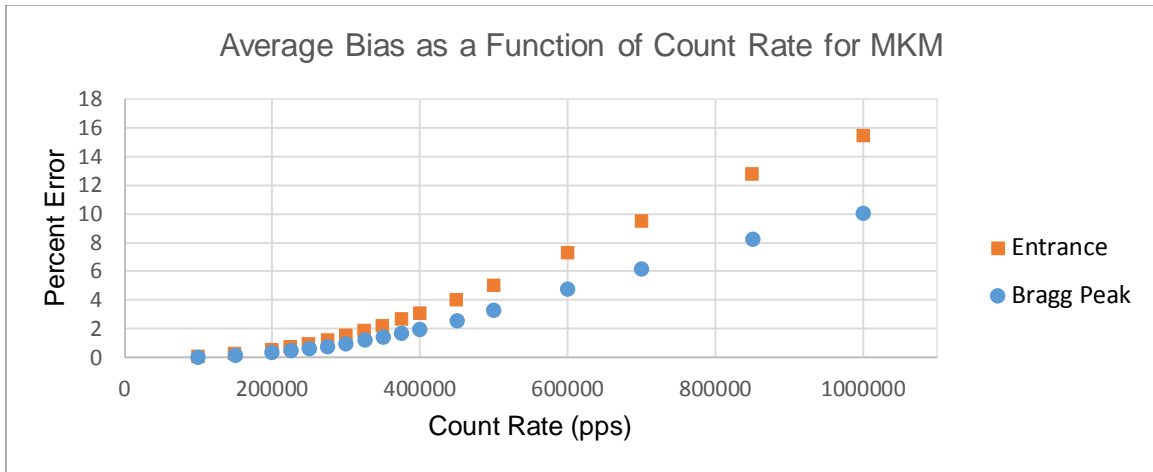


Figure 25. Average bias introduced to MKM RBE by pulse pile-up as a function of count rate.

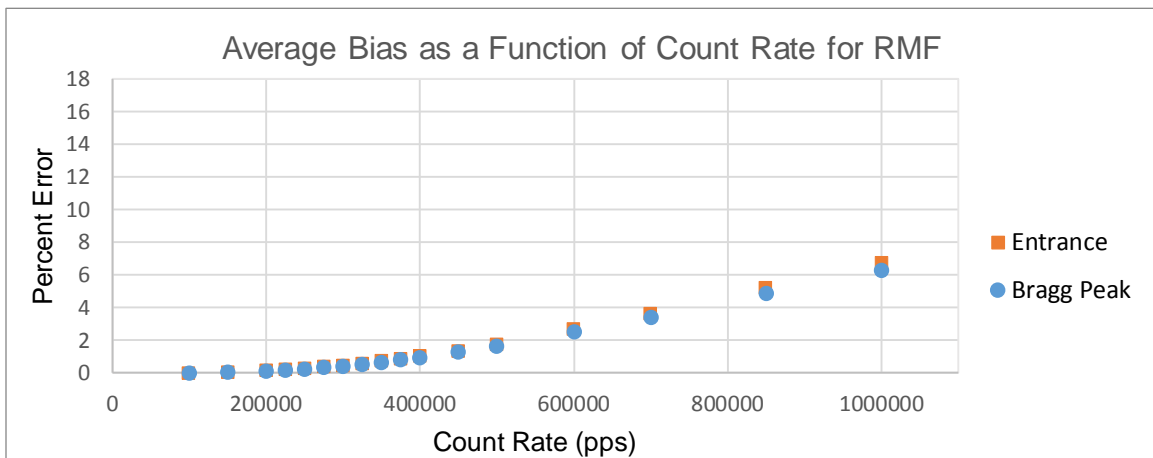


Figure 26. Average bias introduced to RBE_{RMF} by pulse pile-up as a function of count rate.

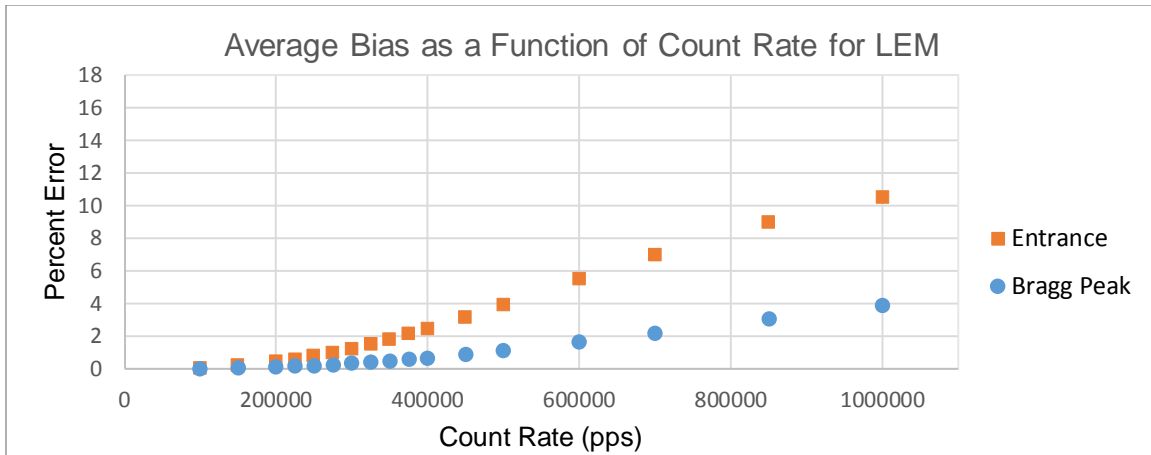


Figure 27. Average bias introduced to RBE_{LEM} by pulse pile-up as a function of count rate. Both entrance regions and Bragg peak are shown.

An uncertainty of $<1.5\%$ was desired for this RBE model, which was found to be associated with a count rate of $2.5E5$ pps based on Figure 25 - Figure 27. Between $2.5E5$ pps and $4E5$ pps, the error introduced roughly doubled in magnitude. As there is no appreciable difference between achieving count rates of $2.5E5$ pps and $4E5$ pps, $2.5E5$ pps was selected to reduce the error to $<1.5\%$. An example of the pile-up spectra compared to the original spectra is shown in Figure 28 - Figure 30 to provide the scale of pile-up occurring at this rate. Above a count rate of roughly $4E5$ pps, the uncertainty starts to increase quite rapidly, as can also be seen in Figure 25 - Figure 27. For comparison, an example of the pile-up spectra compared to the original is shown in Figure 31. As there are no means of assessing the uncertainty in the pile-up rejection system of the detector, this simulation represents the complete lack of a rejection system which indicates that count rates can likely be pushed slightly higher than the values quoted here when used with proper electronics.

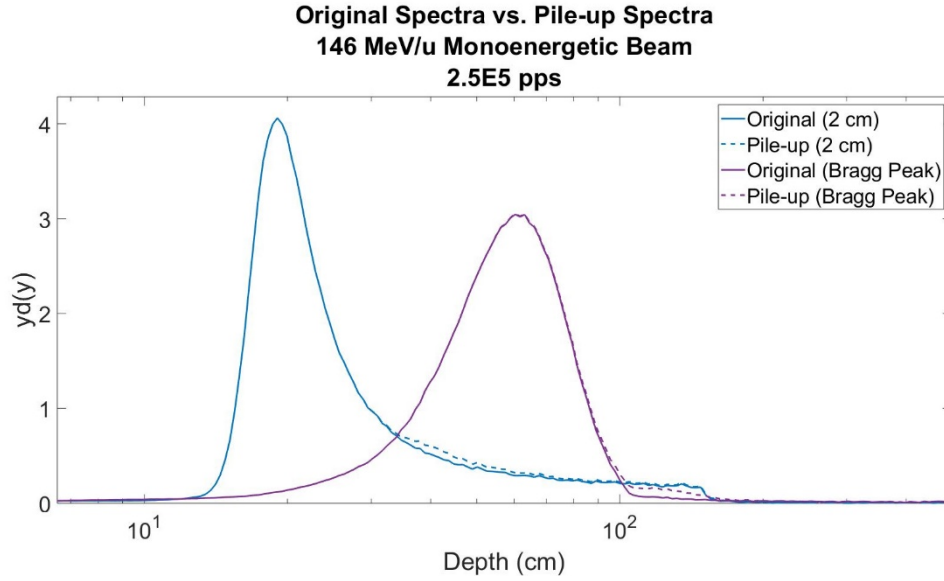


Figure 28. Example of the dose weighted microdosimetric spectra for both original and pile-up situations at a dose rate of 2.5E5 pps.

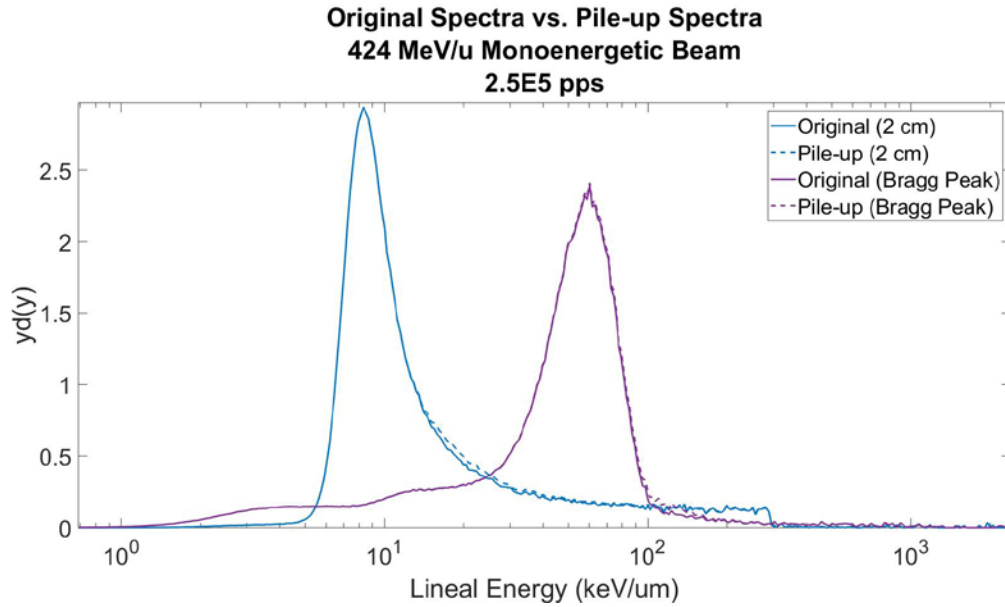


Figure 29. Example of the dose weighted microdosimetric spectra for both original and pile-up situations at a dose rate of 2.5E5 pps.

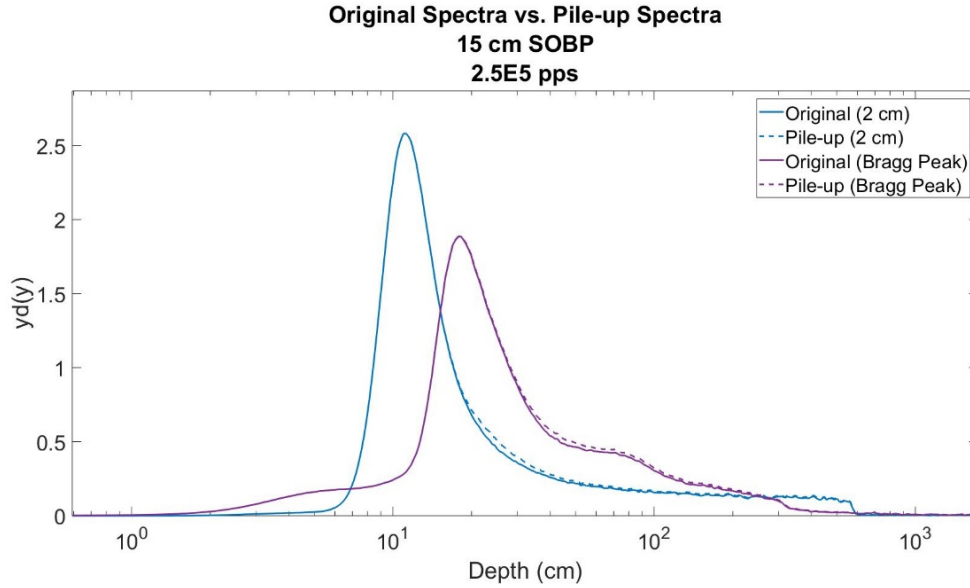


Figure 30. Example of the dose weighted microdosimetric spectra for both original and pile-up situations at a dose rate of 2.5E5 pps.

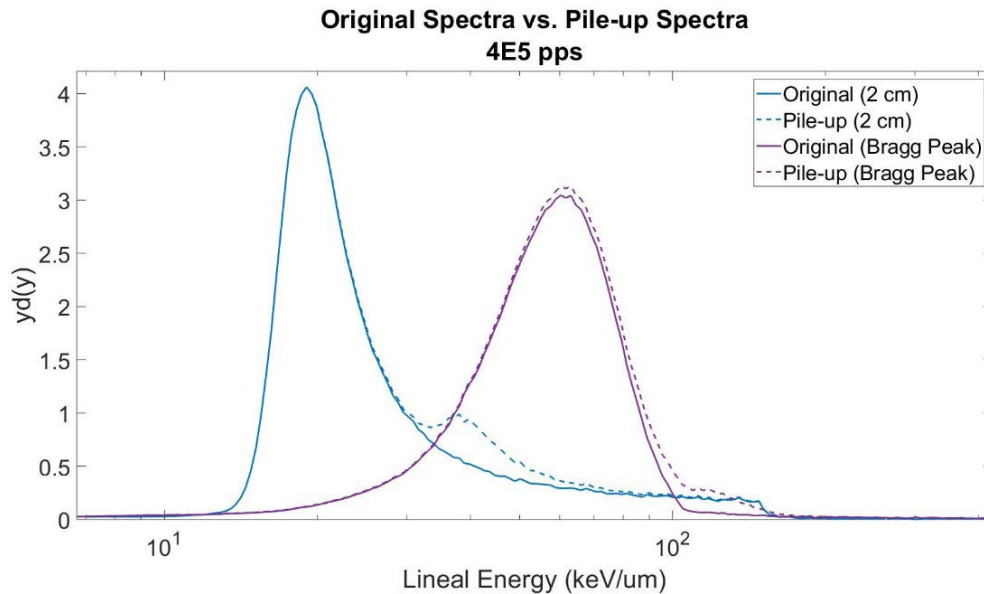


Figure 31. Example of the dose weighted microdosimetric spectra for both original and pile-up situations at a dose rate of 4E5 pps, the count rate at which uncertainty began to drastically increase through the RBE models. This example is for a 146 MeV/u beam.

For scattered beams, this dose rate is nearly achievable at clinical scales.

For these beamlines, clinical count rates are counted on the scale of 10^7 pps over

a $10 \times 10 \times 10 \text{ cm}^3$ volume [3]. As the cross section of the detector is πr^2 , with a radius of 1.27 cm, 5.07×10^5 particles cross the detector per second. This falls nearly within the range investigated with acceptable results, indicating that scattered beams will likely not require much adjustment beyond normal clinical fields or dose rates.

However, this problem increases substantially for scanning beams. Instead of the spill of particles being spread over a large treatment field as is done with scattered beams, for scanning beams the entire spill of particles is delivered in a spot that is on the order of millimeters in diameter and is typically smaller than the detector. This results in a very high particle count rate and indicates that a scanning beam must be able to tune down its clinical dose rate in order to prevent dramatic pile-up error. While two centers indicated that they are unable to do this on the IROC Houston clinical beam survey, this is expected to be achievable in the majority of clinical beams. This is supported in literature, as count rates have been quoted to be tuned down to 6×10^3 pps for scanning beams at the Heavy Ion Medical Accelerator in Chiba [15]. This particle rate can be used accurately in the context of pulse pile-up.

Table 14. Shows the bias introduced to lineal energy values by pulse pile-up in the entrance and Bragg peak regions with a particle rate of 2.5E5 particles per second. Bias is expressed as a percent difference between the perturbed values and true lineal energy values.

Beam	Lineal Energy	Percent Difference (%)					
		Entrance	Avg.	Max.	Bragg Peak	Avg.	Max.
146 MeV/u Monoenergetic	\bar{y}_F	0.11	2.19	2.26	1.14		
	\bar{y}_D	2.27	2.19	2.27	2.26		
	y^*	3.01	2.90	3.08	2.26		
424 MeV/u Monoenergetic	\bar{y}_F	2.26	2.26	2.27	2.26		
	\bar{y}_D	2.26	2.26	2.29	2.26		
	y^*	2.14	1.99	2.18	1.34		
7 cm SOBP	\bar{y}_F	2.25	2.26	2.26	2.26	2.26	2.26
	\bar{y}_D	2.26	2.26	2.27	2.25	2.26	2.27
	y^*	2.11	2.13	2.16	1.69	1.57	1.94

Table 15. Displays the percent standard deviation, at the 1σ level, introduced in lineal energy values by pulse pile-up for the entrance and Bragg peak regions with a particle rate of $2.5E5$ particles per second.

Beam	Lineal Energy	Standard Deviation (%)					
		Entrance	Avg.	Max.	Bragg Peak	Avg.	Max.
146 MeV/u Monoenergetic	\bar{y}_F	0.16	0.16	0.16	0.16		
	\bar{y}_D	0.17	0.17	0.19	0.16		
	y^*	0.22	0.21	0.22	0.16		
424 MeV/u Monoenergetic	\bar{y}_F	0.16	0.16	0.17	0.16		
	\bar{y}_D	0.22	0.19	0.23	0.18		
	y^*	0.02	0.17	0.18	0.15		
7 cm SOBP	\bar{y}_F	0.01	0.00	0.01	0.01	0.01	0.01
	\bar{y}_D	0.04	0.04	0.05	0.03	0.03	0.04
	y^*	0.02	0.02	0.02	0.01	0.01	0.02

2.3.2.8 Wall Effects

The bias introduced by repressing the microdosimetric spectra in the low lineal energy region and shifting the peak is described in Table 16. The incorporation of wall effects in the spectra resulted in a systematic shift to higher lineal energy values on the order of 1-10%, for \bar{y}_F , and on the order of 0.02% for \bar{y}_D and y^* values.

The variance centered around this bias is similarly presented in Table 17. The overall variance introduced by repression uncertainty was low, ranging from

0.10% in the entrance region to 2.0% in the Bragg peak for \bar{y}_F . For the other lineal energy values, the average variance did not exceed 0.5% across all values.

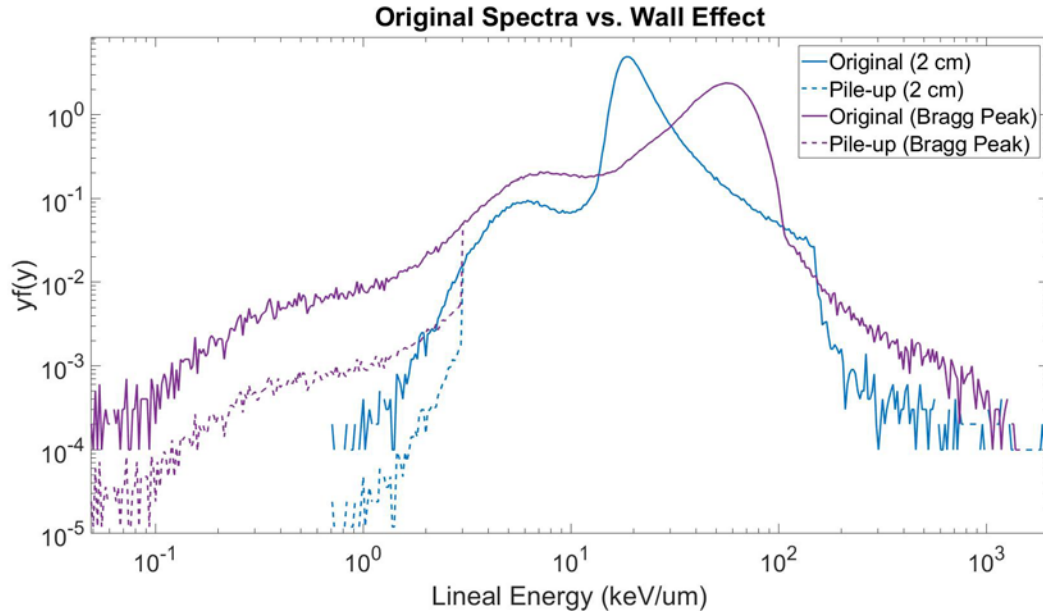


Figure 32. Example of the frequency weighted microdosimetric spectra for both original and wall effect simulations. Note the log scale on both the x- and y-axis.

Table 16. Average bias introduced to lineal energy values by wall effects in the entrance and Bragg peak regions, expressed as a percent difference between the perturbed values and true lineal energy values.

Beam	Lineal Energy	Percent Difference (%)					
		Entrance	Avg.	Max.	Bragg Peak	Avg.	Max.
146 MeV/u Monoenergetic	\bar{y}_F	0.11	0.10	0.26	1.14		
	\bar{y}_D	0.01	0.01	0.02	<0.01		
	y^*	0.01	0.01	0.02	0.04		
424 MeV/u Monoenergetic	\bar{y}_F	1.11	10.6	23.6	26.5		
	\bar{y}_D	0.26	1.96	3.05	2.06		
	y^*	0.21	0.46	0.99	2.03		
7 cm SOBP	\bar{y}_F	2.06	1.45	3.10	9.05	10.1	21.0
	\bar{y}_D	0.12	0.24	0.46	1.11	1.30	2.86
	y^*	0.12	0.22	0.43	0.80	0.81	1.31

Table 17. Percent standard deviation, at the 1σ level, introduced in lineal energy values by wall effects for the entrance and Bragg peak regions.

Beam	Lineal Energy	Standard Deviation (%)					
		Entrance	Avg.	Max.	Bragg Peak	Avg.	Max.
146 MeV/u Monoenergetic	\bar{y}_F	0.01	0.01	0.02	0.11		
	\bar{y}_D	<0.01	<0.01	<0.01	<0.01		
	y^*	<0.01	<0.01	<0.01	<0.01		
424 MeV/u Monoenergetic	\bar{y}_F	0.10	0.19	0.99	2.57		
	\bar{y}_D	0.02	0.18	0.28	0.19		
	y^*	0.02	0.40	0.09	0.18		
7 cm SOBP	\bar{y}_F	0.46	0.32	0.69	2.02	2.26	4.72
	\bar{y}_D	0.03	0.05	0.10	0.25	0.29	0.64
	y^*	0.03	0.49	0.10	0.18	0.18	0.29

2.3.2.9 Total Uncertainty

The total bias was summed for each of the four systematic sources of error. This bias is presented numerically in Table 18 for points in the entrance region and in the Bragg peak. The bias is also represented by the solid blue line in the following figures. The average difference between the Monte Carlo calculated RBE and the average perturbed RBE was -9.2% for \bar{y}_F values. This was roughly twice the magnitude of the average uncertainty introduced into \bar{y}_D and y^* values.

The total variance was added in quadrature for each source, and is similarly presented in Table 19. The error bars in the following figures represent the 1σ standard deviation of the total error.

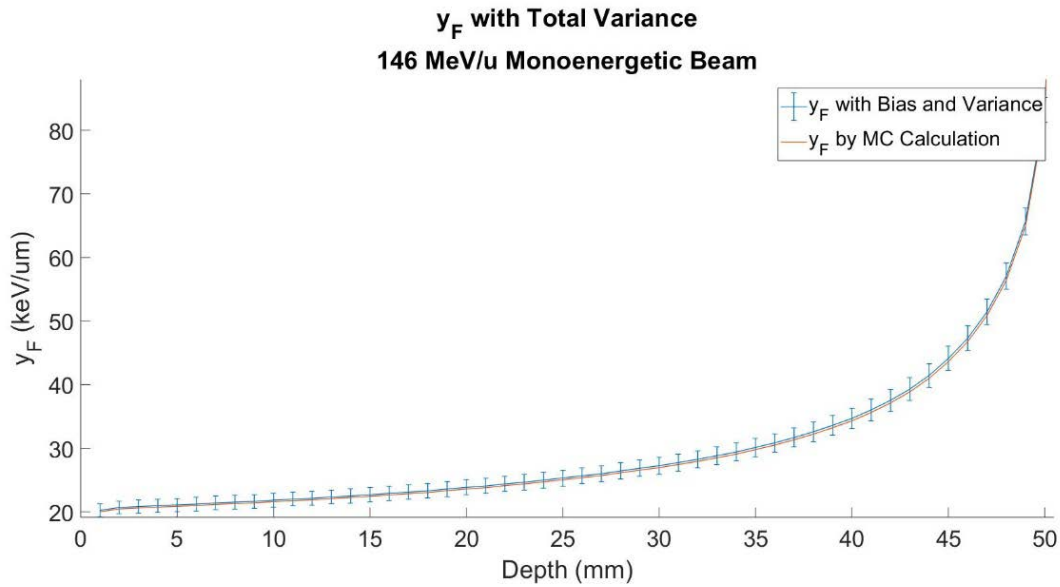


Figure 33. Frequency mean lineal energy with added bias and uncertainty as a function of depth for 146 MeV/u monoenergetic beam.

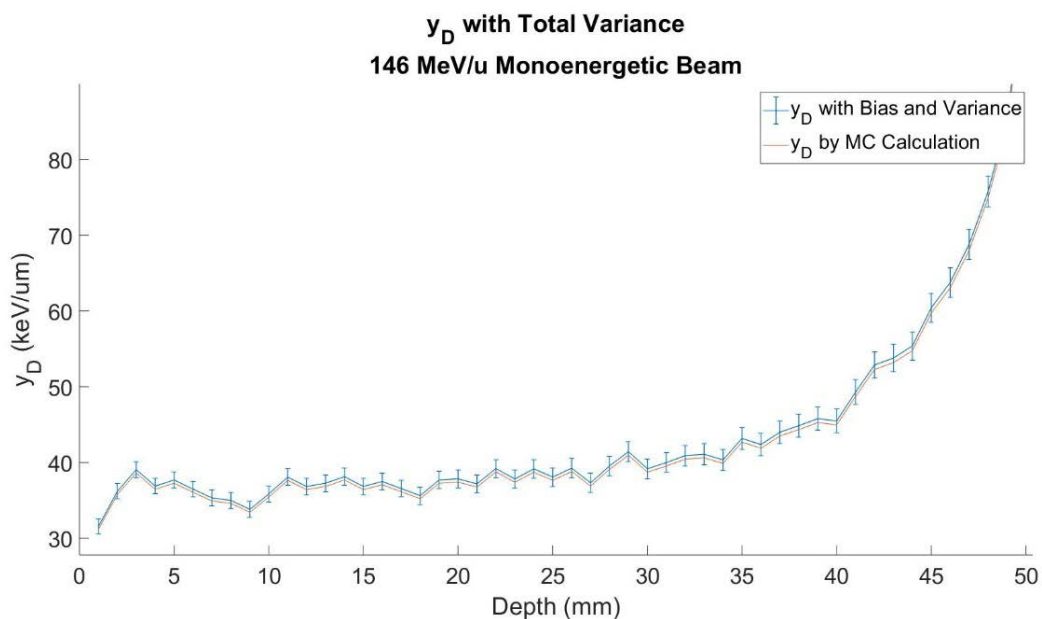


Figure 34. Dose mean lineal energy with added bias and uncertainty as a function of depth for 146 MeV/u monoenergetic beam.

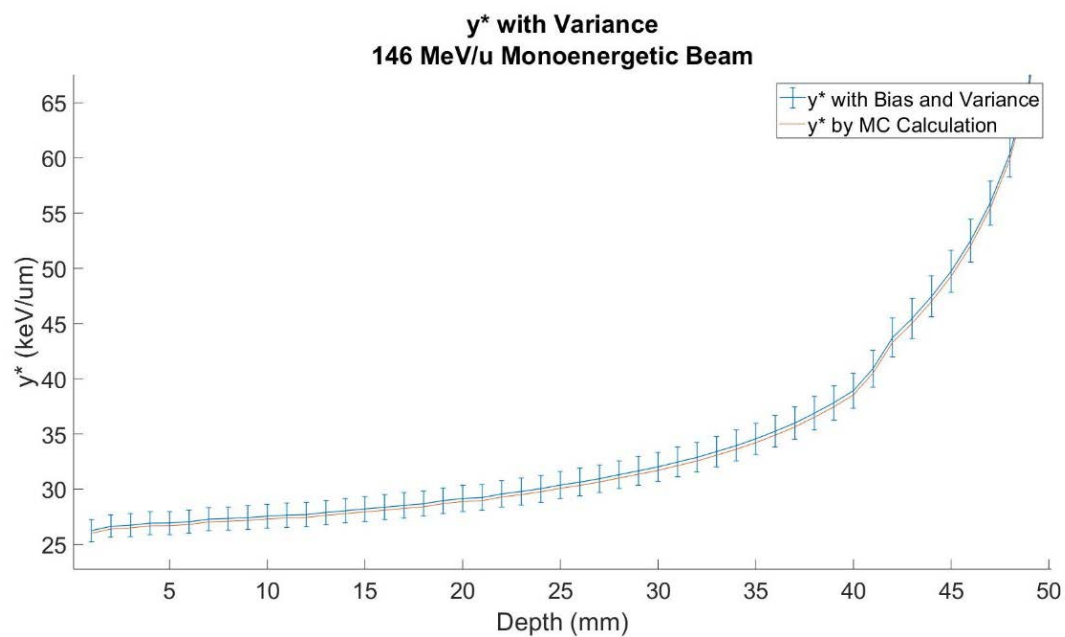


Figure 35. Saturation corrected dose mean lineal energy with added bias and uncertainty as a function of depth for 146 MeV/u monoenergetic beam.

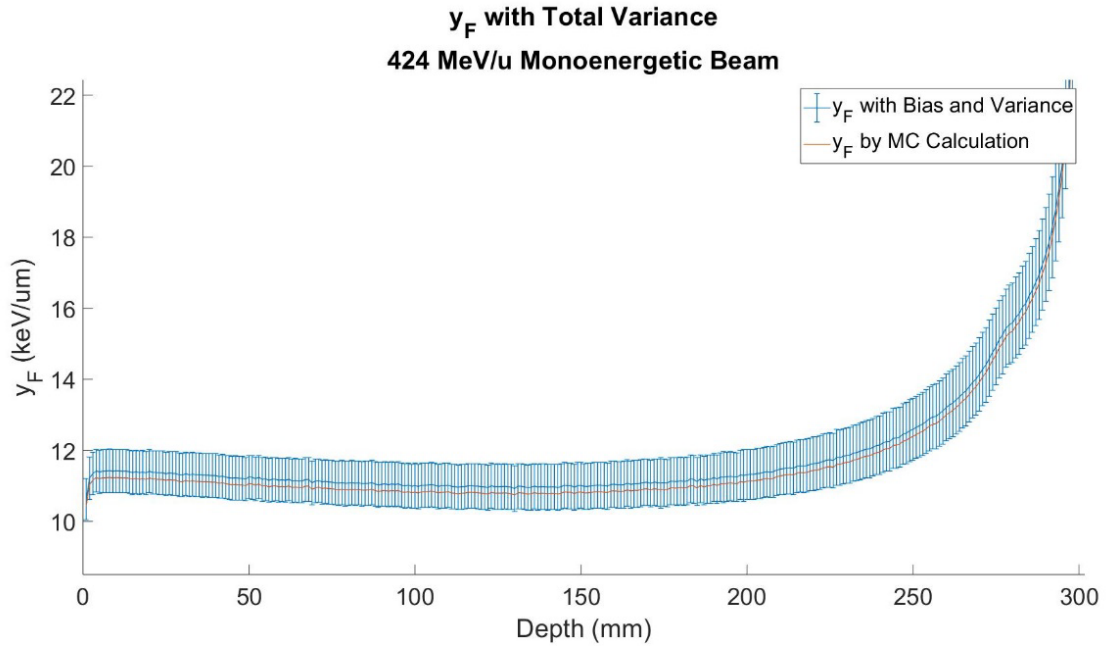


Figure 36. Frequency mean lineal energy with added bias and uncertainty as a function of depth for 424 MeV/u monoenergetic beam.

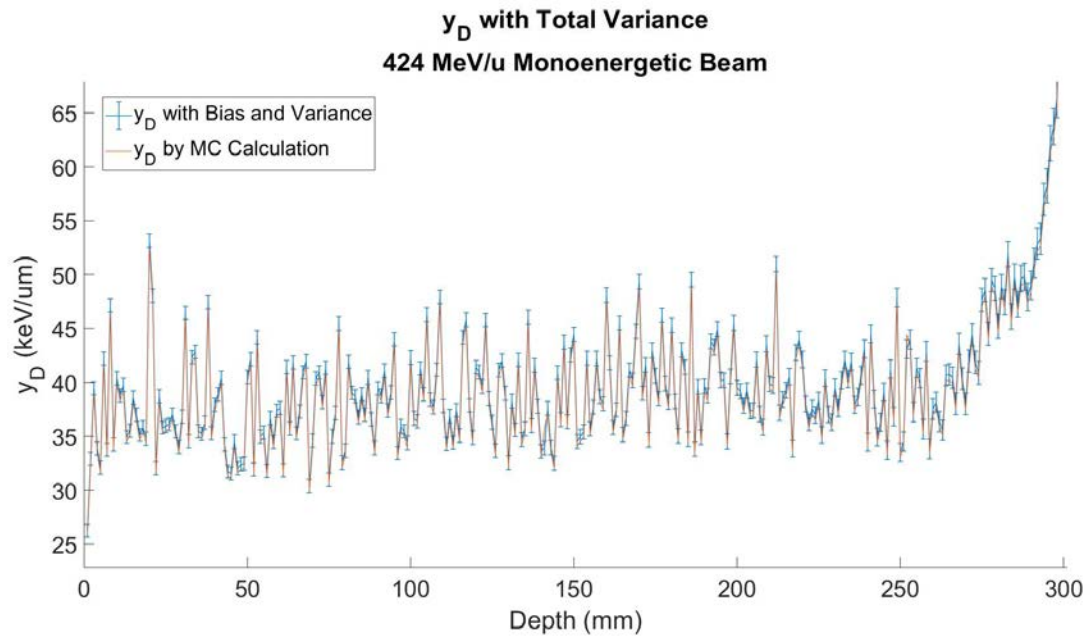


Figure 37. Dose mean lineal energy with added bias and uncertainty as a function of depth for 424 MeV/u monoenergetic beam.

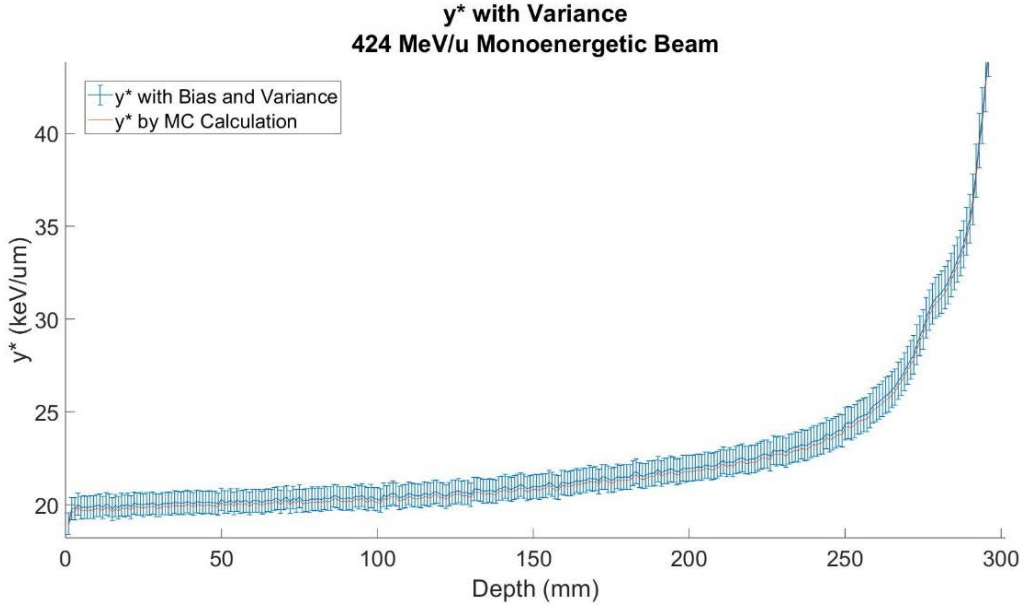


Figure 38. Saturation corrected dose mean lineal energy with added bias and uncertainty as a function of depth for 424 MeV/u monoenergetic beam.

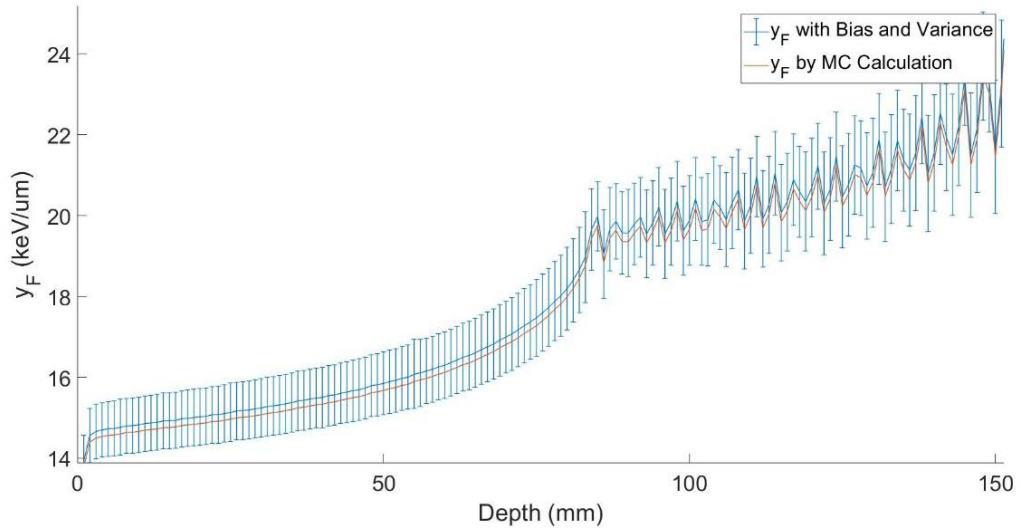


Figure 39. Frequency mean lineal energy with added bias and uncertainty as a function of depth for a 7 cm SOBP.

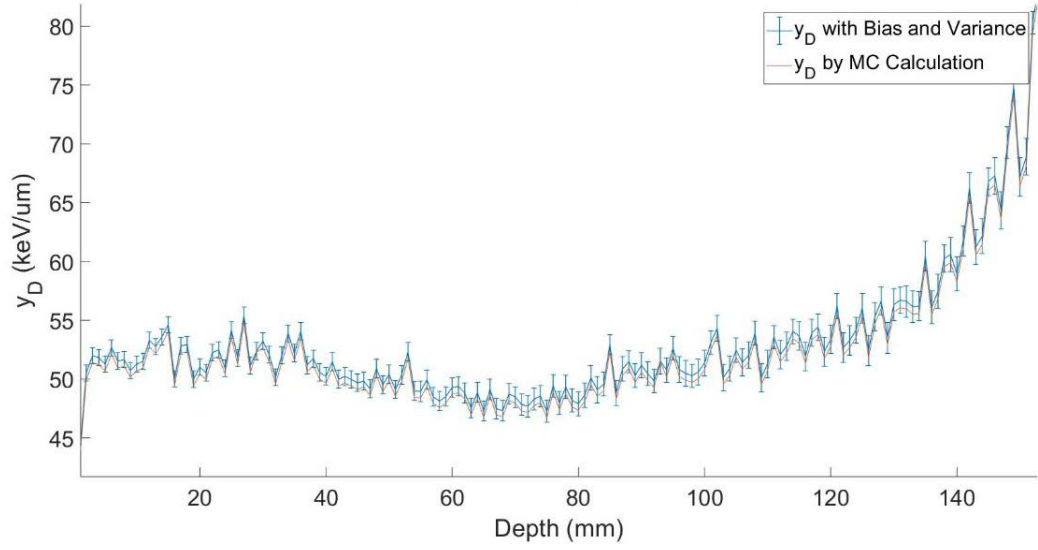


Figure 40. Dose mean lineal energy with added bias and uncertainty as a function of depth for a 7 cm SOBP.

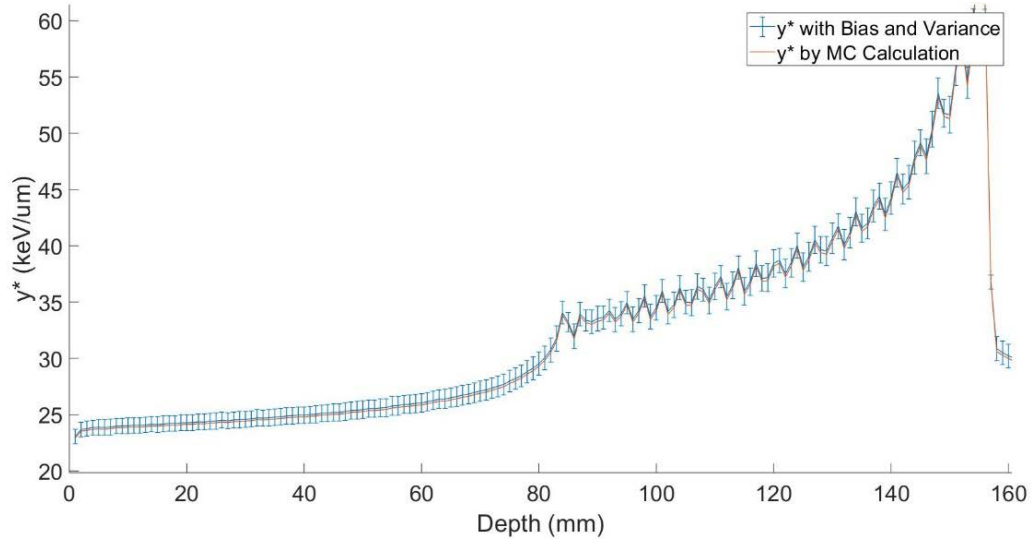


Figure 41. Saturation corrected dose mean lineal energy with added bias and uncertainty as a function of depth for a 7 cm SOBP.

Table 18. Average bias introduced to lineal energy values by systematic sources of error (W-value calibration, low energy cutoff, pulse pile-up, and wall effects) in the entrance and Bragg peak regions.

Beam	Lineal Energy	Percent Difference (%)					
		Entrance	Avg.	Max.	Bragg Peak	Avg.	Max.
146 MeV/u Monoenergetic	\bar{y}_F	-3.34	-3.39	-3.24	-4.27		
	\bar{y}_D	-3.21	-3.22	-3.20	-3.21		
	y^*	-3.79	-3.61	-3.78	-2.96		
424 MeV/u Monoenergetic	\bar{y}_F	-4.69	-1.41	-3.61	-2.98		
	\bar{y}_D	-3.58	-5.27	1.37	-5.33		
	y^*	-3.00	-4.50	-2.76	-4.06		
7 cm SOBP	\bar{y}_F	-4.20	-5.13	-3.47	-1.30	-1.42	-7.55
	\bar{y}_D	-3.59	-3.69	-2.60	-4.67	-4.85	-3.00
	y^*	-2.85	-3.02	-2.71	-3.21	-3.04	-2.71

Table 19. Average variance introduced to lineal energy values by systematic sources of error (W-value calibration, low energy cutoff, pulse pile-up, and wall effects) in the entrance and Bragg peak regions.

Beam	Lineal Energy	Standard Deviation (%)					
		Entrance	Avg.	Max.	Bragg Peak	Avg.	Max.
146 MeV/u Monoenergetic	\bar{y}_F	1.16	1.31	2.22	2.41		
	\bar{y}_D	1.79	1.94	2.97	3.20		
	y^*	1.17	1.30	1.94	2.00		
424 MeV/u Monoenergetic	\bar{y}_F	0.63	0.65	0.90	1.18		
	\bar{y}_D	2.50	1.85	2.50	2.92		
	y^*	0.61	0.70	1.18	1.62		
7 cm SOBP	\bar{y}_F	0.83	0.86	0.96	1.10	1.14	1.37
	\bar{y}_D	2.71	2.69	2.94	2.84	2.88	3.54
	y^*	0.70	0.76	0.94	1.19	1.17	1.49

2.4 Discussion

The bias introduced had a noticeable impact on the lineal energy values, ranging from 0.01-5% on average. However, as this is a proposed systematic shift, a correction factor can be used to adjust these values. The lowest bias was seen in the y^* values, which is encouraging as these are the values typically used as RBE input parameters in this study.

The average variance introduced by random physical measurement based noise in both \bar{y}_F and y^* values was less than 1%, indicating that the uncertainty should propagate to reasonable values in the RBE model assessment. Variance in \bar{y}_D values averaged 2.3%, but did not exceed 3.5% at any point. The variance introduced into the 7 cm SOBP was the lowest of the clinical beams assessed, which is interesting as this spectra was anticipated to have the highest fragment contribution and therefore the potential for the greatest impact at low lineal energy values.

3 Specific Aim 2

3.1 Introduction

The second specific aim of this study was to calculate RB by each model and propagate measurement based uncertainty into final RBE values. In order to accomplish this, RBE was first calculated using empirical Monte Carlo data. This is referred to as the true RBE throughout the results. For the two models that require Monte Carlo inputs (RMF and LEM), methods of estimating the RBE based on pure lineal energy inputs were created. The uncertainty introduced by

these methods in estimating RBE was quantified for these two models. Next, the RBE was calculated using the simulated measurement-based microdosimetric spectra which were perturbed in the first specific aim by eight sources of uncertainty. For MKM, this resulted in two sources of uncertainty, bias and variance, in the final simulated RBE values as compared to true RBE. For the RMF and LEM models, this yielded uncertainty in the form of measurement based bias and variance, with additional estimation based uncertainty. Results are presented here for each uncertainty type and each model, compared against true Monte Carlo calculated RBE for reference.

3.2 Materials and Methods

3.2.1 Monte Carlo

In order to calculate RBE based on RMF and LEM models, Monte Carlo calculations beyond those used in microdosimetric data were needed. These include both calculation of kinetic energy spectra and dose distributions. Using these spectra in combination with the simulated measurement-based microdosimetric spectra, respective α and β parameters were calculated for each RBE model.

3.2.1.1 Dose Distribution

In order to calculate RBE using LEM, the dose contribution by each fragment to the overall beam was needed. These distributions were generated for each energy of monoenergetic carbon beam, as well as for the SOBPs. In

addition to primary carbon, the dose contribution from the following fragments was evaluated: H, He, Li, Be, B, secondary C, N, O, and F.

3.2.1.2 Kinetic Energy

In order to calculate input values for LEM, the kinetic energy spectra of both the primary carbons and each secondary fragment was needed for each depth and primary carbon energy assessed. This data was initially generated for all ten contributing ion species (Primary C, H, He, Li, Be, B, secondary C, N, O, F). However, the clinical LEM tables provided required inputs only from the first seven of these ten species.

3.2.2 MKM

In order to calculate RBE_{MKM} , dose and frequency lineal energy spectra were first generated from GEANT4 Monte Carlo simulations for a range of clinically realistic monoenergetic carbon beams (120 MeV/u to 440 MeV/u). From these spectra, corresponding y_D and y_F values were calculated as a function of well depth and initial beam energy. Using the formalism described above, y^* was calculated by correcting y_D for saturation. From here, α^* was calculated for carbon ions using the first term of the linear-quadratic equation of surviving fraction. A β value of $0.05 Gy^{-2}$ and r_d value of $0.42 \mu m$ were used for this calculation.

Once α_C was calculated for carbon ions as a function of beam energy and depth, the resulting RBE was calculated using the linear-quadratic method. The remaining parameters involved were fixed as a function of depth at the following

values obtained using LQ survival curves of the reference radiation: $\beta_C = 0.05 \text{ Gy}^{-2}$, $\alpha_X = 0.19 \text{ Gy}^{-1}$, and $\beta_X = 0.05 \text{ Gy}^{-2}$. As all other parameters are fixed aside from α_C and physical dose, with a single TEPC measurement RBE can be calculated by MKM.

3.2.3 RMF

3.2.3.1 Calculation by Monte Carlo

The RBE was first calculated by RMF following the strict definition of the model, that is, using empirical Monte Carlo calculations and the formulism described in Section 3.4.3. Monte Carlo calculated values for α and β as a function of depth and initial beam energy were used along with reference alpha and beta values and physical dose to calculate RBE.

3.2.3.2 RBE by Estimation

In order to estimate the RBE_{RMF} , the Monte Carlo derived α values for both 146 and 424 MeV/u monoenergetic beams were plotted versus y^* , as seen by the solid line in Figure 39 below. 146 and 424 MeV/u beams were chosen as the represent both ends of the clinical beam energy range and serve as a calculation test data set. Next, these functions were fit with a single third order polynomial using CurveFinder software. Third order was selected as it resulted in the lowest fit error as calculated by MatLab in comparison with the test data sets. The resulting polynomial, the parameters of which can be seen in Table 20, estimates the α value for monoenergetic carbon beams using solely y^* values. This

process was repeated for SOBP α values, using true α values from a test set belonging to the 7 cm SOBP. The true and polynomial fit values are shown in Figure 40 for the SOBP. The monoenergetic and SOBP beams were fit separately, as they followed noticeable different trends as functions of y^* . Next, the same process was repeated for the beta values of both monoenergetic beams and SOBPs, the plots of which are overlaid on Figure 39 and Figure 40. The final two rows of Table 20 display the parameters for these polynomial fits.

These fits were used to generate alpha and beta values of carbons, which were used in the RBE formula along with physical dose and reference alpha and beta values to calculate RBE. The RBE estimated with the polynomial fits of the monoenergetic beams were then validated using three additional beam energies, whose Bragg peak ranges were spaced roughly equally between the two test sets. In order to quantify the accuracy of the estimation, the percent difference between the Monte Carlo simulated RBE_{RMF} and the estimated RBE was calculated. This process was repeated for the SOBP estimations, using both 10 cm and 10 cm SOBP beams as validation data sets. Results are shown for both test and validation estimations in Section 3.3.3.

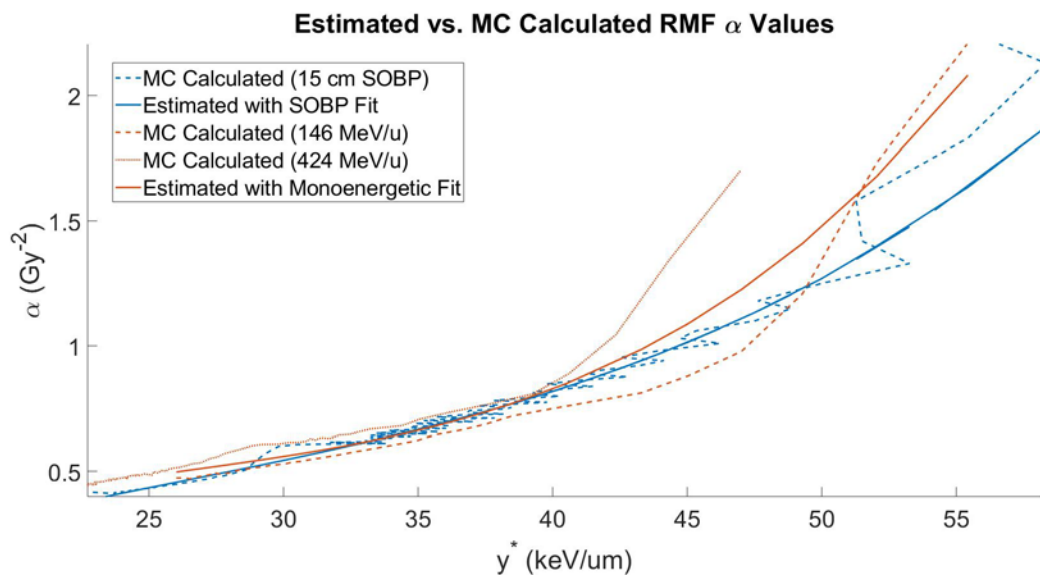


Figure 42. RMF α values calculated by Monte Carlo and estimated by fit (solid line).

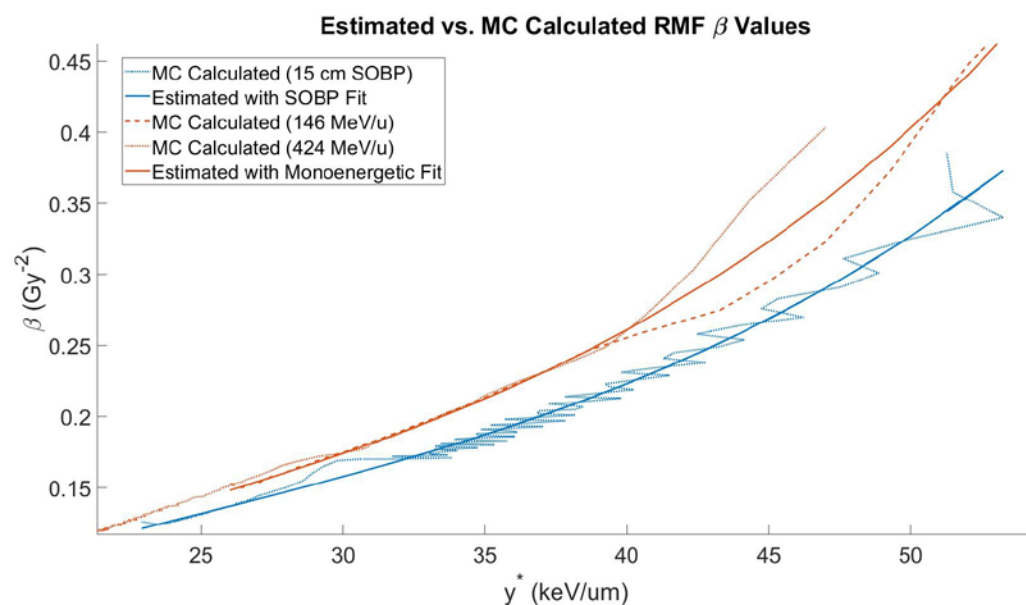


Figure 43. RMF β values calculated by Monte Carlo and estimated by fit (solid line).

Table 20. Polynomial variables used to estimate RMF β values.

$x = a + by^* + cy^{*2} + dy^{*3}$				
x	a	b	c	d
Monoenergetic Fit Parameters				
α	-6.88E-1	1.07E-1	-3.54E-3	4.53E-5
β	-5.38E-2	1.27E-2	-3.18E-4	4.93E-6
SOBP Fit Parameters				
α	-4.73E-1	6.41E-2	-1.64E-3	2.11E-5
β	-5.32E-2	1.23E-2	-2.98E-4	4.08E-6

3.2.4 LEM

3.2.4.1 Calculation by Monte Carlo

LEM was first used to calculate RBE and biological dose according to the methods explained on page 28, yielding the “true” RBE based on the “true” α and β . The calculation of RBE_{LEM} , as described in the introduction to RBE on page 28, uses kinetic energy rather than lineal energy to calculate α and β . As such, there is no direct relationship between the physical measurements made by the TEPC and the resulting RBE. In order to address this, several methods of linking lineal energy values to α and β were explored for LEM, which would then allow a linking between y^* and RBE_{LEM} .

3.2.4.2 Estimation: Pristine Microdosimetric Spectra

The first method explored was to plot the true α and β (based on the Monte Carlo simulations) as direct functions of y^* , as was done with RMF. α and β were plotted for 146 MeV/u and 424 MeV/u monoenergetic beams as test data sets, and then fit with polynomials using CurveFinder software. Values of true α along with those estimated by the fit are shown in Figure 41, with corresponding data for β in Figure 42. The parameters of the polynomial fit are described in Table 22. This process was repeated for the 7 cm SOBP, and are plotted in the same figures. Similarly to RMF, noticeably different trends were seen in α and β values as functions of y^* , on the order of several percent. Fitting both monoenergetic beams and SOBP together would likely cause a dramatic increase in estimation uncertainty. Several other clinical energies (218 MeV/u, 276 MeV/u, 330 MeV/u monoenergetic beams and 5 and 10 cm SOBP beams) were used to validate these fits, and the percent difference between the estimated and true values was calculated as a means of assessing their accuracy. As preliminary uncertainty analysis revealed that this estimation method yielded notable uncertainty and therefore room for improvement, another means of estimating RBE was investigated.

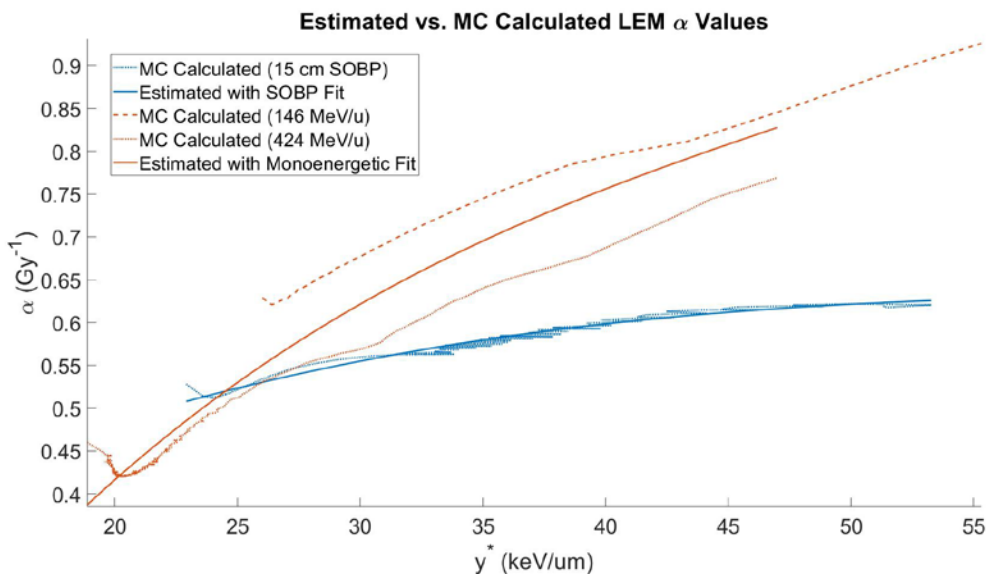


Figure 44. LEM α values calculated by Monte Carlo and estimated by fit (solid line).

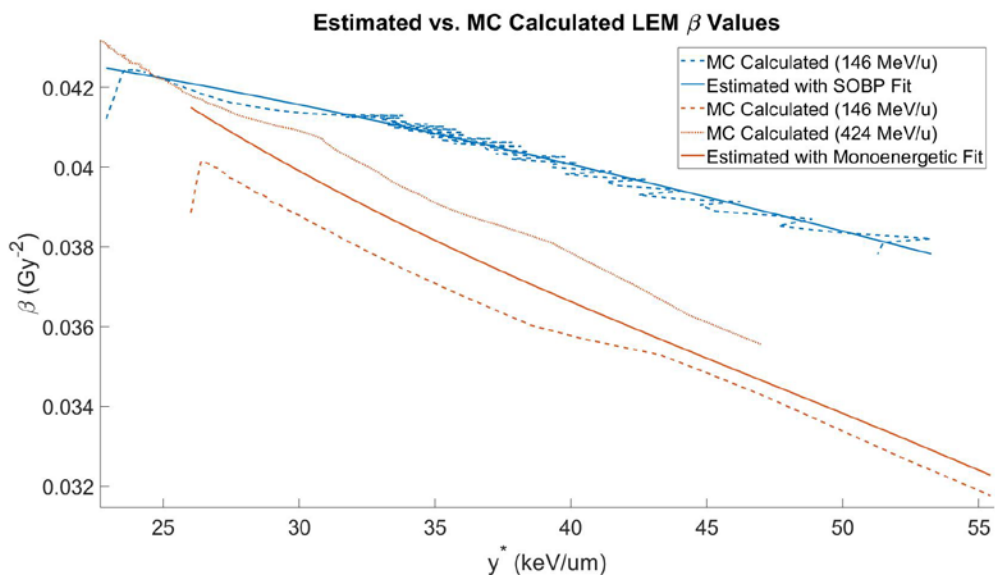


Figure 45. True LEM β values (based on Monte Carlo calculations and the definition of LEM), and those estimated by a polynomial fit based on y^* (solid line).

Table 21. Polynomial variables used to estimate LEM α and β values.

$x = a + by^* + cy^{*2} + dy^{*3}$				
x	a	b	c	d
Monoenergetic Fit Parameters				
α	-3.51E-1	5.39E-2	-8.98E-4	6.06E-6
β	5.92E-2	-1.01E-3	1.55E-5	-1.09E-7
SOBP Fit Parameters				
α	2.34E-1	1.68E-2	-2.37E-4	1.12E-6
β	-5.32E-2	1.23E-2	-2.98E-4	4.08E-6

3.2.4.3 Estimation: Cut Microdosimetric Spectra

3.2.4.3.1 Introduction

Microdosimetric spectra incorporate contributions from both primary particles and their corresponding fragments in a mixed radiation field. Particles of varying charges and kinetic energy impart varying energies, although there is a overlap in lineal energy between primary and various secondary particles. Figure 43 below, which overlays the contribution of each fragment to the total microdosimetric spectra at the Bragg peak of a 300 MeV/u carbon beam. Problematically, from a LEM modeling standpoint, these fragments, which overlap in terms of microdosimetric properties, have different alpha and beta values, leading to a different RBE based on particle type.

Though the overlap is notable, it is still possible to distinguish two principal peaks in the spectra. The first peak, located at roughly $y \approx 131 \text{ keV}/\mu\text{m}$, is comprised of the primary portion of the beam, while the other, at $y \approx 25 \text{ keV}/\mu\text{m}$,

consists of the remaining fragments [32]. Similar data was produced by Tran and Bolst, who presented the contribution of each particle to the microdosimetric beam for heavy ion beams, including Nitrogen and Oxygen. This data supported the trend of the main peak, which is composed primarily of carbon, that drops off rapidly with lineal energy. Similarly, a considerable overlap between carbon and boron contributions was noted [33].

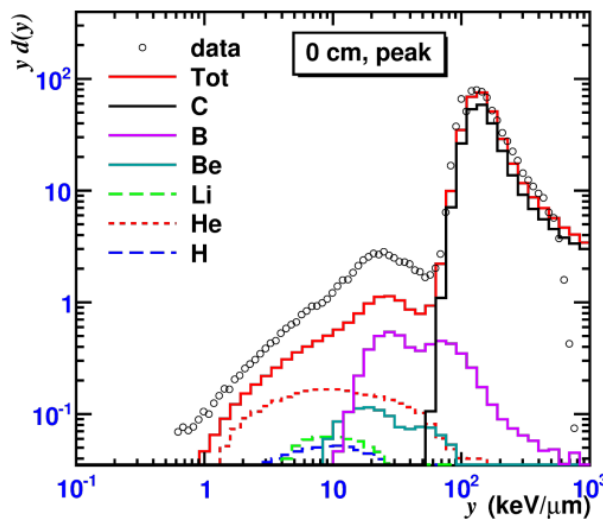


Figure 46. Microdosimetric spectra of a 300 MeV/u carbon beam subdivided by fragment using MCHIT calculations. Figure taken from [32].

Translating this overlay to the Monte Carlo data used in this study was complicated as only the total microdosimetric spectra was generated rather than that scored by ion species. The distinction between primary and secondary components is easiest viewed through the frequency spectra, and is shown for three unique depths of a 146 MeV/u monoenergetic spectra based on the Monte Carlo calculated microdosimetric spectra generated for this study. These spectra were compared to the dose distribution generated for this study, to determine the

contribution by fragment that made up the primary and secondary peaks. The first depth, 2 cm, is located in the entrance region before much beam fragmentation occurs, at a point where the beam should primarily be composed of carbon ions (87%). As can be seen with the blue line in Figure 44, the primary peak is centered at 20 keV/ μm and is quite distinct. Here, the peak drops off sharply at lower lineal energy values and has few events below 5% of the peak height. At the next depth, the contribution of carbon increases to 92%. The primary peak also shifts to higher lineal energy values, and is centered around 60 keV/ μm . This is expected, as the primary carbons reach the end of their range and begin to slow down, distributing more energy per path length. The dose contribution by fragments is far higher at the peak than in the entrance, as the contamination increased. At this depth, a small peak is seen at lower lineal energies, around 7 keV/ μm , corresponding to fragment contribution. In the tail, at 28 cm, the distribution is centered around 1 keV/ μm , as the only beam contributions are due to low lineal energy fragments. The lineal energy pattern across depths supports spectra subdivision based on the contribution of primary and secondaries as compared to the microdosimetric distribution pattern.

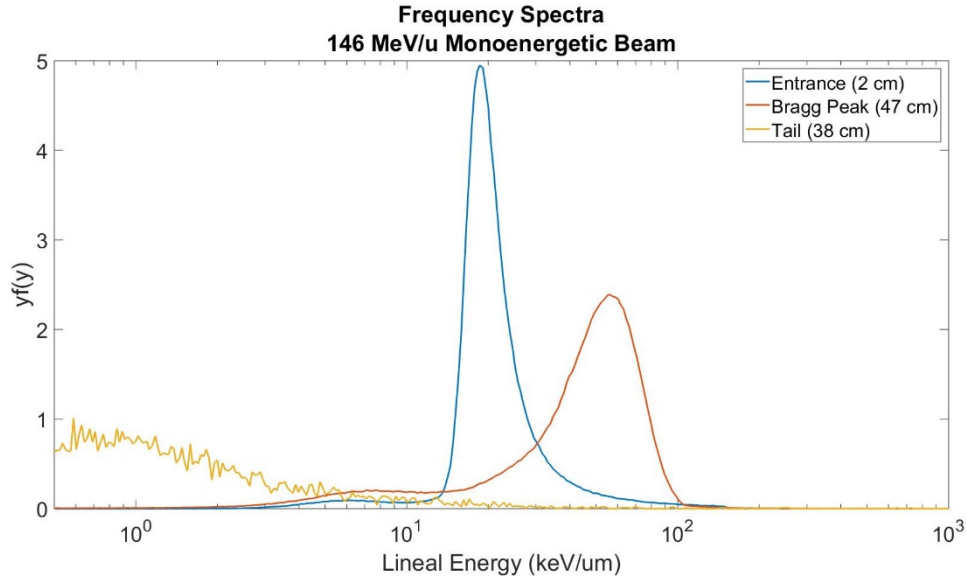


Figure 47. Frequency weighted microdosimetric spectra at entrance, Bragg peak, and tail regions for 146 MeV/u monoenergetic beam.

Similar phenomenon are shown in Figure 45 and Figure 46, which display the microdosimetric spectra at the same regions for the 424 MeV/u monoenergetic beam and the 7 cm SOBP respectively. For the 424 MeV/u monoenergetic beam, the secondary peak corresponding to the fragments is appreciably more prominent than that of the 146 MeV/u beam. This is due to the increased entrance region, which allows for greater fragment contribution. At the Bragg peak, the primary and secondary peaks are roughly equal in signal size as a result of this fragmentation. In the tail, the primary peak drops off and only the fragment peak exists, centered about 3 keV/ μ m. For the SOBP, the pattern is similar. However, the primary peak at the entrance region and the center of the SOBP are much closer in lineal energy. Also worth noting is the difference in signal size between the primary and secondary peaks at the SOBP center, which

shows how much higher the contribution of fragments is in SOBP as compared to the monoenergetic spectra.

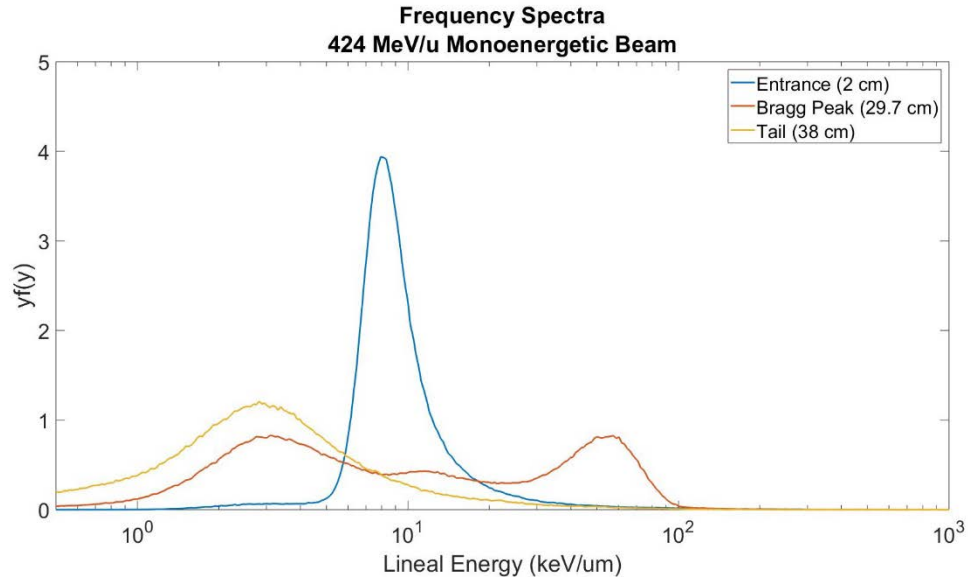


Figure 48. Frequency weighted microdosimetric spectra at entrance, Bragg peak, and tail regions for 424 MeV/u monoenergetic beam.

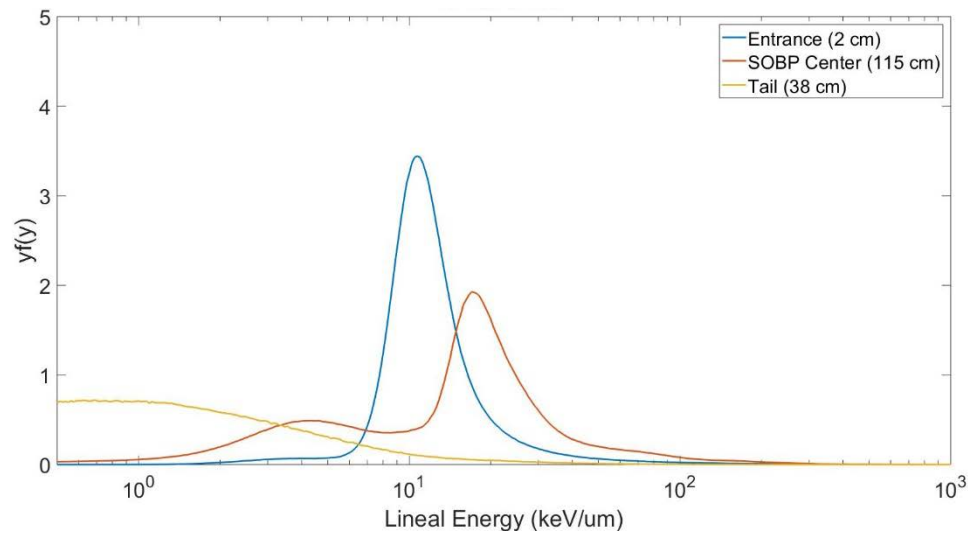


Figure 49. Frequency weighted microdosimetric spectra at entrance, SOBP, and tail regions for a 7 cm SOBP.

Using this foundation, it was proposed that dividing the microdosimetric spectra would create a more accurate estimation between the α and β components of the LEM model and y^* .

3.2.4.3.2 Cutting the Spectra

The spectra was divided at a calculated cut point. This cut point was established with the goal of generically separating the primary peak from fragments. This is complicated because the primary peak moves dramatically as depth increases (and the primary carbons slow down, increasing their lineal energy deposition). Therefore, the cut was defined as a function of primary peak height. It was determined that 20% of the peak height allowed the accurate division of the spectra into primary and secondary components.

While the fit was applied at each depth, the estimation did not work well in the region distal to the Bragg peak. Here, the fragmentation mix is critically important and the dose consists only of secondary fragments. Clinically, this region is not very important as it lies beyond the typical volume of interest and the total physical dose is low. As a result, the fit was optimized for use within the entrance and Bragg peak regions. Once the spectra was cut in two according to the primary peak, all lineal energy values were recalculated individually for each of the two portions of the microdosimetric spectrum.

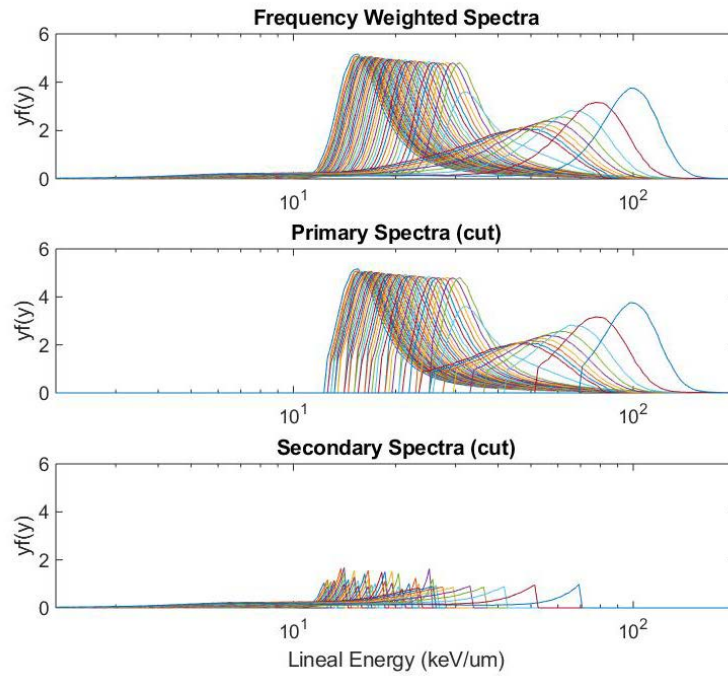


Figure 50. Frequency weighted microdosimetric spectra cut into primary and secondary peaks for 146 MeV/u monoenergetic beam.

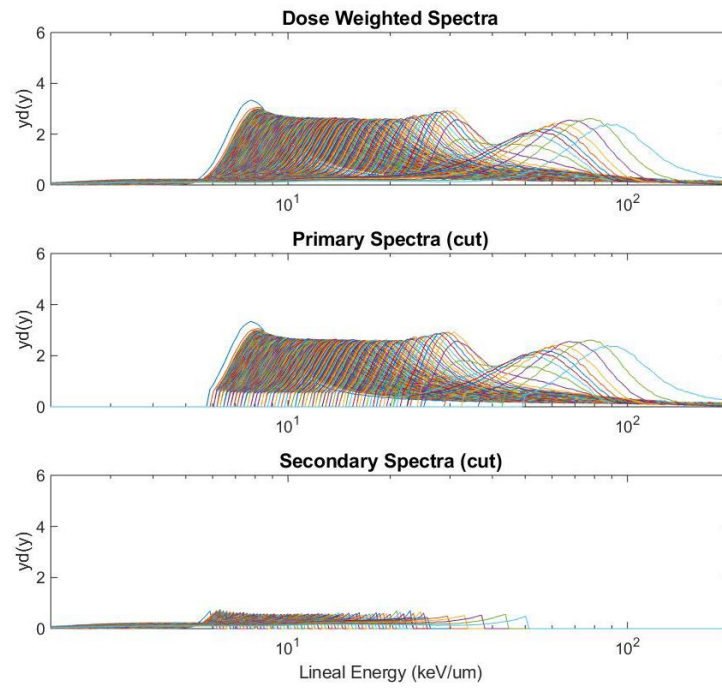


Figure 51. Dose weighted microdosimetric spectra cut into primary and secondary peaks for 146 MeV/u monoenergetic beam.

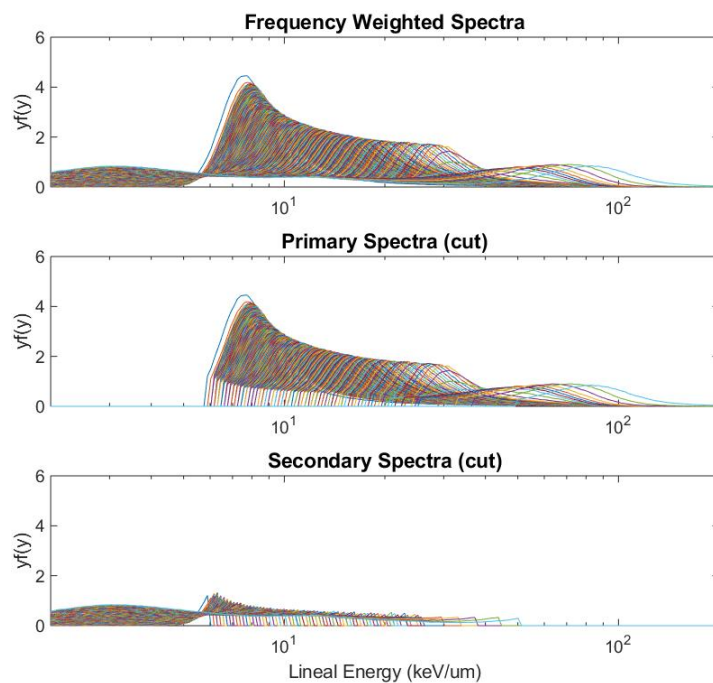


Figure 52. Frequency weighted microdosimetric spectra cut into primary and secondary peaks for 424 MeV/u monoenergetic beam.

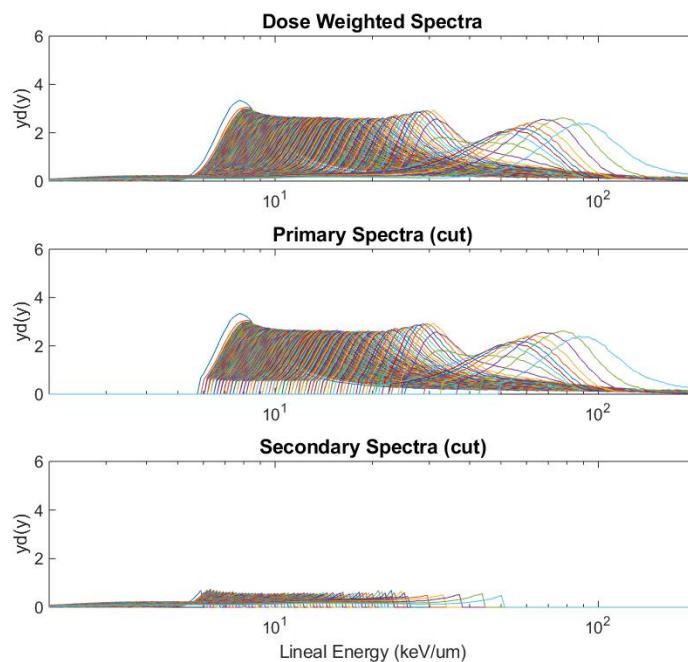


Figure 53. Dose weighted microdosimetric spectra cut into primary and secondary peaks for 424 MeV/u monoenergetic beam.

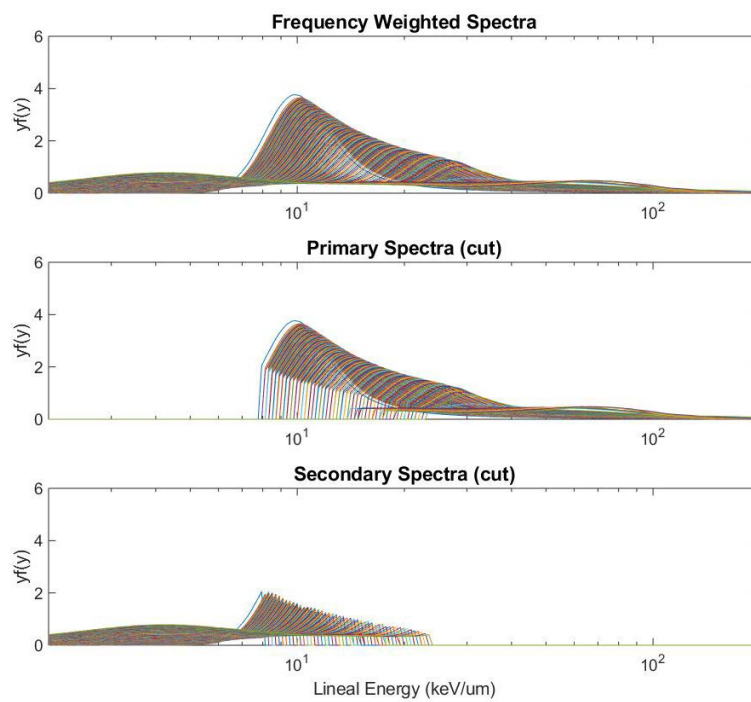


Figure 54. Frequency weighted microdosimetric spectra cut into primary and secondary peaks for 7 cm SOB.

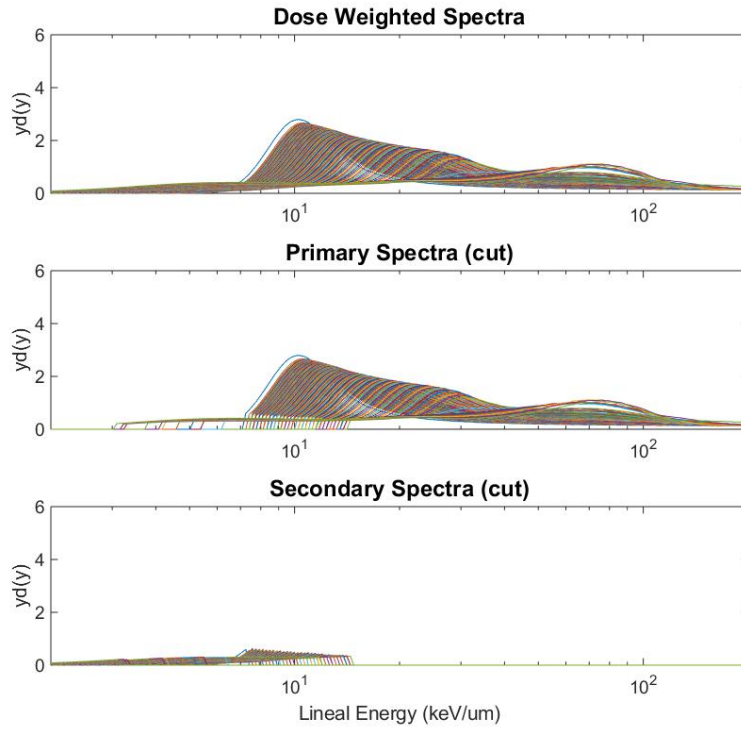


Figure 55. Dose weighted microdosimetric spectra cut into primary and secondary peaks for 7 cm SOBPs.

3.2.4.3.3 Calculating alpha and beta values

Cutting the microdosimetric spectra allowed for separate estimation of the primary and secondary α and β values. In order to estimate these values, the true α and β were isolated for each primary fragment (i.e. α_C and β_C for carbon and α_B and β_B for boron) and plotted as functions of $y^*_{Primary}$. These are represented by the solid lines in Figure 53 and Figure 54. Next, α and β values from both 146 MeV/u and 424 MeV/u monoenergetic clinical beams were plotted on overlay, and CurveFinder software was used to independently fit α as a

function of $y^*_{Primary}$ for both energies combined. This fit is represented by the dotted lines in Figure 53, the polynomials used for which are shown in Table 22.

This same fitting process was repeated with β of primary contributors as a function of $y^*_{Primary}$, the fit of which is shown in Figure 54. A similar procedure was then conducted with the SOBP, however, only the 7 cm SOBP was used to create the α and β fits to allow the other SOBPs to serve as validation sets for the model. These polynomial values are shown in Table 23. Monoenergetic and SOBP setups were assessed independently of each other, as they had noticeable different trends in α and β values as functions of lineal energy.

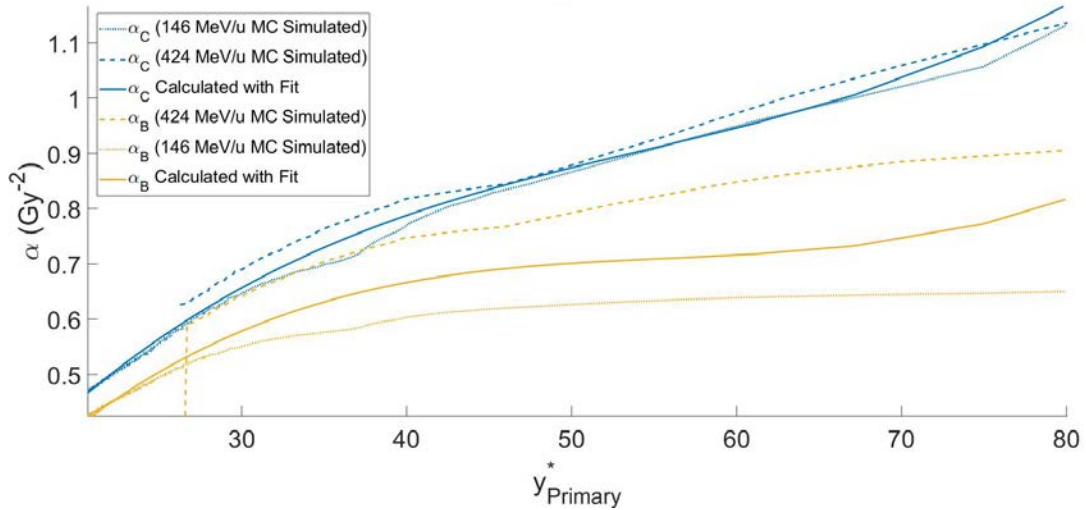


Figure 56. Shows the primary alpha values as a function of $y^*_{Primary}$ calculated by Monte Carlo for 146 MeV/u and 424 MeV/u monoenergetic beams and fit with the polynomial described in Table 22. Primary carbon α values are shown in blue, while boron α values are shown in yellow. The solid lines represent the fit polynomials.

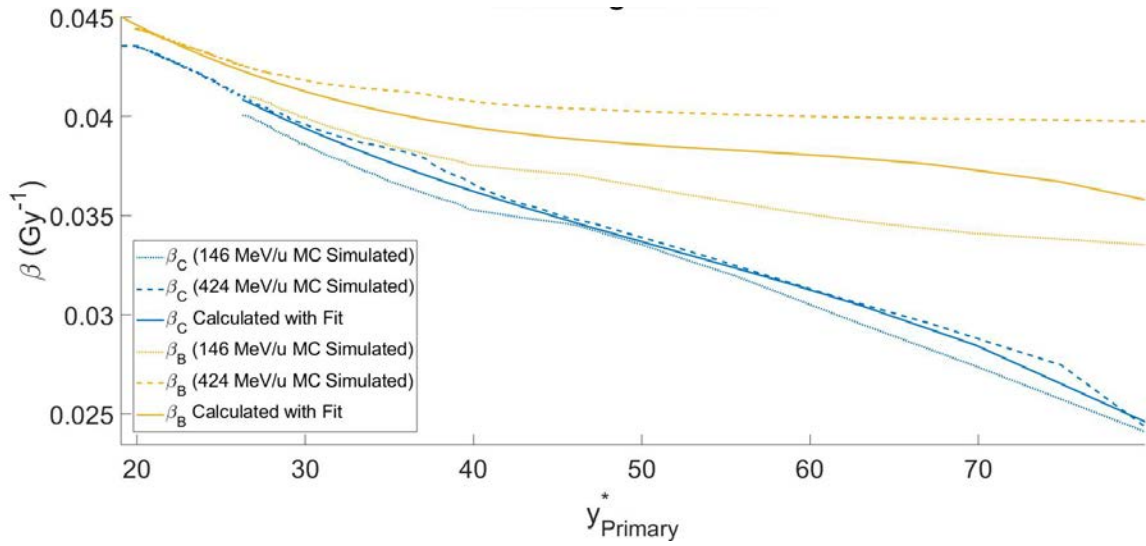


Figure 57. Shows the primary β values as functions of $y^*_{Primary}$ calculated by Monte Carlo for 146 MeV/u and 424 MeV/u monoenergetic beams and fit with the polynomial described in Table 20. Primary carbon β values are shown in blue, while boron β values are shown in yellow. The solid lines represent the fit polynomials.

Table 22. Polynomial variables used to estimate α and β values of the primary peak of monoenergetic beams.

Monoenergetic Primary Fits				
$x = a + by^*_{Primary} + cy^*_{Primary}{}^2 + dy^*_{Primary}{}^3$				
x	a	b	c	d
α_C	-3.11E-1	5.27E-2	-8.34E-4	5.08E-6
α_B	-3.35E-1	5.33E-2	-9.27E-4	5.51E-6
β_C	5.81E-2	-9.58E-4	1.38E-5	-8.82E-8
β_B	5.82E-2	-9.69E-4	1.64E5	-9.74E-8

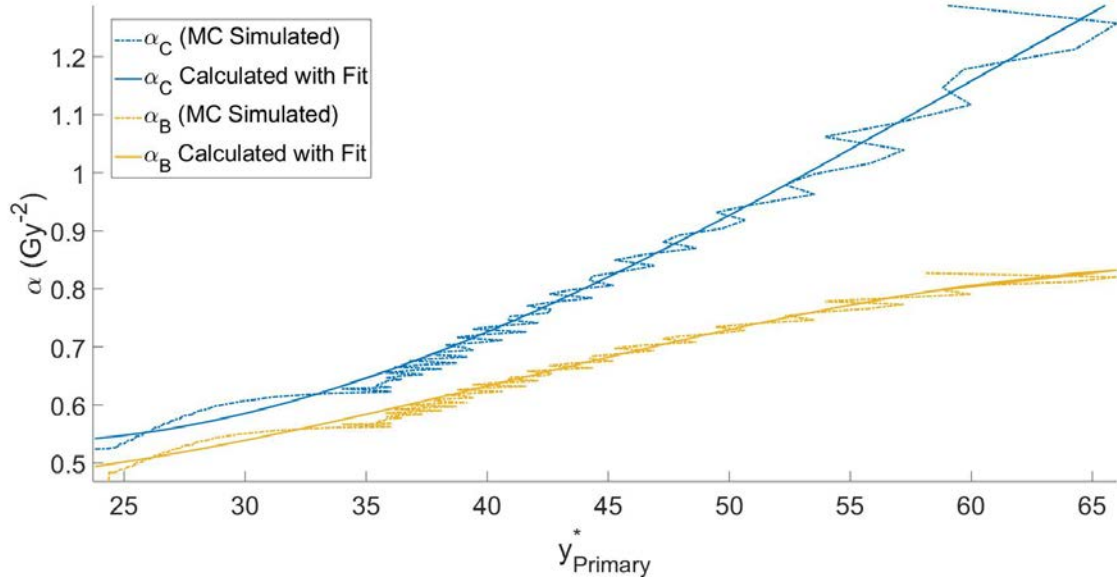


Figure 58. Shows the primary α values as a function of $y^*_{Primary}$ calculated by Monte Carlo for the 7 cm SOBP and fit with the polynomial described in Table 23. Primary carbon α values are shown in blue, while boron α values are shown in yellow. The solid lines represent the fit polynomials.

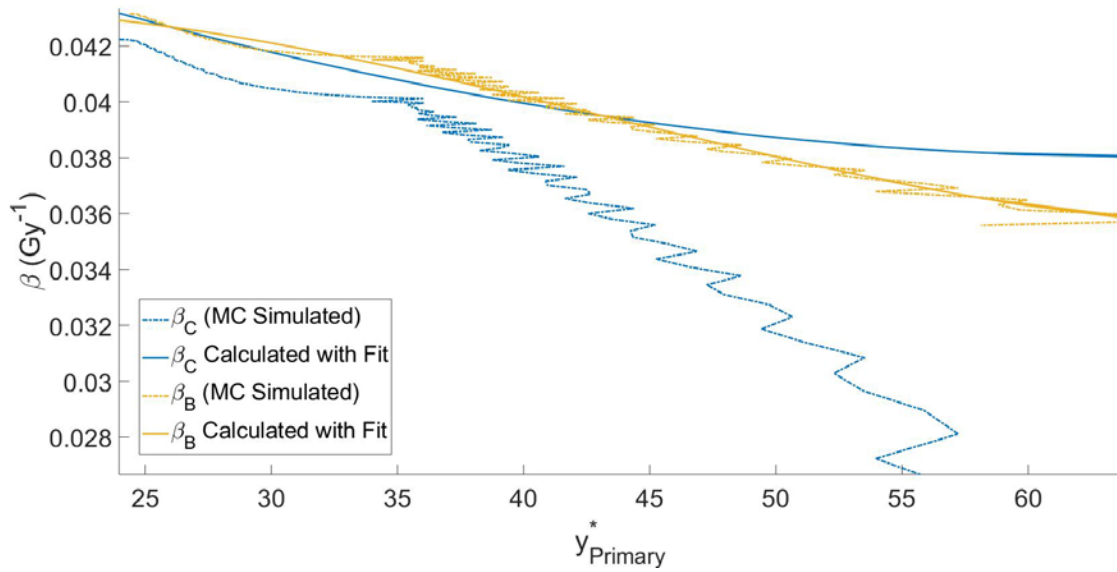


Figure 59. Shows the primary β values as functions of $y^*_{Primary}$ calculated by Monte Carlo for a 7 cm SOBP and fit with the polynomial described in Table 23. Primary carbon β values are shown in blue, while boron β values are shown in yellow. The solid lines represent the fit polynomials.

Table 23. Polynomial variables used to estimate α and β values of the primary peak of SOBP spectra.

SOBP Primary Fits				
$x = a + by^*_{Primary} + cy^*_{Primary}{}^2 + dy^*_{Primary}{}^3$				
x	A	b	c	d
α_C	6.33E-2	2.27E-2	-2.33E-4	0
α_B	6.33E-2	2.27E-2	-2.33E-4	0
β_C	5.09 E-2	-3.95E-4	3.03E-6	0
β_B	4.07E-2	3.45E-4	-1.29E5	9.87E-8

Next, this same process of plotting and fitting the α and β values was repeated for the fragments as a function of $y^*_{Secondary}$. Typically the Monte Carlo calculated fragments were fit with less accuracy than the primaries, but this error was of less significance due to the lower overall dose contribution. The analogous estimated and calculated α and β values for the secondaries are shown in Figure 57 - Figure 60 below, and subsequent fit parameters in Table 24 and Table 26.

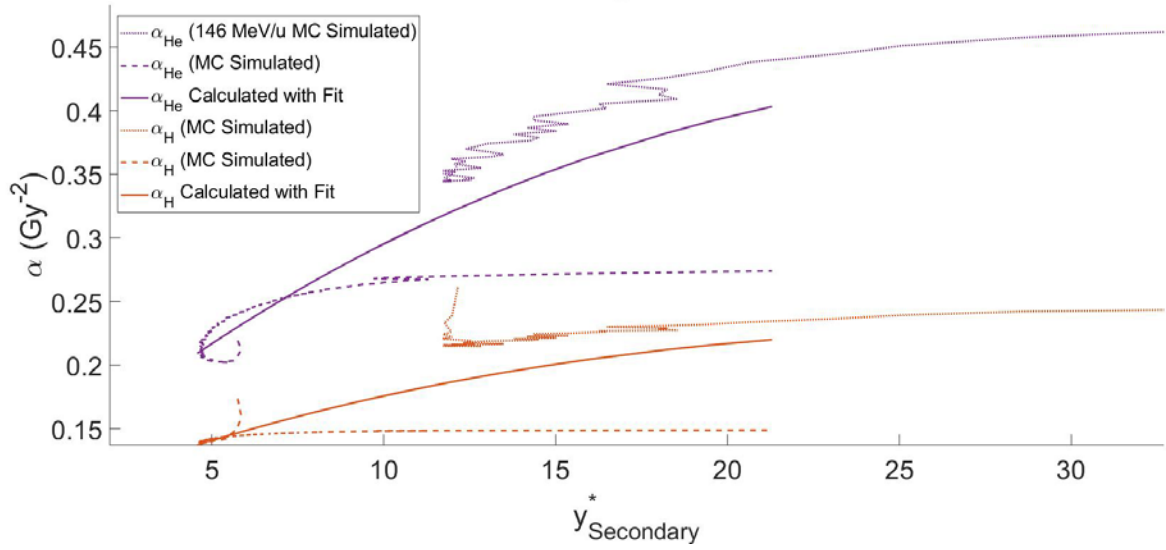


Figure 60. Shows the secondary alpha values as a function of $y^*_{\text{Secondary}}$ calculated by Monte Carlo for 146 MeV/u and 424 MeV/u monoenergetic beams and fit with the polynomial described in Table 24. Helium α values are shown in purple, while proton α values are shown in orange. The solid lines represent the fit polynomials.

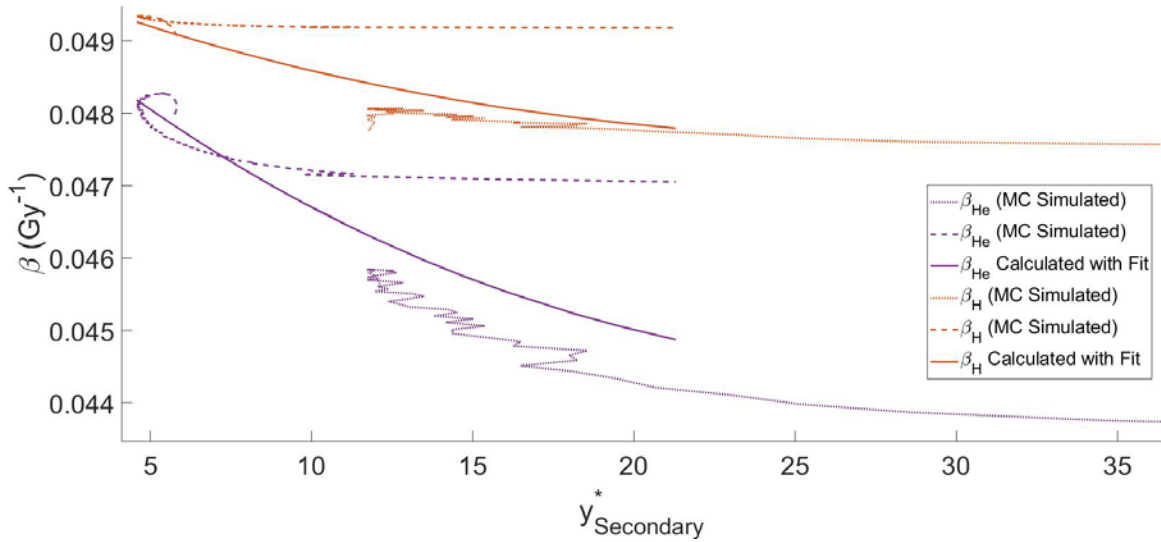


Figure 61. Shows the secondary β values as a function of $y^*_{\text{Secondary}}$ calculated by Monte Carlo for 146 MeV/u and 424 MeV/u monoenergetic beams and fit with the polynomial described in Table 24. Helium β values are shown in purple, while proton β values are shown in orange. The solid lines represent the fit polynomials.

Table 24. Polynomial variables used to estimate α and β values of the secondary peak of monoenergetic beams.

Monoenergetic Secondary Fits				
$z = e + fy^*_{\text{Secondary}} + gy^*_{\text{Secondary}}^2 + hy^*_{\text{Secondary}}^3$				
z	e	f	g	h
α_{He}	4.46	-1.12	1.29E-1	4.80E-3
α_{H}	-1.09E-1	7.50E-2	-6.60E-3	1.93E-4
β_{He}	9.10E-2	-1.30E-2	1.21E-3	-3.82E-5
β_{H}	5.43E-3	-1.51E-4	1.36E-4	-4.10E-6

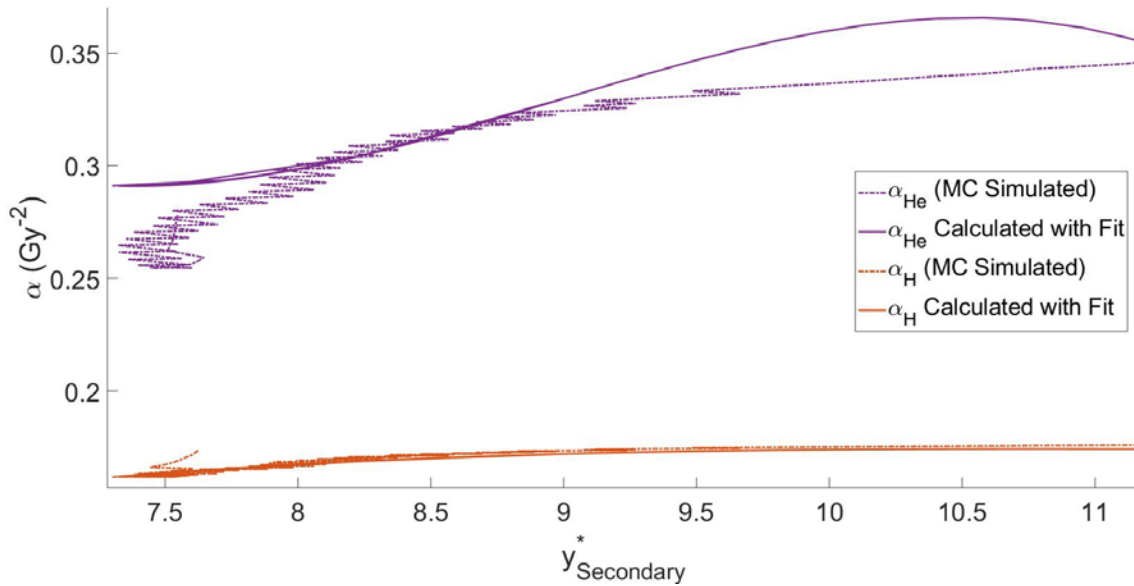


Figure 62. Shows the secondary alpha values as a function of $y^*_{\text{Secondary}}$ calculated by Monte Carlo for a 7 cm SOBP and fit with the polynomial described in Table 26. Helium α values are shown in purple, while proton α values are shown in orange. The solid lines represent the fit polynomials.

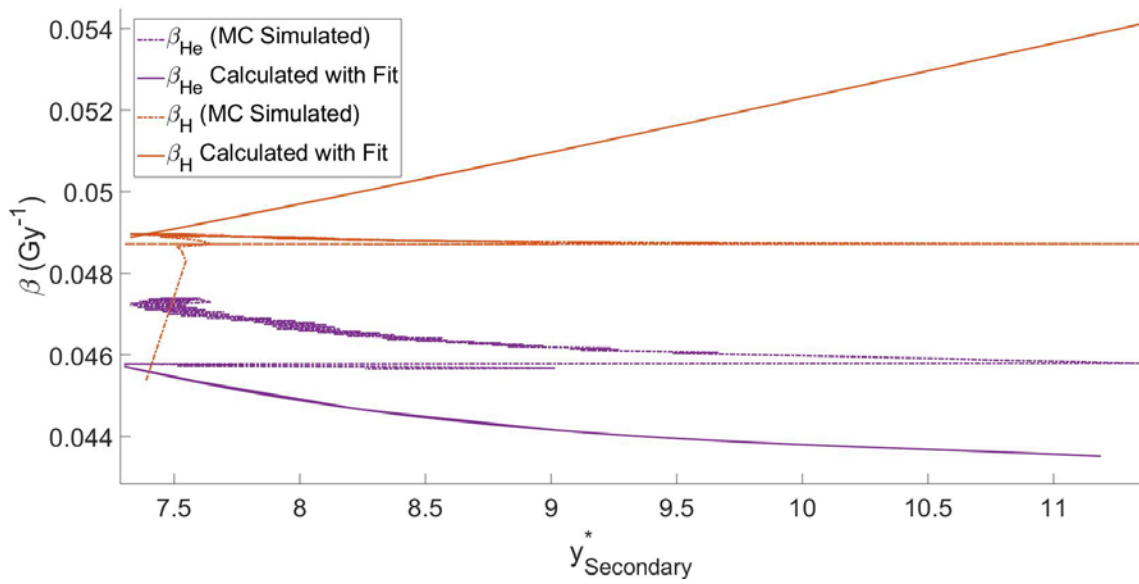


Figure 63. Shows the secondary β values as a function of $y^*_{\text{Secondary}}$ calculated by Monte Carlo for a 7 cm SOBPs and fit with the polynomial described in Table 25. Helium β values are shown in purple, while proton β values are shown in orange. The solid lines represent the fit polynomials.

Table 26. Polynomial variables used to estimate α and β values of the secondary peak of SOBPs spectra.

SOBP Secondary Fits				
$z = e + fy^*_{\text{Secondary}} + gy^*_{\text{Secondary}}{}^2 + hy^*_{\text{Secondary}}{}^3$				
z	e	f	g	h
α_{He}	6.33E-2	2.27E-2	-2.33E-4	0
α_{H}	4.96E-1	-2.20E-2	6.5E-4	-5.34E-6
β_{He}	5.09 E-2	-3.95E-4	3.03E-6	0
β_{H}	4.07E-2	3.45E-4	-1.29E5	9.87E-8

Next, the calculated percent weighting from above was used to properly weight final $\bar{\alpha}$ and $\bar{\beta}$ values. These values were then combined with both reference α_X and β_X values and physical dose to calculate an estimated RBE.

3.2.4.3.4 Determining Percent Contribution

After both primary and secondary α and β values are calculated from microdosimetric values, a method of recombining both $\alpha_{Primary}$ and $\alpha_{Secondary}$, and $\beta_{Primary}$ and $\beta_{Secondary}$ into a comprehensive $\bar{\alpha}$ and $\bar{\beta}$ values for RBE calculations is needed. In the empirical LEM calculations, this is done with the weighted dose distribution by fragment. As this is not possible to measure, however, the following method was designed.

In order to accomplish this, a weighted average of the dose mean lineal energy was used. This method, introduced by Booz, Fidorra, and Feinendegen, indicates that the \bar{y}_D of each component, i , may be added according to its dose fraction, as shown in Equation 36 below [34].

Equation 35

$$\bar{y}_D = \sum_{i=1}^n \frac{D_i}{D} * \bar{y}_{D,i}$$

When implemented in the cut spectra, the percent contribution p is divided into that of primaries and that of secondaries. As a result, Equation 37 was determined.

Equation 36

$$\bar{y}_D = \bar{y}_{D,Primary} p_{Primary} + \bar{y}_{D,Secondary} (1 - p_{Primary})$$

Once all lineal energy values are calculated for the cut and uncut spectra, the contributions can be calculated simply using the following rearrangement.

Equation 37

$$p_{Primary} = \frac{\bar{y}_{D,Secondary} - \bar{y}_D}{\bar{y}_{D,Secondary} - \bar{y}_{D,Primary}}$$

Upon referring to Figure 43, it is noted that the contribution of boron falls relatively within the primary peak of the microdosimetric spectra. Therefore, it is reasonable to assume that the lineal energy due to the primary peak can be further subdivided into that of carbon and that of boron to provide a better fit. In each pristine spectra analyzed, the percent contribution of boron increased in an approximately linear fashion from 0% to 30% in the depth leading up to the Bragg peak. The percent of the primary peak due to carbon was then considered to be the remainder of this value; this is shown mathematically in equation 45. While the percent boron increased to more than 40% by the distal edge of an SOBP, this had little impact on the overall fit of α and β values. As a result, the percent contribution of boron was calculated using the same formula as that in the pristine peak for simplicity, i.e., Equation 46.

Equation 38

$$p_C = (1 - p_B) * p_{Primary}$$

Equation 39

$$p_B = \left(\left(\frac{0.3}{PeakDepth} \right) * Depth \right) * p_{Primary}$$

The percent contribution of the fragments was also further subdivided, where helium and protons were considered as 40% and 60% of the fragment contribution relatively, based on the Monte Carlo dose distributions generated for this study. Similarly to the contribution of carbon and boron, these ratios were observed to be slightly different in their respective percent contribution to the SOBP. However, using the same ratios for both the pristine peak and the SOBP

resulted in an addition of less than 1% error and were therefore kept the same out of simplicity. The relative components are shown mathematically in equations 47 and 48.

$$\text{Equation 40} \quad p_{He} = 0.4 * p_{Secondary}$$

$$\text{Equation 41} \quad p_H = 0.6 * p_{Secondary}$$

Examples of the percent contribution calculated using this method is shown in comparison to the percent contribution calculated using Monte Carlo for two monoenergetic beams and an SOBP. The accuracy of each of these methods is highly dependent on the location of the cut between the primary and secondary portions of the spectra described above, and is a parameter that was used in the determination of the 20% peak lineal energy height cutoff threshold.

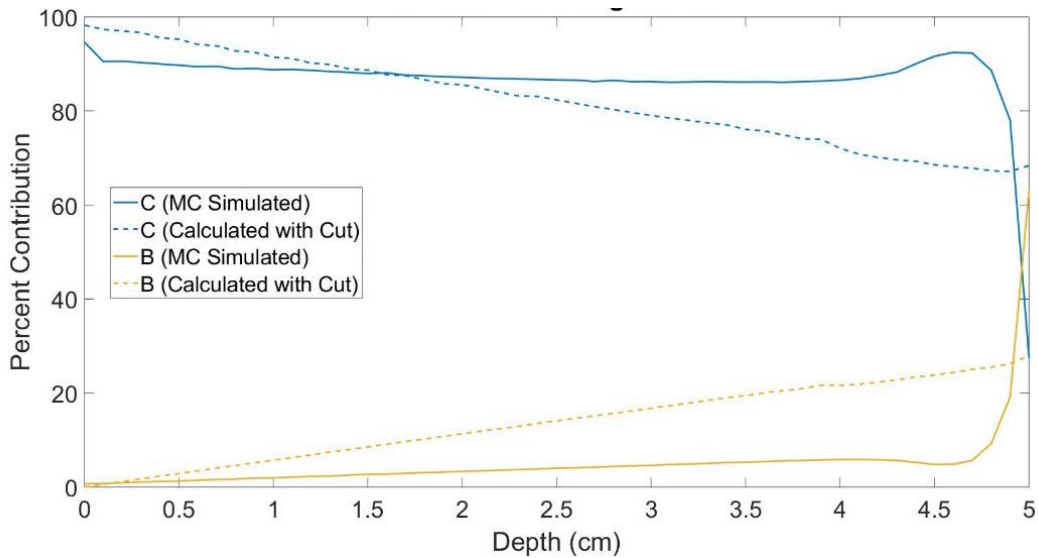


Figure 64. Contribution of carbon and boron calculated with Monte Carlo (solid lines) and that estimated by the cut spectra (dashed lines) for 146 MeV/u monoenergetic beam. Carbon contribution is shown in blue and boron contribution is shown in yellow.

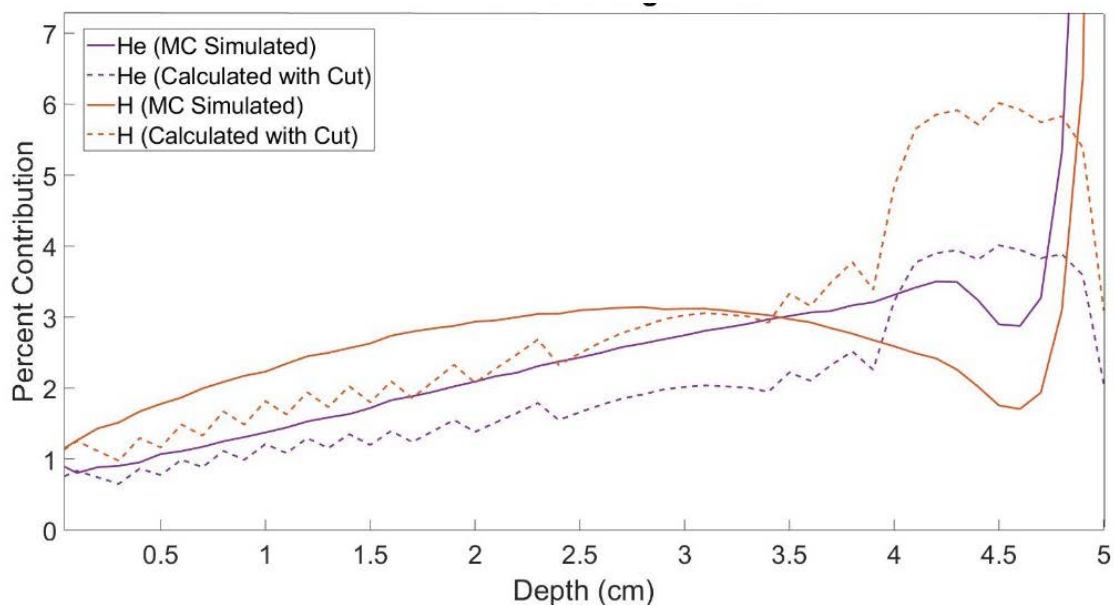


Figure 65. Contribution of helium and protons calculated with Monte Carlo (solid lines) and that estimated by the cut spectra (dashed lines) for 146 MeV/u monoenergetic beam. Helium contribution is shown in purple and boron contribution is shown in orange.

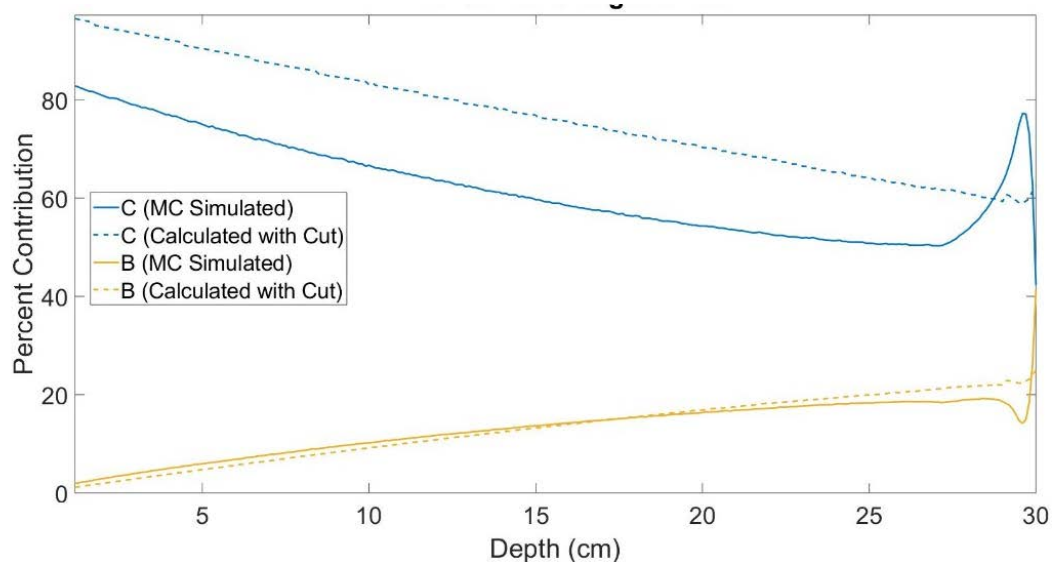


Figure 66. Contribution of carbon and boron calculated with Monte Carlo (solid lines) and that estimated by the cut spectra (dashed lines) for a 424 MeV/u monoenergetic beam. Carbon contribution is shown in blue and boron contribution is shown in yellow.

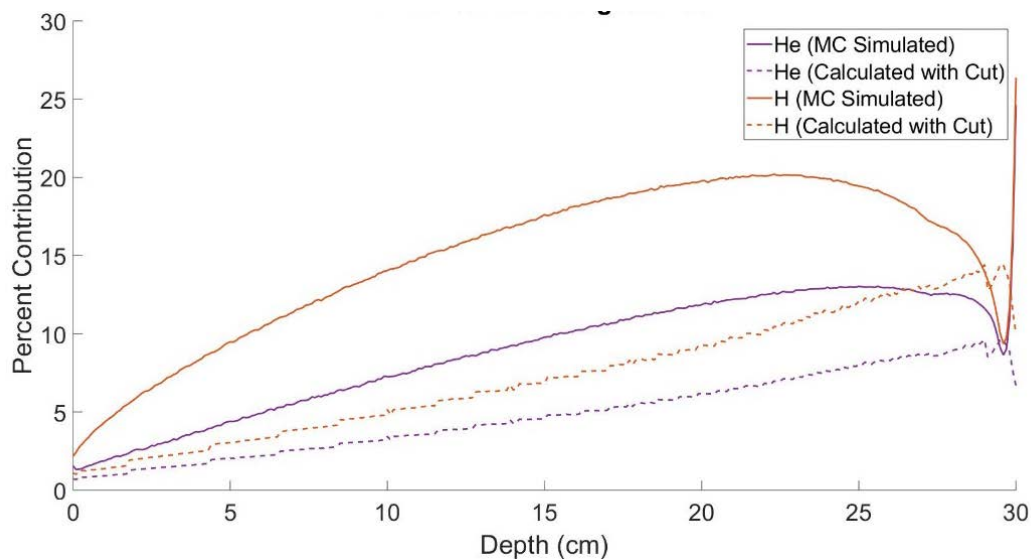


Figure 67. Contribution of helium and protons calculated with Monte Carlo (solid lines) and that estimated by the cut spectra (dashed lines) for a 424 MeV/u monoenergetic beam. Helium contribution is shown in purple and boron contribution is shown in orange.

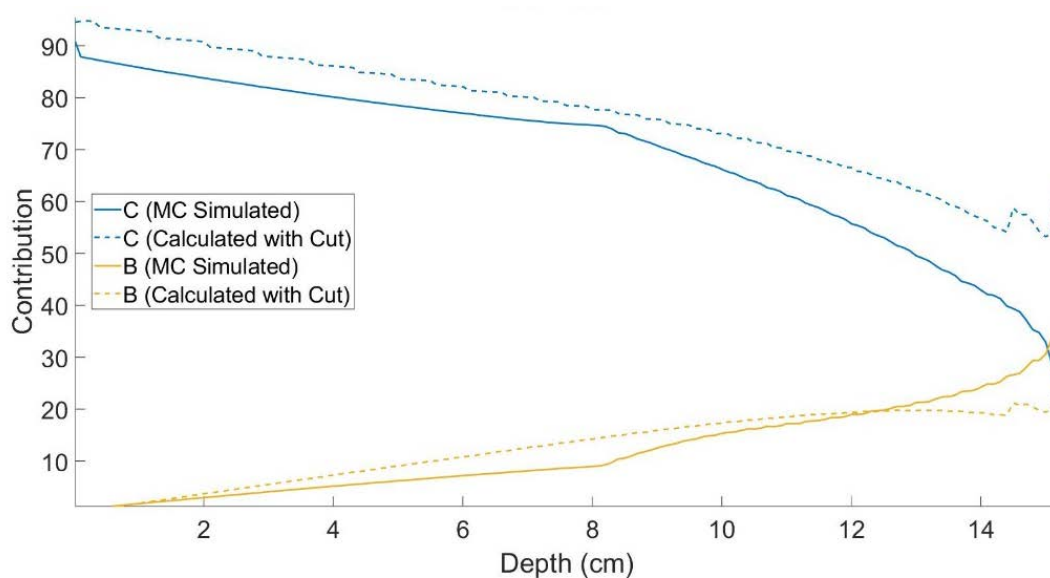


Figure 68. Contribution of carbon and boron calculated with Monte Carlo (solid lines) and that estimated by the cut spectra (dashed lines) for a 7 cm SOBP. Carbon contribution is shown in blue and boron contribution is shown in yellow.

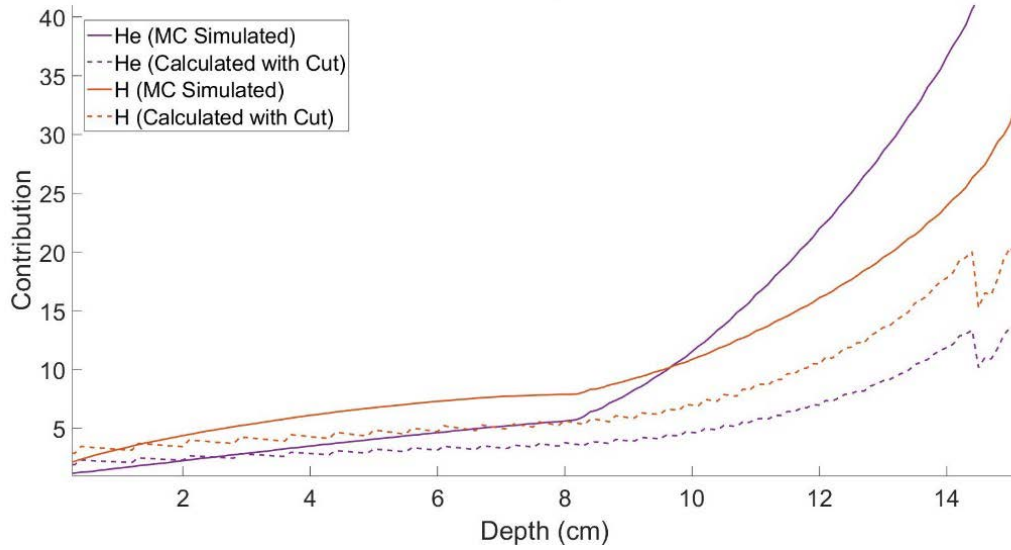


Figure 69. Contribution of helium and protons calculated with Monte Carlo (solid lines) and that estimated by the cut spectra (dashed lines) for a 7 cm SOBP. Helium contribution is shown in purple and boron contribution is shown in orange.

3.2.5 Adding Uncertainty

Introducing systematic and measurement based uncertainty into the LEM and RMF calculations was performed by perturbing the microdosimetric spectra in the same manner as that done for the MKM model. For the RBE_{RMF} , α and β were calculated for each perturbed spectra as a function of y^* . RBE was then calculated using these estimated values. For the RBE_{LEM} , the procedure of cutting the spectra was repeated as detailed above. From the cut spectra, $y^*_{Primary}$ or $y^*_{Secondary}$ were calculated and used to estimate each α and β value and the resulting RBE and biological dose. This process provided a means of estimating RBE_{LEM} using microdosimetric measurements alone.

3.3 Results

The propagated uncertainty is presented in the following manner. First, the effect of the physical measurement based uncertainty is presented as a function of each source for all lineal energy values. This is divided into both random uncertainties and into combination random and systematic uncertainties. For the former, the uncertainty is quantified as a percent standard deviation from the mean, which is equal to the simulated lineal energy. For the latter, the systematic shift is quantified as a percent difference between the mean of the 200 shifted values and the simulated lineal energy values. The random portion of the shift is distributed about this new mean, providing a 1σ percent uncertainty about this value. Each random uncertainty component is added in quadrature to give a final uncertainty in lineal energy due to physical measurements. Additionally, the percent difference from each systematic shift is summed to yield an overarching anticipated correction.

Next, the final uncertainty propagated through to each RBE model is assessed. This follows the same format, assessing both random and systematic errors separately to give overarching variance and shift in RBE. For LEM, the uncertainty in estimating RBE using microdosimetric inputs is also quantified. However, this estimation error was already propagated through the uncertainty analysis, by shifting and recalculating each LEM value accordingly, and is therefore accounted for in the calculation of systematic shifts. Values are typically presented for the entrance at exactly 2 cm, and for the average and maximum values over the entire entrance region. Similarly, values are shown at exactly the

center of the Bragg peak, and for the average and maximum uncertainties in the range of the SOBP.

3.3.1 Monte Carlo

3.3.1.1 Dose Distribution

The dose distributions calculated by Monte Carlo are displayed in Figure 67 - Figure 69. The total dose is represented by the blue line, beginning in the entrance region at about 25% of the maximum dose and increasing steadily to 100% at the Bragg peak. Within a half of a centimeter beyond the Bragg peak, the total dose drops to 3% and continues to steadily decline with depth. Within that same half centimeter beyond the Bragg peak, the contribution of primary carbon drops to zero as well. As can be seen, the tail contribution is primarily composed of Helium and Hydrogen. Boron has a major contribution in the centimeter beyond the Bragg peak, but drops off quickly after that point. Dose distributions for the remaining beams can be seen in Appendix 6.7.

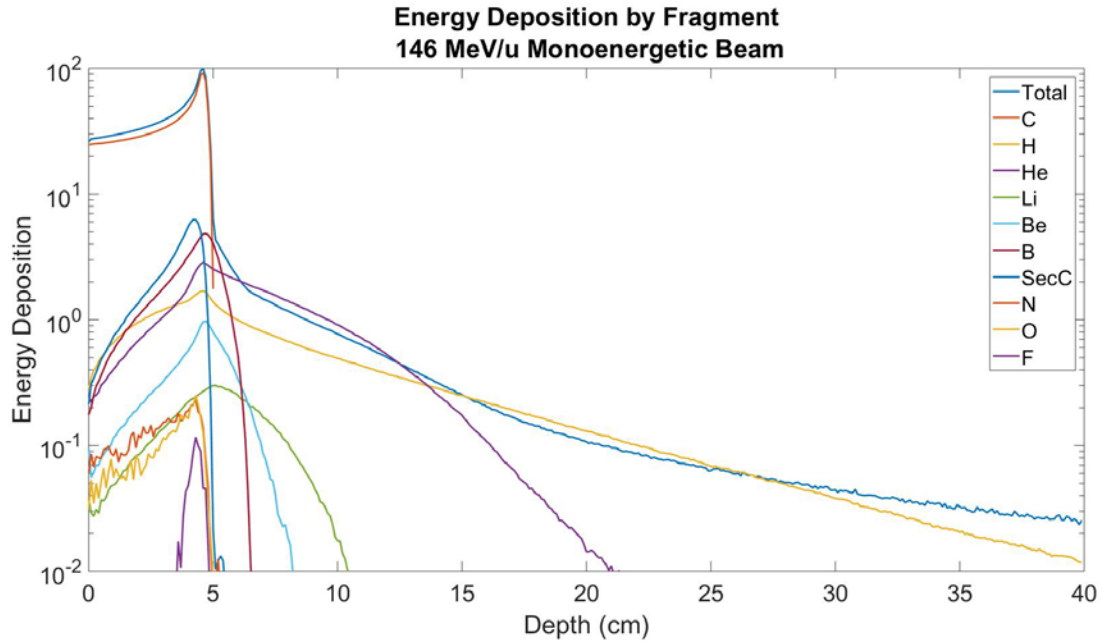


Figure 70. Energy deposition by each fragment as a function of depth for 146 MeV/u monoenergetic beam.

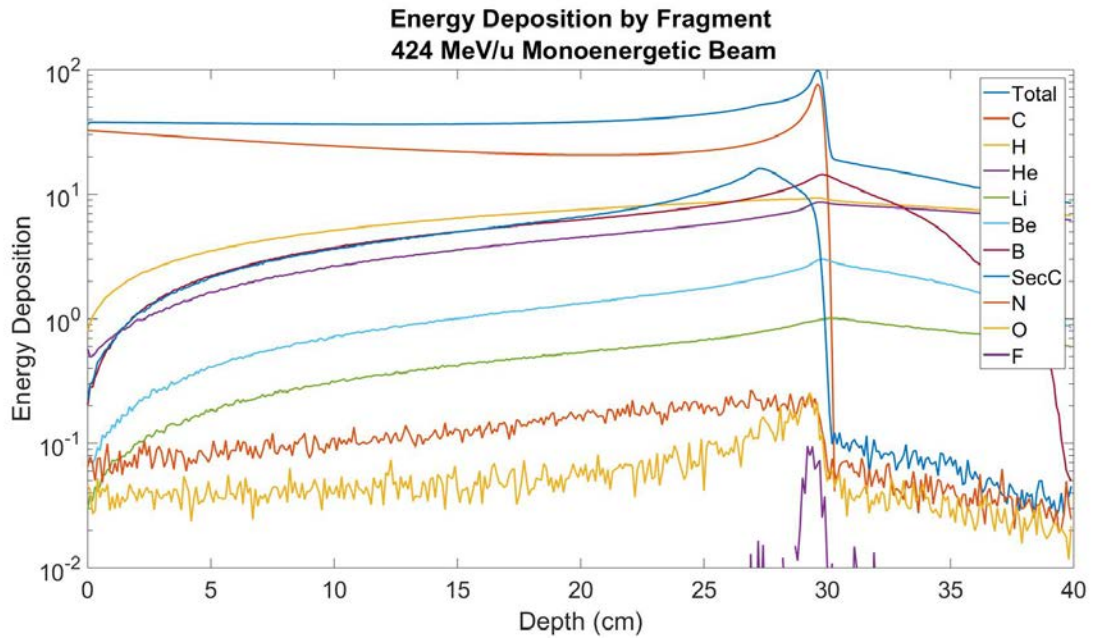


Figure 71. Energy deposition by each fragment as a function of depth for 424 MeV/u monoenergetic beam.

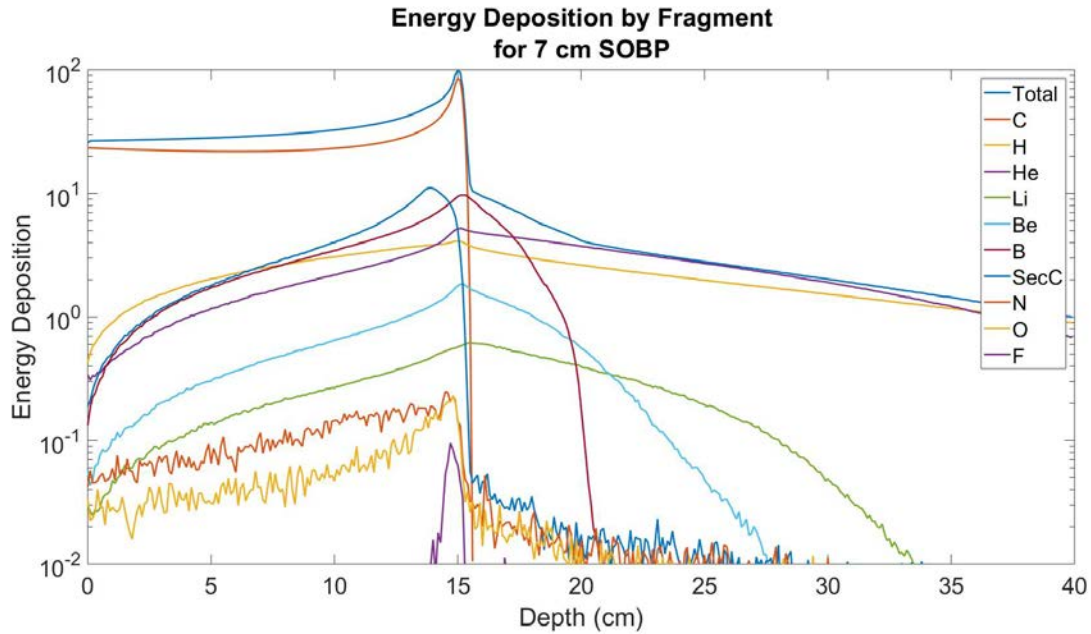


Figure 72. Energy deposition by each fragment as a function of depth for 7 cm SOBP.

3.3.1.2 Kinetic Energy

The average kinetic energy as a function of depth for each of the relevant fragments is shown in Figure 71, Figure 73, and Figure 75 for all dose contributing fragments. However, since the input tables for LEM only provided α and β values for the seven highest contributing particles, the kinetic energy spectra for nitrogen, oxygen, and fluorine were not used in this work. As can be seen in each of these figures, the contribution of each of these fragments were at least an order of magnitude lower than the next highest contributing fragment, indicating that they should have negligible effect on the results.

As can be seen, the kinetic energy of primary carbons drops off sharply approaching the Bragg peak while the kinetic energy of fragments is highly

variable at each depth. This is due to the increase in dose deposition of the primary carbons as they slowed down and reached the end of their range. The fragments were produced as primary nuclei interacted with targets, and therefore had a wider range of energies.

The kinetic energy distribution of primary carbon is shown at several depths in Figure 70, Figure 72, and Figure 74. As expected, the distribution of carbon is narrow, with the distribution widening slightly at higher depths as the kinetic energy decreased. Each of the fragments had a wider distribution, as they were created by carbon nuclei of varying energy. Plots of kinetic energy distributions are shown for fragments in the Appendix for reference.

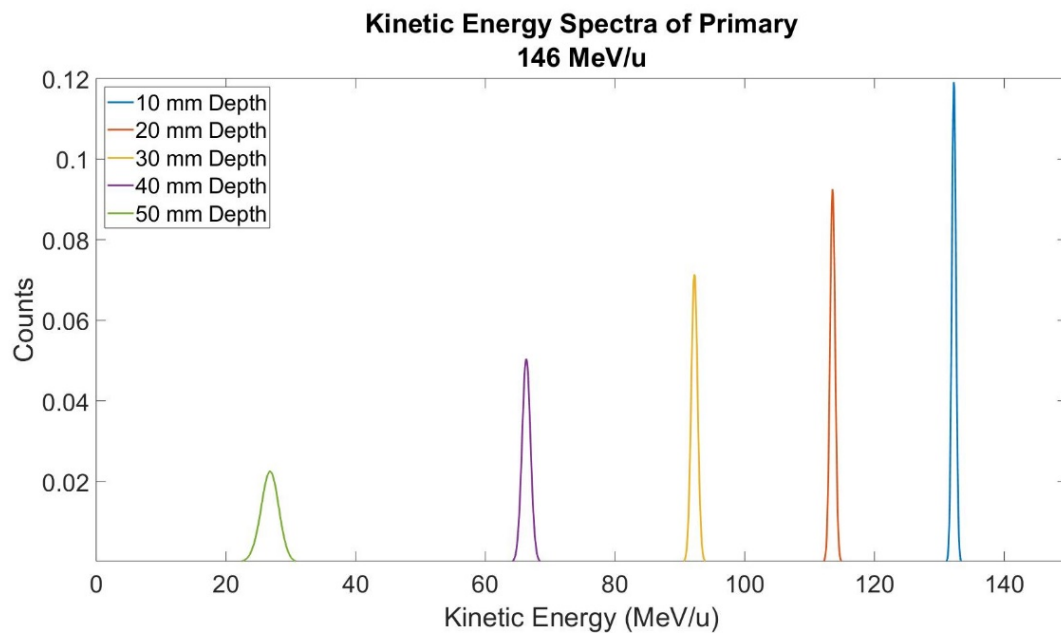


Figure 73. Kinetic energy distribution of primary carbon at five different depths between the entrance and Bragg peak for a 146 MeV/u monoenergetic beam.

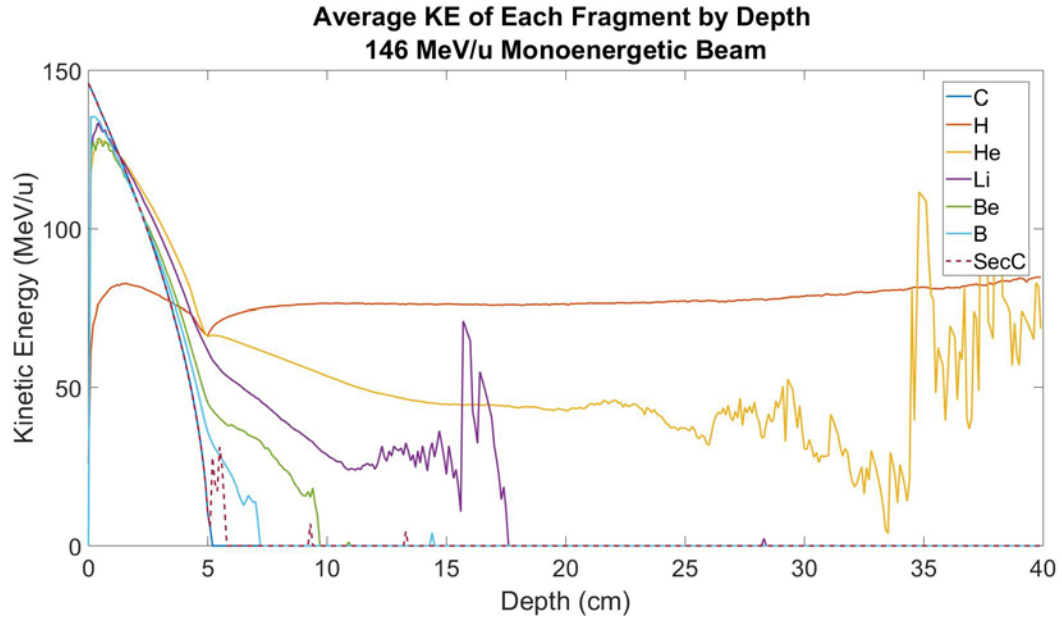


Figure 74. Average kinetic energy as a function of depth for primary carbons and secondary fragments for a 146 MeV/u monoenergetic beam.

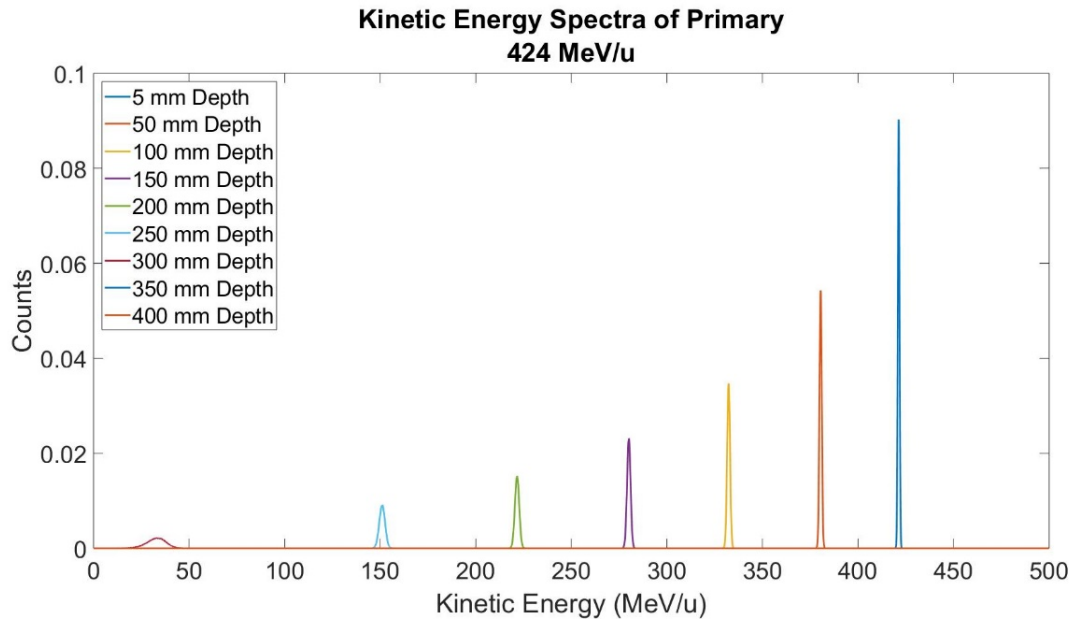


Figure 75. Kinetic energy distribution of primary carbon at five different depths between the entrance and Bragg peak for a 424 MeV/u monoenergetic beam.

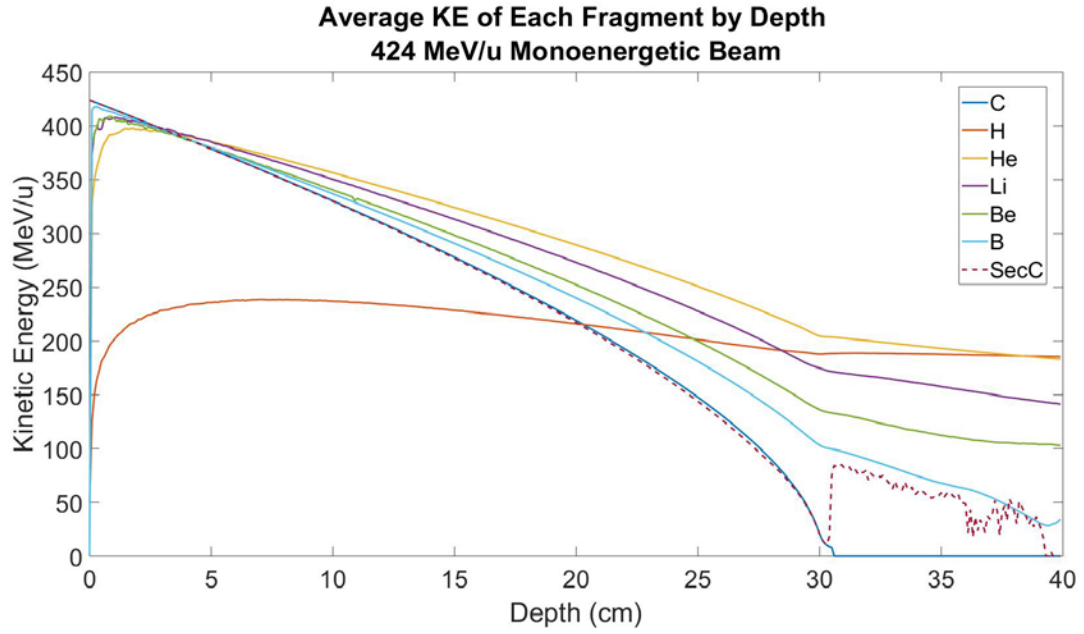


Figure 76. Average kinetic energy as a function of depth for primary carbons and secondary fragments for a 424 MeV/u monoenergetic beam.

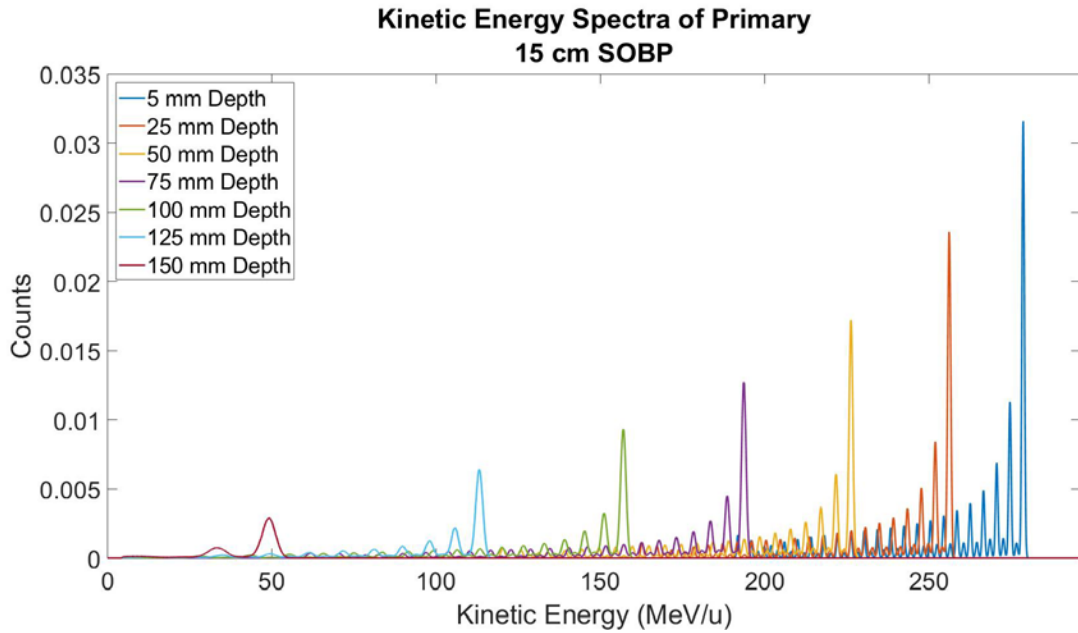


Figure 77. Kinetic energy distribution of primary carbon at five different depths between the entrance and Bragg peak for a 7 cm SOB.

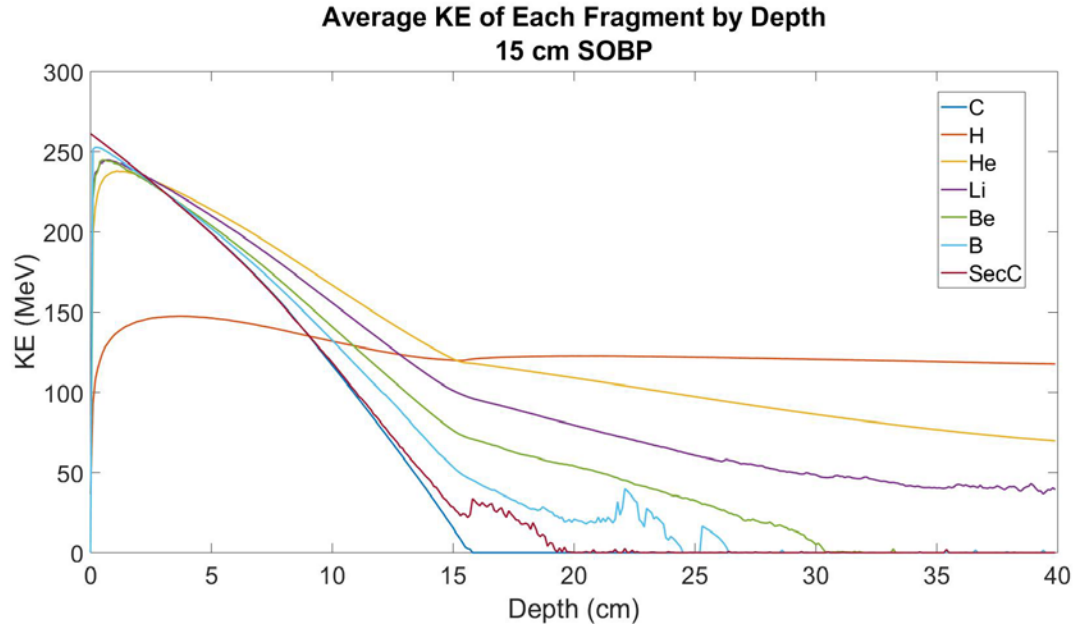


Figure 78. Average kinetic energy as a function of depth for primary carbons and secondary fragments for a 7 cm SOBP.

3.3.2 MKM

3.3.2.1 Calculation

The true RBE_{MKM} calculations were made according to the formulas outlined by the model, in which y^* is the only varying parameter. The RBE is shown on the right y-axis in Figure 76 - Figure 78, along with corresponding biological dose in Gy on the left y-axis. Physical dose is also shown for reference on the location of the Bragg peak. For the monoenergetic beams, the physical dose is normalized to 1 Gy at the entrance. For the SOBP calculations, the physical dose is normalized to 2 Gy throughout the SOBP. While the physical dose is typically weighted so that the biological dose is constant across the SOBP, this allowed for an easier comparison across models.

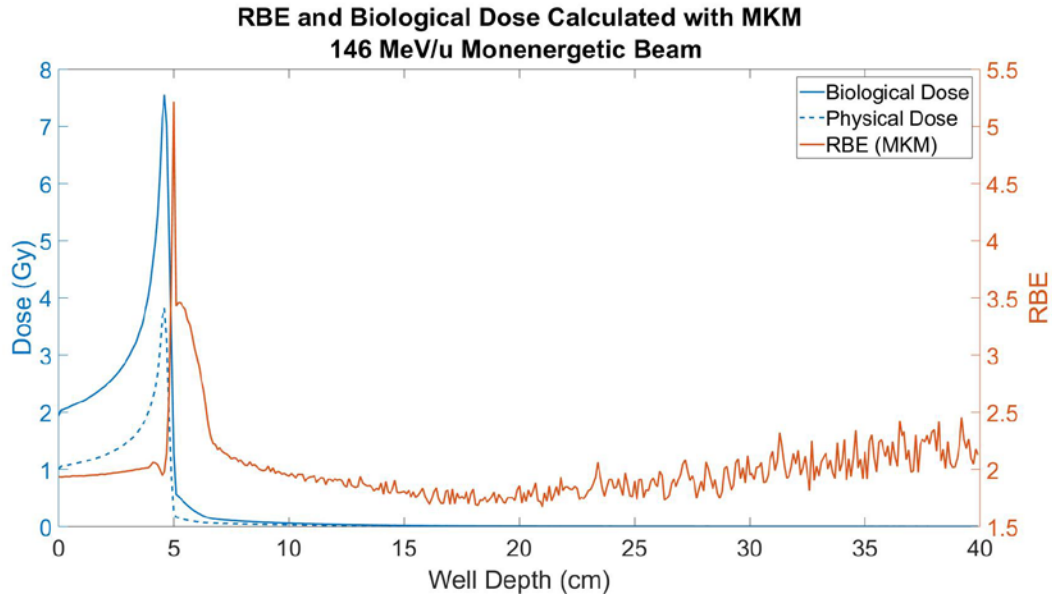


Figure 79. RBE and biological dose calculated with MKM for 146 MeV/u monoenergetic beam.

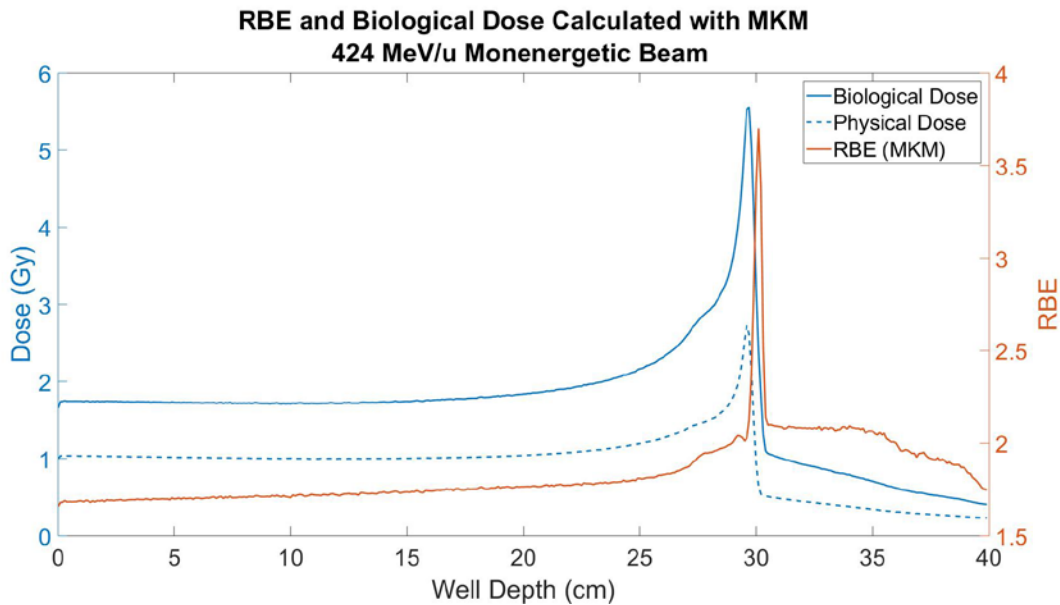


Figure 80. RBE and biological dose calculated with MKM for 424 MeV/u monoenergetic beam.

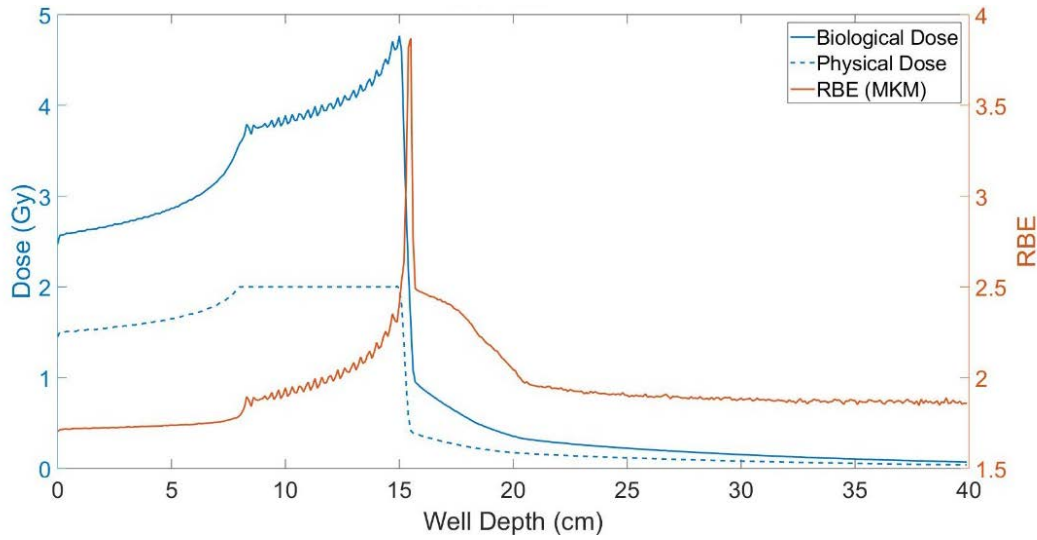


Figure 81. RBE and biological dose calculated with MKM for 7 cm SOBP.

3.3.2.1.1 Propagated Uncertainty

As there is a direct link between y^* and RBE_{MKM} there is no uncertainty introduced through the estimation of RBE. There is, however, physical noise based uncertainty that is introduced. The propagated bias resulting from each of the systematic sources of noise is detailed in , with the true RBE plotted in orange for reference.

Table 27 and is broken down by bias introduced by each source, as well as total bias. The bias was low in the entrance and Bragg peak regions, and did not exceed 2.8%. The bias introduced in the 424 MeV/u monoenergetic beam was, on average, roughly 1% higher than the bias introduced to 146 MeV/u or 7 cm SOBP beam. The pulse pile-up was the greatest contributor to the overall bias for this model. The RBE with bias is shown against purely Monte Carlo calculated RBE in Table 27 for reference. The variance is similarly presented in Table 28. The variance in MKM due to all of the noise sources summed in quadrature was,

at most, 2.2%. The variance in the 146 MeV/u monoenergetic beam was typically 25% higher than that of the other beams. Error bars corresponding to the 1σ standard deviation about the perturbed RBE are shown in Figure 82 - Figure 83, with the true RBE plotted in orange for reference.

Table 27. Displays the bias introduced into calculated RBE_{MKM} by each source of uncertainty.

Beam	Bias Source	Percent Difference (%)					
		Entrance	Avg.	Max.	Bragg Peak	Avg.	Max.
146 MeV/u Monoenergetic	W-Value	0.28	0.28	0.29	0.20		
	Low Energy Cutoff	<0.01	<0.01	<0.01	<0.01		
	Pulse Pile-up	1.49	1.47	1.49	0.89		
	Wall Effect	0.01	0.01	0.02	0.02		
	Total Bias	1.78	1.76	1.79	1.11		
424 MeV/u Monoenergetic	W-Value	0.36	0.37	0.44	0.37		
	Low Energy Cutoff	<0.01	<0.01	<0.01	<0.01		
	Pulse Pile-up	1.00	0.94	1.01	0.92		
	Wall Effect	0.11	0.89	1.36	1.30		
	Total Bias	1.54	2.29	2.79	2.67		
7 cm SOBP	W-Value	0.37	0.38	0.41	0.36	0.41	4.53
	Low Energy Cutoff	<0.01	<0.01	<0.01	<0.01	<0.01	<0.01
	Pulse Pile-up	0.94	0.94	0.95	0.71	0.74	0.87
	Wall Effect	0.05	0.95	0.18	0.35	0.36	0.63
	Total Bias	1.36	1.42	1.54	1.41	1.51	1.67

Table 28. Variance introduced into calculated RBE_{MKM} by each source of uncertainty.

Beam	Source	1 σ Standard Deviation (%)					
		Entrance	Avg.	Max.	Bragg Peak	Avg.	Max.
146 MeV/u Monoenergetic	Counting Statistics	0.04	0.04	0.20	0.01		
	Mean Chord Length	0.13	0.13	0.14	0.10		
	Electronic Noise	0.33	0.32	0.34	0.13		
	Gain Instability	0.01	0.02	0.02	0.01		
	W-Value	2.10	2.09	2.12	1.65		
	Low Energy Cutoff	<0.01	<0.01	<0.01	<0.01		
	Pulse Pile-up	0.02	0.02	0.02	<0.01		
	Wall Effect	<0.01	<0.01	<0.01	<0.01		
	Total Variance	2.13	2.12	2.15	1.66		
424 MeV/u Monoenergetic	Counting Statistics	0.08	0.09	0.68	0.01		
	Mean Chord Length	0.09	0.10	0.11	0.10		
	Electronic Noise	0.08	0.06	0.10	0.14		
	Gain Instability	0.01	0.01	0.01	0.01		
	W-Value	1.45	1.55	1.83	1.68		
	Low Energy Cutoff	<0.01	<0.01	<0.01	<0.01		
	Pulse Pile-up	<0.01	0.04	0.04	0.01		
	Wall Effect	0.01	0.05	0.07	0.05		
	Total Variance	1.46	1.56	1.86	1.69		
7 cm SOBP	Counting Statistics	0.07	0.10	0.26	0.08	0.11	0.66
	Mean Chord Length	0.09	0.09	0.09	0.09	0.09	0.09
	Electronic Noise	0.07	0.06	0.09	0.03	0.04	0.06
	Gain Instability	0.01	0.01	0.01	0.01	0.01	0.01
	W-Value	1.45	1.46	1.48	1.50	1.49	1.52

	Low Energy Cutoff	<0.01	<0.01	<0.01	<0.01	<0.01	<0.01
	Pulse Pile-up	0.01	0.07	0.07	0.05	0.05	0.06
	Wall Effect	<0.01	0.01	0.01	0.02	0.02	0.04
	Total Variance	1.46	1.47	1.51	1.51	1.50	1.66

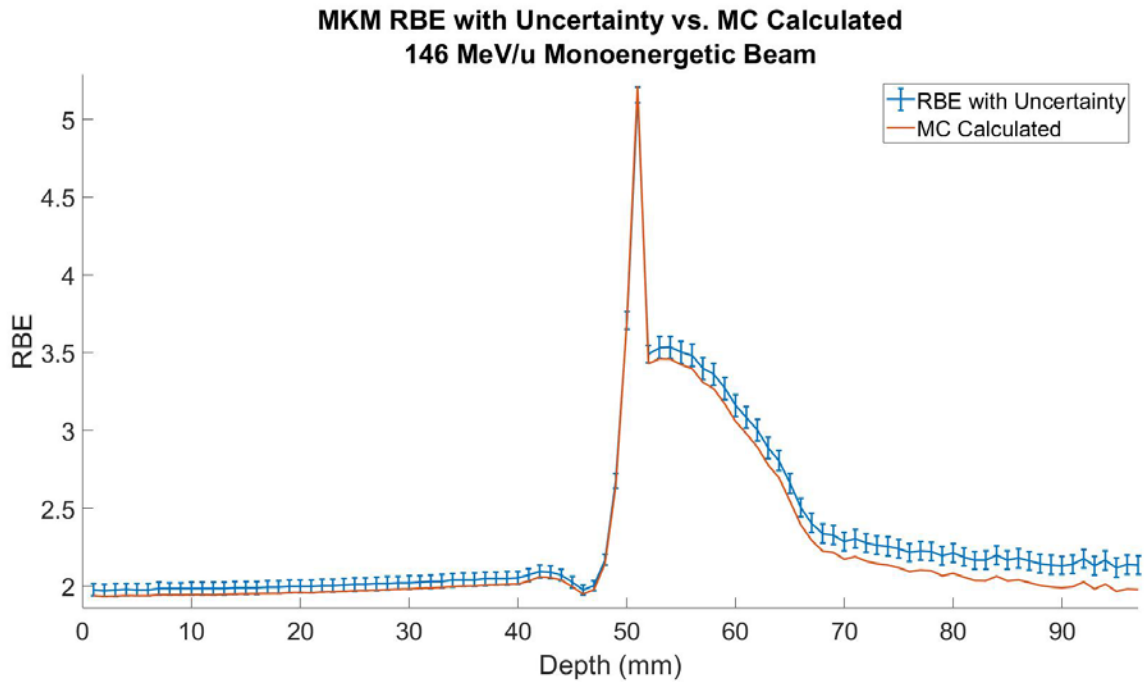


Figure 84. RBE_{MKM} with added bias (blue line) and uncertainty (error bars) as a function of depth for 146 MeV/u monoenergetic beam. Monte Carlo calculated RBE shown in orange.

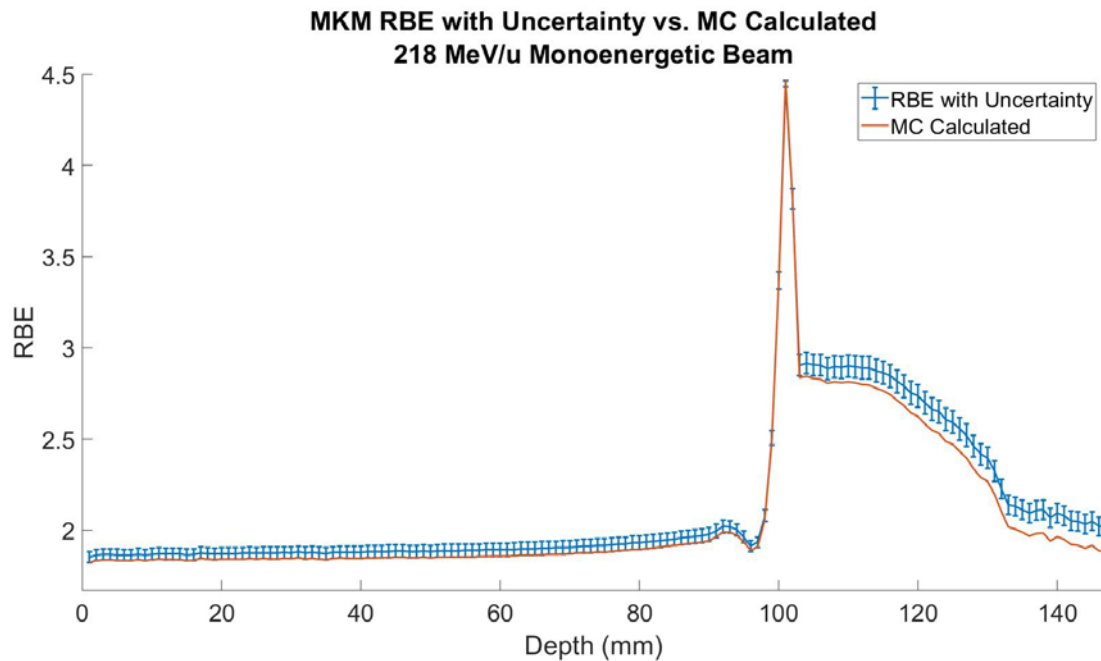


Figure 85. RBE_{MKM} with added bias (blue line) and uncertainty (error bars) as a function of depth for 218 MeV/u monoenergetic beam. Monte Carlo calculated RBE shown in orange.

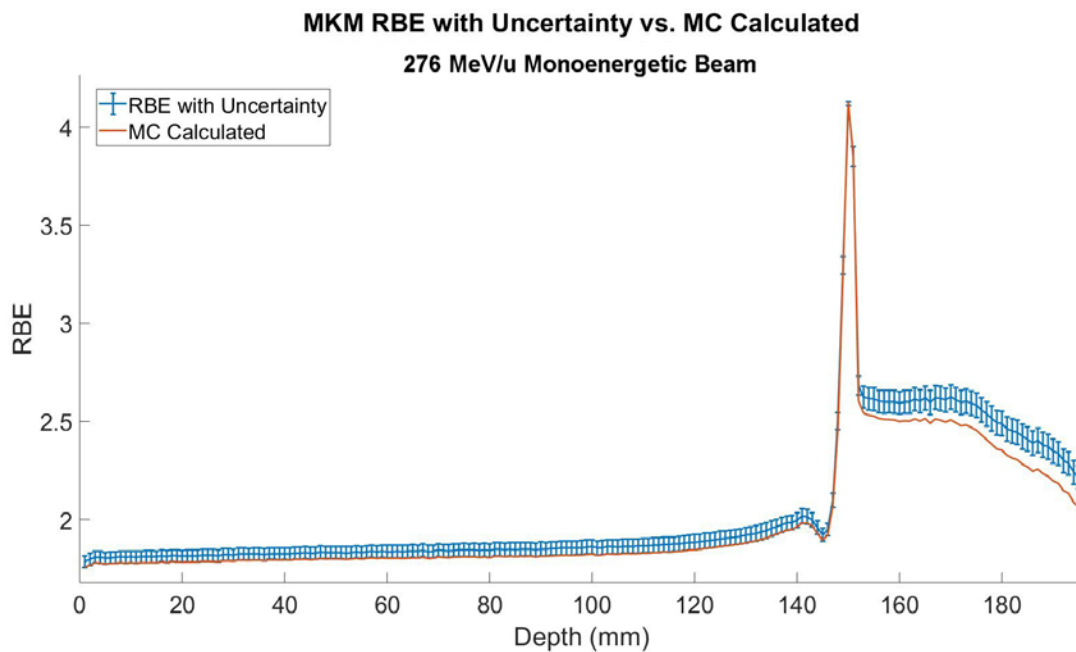


Figure 86. RBE_{MKM} with added bias (blue line) and uncertainty (error bars) as a function of depth for 276 MeV/u monoenergetic beam. Monte Carlo calculated RBE shown in orange.

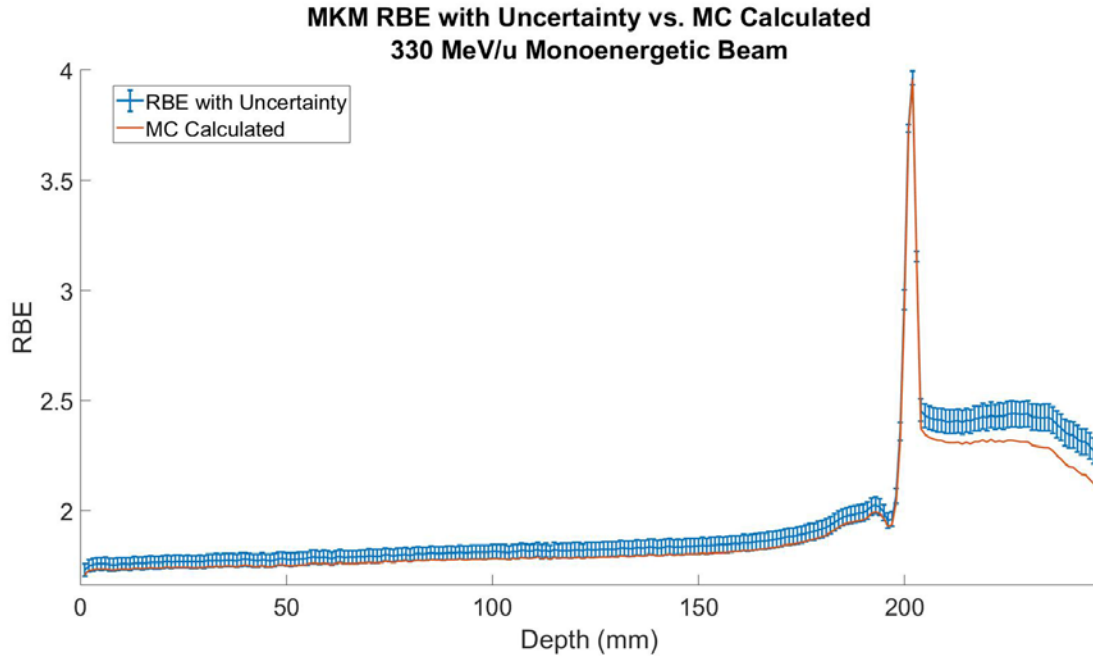


Figure 87. RBE_{MKM} with added bias (blue line) and uncertainty (error bars) as a function of depth for 330 MeV/u monoenergetic beam. Monte Carlo calculated RBE shown in orange.

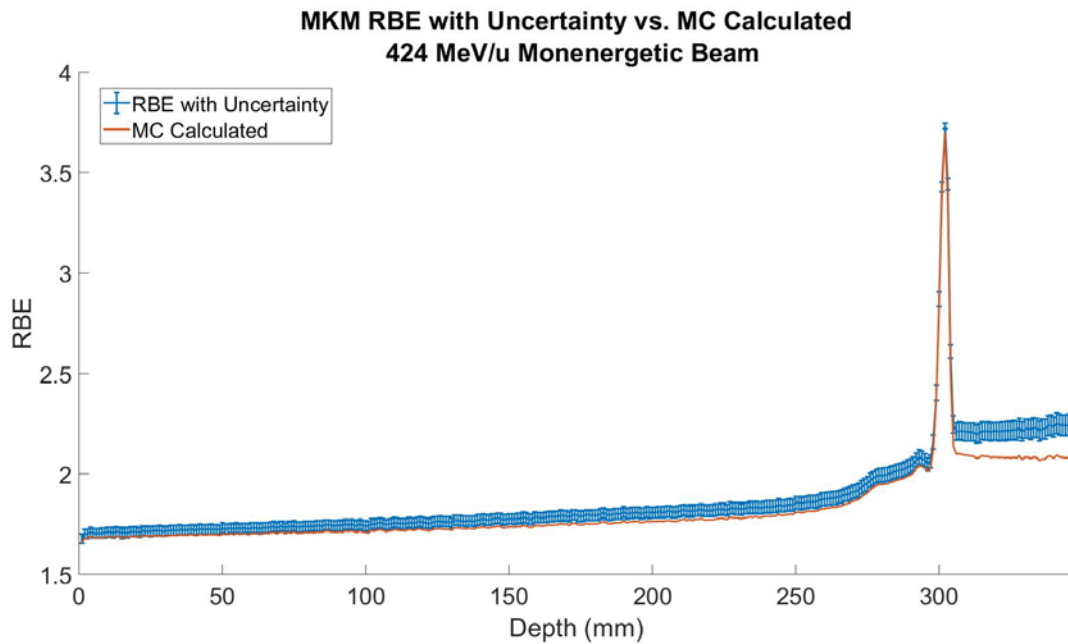


Figure 88. RBE_{MKM} with added bias (blue line) and uncertainty (error bars) as a function of depth for 424 MeV/u monoenergetic beam. Monte Carlo calculated RBE shown in orange.

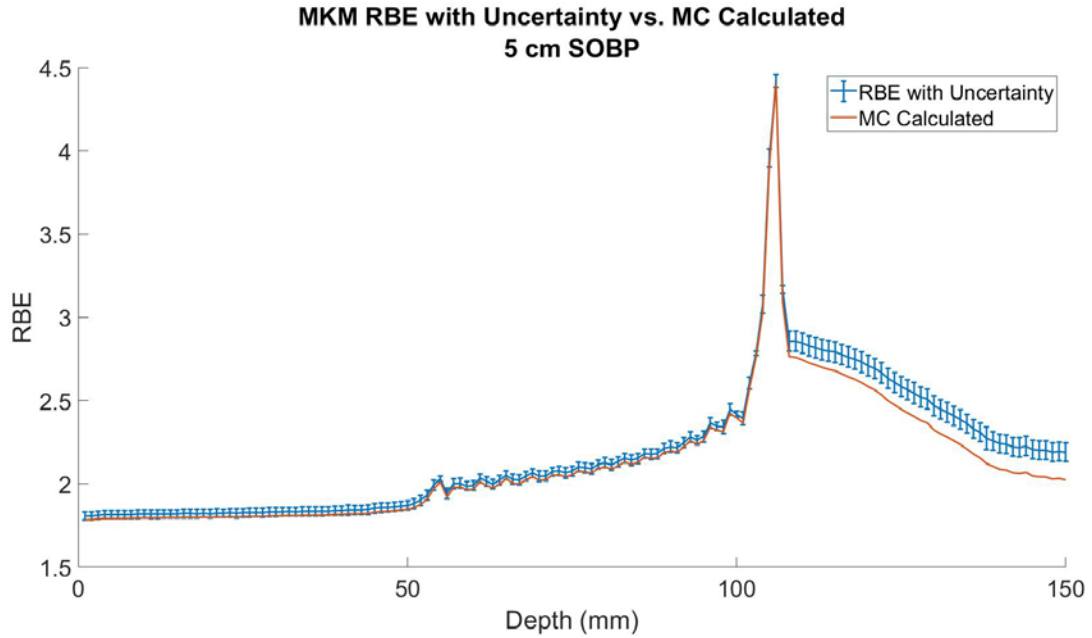


Figure 89. RBE_{MKM} with added bias (blue line) and uncertainty (error bars) as a function of depth for a 5 cm SOBP. Monte Carlo calculated RBE shown in orange.

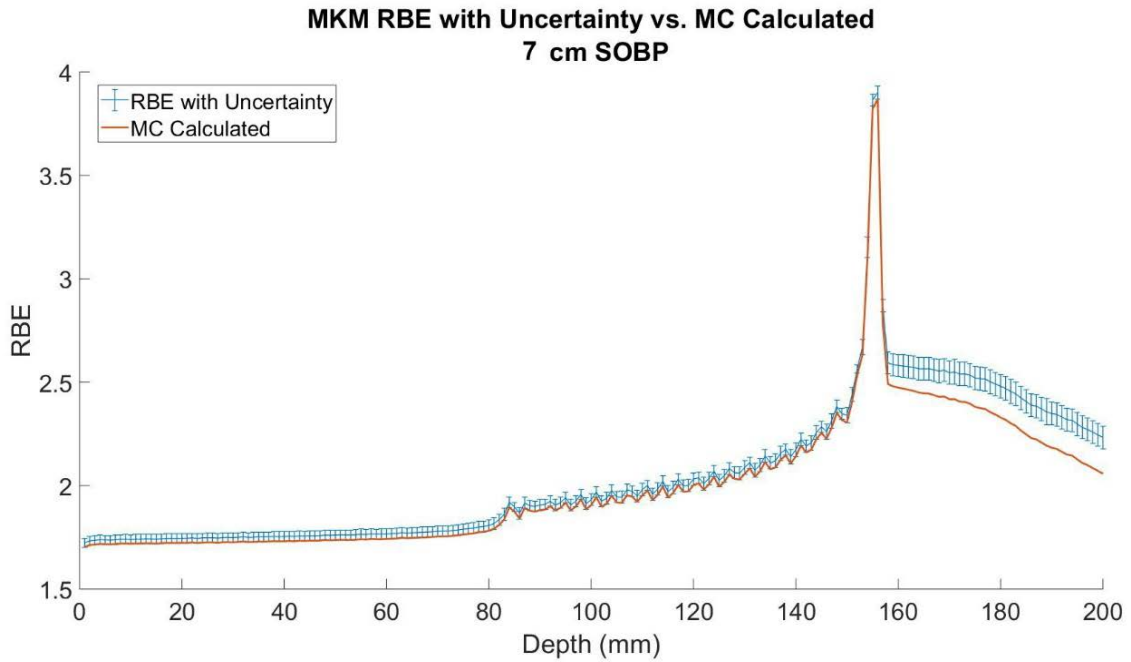


Figure 90. RBE_{MKM} with added bias (blue line) and uncertainty (error bars) as a function of depth for a 7 cm SOBP. Monte Carlo calculated RBE shown in orange.

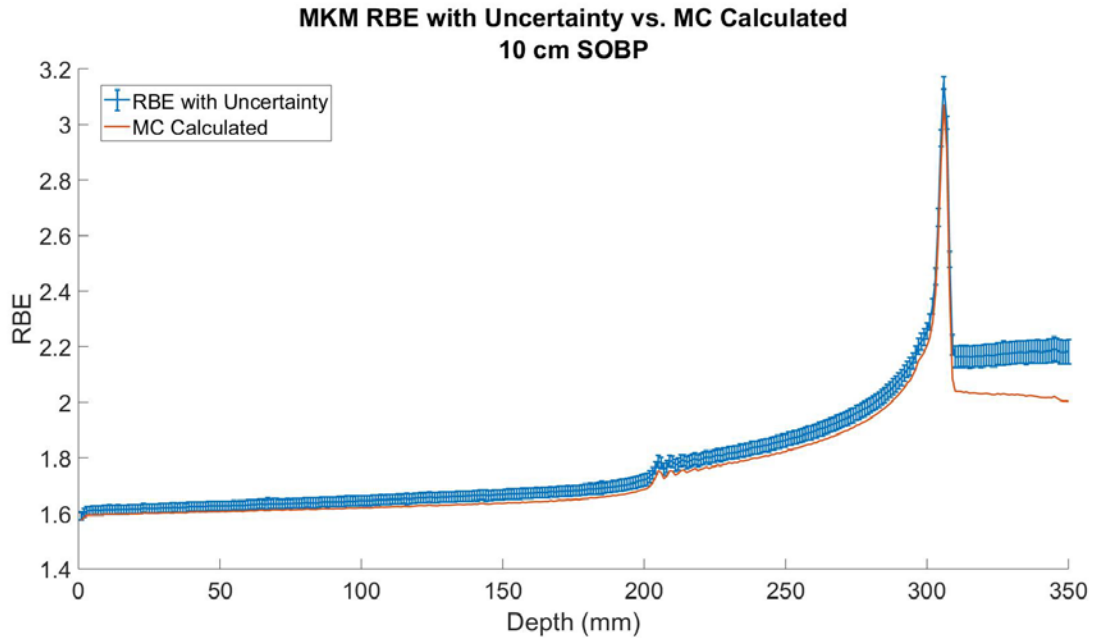


Figure 91. RBE_{MKM} with added bias (blue line) and uncertainty (error bars) as a function of depth for a 10 cm SOBP. Monte Carlo calculated RBE shown in orange.

3.3.2.1.2 All Uncertainty

The total uncertainty produced by each of the sources is shown in Table 29 for direct comparison across uncertainty introduced by both bias and variance.

Table 29. Total uncertainty introduced in RBE_{MKM} by physical measurement based noise.

Beam	Uncertainty Source	Entrance	Avg.	Max.	Bragg Peak	Avg.	Max.
146 MeV/u Monoenergetic	Bias (% Difference)	1.78	1.76	1.79	1.11		
	Variance (% St. Dev., 1σ)	2.13	2.12	2.15	1.66		
424 MeV/u Monoenergetic	Bias (% Difference)	1.54	2.29	2.79	2.67		
	Variance (% St. Dev., 1σ)	1.46	1.56	1.86	1.69		
7 cm SOBP	Bias (% Difference)	1.36	1.42	1.54	1.41	1.51	1.67
	Variance (% St. Dev., 1σ)	1.46	1.47	1.51	1.51	1.50	1.66

3.3.3 RMF

3.3.3.1 Calculation

Plots of RBE and biological dose are plotted as functions of depth and initial beam energy for a 146 MeV/u monoenergetic beam, a 424 MeV/u monoenergetic beam, and a 7 cm SOBP respectively in Figure 89 - Figure 91.

Physical dose is represented by the dashed line for reference.

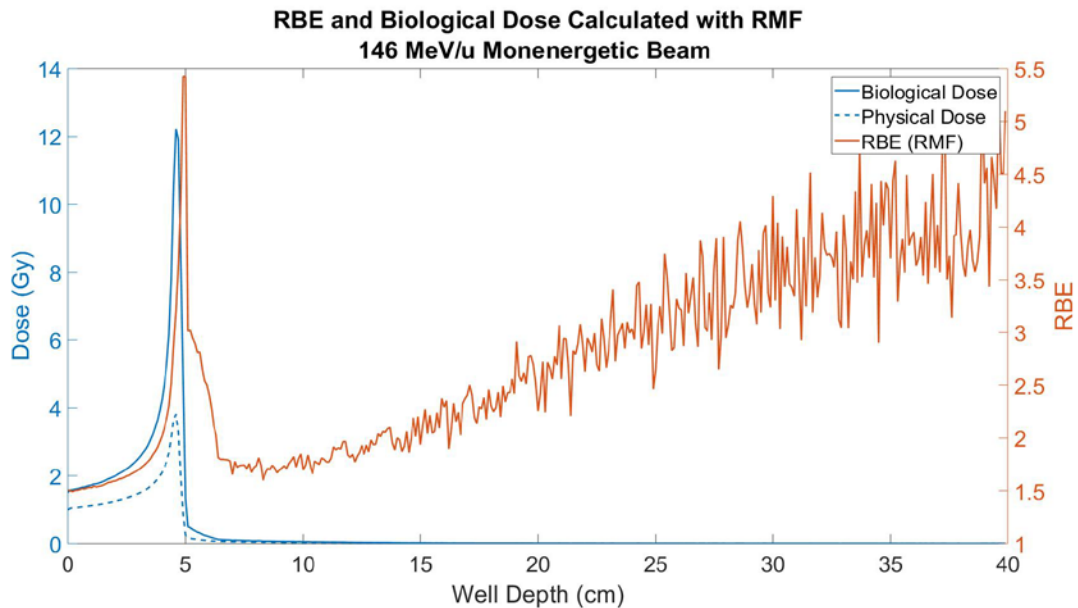


Figure 92. RBE (right axis) and biological dose (left axis) calculated with RMF for 146 MeV/u monoenergetic beam. Physical dose normalized to 1 Gy at the entrance is plotted in the dotted line for reference.

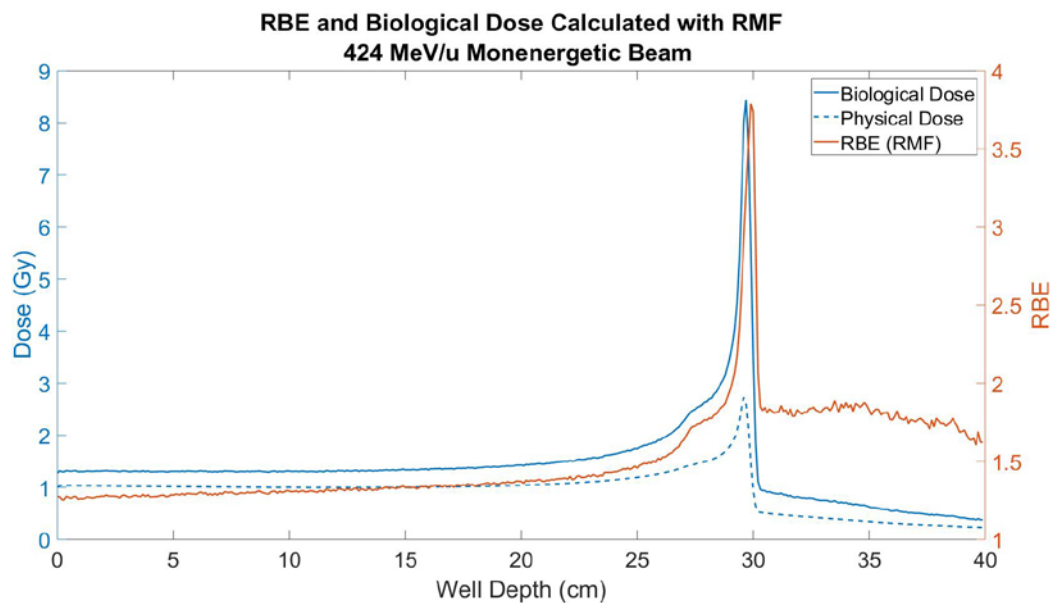


Figure 93. RBE (right axis) and biological dose (left axis) calculated with RMF for 424 MeV/u monoenergetic beam. Physical dose normalized to 1 Gy at the entrance is plotted in the dotted line for reference.

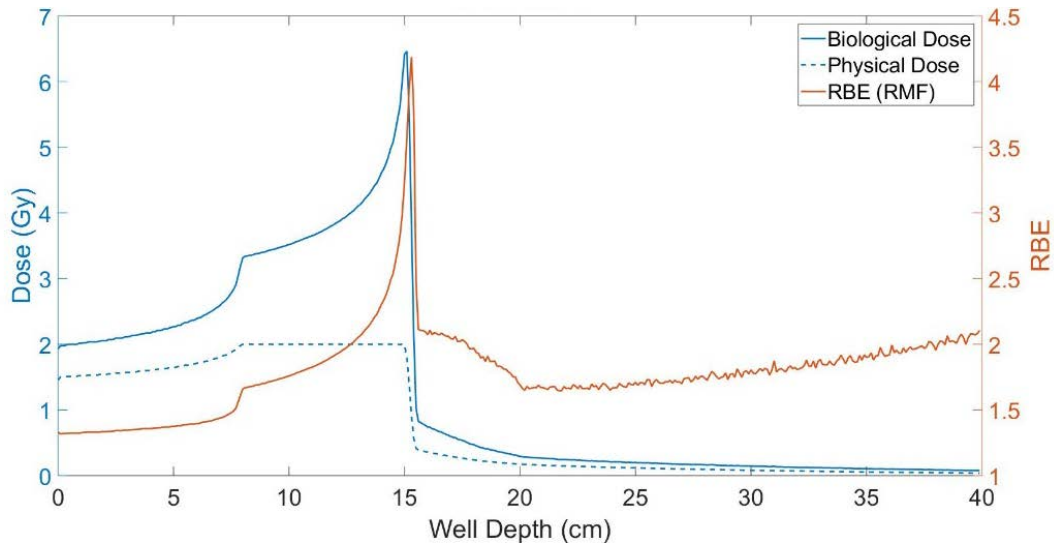


Figure 94. RBE (right axis) and biological dose (left axis) calculated with RMF for 7 cm SOBP. Physical dose normalized to 2 Gy throughout the SOBP is plotted in the dotted line for reference.

3.3.3.2 Estimation

The error induced by estimating RBE_{RMF} through polynomial fitting of alpha and beta is described with a percent difference from the original RBE. This percent difference is shown in Table 30 for an entrance point, 2 cm, and for the center of the Bragg peak. Additionally, the average and maximum values are presented for both the entrance and Bragg peak regions, as applicable. The estimated and calculated RBE are shown for the entrance through the distal edge of the Bragg peak in Figure 92 - Figure 98. The respective percent difference is shown on the y-axis in these figures. On average, uncertainty introduced by RBE estimation was 2.4% in the entrance region and 1.8% in the Bragg peak region. Maximum estimation uncertainty at any one point did not exceed 10%. A current limitation of the estimation method is that the fit only

applies to the entrance and Bragg peak regions. After this point, the fit is typically off by at least an order of magnitude.

Table 30. Percent difference between RBE calculated by Monte Carlo and RBE calculated by estimation. Results are compared for test data sets (146 MeV/u, 424 MeV/u, 7 cm SOBP) to validation data sets (218 MeV/u, 276 MeV/u, 330 MeV/u, 5 cm SOBP, 10 cm SOBP).

Beam	Percent Difference (%)					
	Entrance	Avg.	Max.	Bragg Peak	Avg.	Max.
146 MeV/u Monoenergetic	2.55	3.20	9.87	1.80		
218 MeV/u Monoenergetic	4.91	3.35	8.68	0.36		
276 MeV/u Monoenergetic	3.50	3.21	7.38	1.93		
330 MeV/u Monoenergetic	3.30	2.23	4.15	0.10		
424 MeV/u Monoenergetic	0.13	-0.40	-5.79	1.95		
5 cm SOBP	1.81	1.87	2.30	1.33	1.99	6.91
7 cm SOBP	-0.34	0.09	1.05	2.81	-0.01	3.37
10 cm SOBP	-4.63	-3.59	-5.14	-2.97	-4.44	-5.78
Average	2.68	2.37	5.55	1.50	2.76	5.35

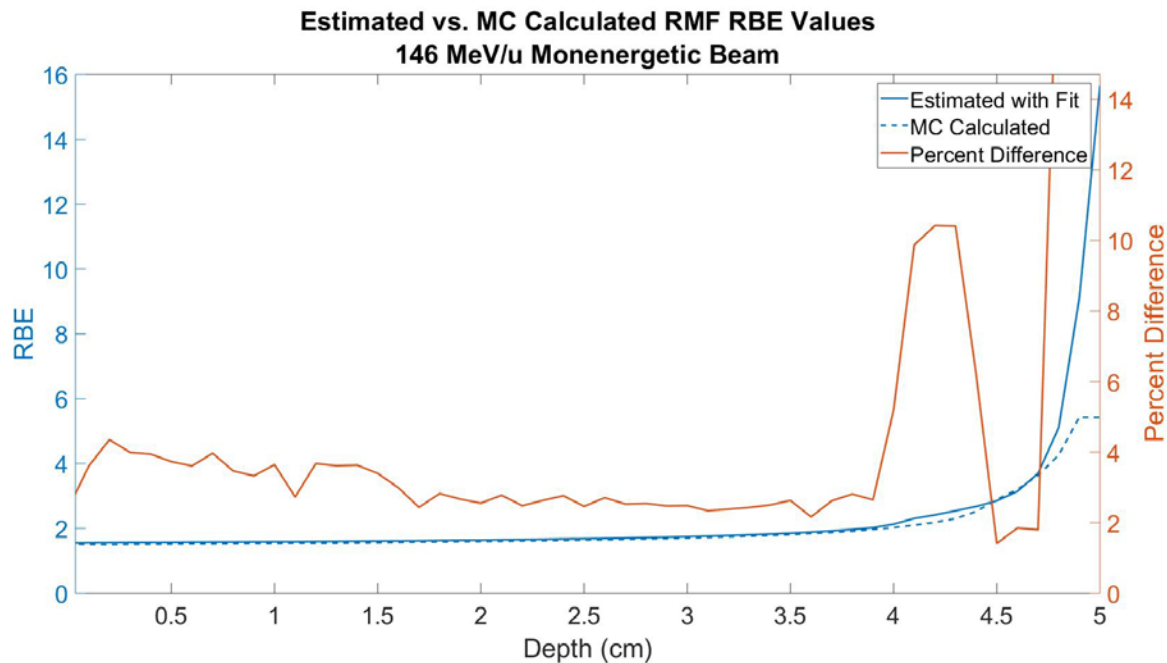


Figure 95. Estimated and Monte Carlo calculated RBE_{RMF} values for a 146 MeV/u monoenergetic beam. Percent difference between the two values is shown on the right axis.

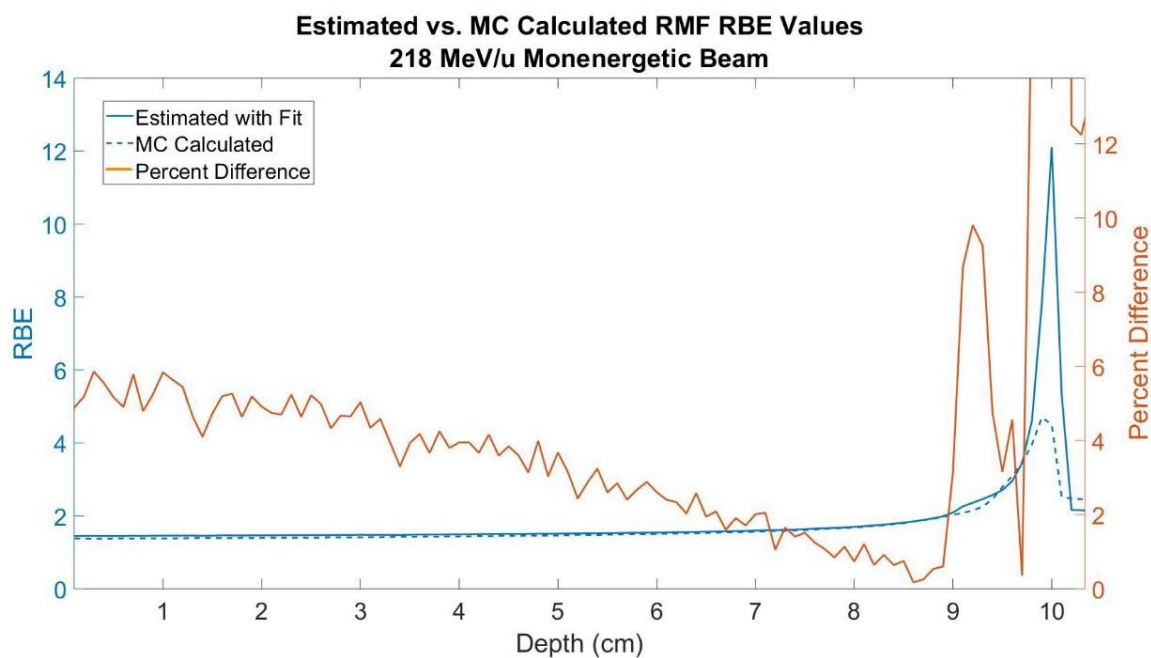


Figure 96. Estimated and Monte Carlo calculated RBE_{RMF} values for a 218 MeV/u monoenergetic beam. Percent difference between the two values is shown on the right axis.

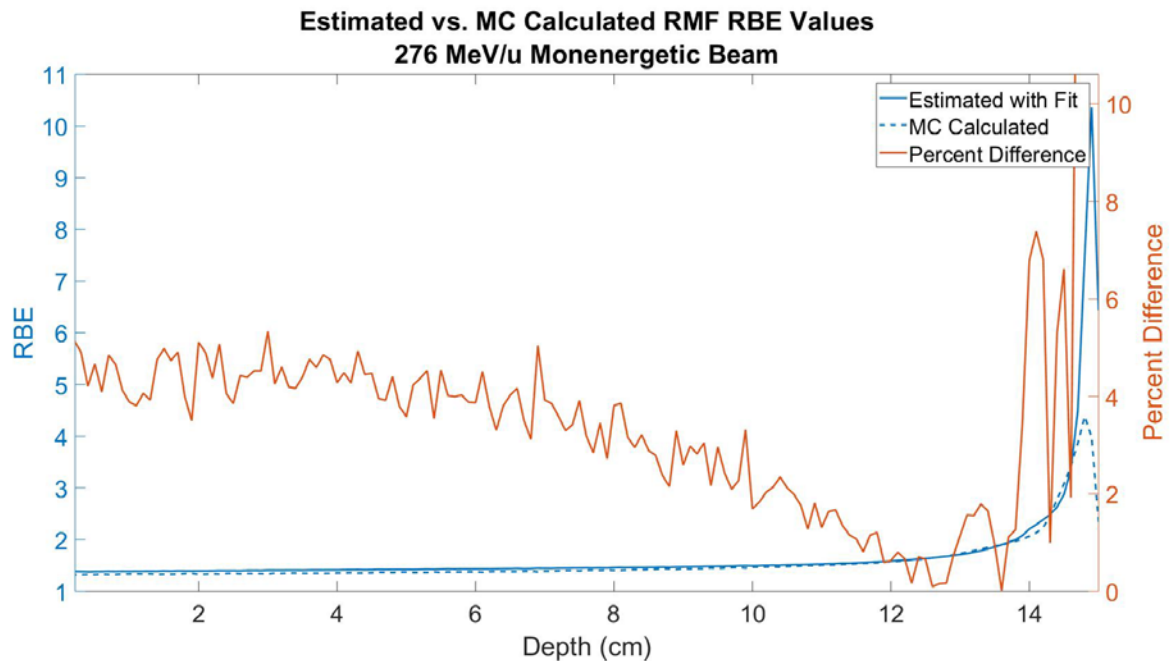


Figure 97. Estimated and Monte Carlo calculated RBE_{RMF} values for a 276 MeV/u monoenergetic beam. Percent difference between the two values is shown on the right axis.

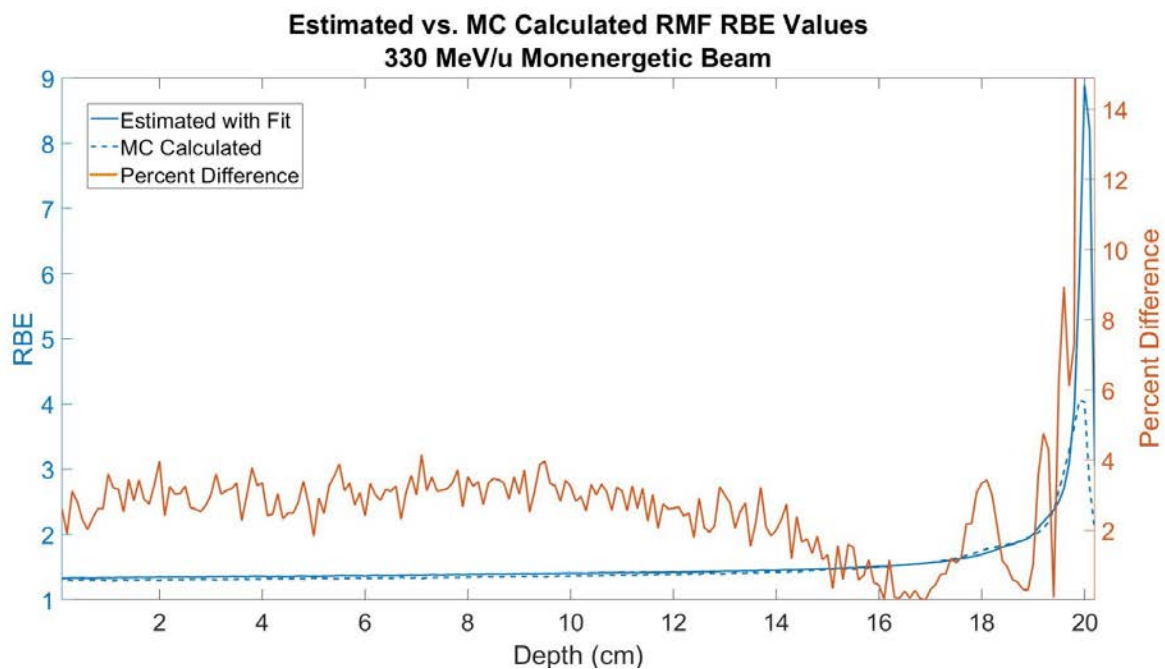


Figure 98. Estimated and Monte Carlo calculated RBE_{RMF} values for a 330 MeV/u monoenergetic beam. Percent difference between the two values is shown on the right axis.

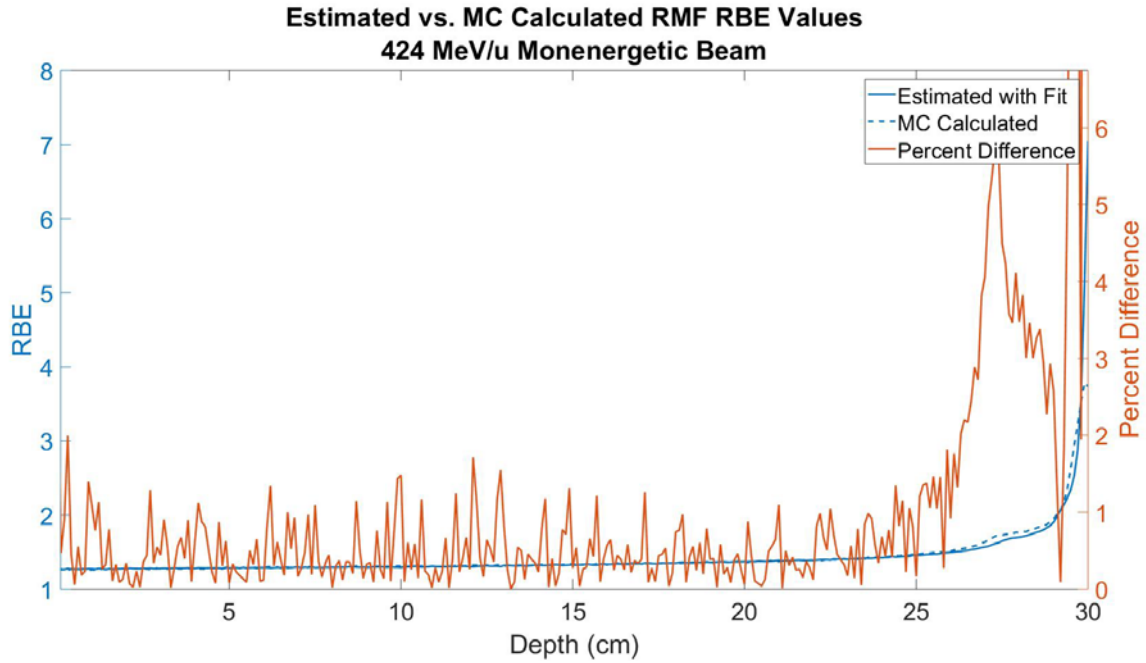


Figure 99. Estimated and Monte Carlo calculated RBE_{RMF} values for a 424 MeV/u monoenergetic beam. Percent difference between the two values is shown on the right axis.

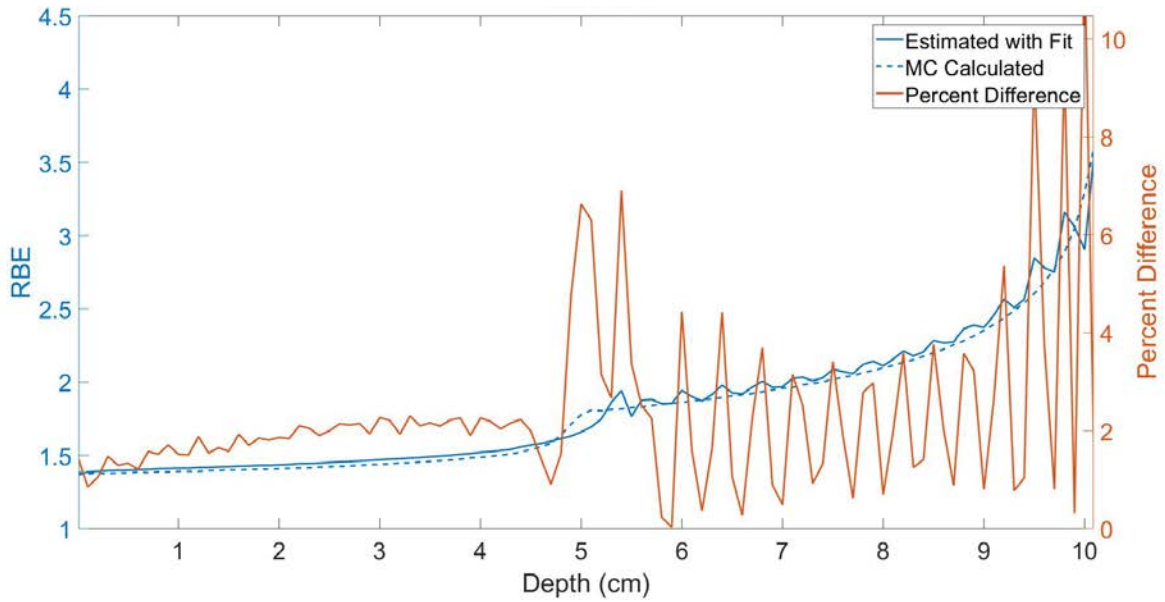


Figure 100. Estimated and Monte Carlo calculated RBE_{LEM} values for a 5 cm SOBP. Percent difference between the two values is shown on the right axis.

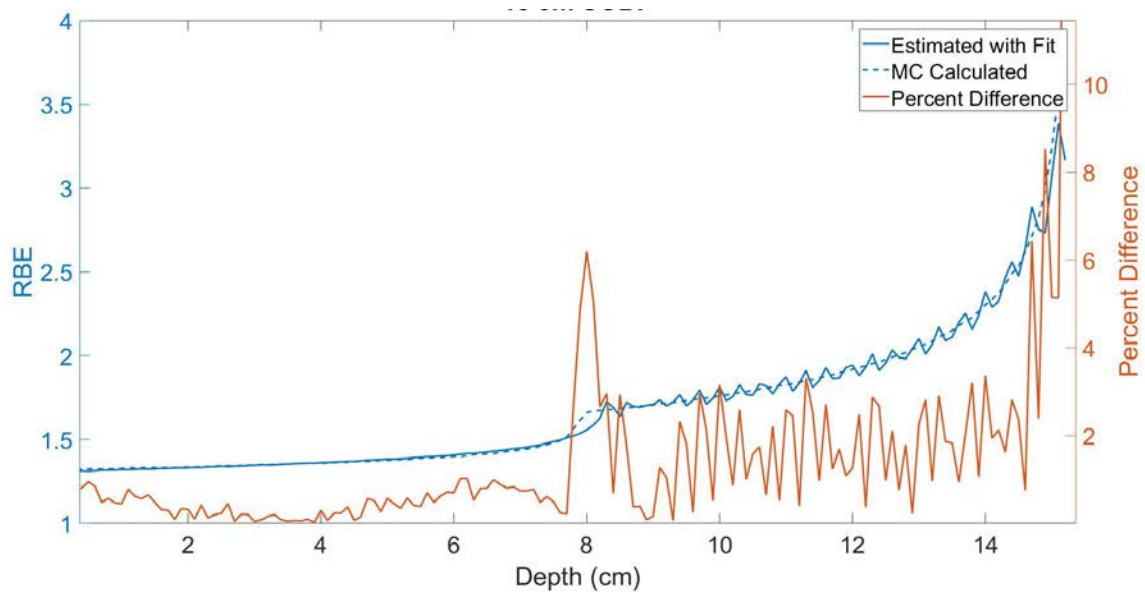


Figure 101. Estimated and Monte Carlo calculated RBE_{LEM} values for a 7 cm SOBP. Percent difference between the two values is shown on the right axis.

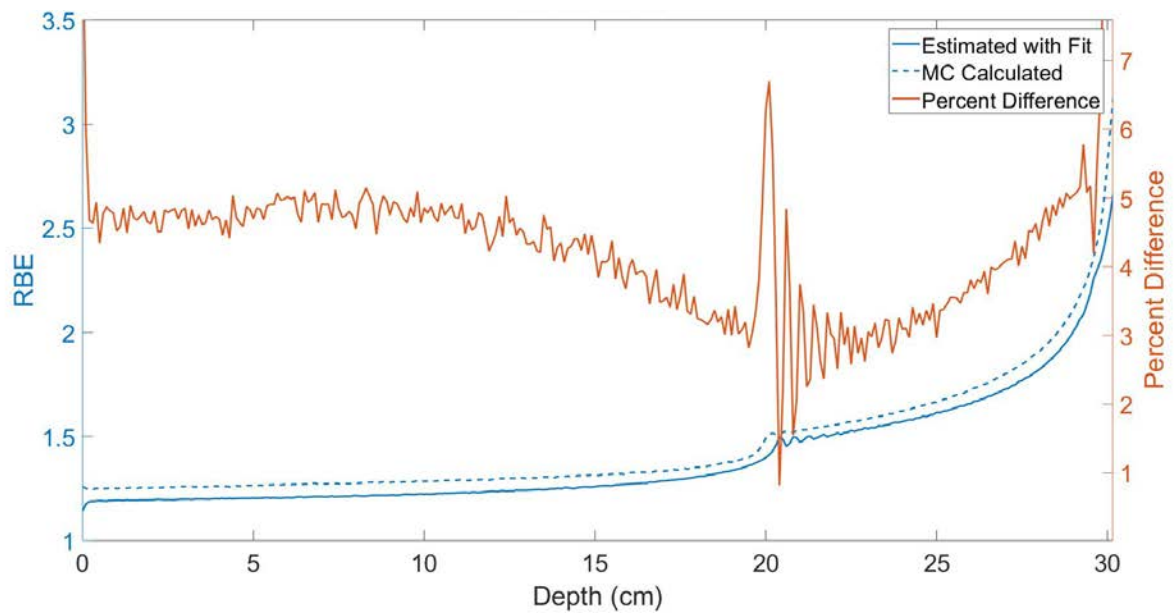


Figure 102. Estimated and Monte Carlo calculated RBE_{LEM} values for a 10 cm SOBP.

3.3.3.3 Propagated Uncertainty

The method of estimating RBE was integrated with the uncertainty in the underlying microdosimetric calculations, and subsequently accounted for in error quantification. Figure 100 - Figure 107 show the estimated RBE with incorporated bias against the true RBE calculated with Monte Carlo. The highest absolute difference introduced independently by a source was 3.6%, contributed by pulse pile-up in the low energy monoenergetic beam. The average bias was just 2.8% throughout all energies, and reached 5.4% at most. The bias contributed by W-value calibration alone resulted in an average contribution of 1.1%, comprising the majority of the error.

The total variance introduced by all eight uncertainty sources are described with error bars in Figure 100 - Figure 107 representing the 1σ standard deviation. The error bars are centered about the estimated RBE with bias, and the true RBE is shown for reference. The largest source of variance was typically due to the W-value and energy calibration, followed by electronic noise and mean chord length, respectively. The variance due to both wall effects and low energy cutoff was typically below 0.01%, however the contribution by the wall effects increased to 0.32% in high energy monoenergetic beams.

Table 31. Bias introduced into calculated RBE_{RMF} by each source of uncertainty, expressed as a percent difference between the shifted and true RBE. Results are compared for test data sets (146 MeV/u, 424 MeV/u, 7 cm SOBP) to validation data sets (218 MeV/u, 276 MeV/u, 330 MeV/u, 5 cm SOBP, 10 cm SOBP).

Beam	Bias Source	Percent Difference (%)					
		Entrance	Avg.	Max.	Bragg Peak	Avg.	Max.
146 MeV/u Monoenergetic	W-Value	0.81	0.85	1.43	1.77		
	Low Energy Cutoff	<0.01	<0.01	<0.01	<0.01		
	Pulse Pile-up	2.10	2.20	3.30	3.61		
	Wall Effect	0.01	0.01	0.03	0.07		
	Total Bias	2.91	3.07	4.76	5.44		
218 MeV/u Monoenergetic	W-Value	0.58	0.73	1.52	1.72		
	Low Energy Cutoff	<0.01	0.03	<0.01	<0.01		
	Pulse Pile-up	1.66	1.75	3.07	3.13		
	Wall Effect	0.04	0.16	0.22	0.27		
	Total Bias	2.28	2.67	4.81	5.12		
276 MeV/u Monoenergetic	W-Value	0.72	0.83	1.66	2.25		
	Low Energy Cutoff	<0.01	<0.01	<0.01	<0.01		
	Pulse Pile-up	1.59	1.63	2.47	2.70		
	Wall Effect	0.08	0.26	0.50	0.65		
	Total Bias	2.39	2.72	4.63	5.61		
330 MeV/u Monoenergetic	W-Value	0.39	0.42	0.83	1.28		
	Low Energy Cutoff	<0.01	<0.01	<0.01	<0.01		
	Pulse Pile-up	1.64	1.53	1.89	2.45		
	Wall Effect	0.12	0.52	0.87	1.22		
	Total Bias	2.15	2.47	3.58	4.95		
424 MeV/u Monoenergetic	W-Value	0.36	0.32	0.38	0.13		
	Low Energy Cutoff	<0.01	<0.01	<0.01	<0.01		

	Pulse Pile-up	1.31	0.94	1.43	0.26		
	Wall Effect	0.10	0.66	0.97	0.48		
	Total Bias	1.77	1.95	2.12	0.86		
5 cm SOBP	W-Value	0.53	0.53	0.57	0.69	0.71	0.92
	Low Energy Cutoff	<0.01	<0.01	<0.01	<0.01	<0.01	<0.01
	Pulse Pile-up	1.90	1.91	1.93	1.77	1.76	1.85
	Wall Effect	0.06	0.06	0.11	0.43	0.49	1.09
	Total Bias	2.48	2.50	2.59	2.89	2.96	3.69
7 cm SOBP	W-Value	0.50	0.67	0.56	0.67	0.66	0.90
	Low Energy Cutoff	<0.01	<0.01	<0.01	<0.01	<0.01	<0.01
	Pulse Pile-up	1.79	1.55	1.83	1.55	1.51	1.60
	Wall Effect	0.10	0.76	0.36	0.76	0.87	1.75
	Total Bias	2.39	2.98	2.75	2.98	3.03	4.25
10 cm SOBP	W-Value	0.46	0.45	0.47	0.47	0.48	0.60
	Low Energy Cutoff	<0.01	<0.01	<0.01	<0.01	<0.01	<0.01
	Pulse Pile-up	1.70	1.55	1.73	1.11	1.11	1.22
	Wall Effect	0.22	1.23	2.02	2.49	2.67	4.38
	Total Bias	2.39	3.24	3.90	4.07	4.25	5.97

Table 32. Variance introduced into calculated RBE_{RMF} by each source of uncertainty, expressed as a percent standard deviation at the 1σ level. Results are compared for test data sets (146 MeV/u, 424 MeV/u, 7 cm SOBP) to validation data sets (218 MeV/u, 276 MeV/u, 330 MeV/u, 5 cm SOBP, 10 cm SOBP).

Beam	Variance Source	1 σ Standard Deviation (%)					
		Entrance	Avg.	Max.	Bragg Peak	Avg.	Max.
146 MeV/u Monoenergetic	Counting Statistics	0.03	0.03	0.14	0.01		
	Mean Chord Length	0.08	0.08	0.08	0.06		
	Electronic Noise	0.31	2.24	0.37	0.10		
	Gain Instability	<0.01	0.01	0.01	0.01		
	W-Value	1.21	1.29	1.29	0.89		
	Low Energy Cutoff	<0.01	<0.01	<0.01	0.01		
	Pulse Pile-up	<0.01	<0.01	<0.01	<0.01		
	Wall Effect	<0.01	<0.01	0.01	0.01		
	Total Variance	1.25	1.24	1.34	0.90		
218 MeV/u Monoenergetic	Counting Statistics	0.06	0.07	0.61	0.04		
	Mean Chord Length	0.14	0.16	0.3	0.38		
	Electronic Noise	0.38	0.42	0.56	0.43		
	Gain Instability	0.02	0.02	0.04	0.05		
	W-Value	2.28	2.65	4.99	6.11		
	Low Energy Cutoff	<0.01	<0.01	<0.01	<0.01		
	Pulse Pile-up	0.03	0.03	0.05	0.03		
	Wall Effect	<0.01	<0.01	0.01	0.01		
	Total Variance	2.31	2.69	5.03	6.14		
276 MeV/u Monoenergetic	Counting Statistics	0.08	0.09	0.77	0.08		
	Mean Chord Length	0.15	0.16	0.32	0.42		
	Electronic Noise	0.29	0.3	0.36	0.2		

	Gain Instability	0.02	0.02	0.04	0.05		
	W-Value	2.41	2.68	5.16	6.82		
	Low Energy Cutoff	<0.01	<0.01	<0.01	<0.01		
	Pulse Pile-up	0.06	0.04	0.06	0.03		
	Wall Effect	<0.01	0.01	0.03	0.04		
	Total Variance	2.43	2.70	5.19	6.83		
330 MeV/u Monoenergetic	Counting Statistics	0.11	0.11	0.49	0.03		
	Mean Chord Length	0.15	0.15	0.22	0.37		
	Electronic Noise	0.23	0.19	0.26	0.03		
	Gain Instability	0.02	0.02	0.03	0.05		
	W-Value	2.59	2.62	3.84	6.45		
	Low Energy Cutoff	<0.01	<0.01	<0.01	<0.01		
	Pulse Pile-up	0.05	0.04	0.07	0.04		
	Wall Effect	0.01	0.03	0.05	0.07		
	Total Variance	2.61	2.63	3.85	6.46		
424 MeV/u Monoenergetic	Counting Statistics	0.01	0.05	0.44	0.01		
	Mean Chord Length	0.06	<0.01	0.02	0.06		
	Electronic Noise	0.06	0.62	0.66	0.29		
	Gain Instability	0.01	0.01	0.01	0.01		
	W-Value	1.05	1.07	1.20	0.92		
	Low Energy Cutoff	<0.01	<0.01	0.02	0.03		
	Pulse Pile-up	<0.01	<0.01	<0.01	0.01		
	Wall Effect	0.01	0.14	0.30	0.32		
	Total Variance	1.22	1.25	1.33	1.02		
5 cm SOBP	Counting Statistics	0.07	0.12	1.26	0.03		
	Mean Chord Length	0.15	0.16	0.17	0.19		
	Electronic Noise	0.26	0.26	0.26	0.04		

	Gain Instability	0.02	0.02	0.02	0.02		
	W-Value	2.62	2.66	2.86	3.17		
	Low Energy Cutoff	<0.01	<0.01	<0.01	<0.01		
	Pulse Pile-up	0.04	0.04	0.05	0.04		
	Wall Effect	<0.01	<0.01	0.01	0.02		
	Total Variance	2.64	2.69	2.95	3.17		
7 cm SOBP	Counting Statistics	0.01	0.04	0.20	0.04	0.06	0.43
	Mean Chord Length	0.06	0.07	0.07	0.07	0.07	0.07
	Electronic Noise	0.62	0.62	0.64	0.65	0.65	0.66
	Gain Instability	0.01	0.01	0.01	0.01	0.01	0.01
	W-Value	1.05	1.06	1.08	1.08	1.08	1.09
	Low Energy Cutoff	<0.01	<0.01	<0.01	<0.01	<0.01	<0.01
	Pulse Pile-up	0.04	0.04	0.04	0.05	0.05	0.05
	Wall Effect	0.01	0.01	0.02	0.05	0.05	0.11
	Total Variance	1.22	1.23	1.27	1.27	1.27	1.35
10 cm SOBP	Counting Statistics	0.23	0.22	2.11	0.06	0.13	1.19
	Mean Chord Length	0.14	0.14	0.14	0.15	0.15	0.20
	Electronic Noise	0.07	0.14	0.19	0.36	0.41	0.83
	Gain Instability	0.02	0.02	0.02	0.02	0.02	0.02
	W-Value	2.25	2.25	2.3	2.37	2.43	3.11
	Low Energy Cutoff	<0.01	<0.01	<0.01	<0.01	<0.01	0.01
	Pulse Pile-up	0.08	0.07	0.10	0.04	0.05	0.07
	Wall Effect	0.01	0.06	0.10	0.13	0.14	0.23
	Total Variance	2.26	2.29	3.09	2.40	2.48	3.41

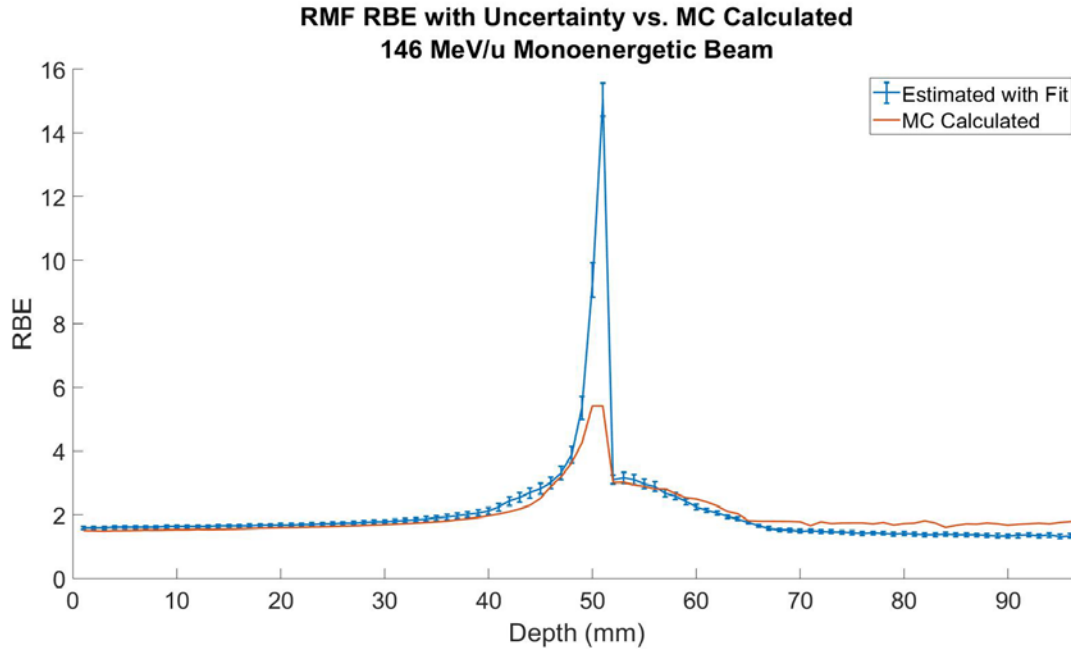


Figure 103. Estimated RBE_{RMF} with added bias (blue line) and uncertainty (error bars) as a function of depth for 146 MeV/u monoenergetic beam. Monte Carlo calculated RBE shown in orange.

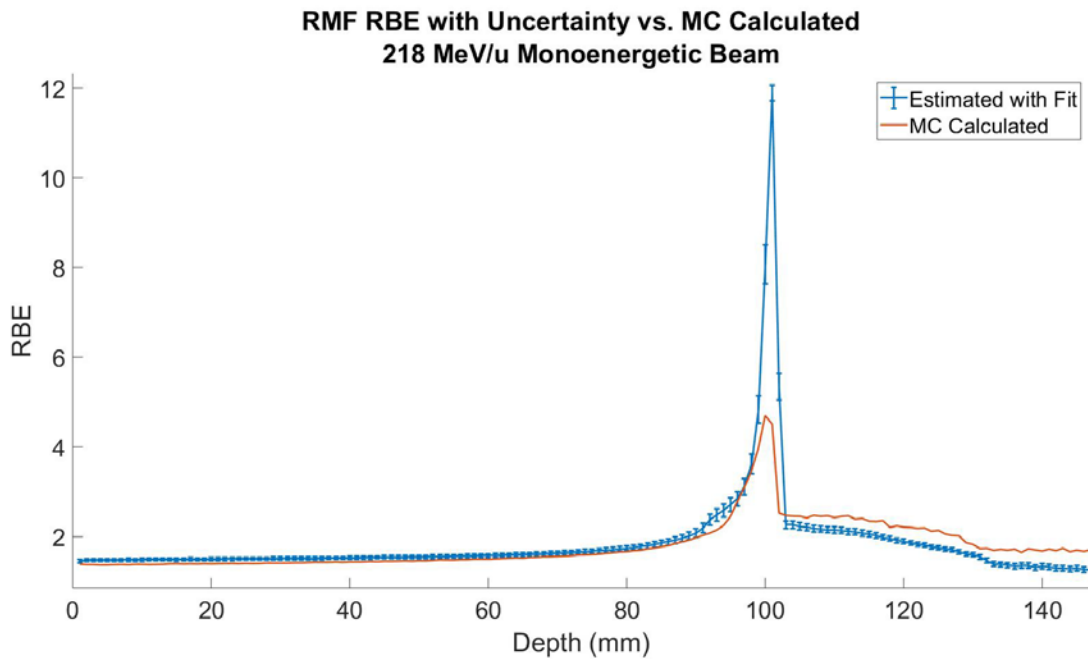


Figure 104. Estimated RBE_{RMF} with added bias (blue line) and uncertainty (error bars) as a function of depth for 218 MeV/u monoenergetic beam. Monte Carlo calculated RBE shown in orange.

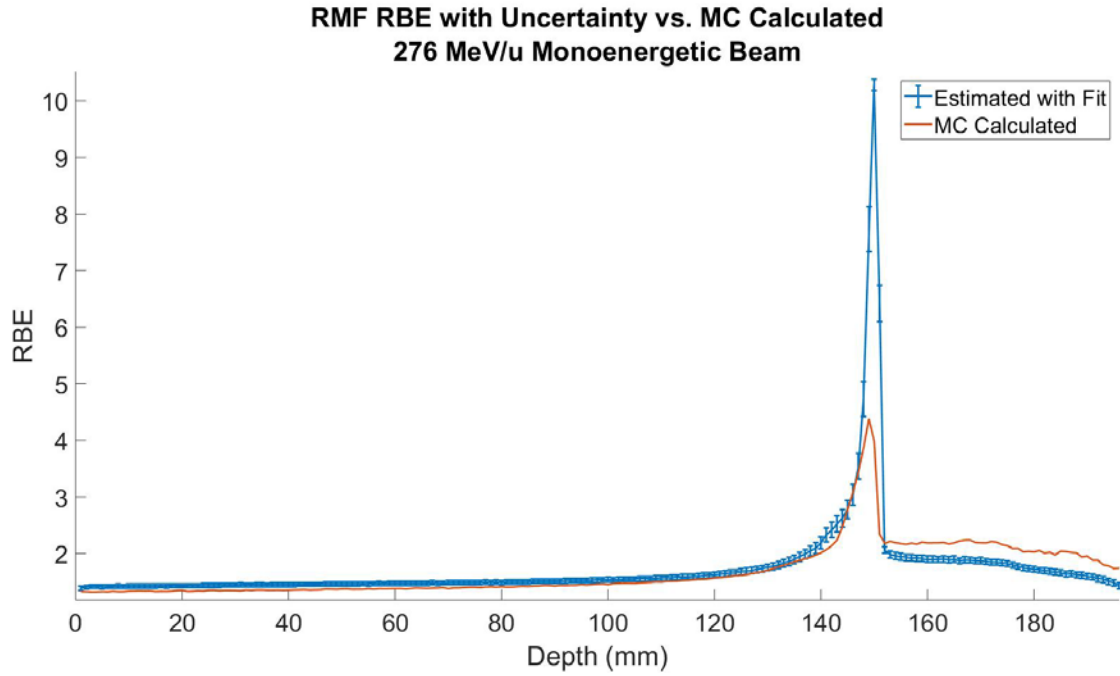


Figure 105. Estimated RBE_{RMF} with added bias (blue line) and uncertainty (error bars) as a function of depth for 276 MeV/u monoenergetic beam. Monte Carlo calculated RBE shown in orange.

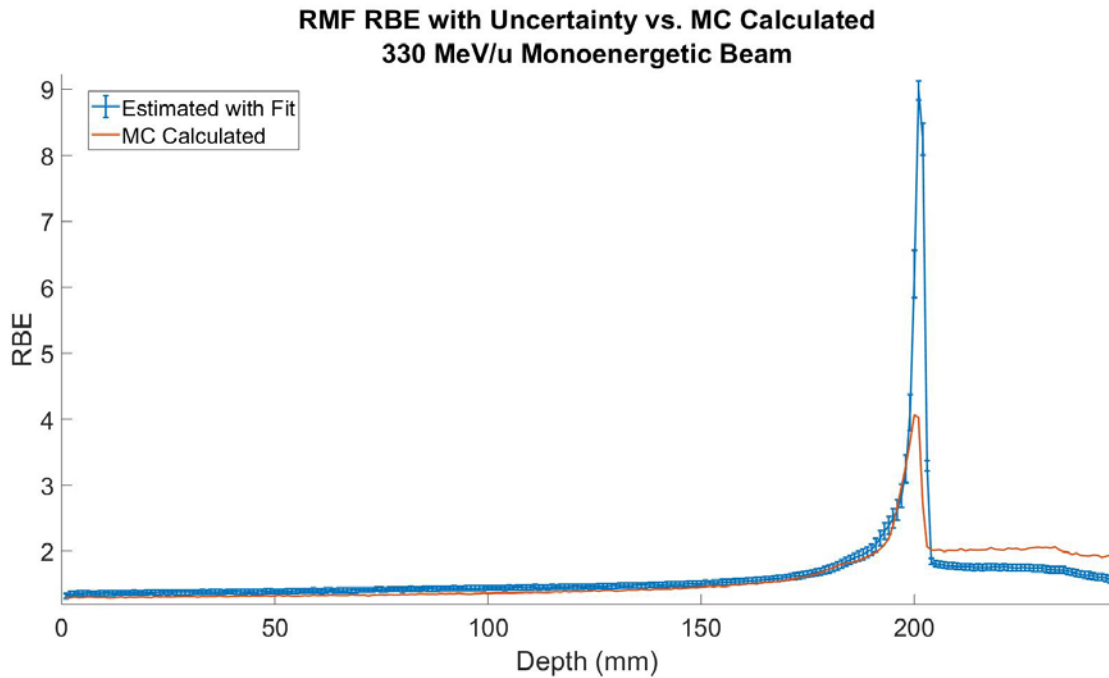


Figure 106. Estimated RBE_{RMF} with added bias (blue line) and uncertainty (error bars) as a function of depth for 330 MeV/u monoenergetic beam. Monte Carlo calculated RBE shown in orange.

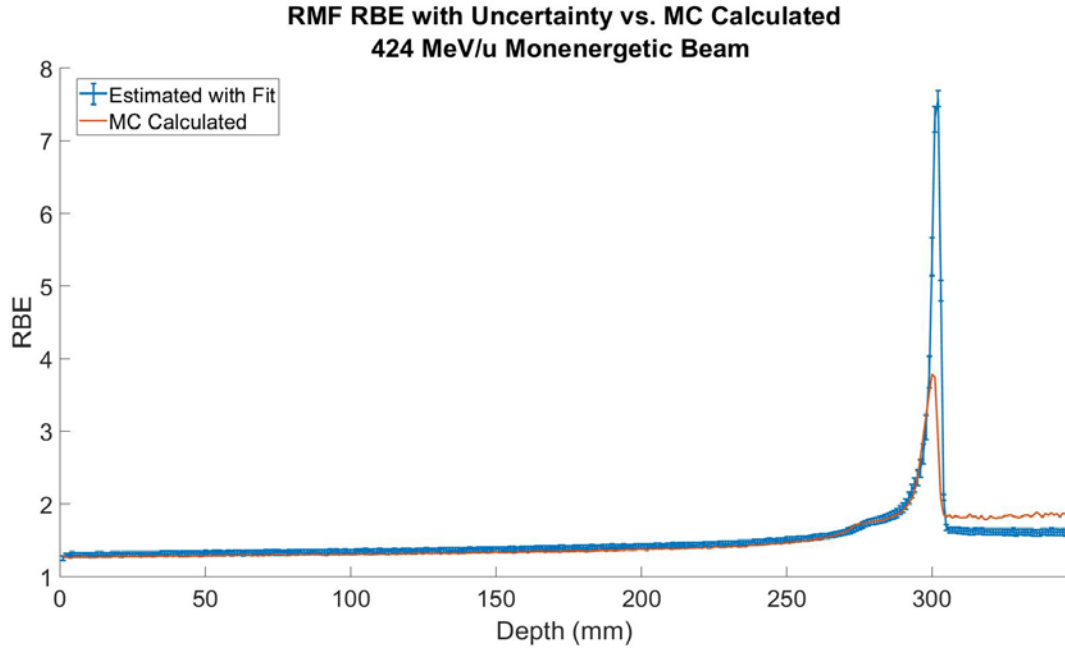


Figure 107. Estimated RBE_{RMF} with added bias (blue line) and uncertainty (error bars) as a function of depth for 424 MeV/u monoenergetic beam. Monte Carlo calculated RBE shown in orange.

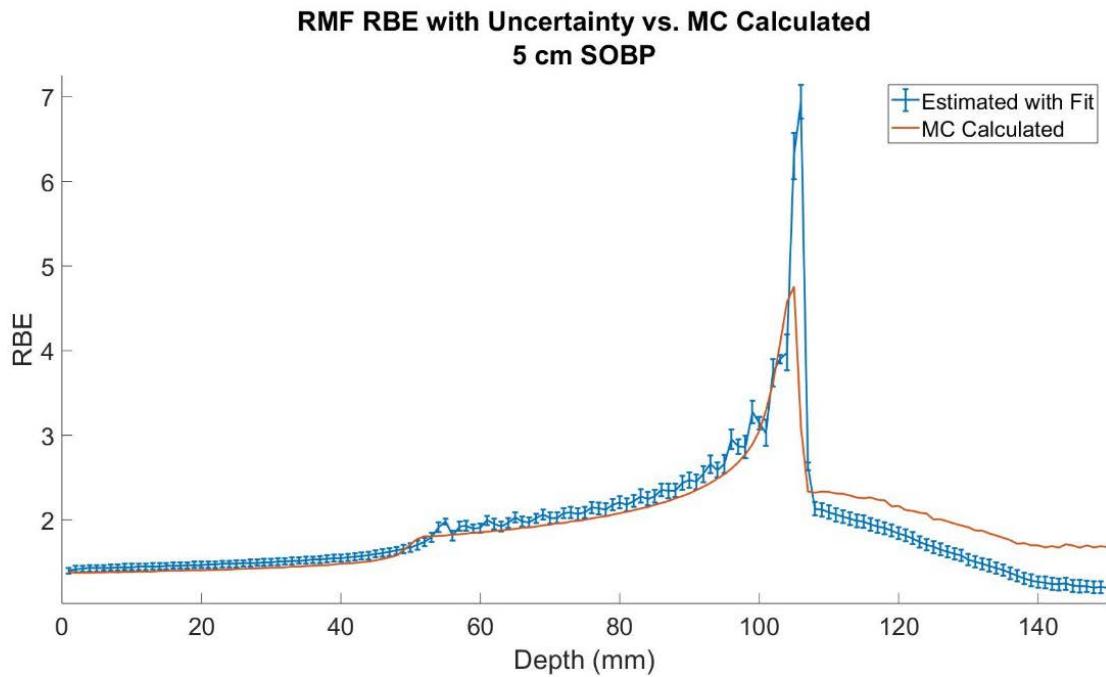


Figure 108. Estimated RBE_{RMF} with added bias (blue line) and uncertainty (error bars) as a function of depth for 5 cm SOBP. Monte Carlo calculated RBE shown in orange.

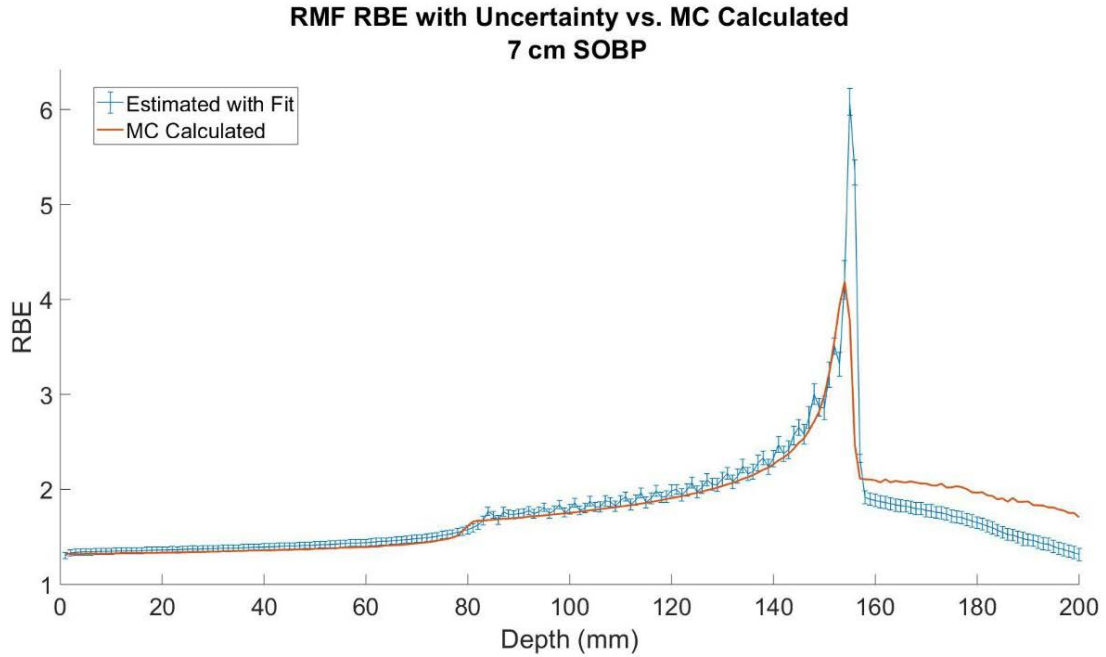


Figure 109. Estimated RBE_{RMF} with added bias (blue line) and uncertainty (error bars) as a function of depth for 7 cm SOBP. Monte Carlo calculated RBE shown in orange.

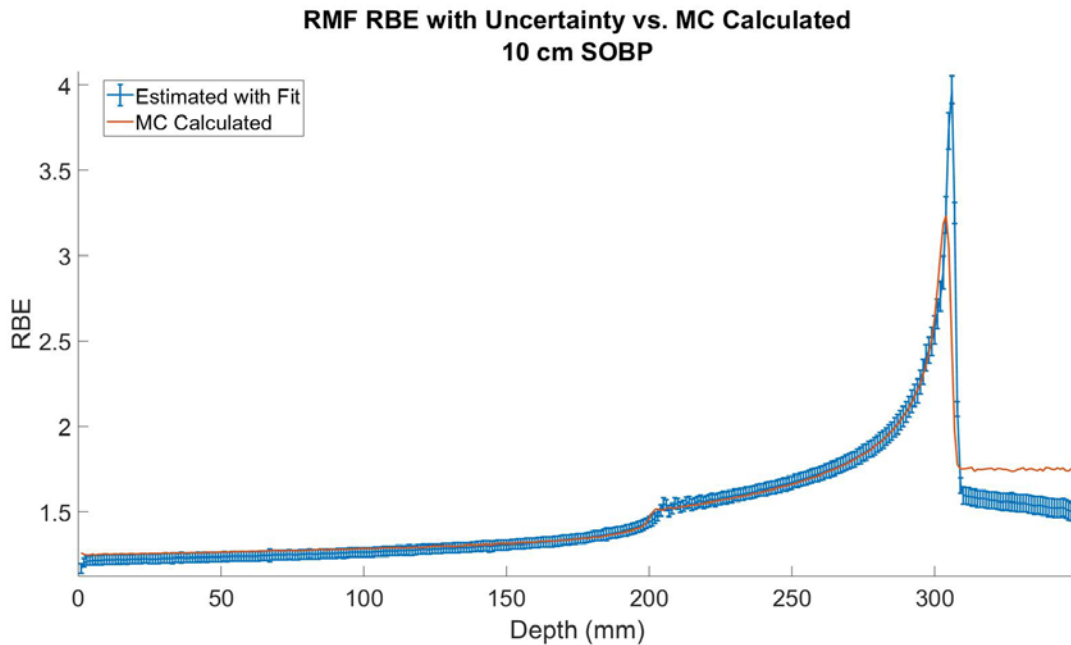


Figure 110. Estimated RBE_{RMF} with added bias (blue line) and uncertainty (error bars) as a function of depth for 10 cm SOBP. Monte Carlo calculated RBE shown in orange.

3.3.3.4 All Uncertainty

Table 33 displays the uncertainty due to the RBE estimation, the bias introduced by the systematic noise sources, and the variance introduced by the random noise. The total bias introduced by each of the four sources resulted in an average increase in RBE by 2.8%. The average uncertainty introduced by the estimation of RBE by RMF was 2.4% across beam energies. The maximum uncertainty due to estimation was found at a depth located 0.5 cm proximally to the Bragg peak for each beam assessed, indicating that there may be a systematic inconsistency here. The maximum uncertainty introduced by the variance in random physical noise was 5.2%, but averaged just 2.1% throughout the range of beams analyzed.

Table 33. Total uncertainty in estimated RBE_{RMF} by each source assessed.

Beam	Uncertainty Source	Entrance	Avg.	Max.	Bragg Peak	Avg.	Max.
146 MeV/u Monoenergetic	Bias (% Difference)	2.91	3.07	4.76	5.44		
	RBE Estimation (% Difference)	2.55	3.20	9.87	1.80		
	Variance (% St. Dev., 1- σ)	1.25	1.24	1.34	0.90		
218 MeV/u Monoenergetic	Bias (% Difference)	2.28	2.67	4.81	5.12		
	RBE Estimation (% Difference)	4.91	3.35	8.68	0.36		
	Variance (% St. Dev., 1- σ)	2.31	2.69	5.03	6.14		
276 MeV/u Monoenergetic	Bias (% Difference)	2.39	2.72	4.63	5.61		
	RBE Estimation (% Difference)	3.50	3.21	7.38	1.93		
	Variance (% St. Dev., 1- σ)	2.43	2.70	5.19	6.83		
330 MeV/u Monoenergetic	Bias (% Difference)	2.15	2.47	3.58	4.95		
	RBE Estimation (% Difference)	3.30	2.46	4.15	0.10		
	Variance (% St. Dev., 1- σ)	2.61	2.63	3.85	6.46		
	Bias	1.77	1.95	2.12	0.86		

424 MeV/u Monoenergetic	(% Difference)						
	RBE Estimation (% Difference)	0.13	-0.4	-5.79	1.95		
	Variance (% St. Dev., 1- σ)	1.22	1.25	1.33	1.02		
5 cm SOBP	Bias (% Difference)	2.48	2.50	2.59	2.89	2.96	3.69
	RBE Estimation (% Difference)	1.81	1.87	2.3	1.33	1.99	6.91
	Variance (% St. Dev., 1- σ)	2.64	2.69	2.95	3.17	2.64	2.69
7 cm SOBP	Bias (% Difference)	2.39	2.98	2.63	2.98	3.03	4.05
	RBE Estimation (% Difference)	-0.34	0.09	1.05	2.81	-0.01	3.37
	Variance (% St. Dev., 1- σ)	1.22	1.23	1.27	1.27	1.27	1.35
10 cm SOBP	Bias (% Difference)	2.39	3.24	3.90	4.07	4.25	5.97
	RBE Estimation (% Difference)	-4.63	-3.59	-5.14	-2.97	-4.44	-5.78
	Variance (% St. Dev., 1- σ)	2.26	2.29	3.09	2.40	2.48	3.41

3.3.4 LEM

3.3.4.1 Calculation

Similarly to those presented by MKM and RMF, the true RBE calculated with Monte Carlo follow in Figure 108 - Figure 110 for the standard energies displayed. Physical dose is shown in each plot for reference.

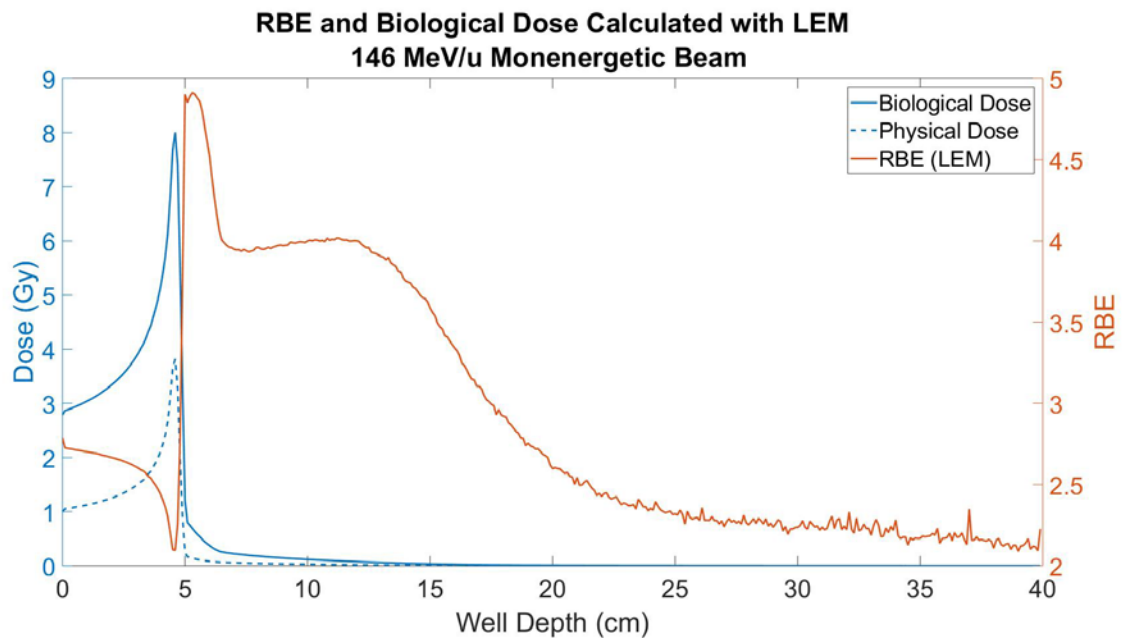


Figure 111. RBE (right axis) and biological dose (left axis) calculated with LEM for 146 MeV/u monoenergetic beam. Physical dose normalized to 1 Gy at the entrance plotted for reference.

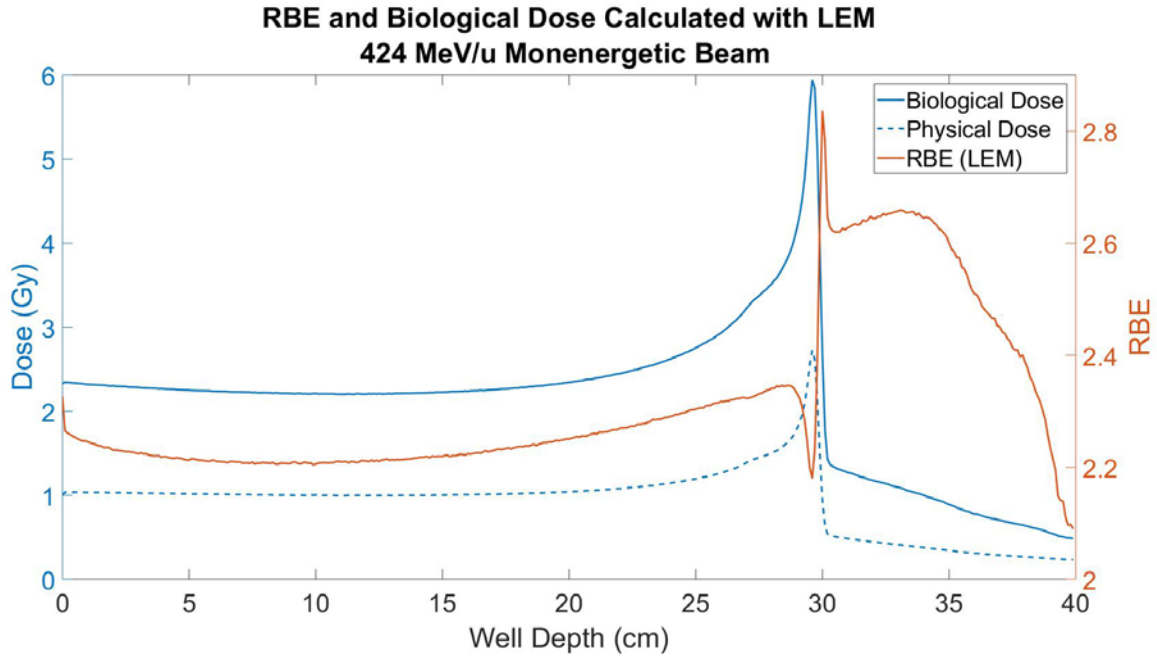


Figure 112. RBE (right axis) and biological dose (left axis) calculated with LEM for 424 MeV/u monoenergetic beam. Physical dose normalized to 1 Gy at the entrance plotted for reference.

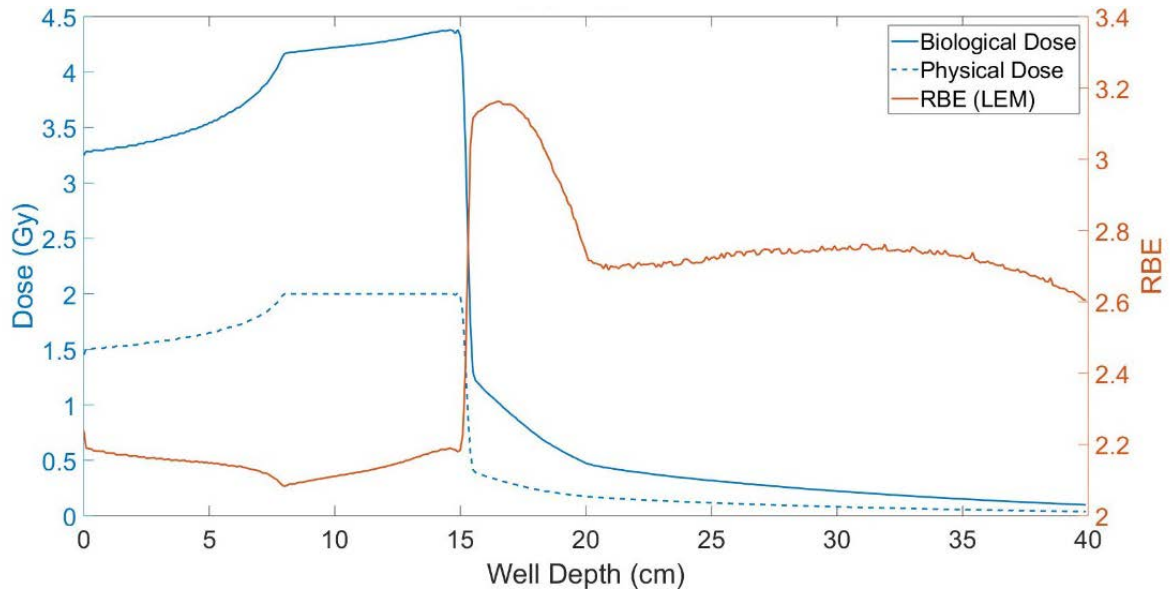


Figure 113. RBE (right axis) and biological dose (left axis) calculated with LEM for a 7 cm SOBP. Physical dose normalized to 2 Gy across the SOBP plotted for reference.

3.3.4.2 Estimation

The uncertainty introduced into RBE_{LEM} was quantified for both the method of estimating one overall α and β value and cutting the microdosimetric spectra to weight $\bar{\alpha}$ and $\bar{\beta}$ values by certain fragments. Similarly to the RMF model, each of these fits is limited in that it cannot accurately predict RBE in the tail region.

3.3.4.2.1 *Uncut Method*

The uncertainty introduced by means of estimating alpha and beta values as functions of y^* is detailed in Table 34 for a range of clinical monoenergetic beams and SOBPs from the entrance to the distal edge of the Bragg peak. This data is represented by a percent difference between the estimated and Monte Carlo calculated RBE, and is presented in Figure 111 - Figure 118. The respective percent difference is shown on the y-axis in these figures. The uncertainty was, on average, 3.6% in the entrance region and 2.2% in the Bragg peak. The error in the 10 cm SOBP was much greater than that in any other beam, likely due to the high fragmentation.

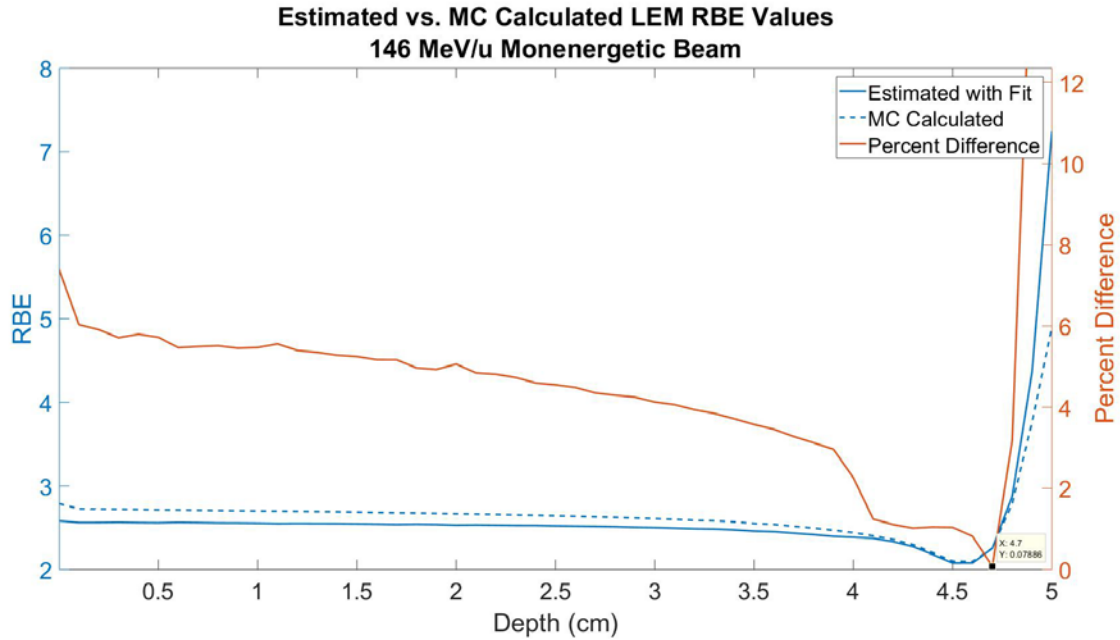


Figure 114. Estimated and Monte Carlo calculated RBE_{LEM} values for a 146 MeV/u monoenergetic beam. Percent difference shown on the y-axis to the right.

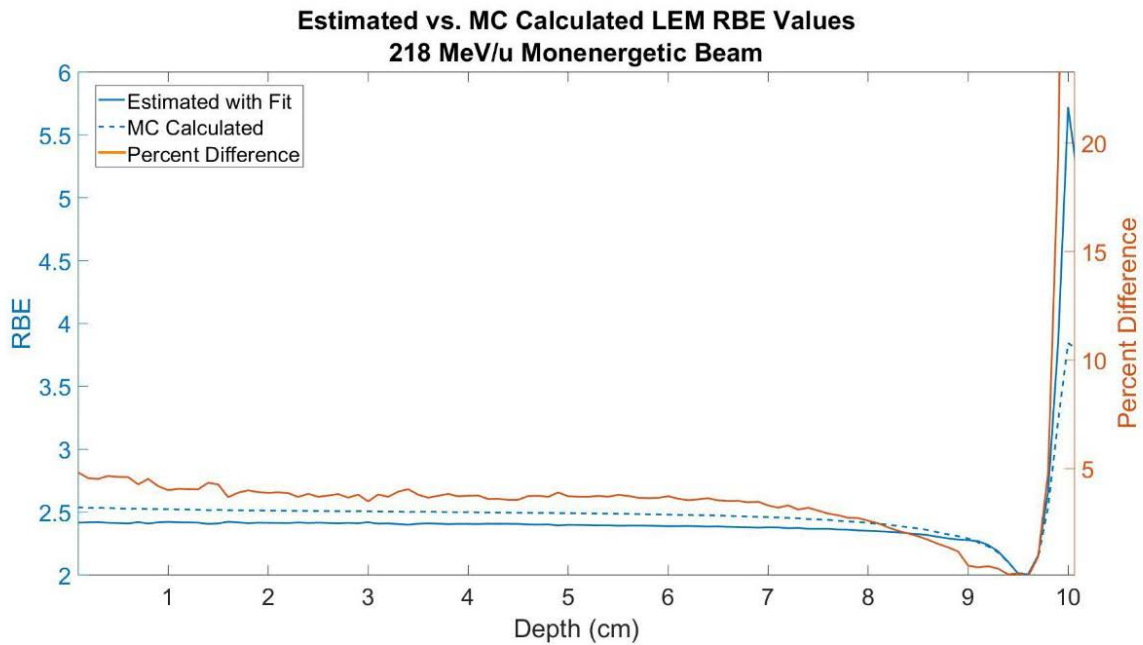


Figure 115. Estimated and Monte Carlo calculated RBE_{LEM} values for a 218 MeV/u monoenergetic beam. Percent difference shown on the y-axis to the right.

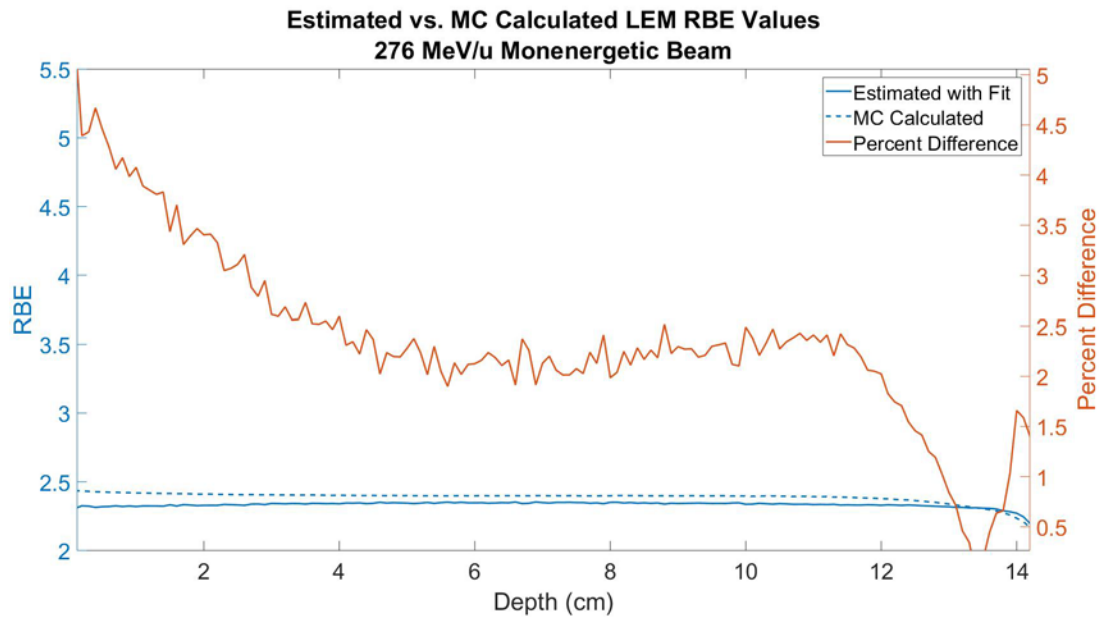


Figure 116. Estimated and Monte Carlo calculated RBE_{LEM} values for a 276 MeV/u monoenergetic beam. Percent difference shown on the y-axis to the right.

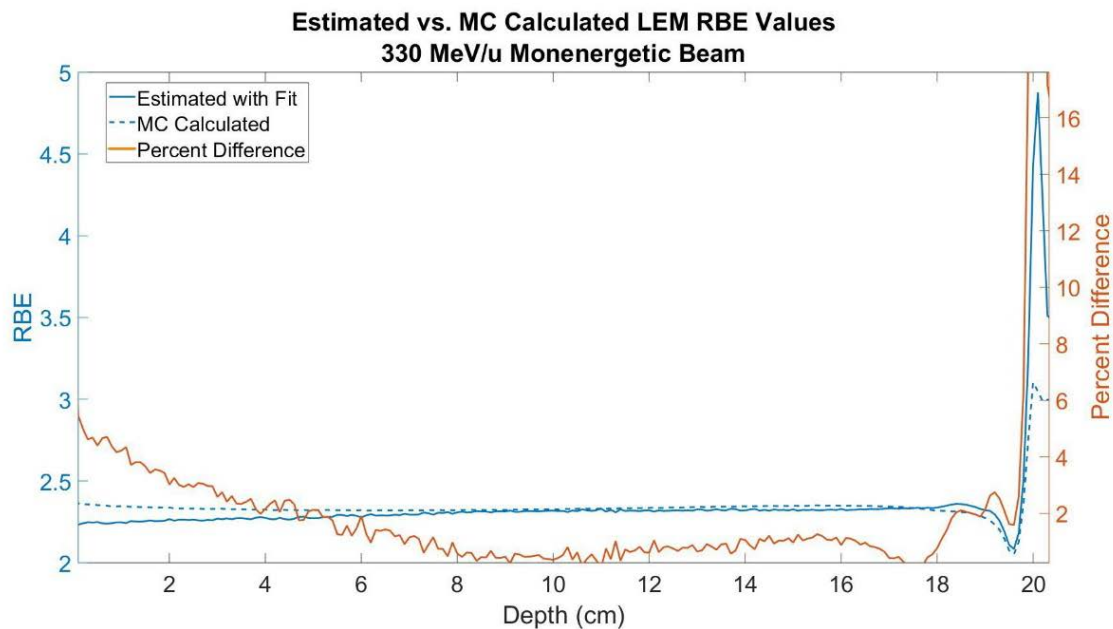


Figure 117. Estimated and Monte Carlo calculated RBE_{LEM} values for a 330 MeV/u monoenergetic beam. Percent difference shown on the y-axis to the right.

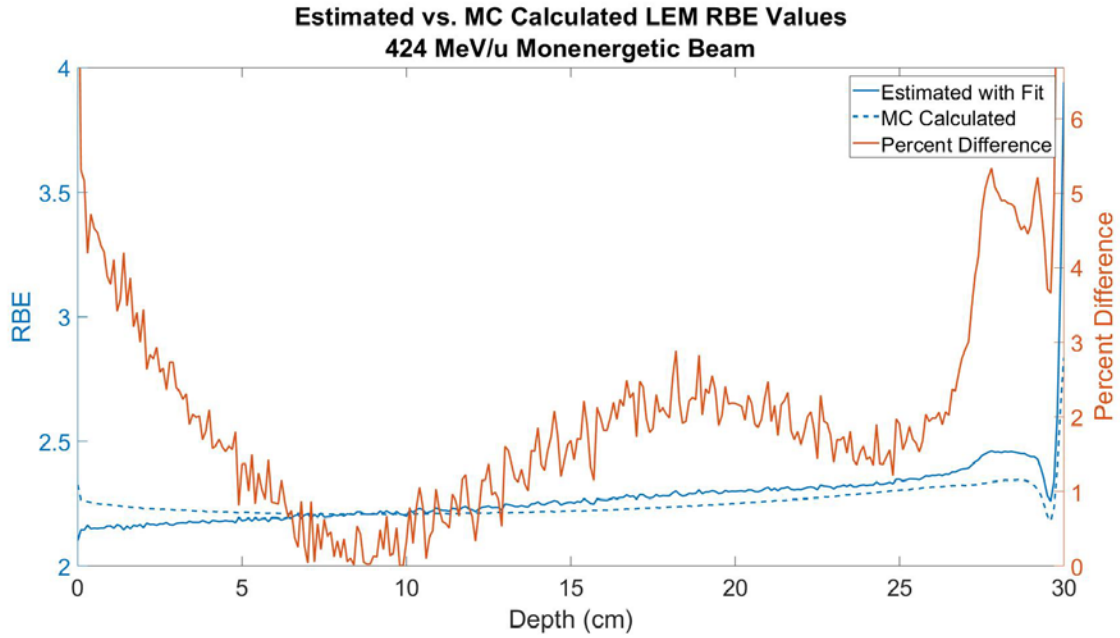


Figure 118. Estimated and Monte Carlo calculated RBE_{LEM} values for a 424 MeV/u monoenergetic beam. Percent difference shown on the y-axis to the right.

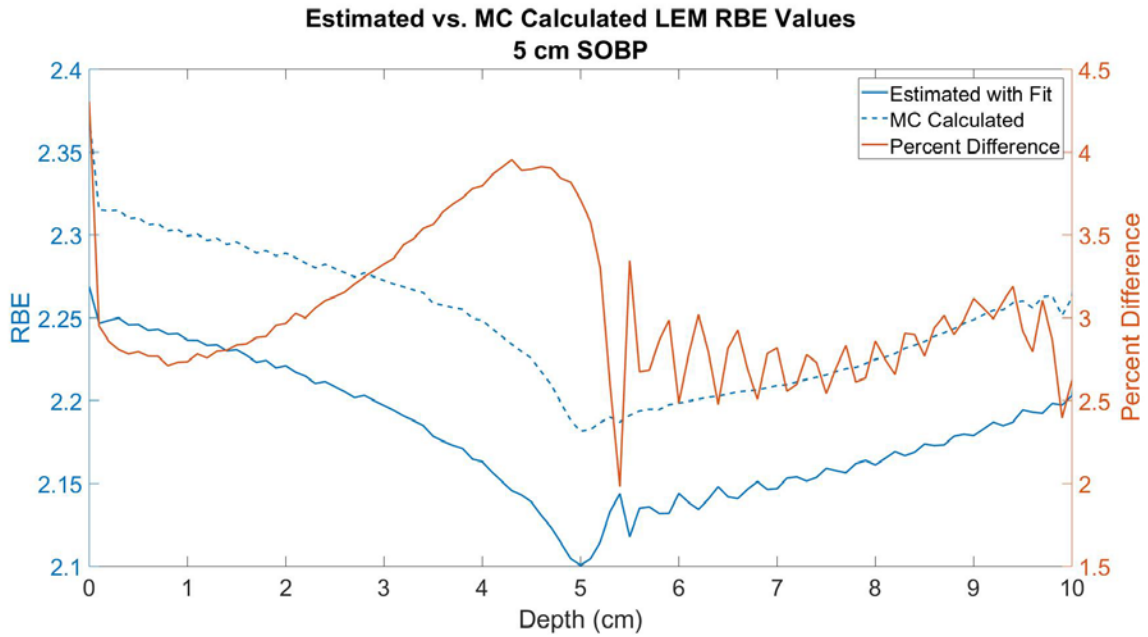


Figure 119. Estimated and Monte Carlo calculated RBE_{LEM} values for a 5 cm SOBP. Percent difference shown on the y-axis to the right.

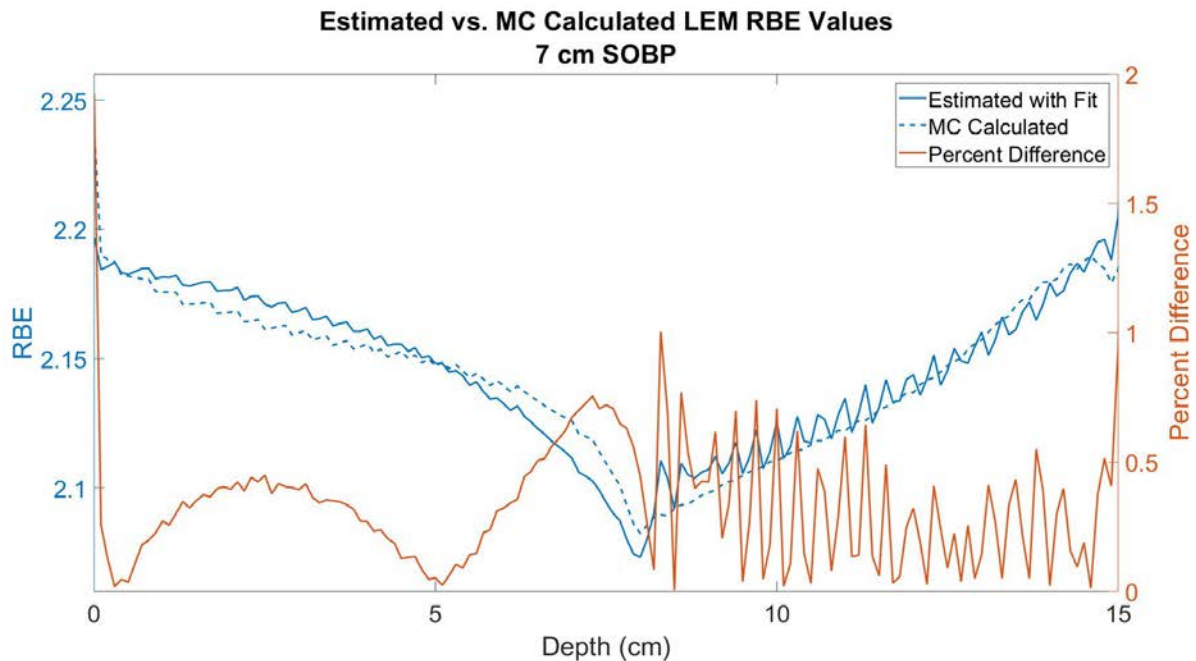


Figure 120. Estimated and Monte Carlo calculated RBE_{LEM} values for a 7 cm SOBP. Percent difference shown on the y-axis to the right.

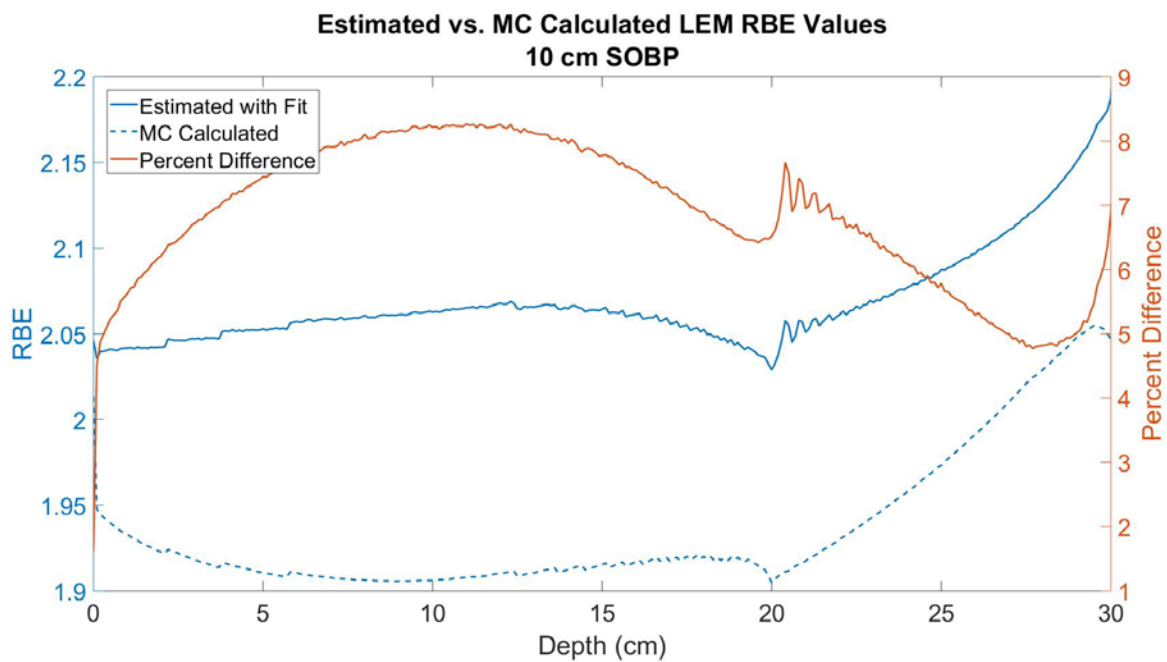


Figure 121. Estimated and Monte Carlo calculated RBE_{LEM} values for a 10 cm SOBP. Percent difference shown on the y-axis to the right.

Table 34. Percent difference between RBE calculated by Monte Carlo simulations and estimated RBE. Results are compared for test data sets (146 MeV/u, 424 MeV/u, 7 cm SOBP) to validation data sets (218 MeV/u, 276 MeV/u, 330 MeV/u, 5 cm SOBP, 10 cm SOBP).

Beam	Percent Difference (%)					
	Entrance	Avg.	Max.	Bragg Peak	Avg.	Max.
146 MeV/u Monoenergetic	-4.93	-4.83	-5.91	-0.82		
218 MeV/u Monoenergetic	-3.91	-3.55	-4.66	-0.05		
276 MeV/u Monoenergetic	-3.47	-2.44	-4.67	2.10		
330 MeV/u Monoenergetic	-3.43	-1.47	-4.99	1.62		
424 MeV/u Monoenergetic	-3.00	1.90	-5.33	3.66		
5 cm SOBP	-2.97	-3.20	-3.96	-2.73	-2.80	-3.35
7 cm SOBP	0.40	0.32	0.76	0.06	0.29	0.77
10 cm SOBP	6.22	7.41	8.27	5.66	5.85	7.67
Average	3.55	3.08	4.82	2.20	2.98	3.93

3.3.4.2.2 Cut Spectra Method

The method of cutting the spectra and estimating resulting lineal energy, α , and β values was used to calculate the RBE up until the distal edge of the Bragg peak or SOBP with good accuracy. The percent difference between the Monte Carlo calculated spectra and the estimated RBE are shown in

Table 35 spanning the full range of clinical energies and SOBPs. Uncertainty was, on average across all energies, 2.7% in the Bragg peak by estimation. The error was similar in the entrance region, averaging just 3.0%. The highest error introduced by estimation was seen in the 424 MeV/u monoenergetic beam. Higher error is expected at this energy, as the fragmentation throughout the roughly 30 cm entrance region was high. Even for this energy, however, the error was reduced in the Bragg peak to just 3.7%.

A further subdivision of the fragment portion was investigated, but considered infeasible due to the direct superposition of lineal energy as seen in. As fragments contribute to, at most, 40% in the entrance and Bragg Peak regions of a monoenergetic beam and 60% in an SOBP, disregarding a further subdivision of the microdosimetric spectra is considered acceptable.

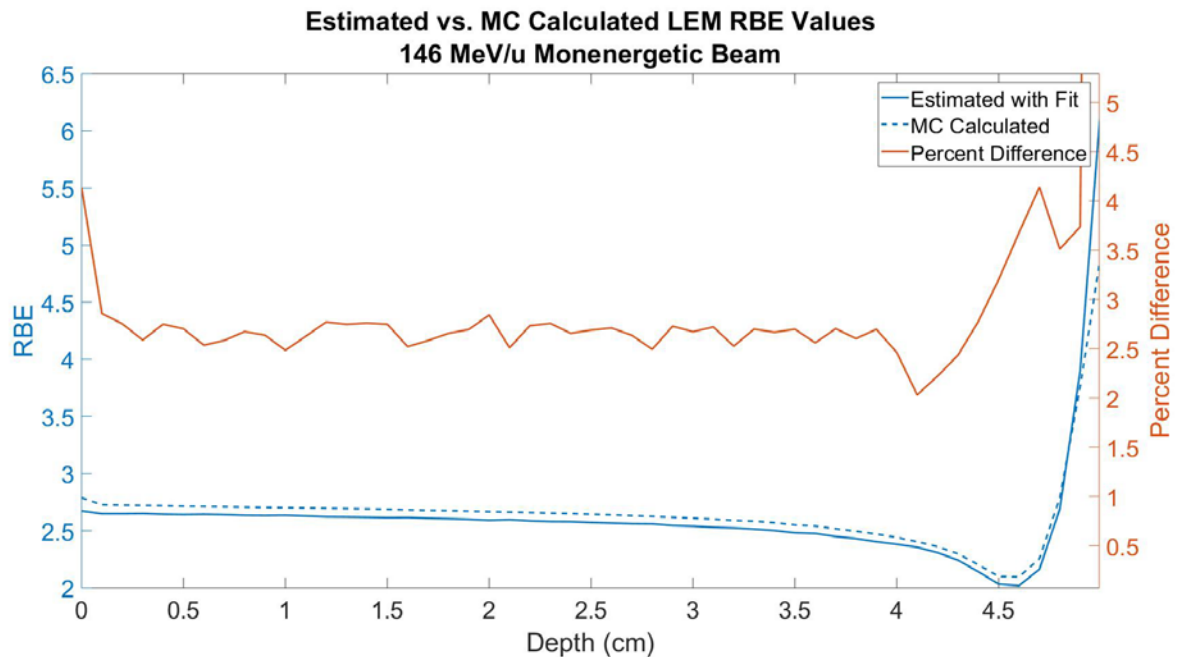


Figure 122. Estimated and Monte Carlo calculated RBE_{LEM} values for a 146 MeV/u monoenergetic beam. Percent difference shown on the right axis for reference.

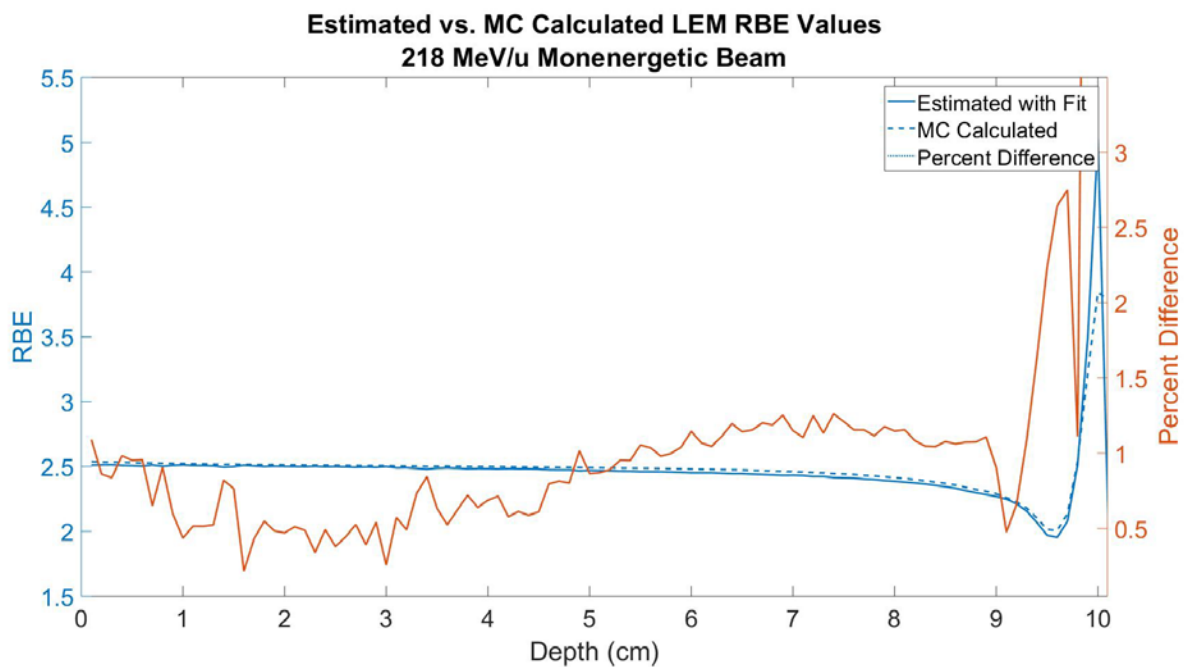


Figure 123. Estimated and Monte Carlo calculated RBE_{LEM} values for a 218 MeV/u monoenergetic beam. Percent difference shown on the right axis for reference.

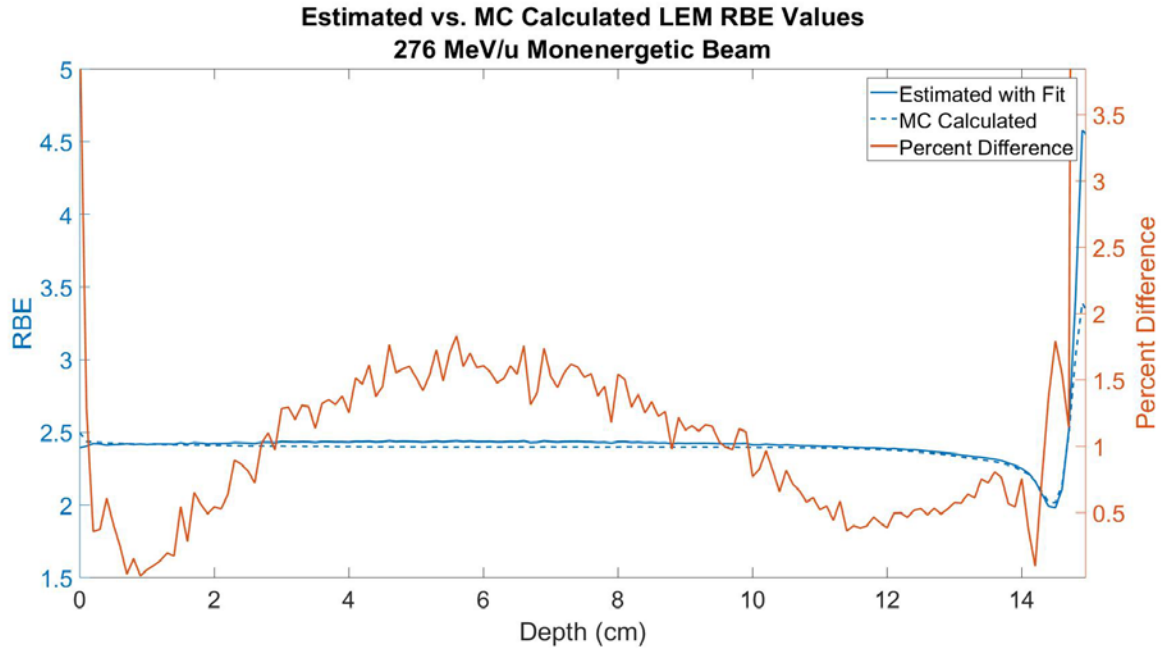


Figure 124. Estimated and Monte Carlo calculated RBE_{LEM} values for a 276 MeV/u monoenergetic beam. Percent difference shown on the right axis for reference.

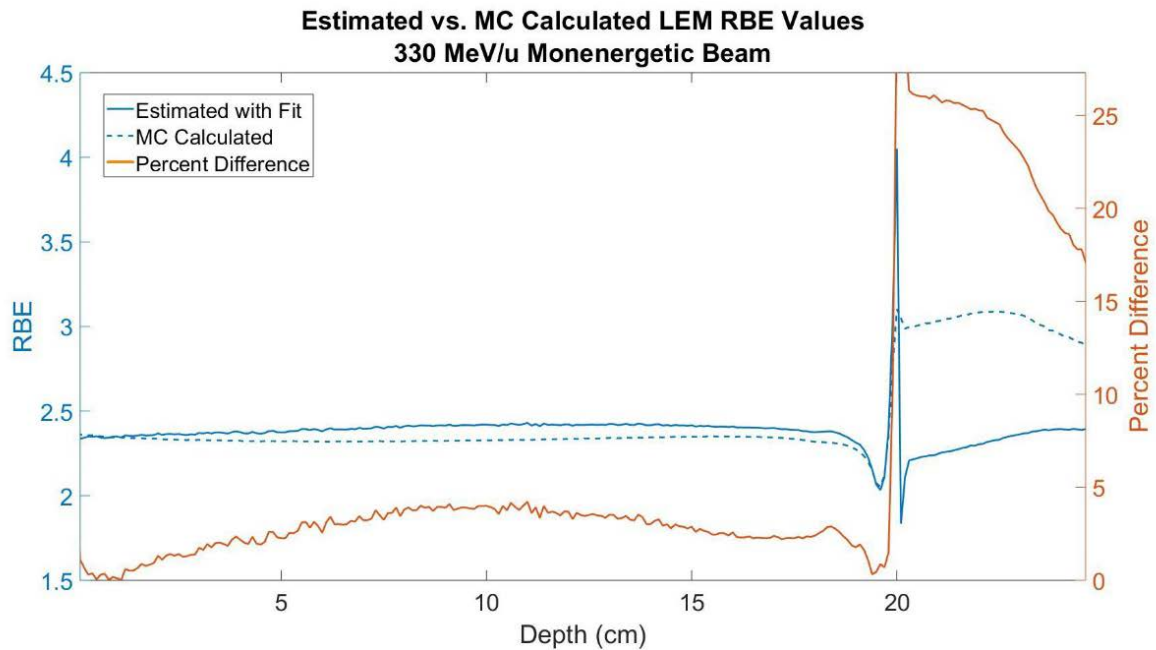


Figure 125. Estimated and Monte Carlo calculated RBE_{LEM} values for a 330 MeV/u monoenergetic beam. Percent difference shown on the right axis for reference.

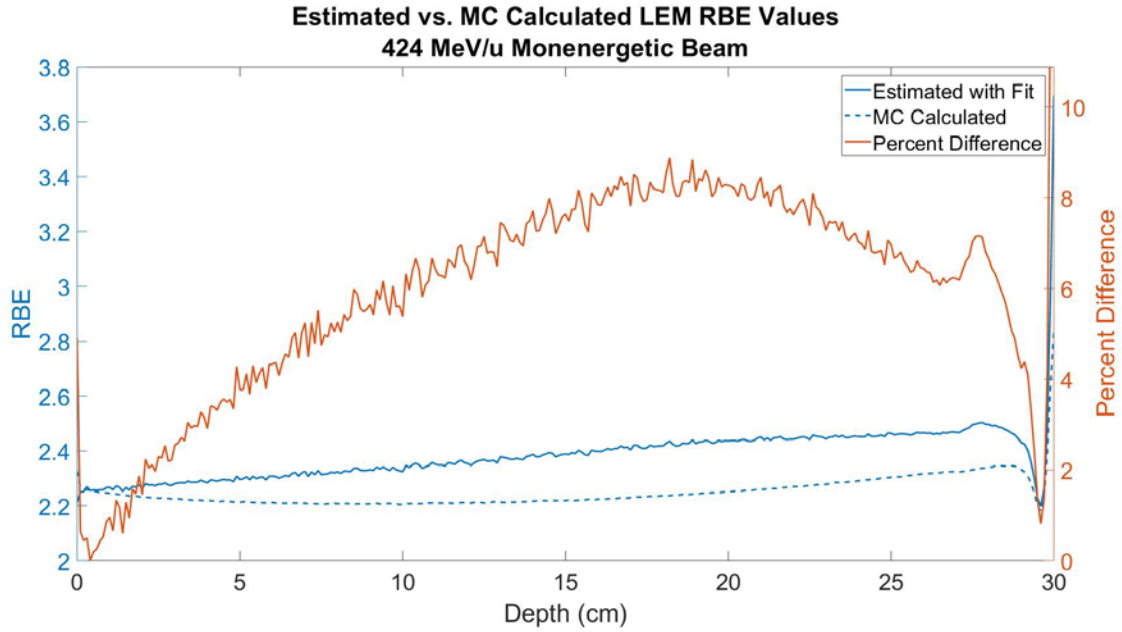


Figure 126. Estimated and Monte Carlo calculated RBE_{LEM} values for a 424 MeV/u monoenergetic beam. Percent difference shown on the right axis for reference.

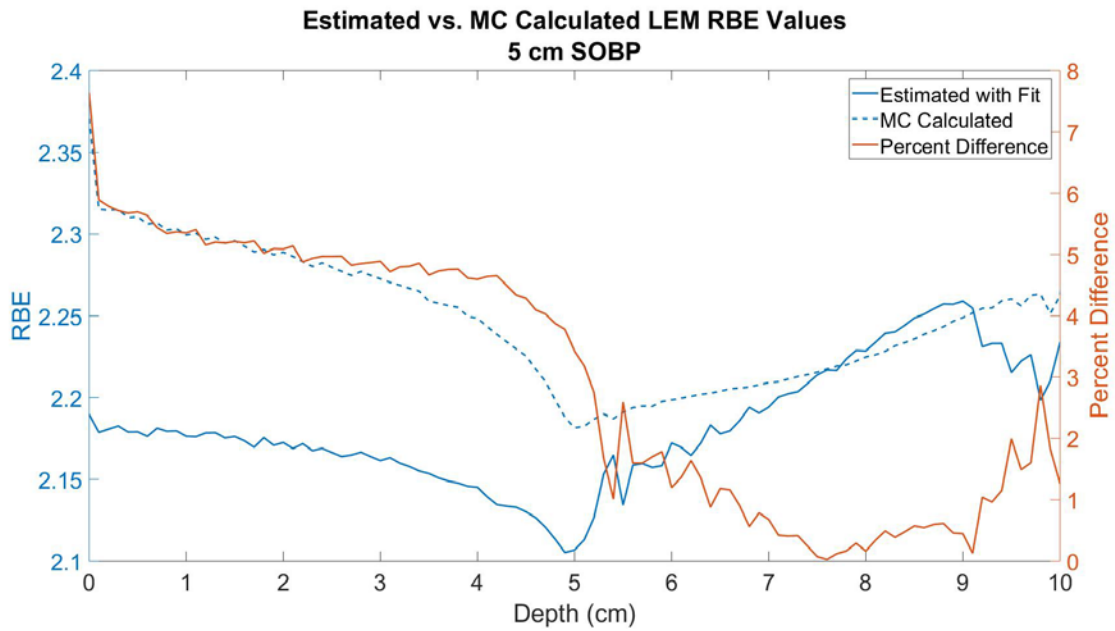


Figure 127. Estimated and Monte Carlo calculated RBE_{LEM} values for a 5 cm SOBP. Percent difference shown on the right axis for reference.

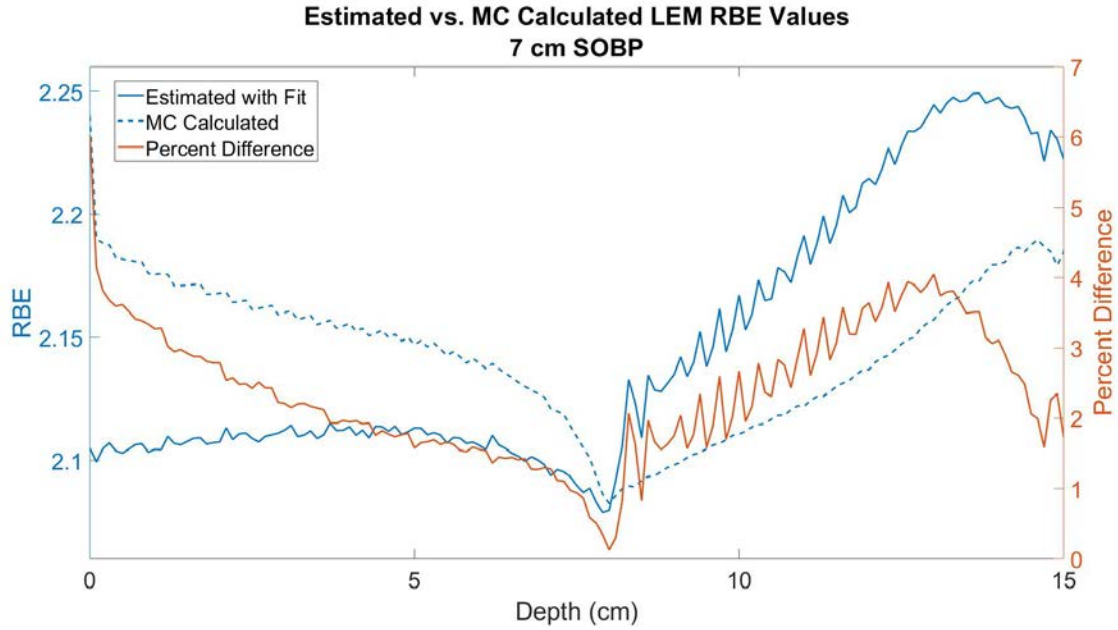


Figure 128. Estimated and Monte Carlo calculated RBE_{LEM} values for a 7 cm SOBP. Percent difference shown on the right axis for reference.

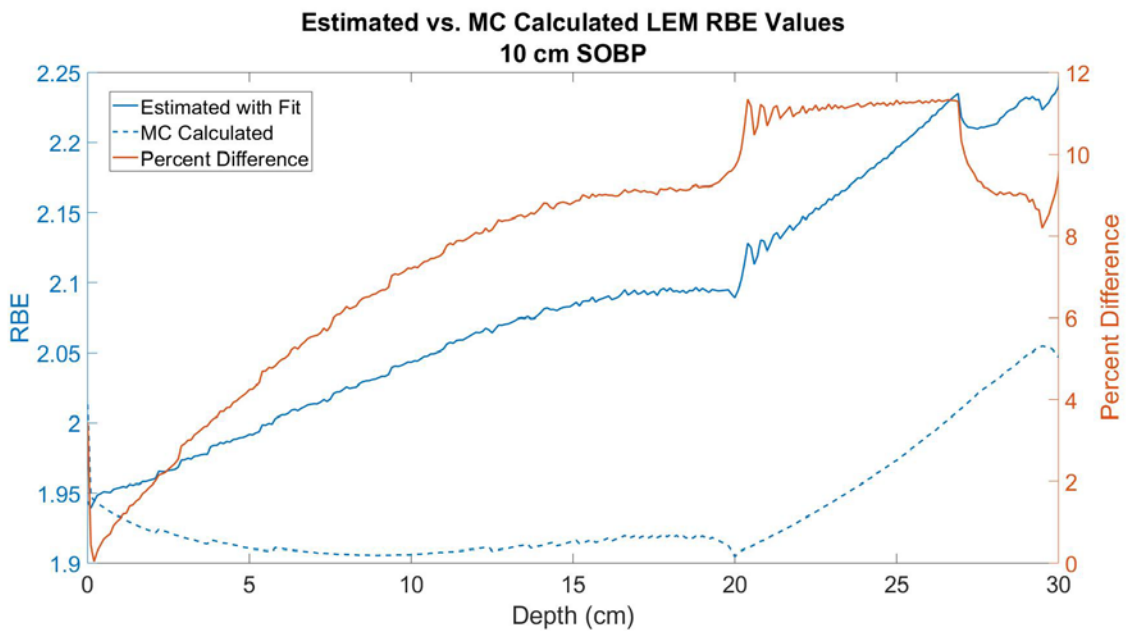


Figure 129. Estimated and Monte Carlo calculated RBE_{LEM} values for a 10 cm SOBP. Percent difference shown on the right axis for reference.

Table 35. Percent difference between RBE calculated by Monte Carlo simulations and RBE calculated by cutting the microdosimetric spectra at select points in both the entrance region and Bragg peak. Results are compared for test data sets (146 MeV/u, 424 MeV/u, 7 cm SOBP) to validation data sets (218 MeV/u, 276 MeV/u, 330 MeV/u, 5 cm SOBP, 10 cm SOBP).

Beam	Percent Difference (%)					
	Entrance	Avg.	Max.	Bragg Peak	Avg.	Max.
146 MeV/u Monoenergetic	-2.84	-2.70	-4.14	-4.14		
218 MeV/u Monoenergetic	-0.47	-0.86	-1.11	-2.75		
276 MeV/u Monoenergetic	0.49	0.75	1.62	-1.5		
330 MeV/u Monoenergetic	0.94	2.90	5.48	-0.46		
424 MeV/u Monoenergetic	1.46	5.99	8.88	0.82		
5 cm SOBP	-5.59	-4.49	-7.17	-0.24	-0.52	2.09
7 cm SOBP	-2.71	-2.17	3.68	2.48	2.82	4.1
10 cm SOBP	1.92	6.04	9.28	11.3	11.1	11.4
Average	2.10	3.36	5.72	3.29	4.43	5.20

3.3.4.3 Propagated Uncertainty

The method of cutting the spectra and estimating RBE was implemented within the uncertainty calculations, and is therefore accounted for in each of the source quantifications. As error was lower by roughly 1% with the method of cutting the spectra, the uncertainty analysis was propagated using that method. Similar results are anticipated with either method, however, as they both require the same lineal energy input parameters. Figure 127 - Figure 134 show the estimated RBE and the estimated RBE with bias against the true RBE calculated

with Monte Carlo. The bias introduced by each of the four sources resulted in an average RBE increase 1.5%, with a maximum increase in 2.1%.

The total variance introduced by all eight uncertainty sources are described with error bars in Figure 127 - Figure 134, representing the 1σ standard deviation. The error bars are centered around the estimated RBE with included bias, and the Monte Carlo calculated RBE is shown for reference. The total variance was typically on the order of 2.0% on average, and did not exceed 2.3%.

Table 36. Bias introduced into estimated RBE_{LEM} by each source of uncertainty, expressed as a percent difference between shifted and true RBE. Results are compared for test data sets (146 MeV/u, 424 MeV/u, 7 cm SOB) to validation data sets (218 MeV/u, 276 MeV/u, 330 MeV/u, 5 cm SOB, 10 cm SOB).

Beam	Bias Source	Percent Difference (%)					
		Entrance	Avg.	Max.	Bragg Peak	Avg.	Max.
146 MeV/u Monoenergetic	W-Value	0.28	0.19	0.30	0.12		
	Low Energy Cutoff	<0.01	<0.01	<0.01	<0.01		
	Pulse Pile-up	1.22	1.05	1.43	0.33		
	Wall Effect	0.01	0.01	0.01	0.01		
	Total Bias	1.50	1.24	1.73	0.46		
218 MeV/u Monoenergetic	W-Value	0.44	0.45	0.11	0.15		
	Low Energy Cutoff	<0.01	<0.01	<0.01	<0.01		
	Pulse Pile-up	1.30	1.35	0.29	0.28		
	Wall Effect	0.03	0.06	0.22	0.03		
	Total Bias	1.77	1.86	0.62	0.46		
276 MeV/u Monoenergetic	W-Value	0.59	0.53	0.61	0.25		
	Low Energy Cutoff	<0.01	<0.01	<0.01	<0.01		
	Pulse Pile-up	1.29	1.10	1.36	0.29		
	Wall Effect	0.05	0.13	0.18	0.07		
	Total Bias	1.93	1.76	1.97	0.60		
330 MeV/u Monoenergetic	W-Value	0.33	0.29	0.33	0.12		
	Low Energy Cutoff	<0.01	<0.01	<0.01	<0.01		
	Pulse Pile-up	1.31	1.06	1.37	0.25		
	Wall Effect	0.08	0.27	0.39	0.16		
	Total Bias	1.71	1.62	1.76	0.53		
424 MeV/u Monoenergetic	W-Value	0.36	0.32	0.38	0.13		
	Low Energy Cutoff	<0.01	<0.01	<0.01	<0.01		

	Pulse Pile-up	1.32	0.97	1.43	0.26		
	Wall Effect	0.11	0.66	0.97	0.48		
	Total Bias	1.79	1.95	2.12	0.86		
5 cm SOBP	W-Value	0.16	0.16	0.17	0.03	0.02	0.10
	Low Energy Cutoff	<0.01	<0.01	<0.01	<0.01	0.01	0.03
	Pulse Pile-up	0.59	0.58	0.63	0.08	0.06	0.30
	Wall Effect	-0.01	-0.01	0.00	-0.05	-0.11	-0.01
	Total Bias	0.74	0.74	0.80	0.07	-0.02	0.38
7 cm SOBP	W-Value	0.13	0.13	0.14	0.07	0.07	0.12
	Low Energy Cutoff	<0.01	<0.01	<0.01	0.01	<0.01	0.01
	Pulse Pile-up	1.45	1.49	1.68	1.42	1.46	1.90
	Wall Effect	-0.03	-0.06	0.00	-0.22	-0.19	-0.12
	Total Bias	1.55	1.55	1.67	1.27	1.35	1.87
10 cm SOBP	W-Value	0.14	0.10	0.14	0.02	0.02	0.06
	Low Energy Cutoff	<0.01	<0.01	<0.01	0.01	0.02	0.07
	Pulse Pile-up	0.51	0.36	0.53	0.05	0.08	0.24
	Wall Effect	-0.12	-0.76	-0.01	-1.29	-1.64	-1.05
	Total Bias	0.52	-0.30	0.65	-1.21	-1.52	-0.86

Table 37. Variance introduced into estimated RBE_{LEM} by each source of uncertainty, expressed as percent uncertainty at the 1σ standard deviation level. Results are compared for test data sets (146 MeV/u, 424 MeV/u, 7 cm SOBP) to validation data sets (218 MeV/u, 276 MeV/u, 330 MeV/u, 5 cm SOBP, 10 cm SOBP).

Beam	Variance Source	1 σ Standard Deviation (%)					
		Entrance	Avg.	Max.	Bragg Peak	Avg.	Max.
146 MeV/u Monoenergetic	Counting Statistics	0.04	0.04	0.20	0.01		
	Mean Chord Length	0.11	0.11	0.12	0.04		
	Electronic Noise	0.28	0.27	0.21	0.05		
	Gain Instability	0.01	0.01	0.02	0.00		
	W-Value	1.72	1.68	1.91	0.58		
	Low Energy Cutoff	<0.01	<0.01	<0.01	<0.01		
	Pulse Pile-up	0.01	0.01	0.02	<0.01		
	Wall Effect	<0.01	<0.01	<0.01	<0.01		
	Total Variance	1.75	1.71	1.95	0.58		
218 MeV/u Monoenergetic	Counting Statistics	0.05	0.05	0.49	<0.01		
	Mean Chord Length	0.11	0.1	0.11	0.03		
	Electronic Noise	0.33	0.31	0.35	0.06		
	Gain Instability	0.02	0.01	0.02	<0.01		
	W-Value	1.81	1.65	1.84	0.55		
	Low Energy Cutoff	<0.01	<0.01	<0.01	<0.01		
	Pulse Pile-up	0.03	0.02	0.04	<0.01		
	Wall Effect	<0.01	<0.01	<0.01	<0.01		
	Total Variance	0.05	0.05	0.49	<0.01		
276 MeV/u Monoenergetic	Counting Statistics	0.06	0.07	0.65	0.01		
	Mean Chord Length	0.12	0.11	0.12	0.04		
	Electronic Noise	0.27	0.28	0.33	0.06		

	Gain Instability	0.02	0.01	0.02	0.01		
	W-Value	1.98	1.79	2.03	0.73		
	Low Energy Cutoff	<0.01	<0.01	<0.01	<0.01		
	Pulse Pile-up	0.05	0.03	0.05	<0.01		
	Wall Effect	<0.01	0.01	0.01	<0.01		
	Total Variance	2.00	1.82	2.08	0.74		
330 MeV/u Monoenergetic	Counting Statistics	0.09	0.09	0.41	<0.01		
	Mean Chord Length	0.12	0.11	0.12	0.04		
	Electronic Noise	0.23	0.26	0.31	0.06		
	Gain Instability	0.02	0.02	0.02	0.01		
	W-Value	2.11	1.88	2.17	0.63		
	Low Energy Cutoff	<0.01	<0.01	<0.01	<0.01		
	Pulse Pile-up	0.04	0.03	0.06	<0.01		
	Wall Effect	<0.01	0.01	0.02	0.01		
	Total Variance	2.13	1.91	2.19	0.64		
424 MeV/u Monoenergetic	Counting Statistics	0.01	0.12	1.06	<0.01		
	Mean Chord Length	0.12	0.11	0.13	0.04		
	Electronic Noise	0.15	0.22	0.30	0.06		
	Gain Instability	0.02	0.01	0.02	<0.01		
	W-Value	2.00	1.81	2.06	0.06		
	Low Energy Cutoff	<0.01	<0.01	<0.01	<0.01		
	Pulse Pile-up	0.06	0.04	0.06	<0.01		
	Wall Effect	0.01	0.04	0.05	0.02		
	Total Variance	2.01	1.84	2.20	0.62		
5 cm SOBP	Counting Statistics	0.02	0.04	0.46	<0.01	0.01	0.10
	Mean Chord Length	0.05	0.05	0.05	0.02	0.02	0.04
	Electronic Noise	0.1	0.1	0.11	0.04	0.04	0.13

	Gain Instability	0.01	0.01	0.01	<0.01	<0.01	<0.01
	W-Value	0.87	0.86	0.88	0.3	0.29	0.62
	Low Energy Cutoff	<0.01	<0.01	<0.01	<0.01	<0.01	0.01
	Pulse Pile-up	0.01	0.01	0.02	<0.01	<0.01	0.04
	Wall Effect	<0.01	<0.01	<0.01	0.01	0.01	0.04
	Total Variance	0.88	0.88	0.99	0.30	0.29	0.63
7 cm SOBP	Counting Statistics	0.12	0.13	0.38	0.10	0.15	1.06
	Mean Chord Length	0.12	0.12	0.13	0.12	0.12	0.12
	Electronic Noise	0.15	0.16	0.18	0.22	0.21	0.23
	Gain Instability	0.02	0.02	0.02	0.02	0.16	0.16
	W-Value	2.01	2.00	2.06	0.00	1.93	1.99
	Low Energy Cutoff	<0.01	<0.01	<0.01	<0.01	<0.01	<0.01
	Pulse Pile-up	<0.01	<0.01	<0.01	<0.01	<0.01	<0.01
	Wall Effect	0.01	0.01	0.02	0.04	0.04	0.04
	Total Variance	2.01	2.01	2.11	1.97	1.95	2.27
10 cm SOBP	Counting Statistics	0.08	0.07	0.69	0.01	0.04	0.44
	Mean Chord Length	0.04	0.03	0.04	0.01	0.02	0.02
	Electronic Noise	0.06	0.11	0.14	0.15	0.17	0.25
	Gain Instability	0.01	<0.01	0.01	<0.01	<0.01	<0.01
	W-Value	0.68	0.54	0.7	0.22	0.25	0.37
	Low Energy Cutoff	<0.01	<0.01	<0.01	<0.01	0.01	0.02
	Pulse Pile-up	0.02	0.02	0.03	0.01	0.01	0.09
	Wall Effect	<0.01	0.03	0.05	0.05	0.07	0.18
	Total Variance	0.68	0.56	0.91	0.27	0.32	0.54

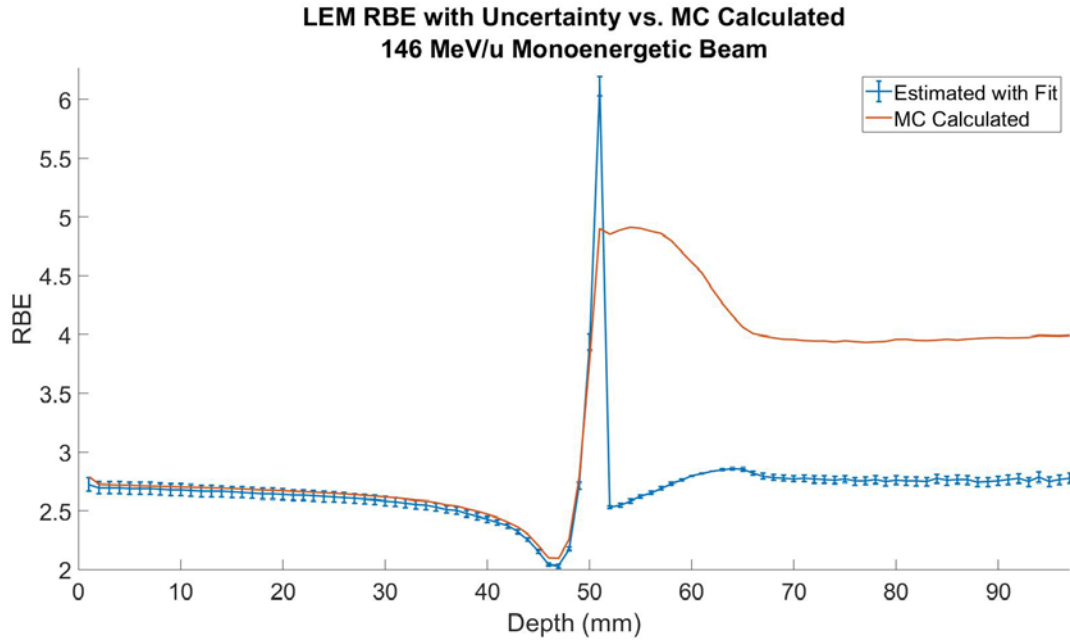


Figure 130. Estimated RBE_{LEM} with added bias (blue line) and uncertainty (error bars) as a function of depth for 146 MeV/u monoenergetic beam. Monte Carlo calculated RBE shown in orange.

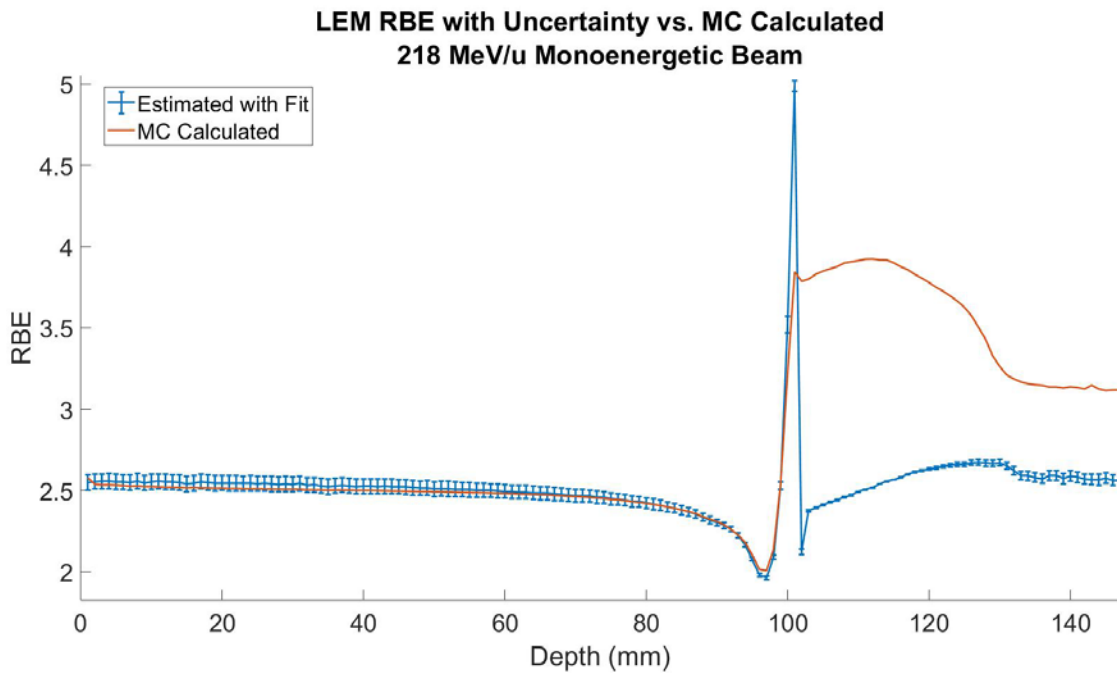


Figure 131. Estimated RBE_{LEM} with added bias (blue line) and uncertainty (error bars) as a function of depth for 218 MeV/u monoenergetic beam. Monte Carlo calculated RBE shown in orange.

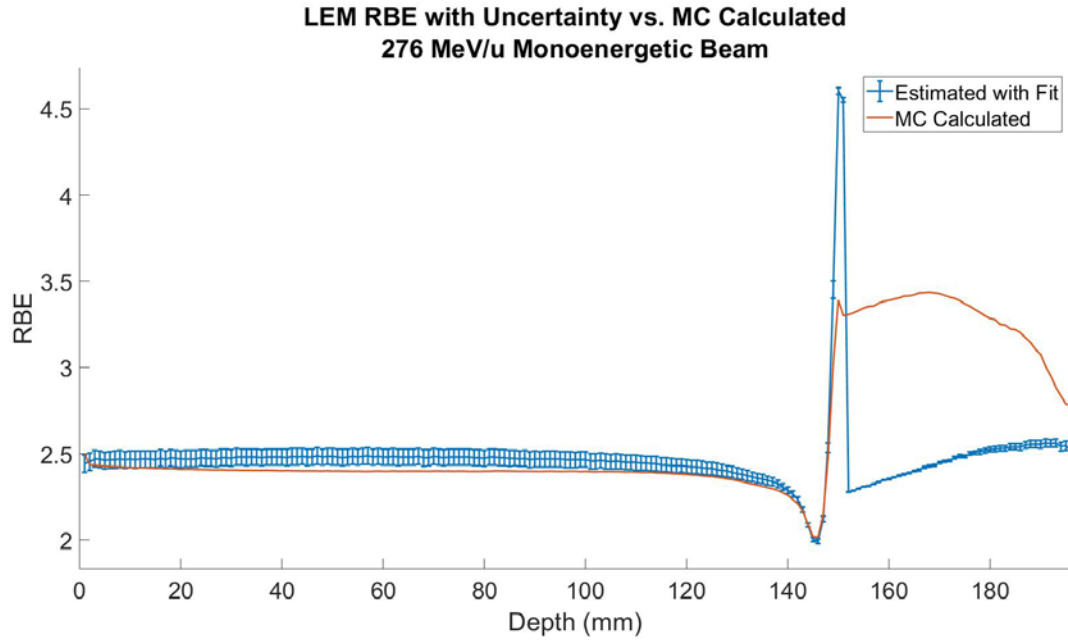


Figure 132. Estimated RBE_{LEM} with added bias (blue line) and uncertainty (error bars) as a function of depth for 276 MeV/u monoenergetic beam. Monte Carlo calculated RBE shown in orange.

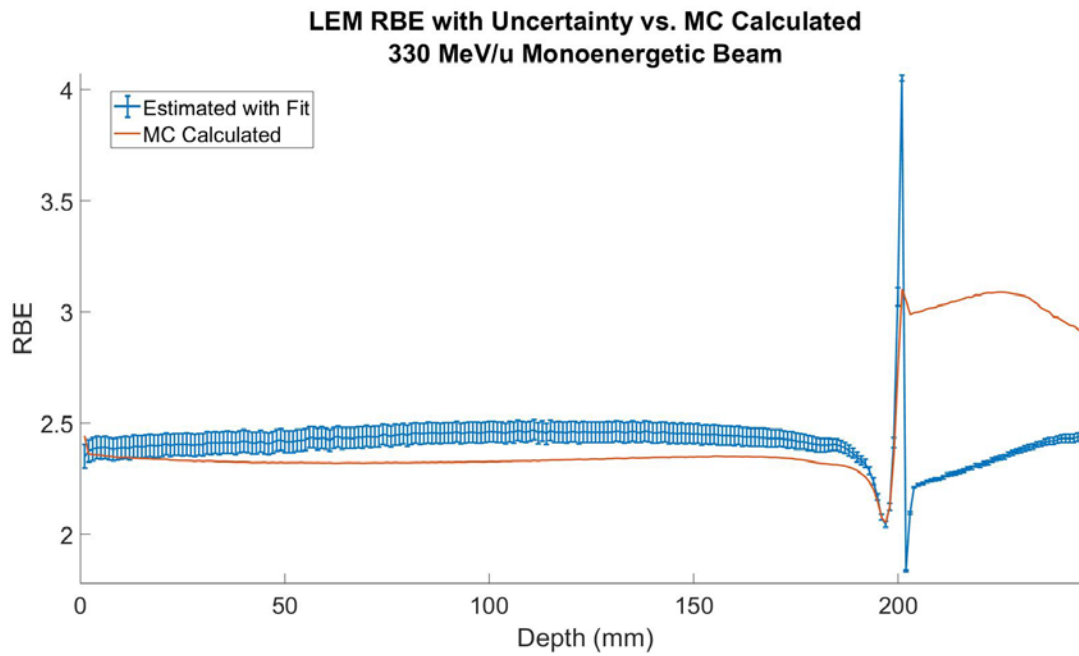


Figure 133. Estimated RBE_{LEM} with added bias (blue line) and uncertainty (error bars) as a function of depth for 330 MeV/u monoenergetic beam. Monte Carlo calculated RBE shown in orange.

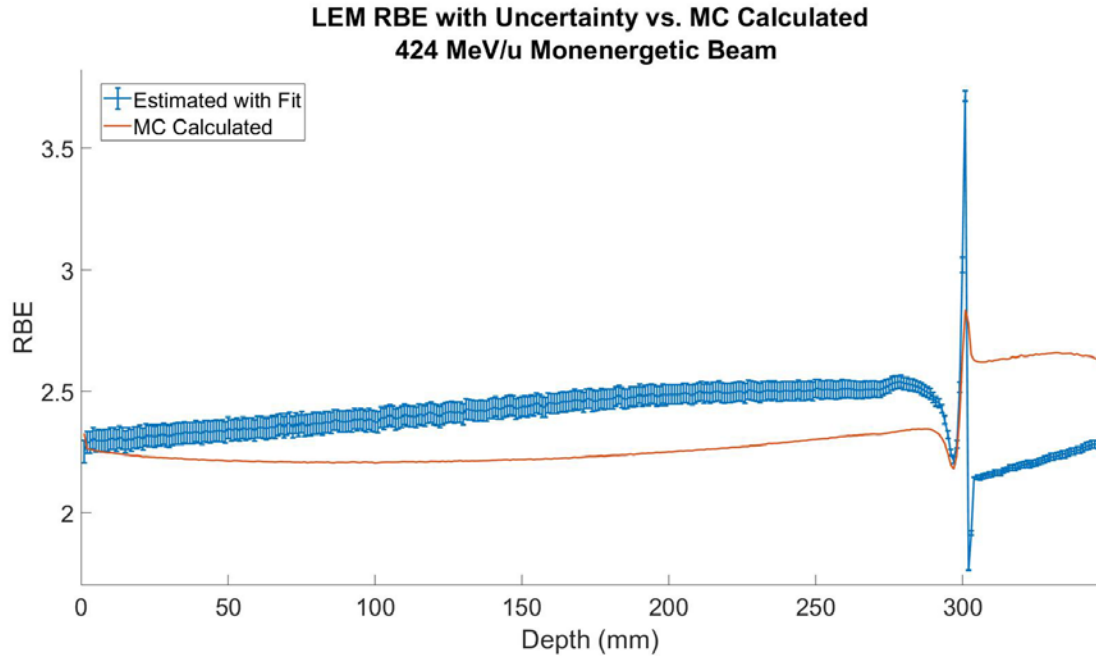


Figure 134. Estimated RBE_{LEM} with added bias (blue line) and uncertainty (error bars) as a function of depth for 424 MeV/u monoenergetic beam. Monte Carlo calculated RBE shown in orange.

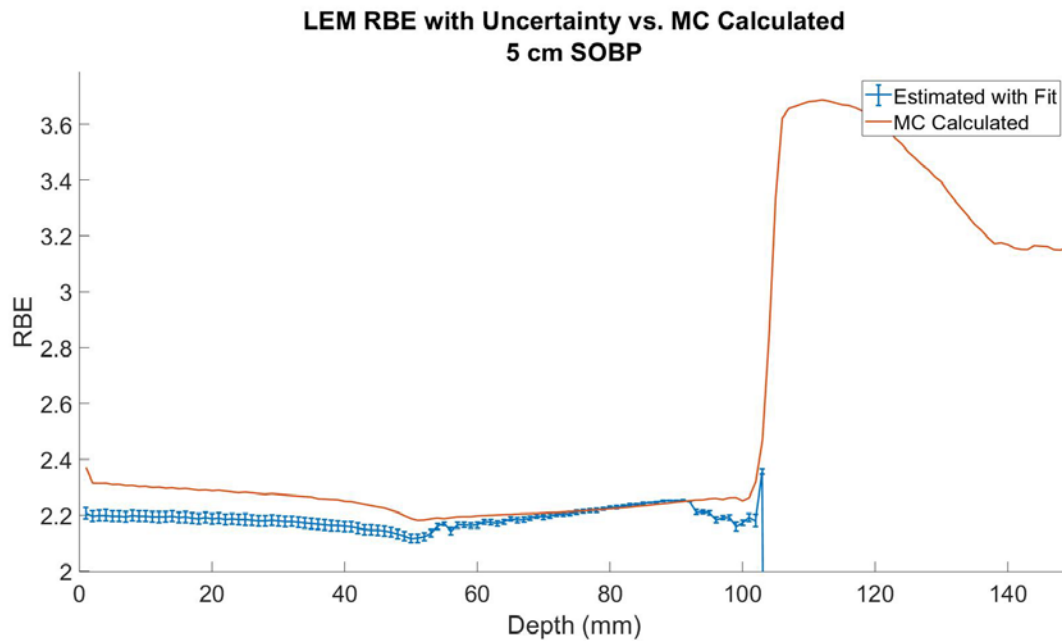


Figure 135. Estimated RBE_{LEM} with added bias (blue line) and uncertainty (error bars) as a function of depth for a 5 cm SOBP. Monte Carlo calculated RBE shown in orange. Estimated RBE reached values of -5 in the tail, and were cutoff to maintain an appropriate scale in the entrance and Bragg peak region.

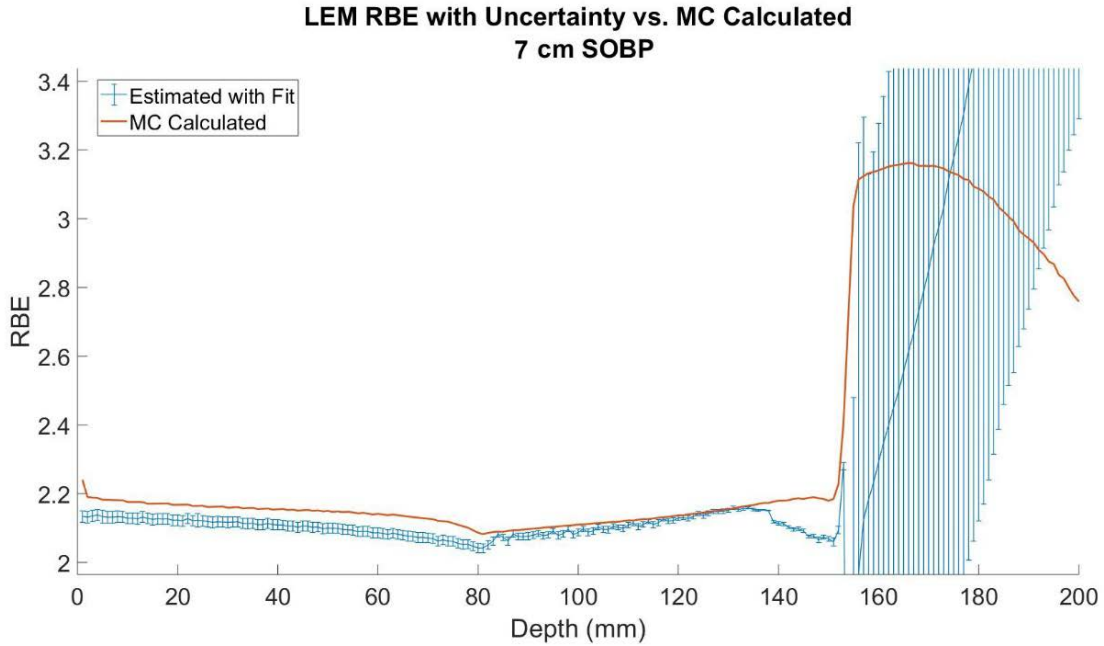


Figure 136. Estimated RBE_{LEM} with added bias (blue line) and uncertainty (error bars) as a function of depth for a 7 cm SOBP. Monte Carlo calculated RBE shown in orange. Estimated RBE reached values of -5 in the tail, and were cutoff to maintain an appropriate scale in the entrance and Bragg peak region.

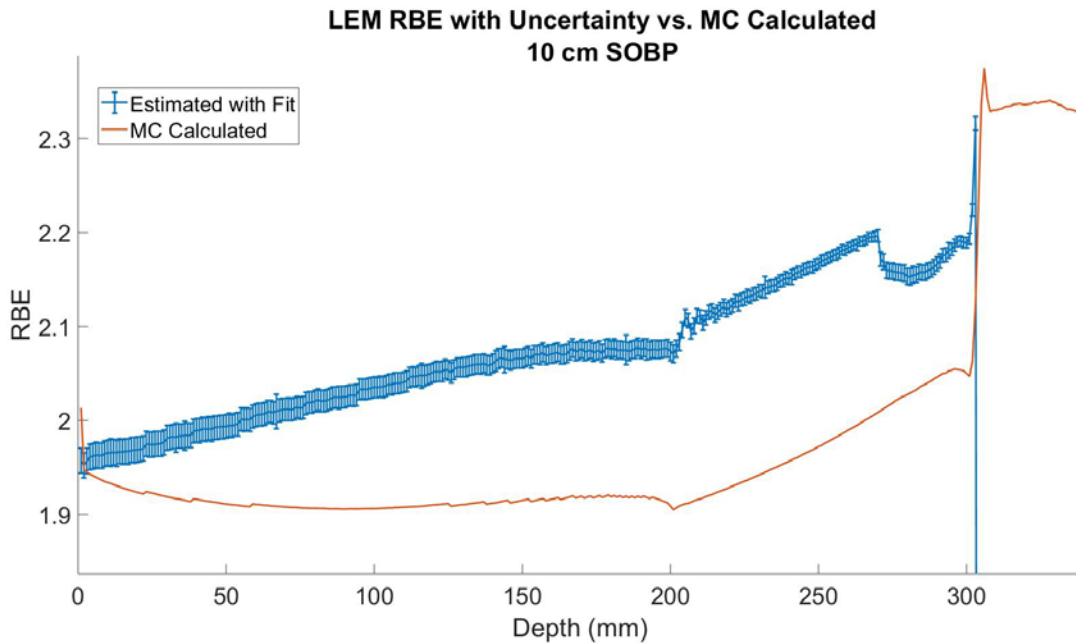


Figure 137. Estimated RBE_{LEM} with added bias (blue line) and uncertainty (error bars) as a function of depth for a 10 cm SOBP. Monte Carlo calculated RBE shown in orange. Estimated RBE reached values of -2 in the tail, and were cutoff to maintain an appropriate scale in the entrance and Bragg peak region.

3.3.4.4 All Uncertainty

The total uncertainty due to each source assessed is displayed in Table 38. On average, the uncertainty in estimating the RBE ranged from 1-6%. The highest uncertainty was found in the entrance region of the 146 MeV/u monoenergetic beam, and the uncertainty averaged 1.8% in other regions and energies explored. The bias was highest in the SOBP region of the 7 cm SOBP beam, reaching a maximum value of 2.1%, while the average across all energies was just 1.5%. The variance introduced by the random physical measurement based noise was low throughout all energies, never exceeding 2.5% standard deviation at the 1σ level. The variance was typically lowest in the Bragg peak region, but did not show particular trends over beam energies.

Table 38. Total uncertainty in estimated RBE_{LEM} by each source assessed.

Beam	Uncertainty Source						
		Entrance	Avg.	Max.	Bragg Peak	Avg.	Max.
146 MeV/u Monoenergetic	Bias (% Difference)	1.50	1.24	1.73	0.46		
	RBE Estimation (% Difference)	-2.84	-2.70	-4.14	-4.14		
	Variance (% St. Dev., 1- σ)	1.75	1.71	1.95	0.58		
218 MeV/u Monoenergetic	Bias (% Difference)	1.77	1.86	0.62	0.46		
	RBE Estimation (% Difference)	-0.47	-0.86	-1.11	-2.75		
	Variance (% St. Dev., 1- σ)	1.84	1.68	1.87	0.56		
276 MeV/u Monoenergetic	Bias (% Difference)	1.93	1.76	1.97	0.60		
	RBE Estimation (% Difference)	0.49	0.75	1.62	-1.50		
	Variance (% St. Dev., 1- σ)	2.00	1.82	2.08	0.74		
330 MeV/u Monoenergetic	Bias (% Difference)	1.71	1.62	1.76	0.53		
	RBE Estimation (% Difference)	0.94	2.9	5.48	-0.46		
	Variance (% St. Dev., 1- σ)	2.13	1.91	2.19	0.64		
424 MeV/u Monoenergetic	Bias (% Difference)	1.79	1.95	2.12	0.86		
	RBE Estimation	1.46	5.99	8.88	0.82		

	(% Difference)						
	Variance (% St. Dev., 1- σ)	2.01	1.84	2.20	0.62		
5 cm SOBP	Bias (% Difference)	0.74	0.74	0.80	0.07	-0.02	0.38
	RBE Estimation (% Difference)	-5.59	-4.49	-7.17	-0.24	-0.52	2.09
	Variance (% St. Dev., 1- σ)	0.88	0.88	0.99	0.30	0.29	0.63
7 cm SOBP	Bias (% Difference)	1.55	1.55	1.67	1.27	1.35	1.87
	RBE Estimation (% Difference)	-2.71	-2.17	3.68	2.48	2.82	4.1
	Variance (% St. Dev., 1- σ)	2.01	2.01	2.11	1.97	1.95	2.27
10 cm SOBP	Bias (% Difference)	0.52	-0.30	0.65	-1.21	-1.52	-0.86
	RBE Estimation (% Difference)	1.92	6.04	9.28	11.3	11.1	11.4
	Variance (% St. Dev., 1- σ)	0.68	0.56	0.91	0.27	0.32	0.54

3.4 Discussion

3.4.1 MKM

The bias introduced in the RBE calculated by MKM was low, averaging 1.8% percent across all energies. The correction factor to account for this bias will be low for MKM. The average variance across beam energies was 1.7%, which falls well within the 5% threshold proposed by the hypothesis. At most, the variance reached 2.2%, which also meets the threshold.

3.4.2 RMF

The bias introduced in the RMF model was higher than that introduced into both LEM and MKM models, exceeding 3.0% in both the low energy monoenergetic beam (146 MeV/u) and the 10 cm SOBP. The average bias was 2.7%, and there were no dramatic deviations from this value. This indicates that it could be possible to apply a uniform correction to the spectra to reduce the uncertainty in RMF.

The average uncertainty in RBE estimation is just 1.5% across all beam energies and falls well within acceptable levels. With a variance introduced by physical noise averaging 1.3%, an overall uncertainty range of 0.2% to 1.8%, on average, is introduced to the spectra which falls within the 5% threshold set by the hypothesis. Uncertainty does exceed this threshold, however, at certain points particularly when combining each uncertainty. The highest uncertainty introduced by estimated RBE occurs at the location 0.5 cm proximally to the Bragg peak. One possible explanation for this lies in the inhomogeneity of the

dose distribution of secondary carbons, which peaks sharply within one millimeter of this same point. This contribution may cause the true α_c to sharply increase in magnitude, which may not be accounted for in the average fit of α_c values across energies.

3.4.3 LEM

The average bias introduced in the RBE_{LEM} was 2.8%, and was highest for high energy monoenergetic beams (424 MeV/u). In the SOBP, the bias ranged from -0.3% in the 10 cm SOBP to 1.6% in the 7 cm SOBP. The 10 cm SOBP was the only RBE to report a negative bias.

The highest source of uncertainty is with the RBE estimation in the SOBP setup, reaching 11% on average across the 10 cm SOBP at worst. However, with the number of parameters used in cutting the microdosimetric spectra, it is likely that this uncertainty could be reduced. Currently, the maximum contribution of boron is assumed to be the same as that in the monoenergetic beam in calculating the percent contribution. As the SOBP has much higher fragment contributions overall, including by boron, this could play a large role in the high uncertainty here. However, the average uncertainty of the estimation was just 1.8% across all energies with the SOBP included. This indicates that the fit is, on average, representative of the true RBE.

The variance introduced by the random physical noise was, on average, just 2.3%. This uncertainty, added with the average uncertainty introduced by the

estimation, introduces an overall average uncertainty range of 0.5% to 4.1%, falling within the 5% threshold set by the hypothesis.

4 Conclusions

The hypothesis that the RBE can be estimated by a physical microdosimetric measurement taken in a carbon beam within 5% accuracy was met for each model, on average. While MKM met this threshold for all conditions evaluated, the uncertainty introduced by estimating the RMF and RBE_{LEM} did exceed this 5% threshold at specific points.

While this feasibility study was investigative in nature, it will also be important to experimentally validate the uncertainty analysis in the future. For many of the sources of noise, this process will be straight forward once the LET-1/2 is purchased. To validate the results for electronic uncertainty, for instance, a noise spectrum will be taken at the highest gain segments of the detector. This spectrum can then be subtracted from that at experimental gain settings to account for electronically produced noise. Pulse pile-up may be analyzed following a similar method, where the spectrum is first taken under extremely high count rates. This can be compared to a low count rate taken under similar conditions, to allow the direct effect of pulse pile-up on the spectra to be quantified.

Future work could also be conducted to explore adjustments of the estimation method for both RMF and LEM models in order to reduce this uncertainty. For the RMF model, a method of fitting DSB yield as a function of y^*

should be investigated, as this relationship is less variable across beam energy. For the LEM models, the parameters involved in estimating the percent contribution could be adjusted between monoenergetic beams and SOBP setups. Currently, these parameters are simply fixed across all calculations.

Though this study investigated the error introduced in MC simulated beams of various clinical energies, other beam parameters, such as the presence of a ridge filter, were not investigated. As most facilities indicated in the preliminary survey that they do use a ridge filter, the effect of this presence on the estimation of RBE_{LEM} should be quantified by repeating this analysis.

It would be interesting to explore a fit for each model in the tail region following the Bragg peak. However, this would require separate models than those used in the entrance region and Bragg peak and would, in turn, complicate the assessment as fragments are not the principal ions fit by the current estimation. This would likely be possible to calculate independently, as Helium and Protons are the primary dose contributors and produce relatively constant dose throughout the tail.

5 Appendix

5.1 Microdosimetry

5.1.1 146 MeV/u Monoenergetic Beam

Table 39. Displays lineal energy values and RBE calculated by each model for 146 MeV/u monoenergetic beam.

146 MeV/u Monoenergetic						
Depth (cm)	\bar{y}_F	\bar{y}_D	y^*	MKM	RMF	LEM
0.5	20.87	37.27	26.70	1.94	1.50	2.72
1.0	21.60	35.45	27.30	1.94	1.53	2.70
1.5	22.46	36.43	27.96	1.95	1.55	2.69
2.0	23.60	37.42	28.88	1.96	1.59	2.67
2.5	25.05	37.65	30.08	1.97	1.63	2.65
3.0	26.95	38.73	31.71	1.98	1.69	2.62
3.5	29.80	42.69	34.22	2.00	1.78	2.57
4.0	34.32	44.97	38.54	2.01	1.97	2.47
4.5	43.63	59.74	49.28	2.00	2.52	2.20
5.0	82.30	104.79	77.87	3.68	5.43	3.76
5.5	16.23	70.31	40.78	3.42	2.90	4.90
6.0	11.64	57.34	33.77	3.06	2.50	4.61
6.5	8.88	43.88	25.73	2.55	1.82	4.06
7.0	7.61	34.55	20.30	2.17	1.78	3.96
7.5	7.08	32.88	19.46	2.12	1.74	3.95
8.0	6.61	24.04	18.89	2.08	1.72	3.96
8.5	6.26	25.52	18.17	2.03	1.66	3.96
9.0	5.93	32.18	17.52	1.99	1.67	3.97
9.5	5.61	24.35	17.18	1.97	1.76	3.99
10.0	5.32	31.63	16.96	1.95	1.85	3.99
10.5	5.11	36.32	17.00	1.96	1.66	4.01
11.0	4.88	54.04	16.67	1.94	1.80	4.00
11.5	4.56	32.48	16.56	1.93	1.89	4.01
12.0	4.33	52.03	16.07	1.89	1.84	4.00
12.5	4.02	26.60	15.59	1.86	1.87	3.96
13.0	3.84	46.17	15.34	1.84	1.98	3.91
13.5	3.62	42.46	15.49	1.85	2.06	3.87
14.0	3.37	26.47	15.06	1.82	1.89	3.77
14.5	3.18	33.55	14.66	1.79	2.06	3.71
15.0	3.03	45.11	14.77	1.80	2.21	3.63

15.5	2.91	64.16	14.78	1.80	2.22	3.47
16.0	2.72	31.35	14.28	1.77	2.38	3.36
16.5	2.69	53.62	15.22	1.84	2.33	3.23
17.0	2.51	33.23	14.96	1.82	2.37	3.11
17.5	2.42	51.27	13.98	1.74	2.14	3.01
18.0	2.38	61.62	14.53	1.79	2.46	2.93
18.5	2.33	75.40	13.73	1.73	2.20	2.85
19.0	2.22	43.99	14.71	1.80	2.56	2.74
19.5	2.10	17.61	13.43	1.70	2.62	2.72
20.0	2.34	172.92	14.95	1.82	2.52	2.62
20.5	2.08	41.69	14.95	1.82	2.72	2.58
21.0	1.97	21.00	13.59	1.72	3.07	2.50
21.5	1.99	37.68	13.68	1.72	2.21	2.52
22.0	2.06	62.49	14.89	1.82	2.90	2.45
22.5	2.11	155.76	15.35	1.85	2.99	2.41
23.0	1.97	38.93	14.38	1.78	2.67	2.39
23.5	2.17	116.14	18.11	2.06	2.97	2.35
24.0	2.05	67.14	16.14	1.91	2.99	2.34
24.5	2.03	91.85	15.26	1.84	2.85	2.35
25.0	2.15	351.99	14.20	1.76	2.46	2.32
25.5	1.99	163.32	14.08	1.75	3.75	2.26
26.0	2.05	101.13	15.57	1.87	3.32	2.30
26.5	1.86	25.41	13.99	1.75	3.18	2.28
27.0	2.00	61.02	16.06	1.91	3.87	2.28
27.5	1.95	59.87	16.00	1.90	2.93	2.28
28.0	1.91	32.03	15.93	1.90	3.90	2.26
28.5	1.89	28.43	15.08	1.83	3.37	2.29
29.0	1.99	52.07	17.41	2.01	3.23	2.26
29.5	2.11	87.24	18.02	2.05	3.78	2.21
30.0	2.13	120.24	18.89	2.12	3.24	2.24
30.5	1.97	33.12	17.56	2.02	3.91	2.23
31.0	2.05	67.54	18.62	2.10	3.34	2.22
31.5	2.06	52.06	19.78	2.19	3.25	2.30
32.0	1.99	40.60	19.15	2.14	3.33	2.24
32.5	1.94	35.37	18.84	2.12	3.75	2.29
33.0	2.04	80.66	17.67	2.03	3.05	2.23
33.5	2.07	88.10	17.34	2.00	3.51	2.18
34.0	1.93	31.31	17.10	1.98	3.82	2.22
34.5	1.88	20.95	16.51	1.94	4.23	2.18
35.0	2.19	286.56	16.20	1.92	4.36	2.17
35.5	2.08	54.35	18.64	2.10	3.69	2.18

36.0	2.10	65.91	18.81	2.11	3.90	2.17
36.5	1.94	29.04	17.62	2.02	3.54	2.20
37.0	2.33	212.14	19.53	2.17	3.61	2.13
37.5	2.35	273.81	20.14	2.22	3.50	2.16
38.0	2.14	53.76	21.59	2.33	4.42	2.15
38.5	1.98	46.56	19.61	2.18	3.98	2.12
39.0	2.02	58.97	17.57	2.02	5.24	2.13
39.5	2.09	60.72	19.69	2.18	4.46	2.17
40.0	2.21	104.21	18.98	2.13	5.10	2.23

5.1.2 218 MeV/u Monoenergetic Beam

Table 40. Displays lineal energy values and RBE calculated by each model for 218 MeV/u monoenergetic beam.

218 MeV/u Monoenergetic						
Depth (cm)	\bar{y}_F	\bar{y}_D	y^*	MKM	RMF	LEM
0.5	16.12	40.82	23.67	1.83	1.37	2.53
1.0	16.31	41.88	23.89	1.84	1.38	2.52
1.5	16.47	37.36	23.88	1.83	1.40	2.52
2.0	16.71	39.51	24.20	1.84	1.39	2.51
2.5	16.89	34.64	24.37	1.84	1.41	2.51
3.0	17.13	33.33	24.57	1.84	1.41	2.51
3.5	17.41	44.62	24.64	1.84	1.43	2.50
4.0	17.73	36.21	25.05	1.85	1.44	2.50
4.5	18.09	35.35	25.43	1.85	1.45	2.50
5.0	18.45	37.00	25.60	1.85	1.46	2.49
5.5	18.98	36.59	26.12	1.85	1.48	2.49
6.0	19.57	37.37	26.65	1.86	1.50	2.48
6.5	20.28	36.09	27.30	1.86	1.52	2.47
7.0	21.23	37.04	28.17	1.87	1.56	2.46
7.5	22.45	38.63	29.37	1.88	1.60	2.45
8.0	24.16	39.62	31.15	1.89	1.67	2.42
8.5	26.62	41.34	33.90	1.92	1.77	2.38
9.0	30.55	47.14	38.48	1.94	1.98	2.31
9.5	37.80	60.45	48.40	1.94	2.46	2.10
10.0	67.88	103.52	75.64	3.34	4.70	3.22
10.5	13.68	61.30	34.98	2.83	2.46	3.85
11.0	11.92	56.10	33.54	2.81	2.43	3.91
11.5	10.35	58.44	31.75	2.76	2.35	3.90
12.0	8.88	49.18	28.75	2.62	2.21	3.78
12.5	7.84	56.41	25.91	2.47	2.14	3.63
13.0	6.89	46.13	22.49	2.27	1.83	3.26
13.5	6.16	33.87	18.24	1.99	1.70	3.15
14.0	5.93	29.83	17.82	1.96	1.68	3.14
14.5	5.69	39.32	17.08	1.92	1.70	3.11
15.0	5.52	35.49	16.73	1.90	1.66	3.11
15.5	5.33	28.10	16.53	1.88	1.66	3.12
16.0	5.21	32.74	16.22	1.87	1.66	3.13
16.5	5.08	37.55	16.12	1.86	1.69	3.13
17.0	4.92	35.16	15.85	1.84	1.69	3.15
17.5	4.78	29.55	15.65	1.83	1.70	3.15

18.0	4.65	24.77	15.70	1.84	1.78	3.15
18.5	4.52	28.34	15.26	1.81	1.72	3.16
19.0	4.42	28.47	15.57	1.83	1.70	3.17
19.5	4.31	33.18	15.12	1.80	1.72	3.18
20.0	4.17	25.09	14.97	1.79	1.78	3.19
20.5	4.09	32.19	15.18	1.81	1.76	3.20
21.0	4.00	36.95	15.22	1.81	1.76	3.20
21.5	3.88	39.72	14.81	1.78	1.78	3.21
22.0	3.79	32.97	15.11	1.81	1.75	3.22
22.5	3.68	36.65	14.62	1.77	1.76	3.23
23.0	3.59	45.99	14.67	1.78	1.87	3.23
23.5	3.43	24.81	14.30	1.75	1.96	3.22
24.0	3.36	34.19	14.47	1.77	1.77	3.23
24.5	3.31	36.58	14.62	1.78	1.76	3.23
25.0	3.20	38.87	14.41	1.76	1.93	3.22
25.5	3.10	35.86	14.45	1.77	1.87	3.21
26.0	3.00	31.64	14.58	1.78	1.92	3.20
26.5	2.93	82.98	14.14	1.75	2.02	3.17
27.0	2.81	22.51	14.67	1.79	2.00	3.14
27.5	2.80	73.26	14.96	1.81	1.97	3.12
28.0	2.58	25.12	13.42	1.69	1.99	3.08
28.5	2.57	47.85	14.31	1.76	2.25	3.03
29.0	2.47	29.08	14.02	1.74	2.07	2.98
29.5	2.41	47.46	13.57	1.71	2.09	2.94
30.0	2.37	54.69	13.66	1.72	2.12	2.90
30.5	2.27	50.98	12.94	1.66	2.22	2.83
31.0	2.26	70.31	13.92	1.74	2.21	2.80
31.5	2.19	59.00	13.87	1.73	2.52	2.72
32.0	2.14	46.78	13.98	1.74	2.27	2.68
32.5	2.06	62.30	13.21	1.68	2.24	2.64
33.0	2.16	318.05	13.21	1.68	2.22	2.59
33.5	1.98	24.14	13.96	1.74	2.19	2.52
34.0	2.01	59.88	13.93	1.74	2.46	2.48
34.5	1.92	44.27	13.73	1.72	2.27	2.43
35.0	1.94	157.22	13.18	1.68	2.67	2.38
35.5	1.88	35.15	14.84	1.81	2.68	2.34
36.0	1.84	53.59	13.26	1.69	2.36	2.31
36.5	1.80	54.98	12.72	1.65	2.60	2.28
37.0	1.83	43.92	14.77	1.80	2.75	2.23
37.5	1.79	55.57	14.05	1.75	2.62	2.22
38.0	1.83	73.23	14.50	1.78	2.60	2.17

38.5	1.71	24.65	13.47	1.71	2.81	2.17
39.0	1.74	42.67	13.50	1.71	2.72	2.13
39.5	1.77	72.48	13.70	1.72	2.86	2.13
40.0	1.71	37.59	13.88	1.74	2.50	2.08

5.1.3 276 MeV/u Monoenergetic Beam

Table 41. Displays lineal energy values and RBE calculated by each model for 276 MeV/u monoenergetic beam.

276 MeV/u Monoenergetic						
Depth (cm)	\bar{y}_F	\bar{y}_D	y^*	MKM	RMF	LEM
0.5	13.99	34.15	22.01	1.77	1.32	2.43
1.0	14.10	36.89	22.21	1.78	1.33	2.42
1.5	14.16	39.44	22.24	1.78	1.33	2.42
2.0	14.24	43.42	22.37	1.78	1.35	2.41
2.5	14.29	37.23	22.53	1.79	1.35	2.41
3.0	14.36	36.80	22.61	1.79	1.34	2.41
3.5	14.45	35.57	22.78	1.79	1.35	2.40
4.0	14.52	35.22	22.89	1.79	1.35	2.40
4.5	14.63	41.24	22.95	1.79	1.36	2.40
5.0	14.73	36.66	23.17	1.80	1.37	2.40
5.5	14.87	44.14	23.22	1.80	1.38	2.40
6.0	14.99	38.68	23.42	1.80	1.38	2.40
6.5	15.11	35.91	23.56	1.80	1.39	2.40
7.0	15.30	36.59	23.81	1.81	1.38	2.40
7.5	15.47	37.58	23.96	1.81	1.40	2.40
8.0	15.64	37.11	23.99	1.80	1.41	2.40
8.5	15.90	35.82	24.30	1.81	1.42	2.40
9.0	16.18	37.59	24.60	1.81	1.42	2.40
9.5	16.51	40.66	24.96	1.82	1.45	2.40
10.0	16.87	35.50	25.39	1.82	1.45	2.40
10.5	17.27	38.07	25.68	1.82	1.47	2.40
11.0	17.80	36.21	26.29	1.83	1.50	2.39
11.5	18.43	36.50	26.92	1.83	1.52	2.39
12.0	19.34	37.42	28.01	1.85	1.57	2.38
12.5	20.54	38.65	29.49	1.86	1.61	2.37
13.0	22.10	39.97	31.50	1.88	1.70	2.34
13.5	24.49	45.73	34.84	1.92	1.85	2.31
14.0	27.87	51.37	40.13	1.96	2.01	2.26
14.5	34.42	63.35	49.59	1.89	2.78	2.02
15.0	85.37	215.60	77.48	4.13	3.98	3.39
15.5	11.37	50.33	31.00	2.53	2.17	3.34
16.0	10.43	52.22	29.86	2.50	2.18	3.39
16.5	9.69	47.77	29.53	2.51	2.19	3.42
17.0	8.95	54.06	28.79	2.51	2.19	3.43
17.5	8.14	59.73	27.32	2.46	2.14	3.37

18.0	7.37	47.44	25.19	2.35	2.03	3.28
18.5	6.79	48.64	23.53	2.27	2.04	3.22
19.0	6.27	40.47	22.13	2.20	1.95	3.08
19.5	5.79	45.32	19.84	2.06	1.73	2.79
20.0	5.41	48.78	17.11	1.89	1.69	2.72
20.5	5.21	33.36	16.54	1.85	1.66	2.70
21.0	5.09	35.49	16.18	1.83	1.63	2.69
21.5	4.97	39.87	15.96	1.82	1.66	2.69
22.0	4.85	38.90	15.65	1.80	1.69	2.69
22.5	4.74	39.59	15.46	1.79	1.71	2.68
23.0	4.65	37.58	15.31	1.78	1.62	2.69
23.5	4.56	26.82	15.44	1.79	1.70	2.69
24.0	4.47	37.48	15.04	1.77	1.68	2.69
24.5	4.39	26.99	15.29	1.79	1.66	2.70
25.0	4.31	31.84	15.00	1.77	1.68	2.71
25.5	4.22	29.54	14.70	1.75	1.67	2.71
26.0	4.16	34.50	15.02	1.77	1.75	2.72
26.5	4.08	41.61	14.57	1.74	1.69	2.72
27.0	3.97	26.57	14.62	1.75	1.71	2.72
27.5	3.90	22.53	14.44	1.74	1.71	2.73
28.0	3.87	35.98	14.65	1.75	1.77	2.73
28.5	3.76	30.08	14.12	1.72	1.67	2.74
29.0	3.74	39.37	14.41	1.74	1.70	2.75
29.5	3.67	31.33	14.63	1.76	1.75	2.75
30.0	3.62	58.41	14.43	1.74	1.78	2.75
30.5	3.52	29.09	14.02	1.72	1.79	2.76
31.0	3.45	26.19	14.13	1.73	1.71	2.76
31.5	3.45	40.20	14.56	1.76	1.72	2.77
32.0	3.32	32.30	13.63	1.69	1.79	2.81
32.5	3.26	21.89	14.35	1.74	1.82	2.78
33.0	3.23	38.35	14.11	1.73	1.78	2.78
33.5	3.18	52.70	13.97	1.72	1.86	2.79
34.0	3.10	32.96	14.11	1.73	1.81	2.79
34.5	3.00	28.76	13.51	1.69	1.85	2.80
35.0	2.98	33.55	13.78	1.71	1.86	2.80
35.5	2.93	32.01	14.13	1.73	1.87	2.81
36.0	2.86	30.49	13.53	1.69	1.89	2.80
36.5	2.82	40.98	13.74	1.71	1.85	2.80
37.0	2.76	35.79	13.94	1.72	1.91	2.79
37.5	2.70	32.75	13.80	1.71	1.92	2.80
38.0	2.72	66.45	14.28	1.75	1.94	2.78

38.5	2.58	33.92	13.79	1.71	1.97	2.77
39.0	2.54	29.87	14.38	1.76	2.06	2.75
39.5	2.47	32.21	13.70	1.71	2.00	2.75
40.0	2.47	57.87	13.95	1.73	1.95	2.74

5.1.4 330 MeV/u Monoenergetic Beam

Table 42. Displays lineal energy values and RBE calculated by each model for 330 MeV/u monoenergetic beam.

330 MeV/u Monoenergetic						
Depth (cm)	\bar{y}_F	\bar{y}_D	y^*	MKM	RMF	LEM
0.5	12.69	31.70	20.97	1.73	1.30	2.36
1.0	12.75	40.78	21.03	1.73	1.30	2.34
1.5	12.74	36.22	21.08	1.74	1.29	2.34
2.0	12.75	31.91	21.17	1.74	1.30	2.34
2.5	12.77	35.25	21.25	1.74	1.31	2.33
3.0	12.79	38.00	21.25	1.74	1.31	2.33
3.5	12.82	34.37	21.44	1.75	1.31	2.33
4.0	12.86	37.17	21.56	1.75	1.32	2.33
4.5	12.85	40.51	21.41	1.75	1.32	2.32
5.0	12.86	35.96	21.52	1.75	1.32	2.32
5.5	12.92	40.79	21.66	1.75	1.32	2.32
6.0	12.93	34.25	21.78	1.76	1.33	2.32
6.5	12.99	44.20	21.84	1.76	1.33	2.32
7.0	13.04	40.17	22.04	1.77	1.33	2.32
7.5	13.06	34.90	22.11	1.77	1.34	2.32
8.0	13.09	34.69	22.13	1.77	1.35	2.32
8.5	13.19	37.99	22.44	1.78	1.35	2.32
9.0	13.25	40.27	22.48	1.78	1.35	2.32
9.5	13.31	37.52	22.58	1.78	1.35	2.33
10.0	13.39	35.94	22.71	1.78	1.36	2.33
10.5	13.49	35.76	22.84	1.78	1.37	2.33
11.0	13.58	35.29	22.99	1.79	1.37	2.33
11.5	13.75	41.04	23.17	1.79	1.38	2.33
12.0	13.86	40.38	23.21	1.79	1.39	2.33
12.5	13.96	35.46	23.34	1.79	1.40	2.34
13.0	14.15	44.53	23.53	1.79	1.39	2.34
13.5	14.36	37.51	23.87	1.80	1.41	2.34
14.0	14.56	38.85	24.00	1.80	1.42	2.35
14.5	14.79	35.21	24.36	1.80	1.43	2.35
15.0	15.09	35.29	24.69	1.80	1.45	2.35
15.5	15.45	34.71	25.16	1.81	1.46	2.35
16.0	15.90	37.86	25.68	1.81	1.50	2.35
16.5	16.45	35.76	26.48	1.83	1.53	2.35
17.0	17.16	38.79	27.45	1.84	1.56	2.35
17.5	18.09	38.15	28.85	1.86	1.62	2.34

18.0	19.39	43.87	30.91	1.88	1.73	2.32
18.5	21.22	48.87	34.21	1.94	1.83	2.31
19.0	23.22	49.64	37.35	1.96	1.95	2.29
19.5	27.20	57.67	45.27	1.96	2.38	2.15
20.0	44.83	100.25	69.33	2.93	4.06	2.76
20.5	10.14	47.00	28.74	2.35	2.01	3.00
21.0	9.45	58.35	27.52	2.31	2.01	3.03
21.5	8.98	50.55	27.13	2.31	2.02	3.05
22.0	8.51	52.08	26.74	2.31	2.02	3.08
22.5	8.04	42.58	26.50	2.32	2.02	3.09
23.0	7.57	41.73	25.96	2.31	2.05	3.08
23.5	7.10	48.89	25.10	2.29	1.99	3.02
24.0	6.58	42.20	23.32	2.20	1.93	2.96
24.5	6.19	43.53	22.12	2.14	1.92	2.91
25.0	5.90	46.41	21.42	2.11	1.88	2.85
25.5	5.59	46.08	20.48	2.06	1.84	2.77
26.0	5.33	55.99	19.39	2.01	1.78	2.62
26.5	4.96	38.01	16.97	1.86	1.70	2.46
27.0	4.83	40.26	16.23	1.81	1.68	2.43
27.5	4.73	36.73	16.21	1.81	1.65	2.43
28.0	4.59	26.73	15.69	1.78	1.61	2.41
28.5	4.52	32.33	15.56	1.78	1.66	2.41
29.0	4.45	33.54	15.46	1.77	1.61	2.40
29.5	4.35	27.65	15.20	1.76	1.70	2.40
30.0	4.30	41.51	15.07	1.75	1.66	2.42
30.5	4.20	40.52	14.68	1.73	1.67	2.39
31.0	4.15	31.73	14.75	1.73	1.67	2.40
31.5	4.09	33.99	14.46	1.71	1.67	2.40
32.0	4.04	32.03	14.62	1.73	1.68	2.40
32.5	4.00	33.14	14.75	1.74	1.62	2.40
33.0	3.90	30.06	14.25	1.70	1.65	2.41
33.5	3.88	30.05	14.51	1.72	1.67	2.41
34.0	3.86	46.47	14.65	1.74	1.65	2.41
34.5	3.75	34.29	14.17	1.70	1.67	2.42
35.0	3.70	25.03	14.56	1.73	1.66	2.42
35.5	3.70	28.59	14.78	1.75	1.69	2.43
36.0	3.61	35.55	14.12	1.70	1.70	2.43
36.5	3.55	36.40	13.93	1.69	1.75	2.43
37.0	3.51	31.03	13.97	1.70	1.71	2.43
37.5	3.45	27.78	14.06	1.70	1.66	2.44
38.0	3.41	33.71	14.03	1.70	1.74	2.43

38.5	3.36	35.63	13.82	1.69	1.69	2.44
39.0	3.29	32.83	13.62	1.68	1.72	2.44
39.5	3.24	34.35	13.75	1.69	1.70	2.44
40.0	3.21	44.29	13.53	1.67	1.83	2.45

5.1.5 424 MeV/u Monoenergetic Beam

Table 43. Displays lineal energy values and RBE calculated by each model for a 424 MeV/u monoenergetic beam.

424 MeV/u Monoenergetic						
Depth (cm)	\bar{y}_F	\bar{y}_D	y^*	MKM	RMF	LEM
0.5	11.20	31.66	19.68	1.68	1.27	2.26
1.0	11.23	39.84	19.80	1.69	1.26	2.25
1.5	11.18	38.07	19.60	1.68	1.27	2.24
2.0	11.22	52.46	19.86	1.69	1.28	2.23
2.5	11.15	35.46	19.82	1.69	1.28	2.23
3.0	11.11	36.31	19.80	1.69	1.28	2.23
3.5	11.12	34.99	19.98	1.70	1.28	2.22
4.0	11.10	37.41	19.95	1.70	1.28	2.22
4.5	11.03	31.12	19.97	1.70	1.28	2.22
5.0	11.06	39.99	20.13	1.71	1.29	2.21
5.5	11.01	34.85	20.10	1.70	1.29	2.21
6.0	10.98	37.11	20.07	1.70	1.29	2.21
6.5	10.95	34.80	20.09	1.71	1.30	2.21
7.0	10.94	34.15	20.17	1.71	1.28	2.21
7.5	10.92	30.56	20.28	1.71	1.30	2.21
8.0	10.89	33.20	20.12	1.71	1.30	2.21
8.5	10.88	38.40	20.18	1.71	1.30	2.21
9.0	10.86	38.96	20.17	1.71	1.30	2.21
9.5	10.87	43.44	20.35	1.72	1.31	2.21
10.0	10.82	41.76	20.14	1.71	1.31	2.20
10.5	10.85	45.72	20.47	1.72	1.30	2.21
11.0	10.83	37.32	20.47	1.72	1.31	2.21
11.5	10.79	34.62	20.45	1.72	1.31	2.21
12.0	10.79	40.88	20.41	1.72	1.32	2.21
12.5	10.79	35.82	20.53	1.73	1.31	2.21
13.0	10.74	32.12	20.37	1.72	1.33	2.21
13.5	10.78	35.22	20.56	1.73	1.32	2.21
14.0	10.78	33.18	20.73	1.73	1.33	2.22
14.5	10.83	40.38	20.82	1.74	1.33	2.22
15.0	10.82	43.87	20.82	1.74	1.35	2.22
15.5	10.83	35.20	21.04	1.74	1.33	2.22
16.0	10.86	47.50	21.02	1.74	1.34	2.22
16.5	10.85	34.69	21.07	1.74	1.34	2.23
17.0	10.91	48.71	21.25	1.75	1.34	2.23
17.5	10.90	40.10	21.16	1.75	1.34	2.23

18.0	10.95	44.71	21.32	1.75	1.35	2.24
18.5	10.93	34.28	21.36	1.75	1.36	2.24
19.0	11.05	39.15	21.75	1.77	1.36	2.24
19.5	11.08	39.71	21.71	1.76	1.37	2.25
20.0	11.12	38.99	21.78	1.76	1.37	2.25
20.5	11.19	36.92	21.95	1.77	1.38	2.25
21.0	11.28	39.34	22.09	1.77	1.37	2.26
21.5	11.36	38.79	22.23	1.77	1.38	2.26
22.0	11.43	41.59	22.29	1.77	1.39	2.27
22.5	11.54	37.84	22.52	1.78	1.41	2.27
23.0	11.66	39.00	22.72	1.78	1.41	2.28
23.5	11.81	41.37	22.90	1.78	1.41	2.28
24.0	11.95	34.02	23.23	1.79	1.43	2.29
24.5	12.15	38.62	23.49	1.79	1.45	2.30
25.0	12.39	33.06	24.15	1.81	1.47	2.30
25.5	12.68	40.78	24.51	1.81	1.48	2.31
26.0	13.00	37.05	25.19	1.83	1.52	2.32
26.5	13.39	40.23	25.96	1.84	1.55	2.32
27.0	13.91	37.52	27.25	1.87	1.62	2.32
27.5	14.69	47.02	29.18	1.91	1.72	2.33
28.0	15.35	44.63	30.99	1.95	1.77	2.34
28.5	16.10	49.15	32.47	1.97	1.80	2.35
29.0	17.25	48.39	35.09	1.99	1.91	2.34
29.5	19.82	57.51	42.35	2.03	2.36	2.25
30.0	30.59	99.92	64.34	2.83	3.79	2.64
30.5	8.17	49.42	25.43	2.14	1.83	2.62
31.0	7.74	44.98	24.23	2.09	1.81	2.62
31.5	7.48	46.11	23.97	2.09	1.83	2.63
32.0	7.24	44.86	23.56	2.08	1.83	2.65
32.5	7.05	52.06	23.30	2.08	1.84	2.65
33.0	6.83	48.39	23.18	2.08	1.81	2.66
33.5	6.54	42.45	22.65	2.07	1.85	2.66
34.0	6.36	41.89	22.69	2.08	1.84	2.65
34.5	6.14	38.49	22.55	2.08	1.87	2.64
35.0	5.93	50.81	22.07	2.07	1.86	2.61
35.5	5.68	42.37	21.47	2.04	1.83	2.57
36.0	5.47	48.99	20.65	2.01	1.77	2.52
36.5	5.24	43.21	19.81	1.97	1.77	2.48
37.0	5.08	58.35	18.98	1.92	1.76	2.45
37.5	4.95	46.66	18.84	1.92	1.74	2.42
38.0	4.82	48.92	18.51	1.91	1.78	2.40

38.5	4.69	66.88	18.11	1.89	1.74	2.34
39.0	4.54	41.74	17.72	1.87	1.69	2.26
39.5	4.37	41.69	16.59	1.81	1.64	2.14
40.0	4.21	34.39	15.62	1.75	1.62	2.09

5.1.6 5 cm SOBP

Table 44. Displays lineal energy values and RBE calculated by each model for a 5 cm SOBP.

5 cm SOBP						
Depth (cm)	\bar{y}_F	\bar{y}_D	y^*	MKM	RMF	LEM
0.5	16.83	49.17	25.52	1.79	1.38	2.31
1.0	17.09	49.32	25.81	1.79	1.39	2.30
1.5	17.34	47.87	26.07	1.80	1.40	2.29
2.0	17.61	48.43	26.34	1.80	1.41	2.29
2.5	17.94	47.46	26.73	1.80	1.42	2.28
3.0	18.33	46.06	27.19	1.81	1.44	2.27
3.5	18.82	47.58	27.69	1.81	1.45	2.27
4.0	19.39	46.70	28.40	1.81	1.48	2.25
4.5	20.18	46.02	29.60	1.83	1.52	2.23
5.0	21.32	46.82	31.57	1.85	1.71	2.19
5.5	25.85	53.28	38.47	2.01	1.82	2.19
6.0	23.67	48.99	36.65	1.97	1.85	2.20
6.5	24.88	52.60	39.20	2.03	1.90	2.20
7.0	24.19	51.64	38.91	2.02	1.95	2.21
7.5	25.09	54.25	40.18	2.05	2.00	2.21
8.0	25.36	53.65	42.25	2.10	2.08	2.22
8.5	25.93	58.54	43.38	2.13	2.18	2.23
9.0	25.90	59.74	46.32	2.20	2.31	2.25
9.5	26.31	60.49	48.96	2.26	2.54	2.26
10.0	30.91	81.01	55.34	2.40	3.05	2.25
10.5	29.26	72.40	68.35	3.92	4.76	3.34
11.0	10.11	53.64	32.60	2.75	2.33	3.68
11.5	8.98	58.95	30.62	2.68	2.26	3.67
12.0	7.97	49.17	28.40	2.58	2.17	3.61
12.5	7.12	45.37	25.82	2.45	2.01	3.50
13.0	6.49	48.57	23.60	2.32	1.91	3.39
13.5	6.00	50.73	21.65	2.21	1.79	3.24
14.0	5.61	45.59	19.71	2.09	1.70	3.17
14.5	5.36	38.41	19.04	2.05	1.70	3.16
15.0	5.17	40.19	18.64	2.02	1.68	3.15
15.5	5.01	40.03	18.45	2.01	1.71	3.15
16.0	4.84	36.49	18.21	2.00	1.68	3.16
16.5	4.70	39.64	17.98	1.99	1.71	3.16
17.0	4.57	43.10	17.97	1.99	1.70	3.17
17.5	4.44	54.38	17.71	1.97	1.71	3.17

18.0	4.30	37.61	17.66	1.97	1.72	3.17
18.5	4.18	46.79	17.47	1.96	1.77	3.17
19.0	4.04	36.63	17.51	1.97	1.70	3.19
19.5	3.95	43.64	17.35	1.96	1.75	3.18
20.0	3.81	36.67	17.06	1.94	1.80	3.17
20.5	3.72	51.59	16.96	1.94	1.81	3.17
21.0	3.61	42.04	17.00	1.94	1.83	3.17
21.5	3.50	43.95	16.78	1.93	1.84	3.16
22.0	3.43	52.00	16.97	1.94	1.84	3.16
22.5	3.29	40.07	16.68	1.92	1.85	3.15
23.0	3.23	47.77	16.85	1.94	1.89	3.14
23.5	3.13	48.96	16.76	1.93	1.91	3.12
24.0	3.04	41.33	16.57	1.92	1.93	3.11
24.5	2.96	47.41	16.68	1.93	1.95	3.10
25.0	2.87	48.72	16.50	1.92	1.97	3.09
25.5	2.79	73.80	16.32	1.91	1.97	3.06
26.0	2.74	66.21	16.39	1.91	2.03	3.03
26.5	2.64	52.06	16.29	1.91	1.98	3.00
27.0	2.59	55.83	16.40	1.91	2.03	2.98
27.5	2.51	79.89	16.10	1.89	2.08	2.94
28.0	2.45	52.82	16.33	1.91	2.04	2.91
28.5	2.37	53.60	15.98	1.89	2.10	2.87
29.0	2.33	69.27	16.08	1.89	2.12	2.83
29.5	2.28	47.45	16.44	1.92	2.21	2.80
30.0	2.25	70.42	16.43	1.92	2.24	2.75
30.5	2.16	55.15	15.91	1.88	2.29	2.70
31.0	2.13	77.88	15.79	1.88	2.33	2.67
31.5	2.09	55.80	16.04	1.89	2.29	2.62
32.0	2.06	69.70	15.88	1.88	2.35	2.58
32.5	2.05	87.39	16.18	1.91	2.36	2.54
33.0	2.00	63.67	16.28	1.91	2.41	2.50
33.5	1.97	66.50	16.08	1.90	2.38	2.46
34.0	1.97	99.25	15.81	1.88	2.47	2.42
34.5	1.94	70.94	16.49	1.93	2.52	2.37
35.0	1.92	82.24	16.30	1.92	2.52	2.34
35.5	1.88	74.55	15.89	1.89	2.60	2.31
36.0	1.87	70.72	16.10	1.90	2.57	2.27
36.5	1.85	66.65	16.45	1.93	2.65	2.25
37.0	1.81	55.08	15.82	1.88	2.67	2.23
37.5	1.85	198.61	16.20	1.91	2.70	2.21
38.0	1.83	72.44	16.62	1.94	2.86	2.18

38.5	1.82	82.50	16.57	1.94	2.73	2.16
39.0	1.80	62.55	16.64	1.94	2.84	2.15
39.5	1.80	80.34	16.54	1.94	2.75	2.13
40.0	1.80	117.21	16.61	1.94	2.85	2.11

5.1.7 7 cm SOBP

Table 45. Shows the lineal energy values and RBE calculated by each model as a function of depth for a 7 cm SOBP.

7 cm SOBP						
Depth (cm)	\bar{y}_F	\bar{y}_D	y^*	MKM	RMF	LEM
0.5	14.56	50.69	23.74	1.72	1.32	2.18
1.0	14.66	50.67	23.86	1.72	1.32	2.18
1.5	14.76	54.04	23.96	1.72	1.33	2.17
2.0	14.86	50.44	24.14	1.72	1.33	2.17
2.5	14.97	53.56	24.28	1.73	1.34	2.17
3.0	15.07	52.65	24.43	1.73	1.35	2.16
3.5	15.20	51.60	24.62	1.73	1.35	2.16
4.0	15.33	49.67	24.79	1.73	1.36	2.15
4.5	15.50	49.12	25.03	1.73	1.36	2.15
5.0	15.67	49.82	25.27	1.74	1.38	2.15
5.5	15.90	48.40	25.60	1.74	1.39	2.15
6.0	16.12	48.72	25.85	1.74	1.39	2.14
6.5	16.42	46.75	26.32	1.75	1.41	2.14
7.0	16.81	47.95	26.90	1.75	1.43	2.13
7.5	17.28	46.71	27.78	1.76	1.47	2.11
8.0	17.99	47.36	29.31	1.78	1.61	2.09
8.5	19.75	52.36	33.02	1.87	1.68	2.09
9.0	19.35	50.59	33.30	1.88	1.70	2.10
9.5	19.99	52.02	34.73	1.92	1.73	2.10
10.0	19.66	50.77	34.25	1.91	1.75	2.11
10.5	19.97	51.85	34.77	1.92	1.79	2.11
11.0	20.02	50.72	36.13	1.95	1.82	2.12
11.5	19.85	53.05	35.69	1.94	1.86	2.13
12.0	20.46	52.78	38.18	2.00	1.91	2.14
12.5	20.24	55.38	37.82	1.99	1.96	2.14
13.0	20.82	55.68	40.39	2.06	2.04	2.16
13.5	21.13	59.75	41.29	2.08	2.13	2.17
14.0	21.31	58.28	43.94	2.14	2.26	2.18
14.5	23.14	66.04	48.88	2.25	2.49	2.18
15.0	21.45	66.42	51.28	2.31	2.99	2.18
15.5	27.60	85.94	67.94	3.82	3.78	3.04
16.0	8.96	54.13	29.98	2.47	2.10	3.14
16.5	8.27	51.22	28.85	2.45	2.08	3.16
17.0	7.67	51.45	27.76	2.42	2.06	3.15
17.5	7.14	53.87	26.64	2.38	2.02	3.13

18.0	6.60	49.56	25.34	2.33	1.97	3.09
18.5	6.13	47.38	23.65	2.25	1.91	3.02
19.0	5.78	46.08	22.37	2.18	1.87	2.94
19.5	5.48	47.56	21.25	2.13	1.81	2.87
20.0	5.20	47.53	20.02	2.06	1.71	2.76
20.5	4.96	45.89	18.73	1.98	1.66	2.71
21.0	4.81	41.57	18.28	1.96	1.67	2.69
21.5	4.70	41.46	18.05	1.95	1.68	2.70
22.0	4.58	40.31	17.91	1.94	1.68	2.69
22.5	4.47	39.20	17.63	1.92	1.68	2.70
23.0	4.38	42.90	17.57	1.92	1.67	2.71
23.5	4.29	41.35	17.52	1.92	1.66	2.71
24.0	4.21	45.04	17.29	1.91	1.65	2.72
24.5	4.12	45.36	17.23	1.91	1.69	2.71
25.0	4.03	43.55	17.08	1.90	1.69	2.72
25.5	3.96	41.88	17.04	1.90	1.69	2.74
26.0	3.87	52.32	16.85	1.89	1.73	2.73
26.5	3.80	43.96	16.83	1.89	1.71	2.74
27.0	3.71	42.02	16.67	1.88	1.71	2.73
27.5	3.65	46.26	16.68	1.89	1.71	2.74
28.0	3.58	47.69	16.64	1.89	1.76	2.74
28.5	3.49	37.70	16.54	1.88	1.78	2.74
29.0	3.44	52.01	16.61	1.89	1.78	2.74
29.5	3.38	50.64	16.58	1.89	1.81	2.76
30.0	3.31	57.73	16.42	1.88	1.78	2.76
30.5	3.23	42.41	16.47	1.89	1.82	2.75
31.0	3.18	51.71	16.36	1.88	1.80	2.75
31.5	3.12	57.82	16.25	1.87	1.80	2.75
32.0	3.05	56.77	16.21	1.87	1.82	2.76
32.5	2.98	47.92	16.02	1.86	1.88	2.75
33.0	2.92	54.83	15.94	1.86	1.87	2.74
33.5	2.88	50.61	16.21	1.88	1.87	2.73
34.0	2.81	50.18	16.06	1.87	1.92	2.73
34.5	2.75	47.33	16.03	1.87	1.87	2.73
35.0	2.71	50.79	16.13	1.87	1.92	2.73
35.5	2.65	46.80	15.97	1.86	1.91	2.74
36.0	2.60	56.24	15.97	1.87	1.91	2.71
36.5	2.57	53.15	16.01	1.87	1.93	2.70
37.0	2.51	51.72	16.05	1.87	1.98	2.69
37.5	2.49	82.40	15.96	1.87	1.99	2.69
38.0	2.43	55.18	16.12	1.88	1.99	2.67

38.5	2.37	58.86	15.80	1.86	2.00	2.66
39.0	2.32	49.39	15.83	1.86	2.01	2.64
39.5	2.28	49.08	15.83	1.86	2.05	2.63
40.0	2.24	51.84	15.73	1.86	2.11	2.60

5.1.8 10 cm SOBP

Table 46. Shows the lineal energy values and RBE calculated by each model as a function of depth for a 10 cm SOBP.

10 cm SOBP						
Depth (cm)	\bar{y}_F	\bar{y}_D	y^*	MKM	RMF	LEM
0.5	11.48	51.73	21.32	1.59	1.25	1.94
1.0	11.47	47.28	21.39	1.60	1.25	1.93
1.5	11.47	49.60	21.39	1.60	1.25	1.93
2.0	11.44	48.88	21.42	1.60	1.25	1.92
2.5	11.43	53.78	21.44	1.60	1.26	1.92
3.0	11.42	51.52	21.50	1.60	1.26	1.92
3.5	11.40	50.01	21.51	1.60	1.26	1.92
4.0	11.37	49.21	21.55	1.60	1.26	1.92
4.5	11.33	48.42	21.53	1.60	1.26	1.91
5.0	11.33	50.52	21.59	1.61	1.26	1.91
5.5	11.31	49.02	21.65	1.61	1.27	1.91
6.0	11.30	53.80	21.63	1.61	1.27	1.91
6.5	11.29	50.83	21.72	1.61	1.27	1.91
7.0	11.26	49.07	21.75	1.61	1.27	1.91
7.5	11.24	50.96	21.71	1.61	1.27	1.91
8.0	11.24	50.95	21.81	1.61	1.27	1.91
8.5	11.23	52.44	21.84	1.61	1.28	1.91
9.0	11.22	50.69	21.86	1.62	1.28	1.91
9.5	11.21	50.43	21.96	1.62	1.28	1.91
10.0	11.21	50.79	22.00	1.62	1.28	1.91
10.5	11.22	53.98	22.06	1.62	1.29	1.91
11.0	11.21	51.06	22.09	1.62	1.29	1.91
11.5	11.23	51.47	22.17	1.62	1.29	1.91
12.0	11.24	53.24	22.25	1.63	1.29	1.91
12.5	11.24	51.24	22.27	1.63	1.30	1.91
13.0	11.26	54.75	22.37	1.63	1.30	1.91
13.5	11.28	52.35	22.46	1.63	1.30	1.91
14.0	11.31	52.78	22.58	1.63	1.31	1.91
14.5	11.31	51.91	22.54	1.63	1.31	1.91
15.0	11.36	52.68	22.69	1.64	1.32	1.91
15.5	11.40	50.96	22.84	1.64	1.32	1.92
16.0	11.45	52.29	22.99	1.64	1.32	1.92
16.5	11.51	52.93	23.12	1.64	1.33	1.92
17.0	11.58	53.10	23.33	1.65	1.33	1.92
17.5	11.65	50.53	23.50	1.65	1.34	1.92

18.0	11.75	51.02	23.73	1.65	1.35	1.92
18.5	11.87	51.54	24.03	1.66	1.36	1.92
19.0	12.01	51.91	24.39	1.66	1.38	1.92
19.5	12.19	52.63	24.92	1.67	1.40	1.92
20.0	12.43	50.39	25.78	1.69	1.46	1.91
20.5	13.00	52.96	28.39	1.75	1.51	1.91
21.0	13.02	53.95	28.34	1.75	1.53	1.92
21.5	12.92	53.24	28.14	1.75	1.54	1.92
22.0	13.01	53.89	28.59	1.76	1.55	1.93
22.5	13.05	51.89	28.96	1.77	1.57	1.94
23.0	13.12	50.56	29.47	1.78	1.58	1.94
23.5	13.14	51.70	29.68	1.79	1.60	1.95
24.0	13.16	53.56	30.08	1.80	1.62	1.96
24.5	13.25	52.59	30.59	1.81	1.64	1.96
25.0	13.25	51.82	31.00	1.82	1.66	1.97
25.5	13.30	53.10	31.56	1.84	1.69	1.98
26.0	13.38	52.90	32.20	1.85	1.72	1.99
26.5	13.42	53.47	32.82	1.87	1.75	2.00
27.0	13.50	54.71	33.64	1.89	1.79	2.01
27.5	13.62	55.05	34.67	1.92	1.84	2.02
28.0	13.71	58.93	35.69	1.94	1.90	2.03
28.5	13.82	58.75	37.13	1.98	1.97	2.04
29.0	14.00	60.06	39.15	2.03	2.08	2.05
29.5	14.24	63.54	42.09	2.10	2.25	2.05
30.0	14.52	69.99	46.59	2.20	2.63	2.05
30.5	15.36	83.49	55.23	2.88	3.04	2.34
31.0	7.02	54.41	25.46	2.04	1.75	2.33
31.5	6.76	54.30	24.95	2.03	1.75	2.33
32.0	6.53	54.05	24.61	2.03	1.75	2.34
32.5	6.32	52.77	24.32	2.03	1.75	2.34
33.0	6.13	53.44	23.99	2.03	1.75	2.34
33.5	5.93	52.81	23.59	2.02	1.75	2.33
34.0	5.75	53.29	23.26	2.02	1.76	2.32
34.5	5.58	51.21	23.09	2.02	1.76	2.31
35.0	5.37	49.18	22.51	2.00	1.76	2.30
35.5	5.20	50.15	21.97	1.99	1.74	2.27
36.0	5.04	54.50	21.38	1.97	1.70	2.25
36.5	4.87	49.28	20.88	1.95	1.70	2.22
37.0	4.72	49.81	20.28	1.93	1.68	2.20
37.5	4.60	49.44	19.88	1.91	1.68	2.18
38.0	4.49	54.46	19.46	1.89	1.66	2.16

38.5	4.38	48.98	19.10	1.88	1.64	2.12
39.0	4.28	49.37	18.69	1.87	1.64	2.09
39.5	4.18	53.66	18.24	1.85	1.62	2.04
40.0	4.08	52.03	17.72	1.82	1.61	2.00

5.2 Alpha and Beta values of Each Model

5.2.1 Alpha Values

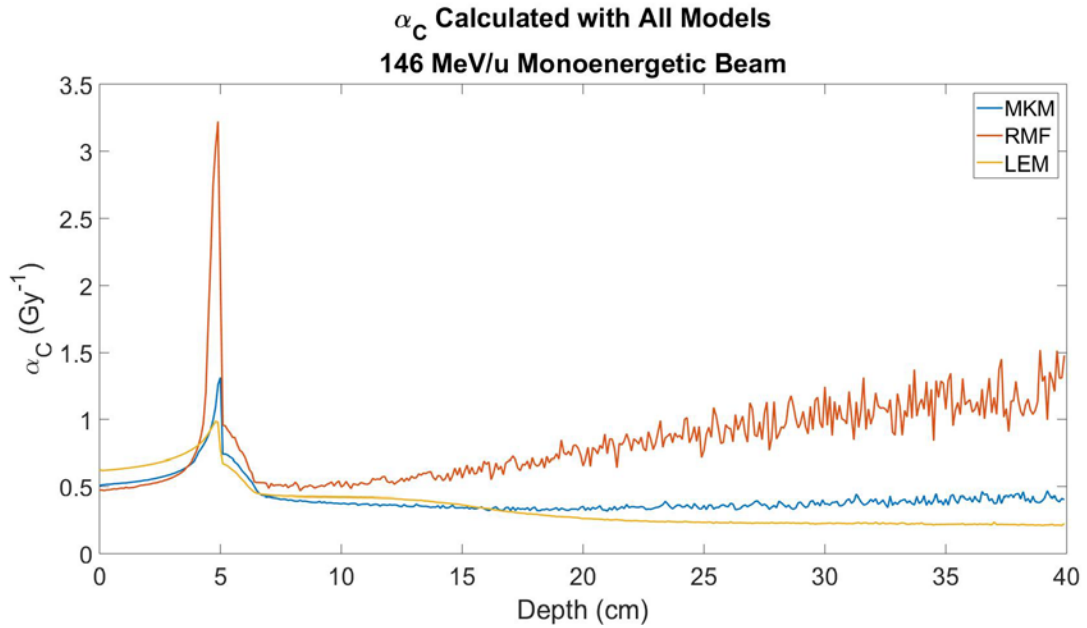


Figure 138. Alpha calculated with all RBE models for 146 MeV/u monoenergetic beam.

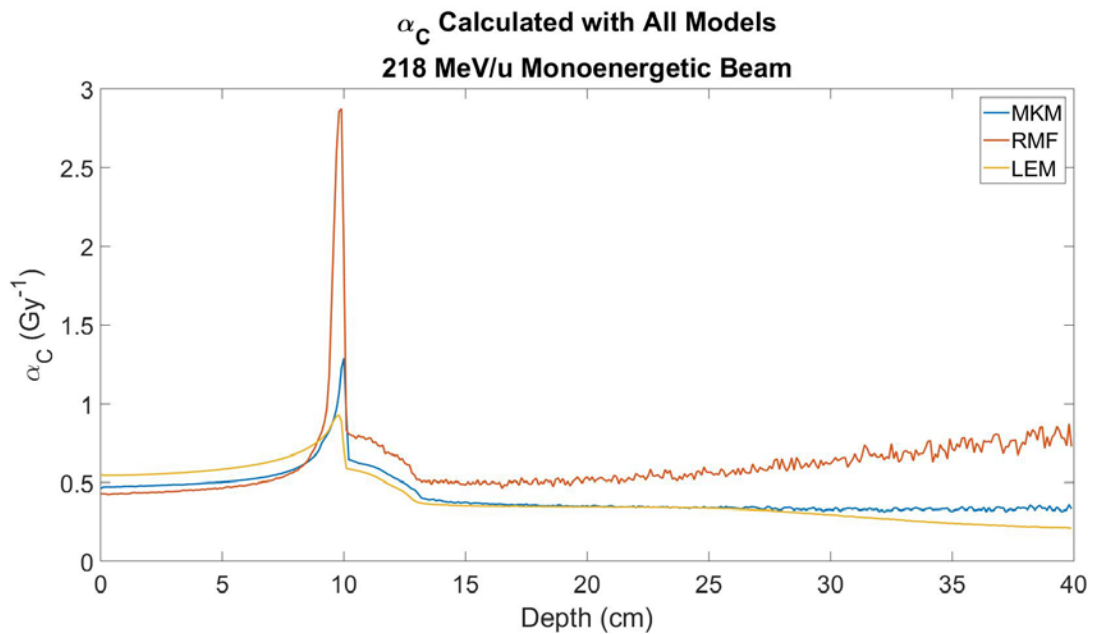


Figure 139. Alpha calculated with all RBE models for 146 MeV/u monoenergetic beam.

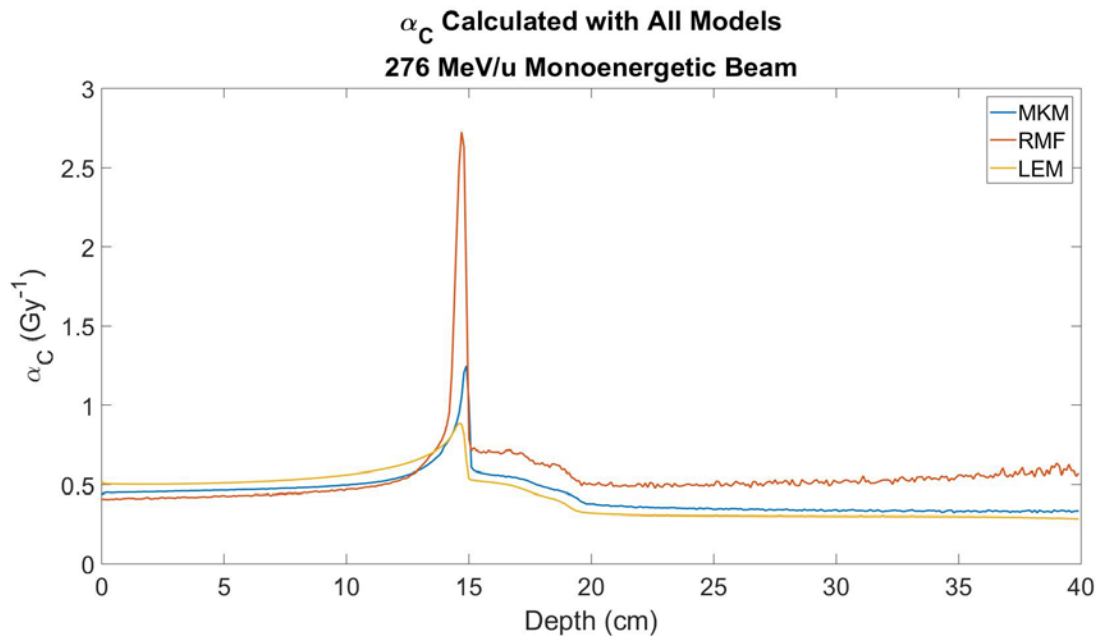


Figure 140. Alpha calculated with all RBE models for 146 MeV/u monoenergetic beam.

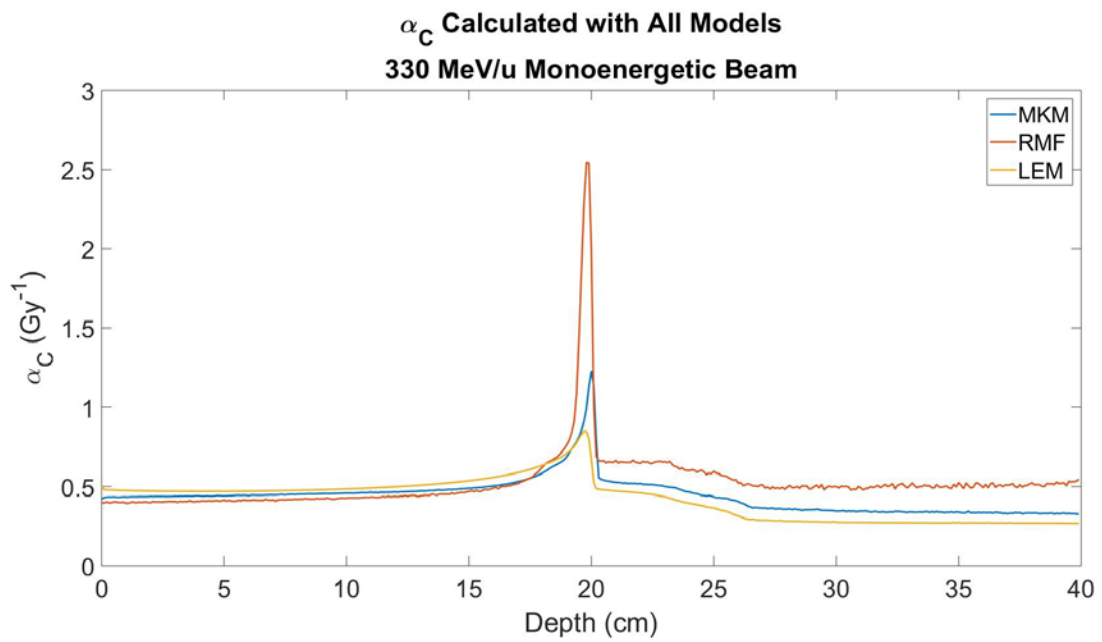


Figure 141. Alpha calculated with all RBE models for 146 MeV/u monoenergetic beam.

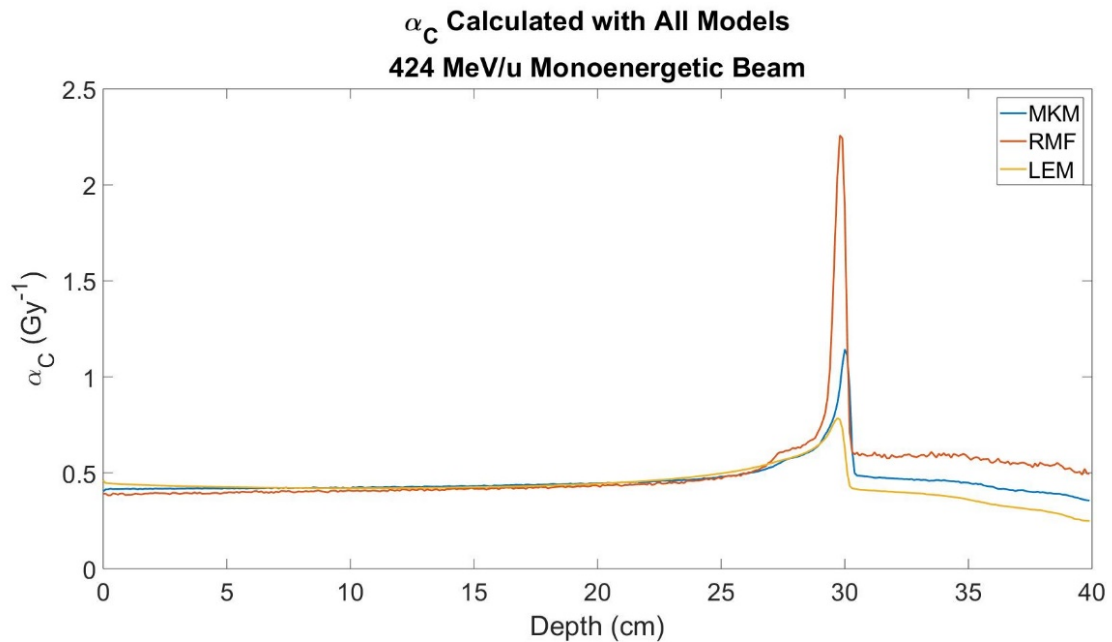


Figure 142. Alpha calculated with all RBE models for 424 MeV/u monoenergetic beam.

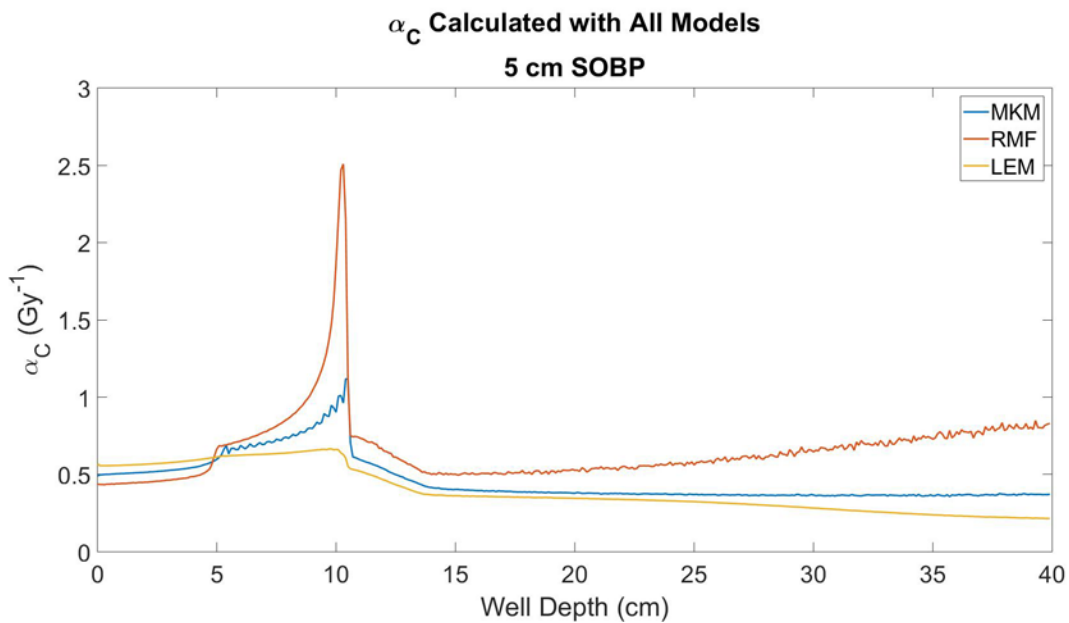


Figure 143. Alpha calculated with all RBE models for 5 cm SOBP.

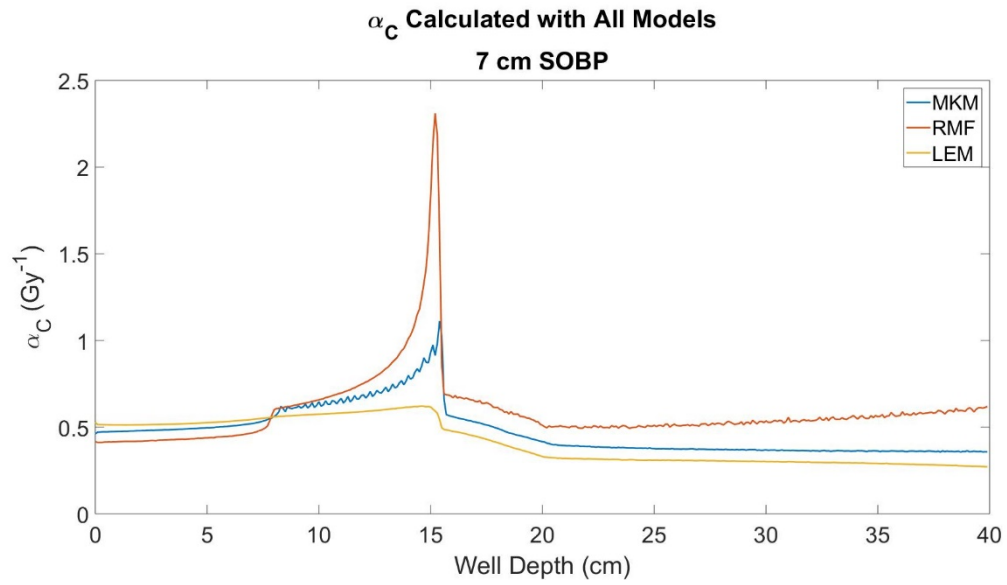


Figure 144. Alpha calculated with all RBE models for 7 cm SOBP.

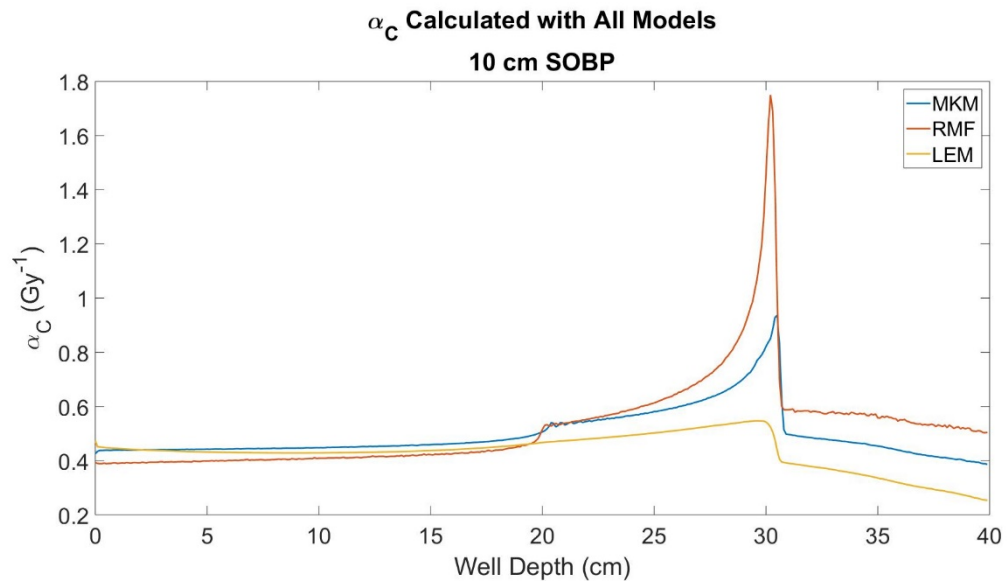


Figure 145 Alpha calculated with all RBE models for 10 cm SOBP.

5.2.2 Beta Values

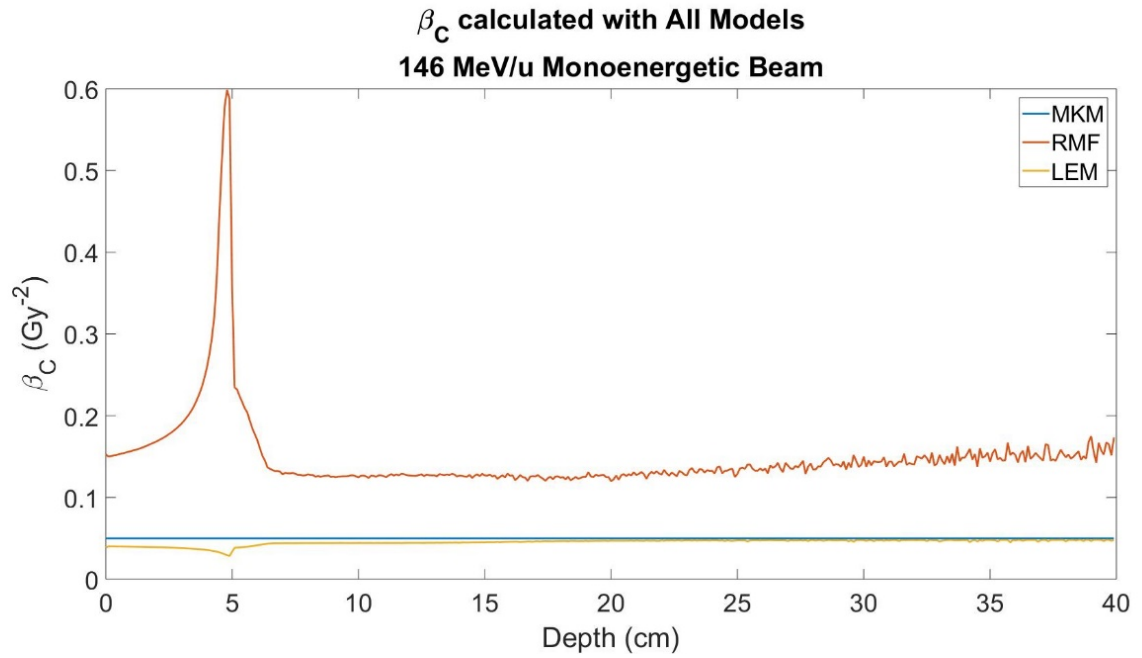


Figure 146. Beta calculated with all RBE models for 146 MeV/u monoenergetic beam.

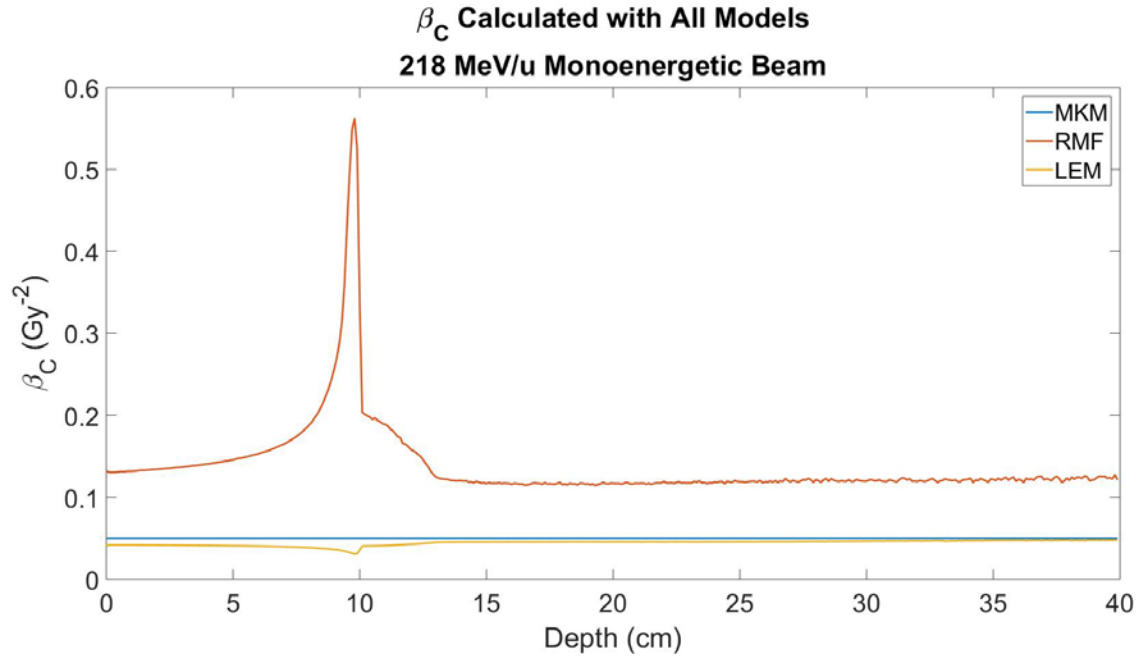


Figure 147. Beta calculated with all RBE models for 218 MeV/u monoenergetic beam.

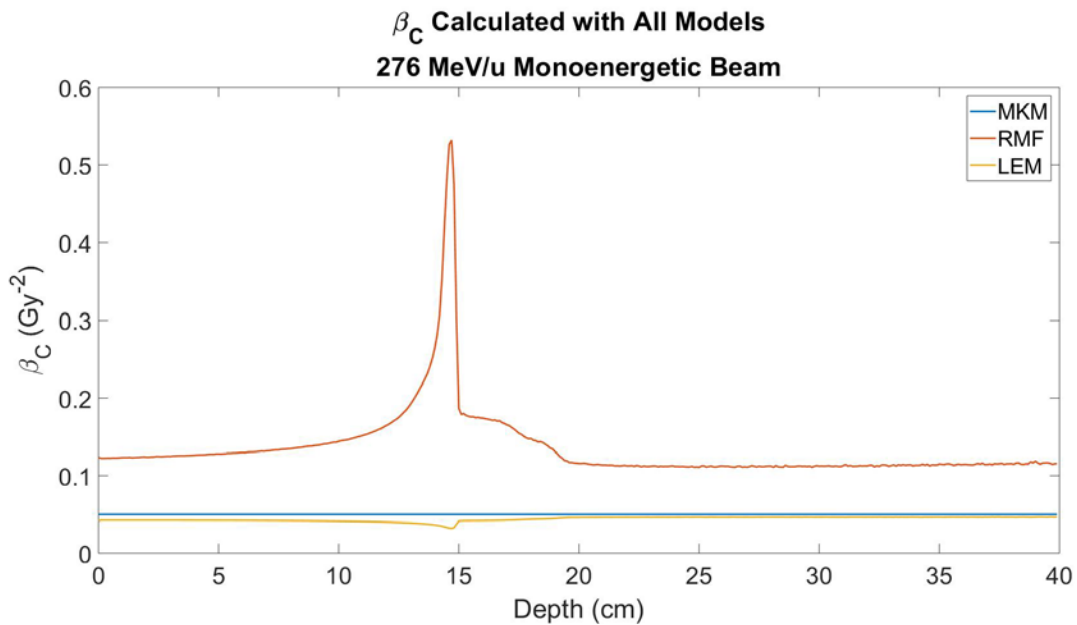


Figure 148. Beta calculated with all RBE models for 276 MeV/u monoenergetic beam.

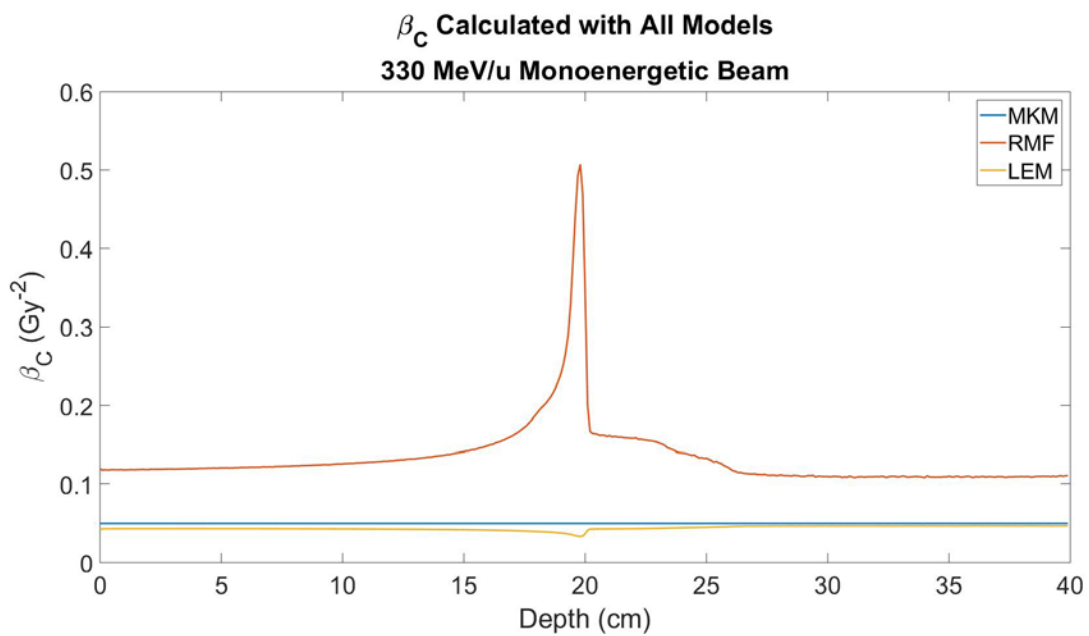


Figure 149. Beta calculated with all RBE models for 330 MeV/u monoenergetic beam.

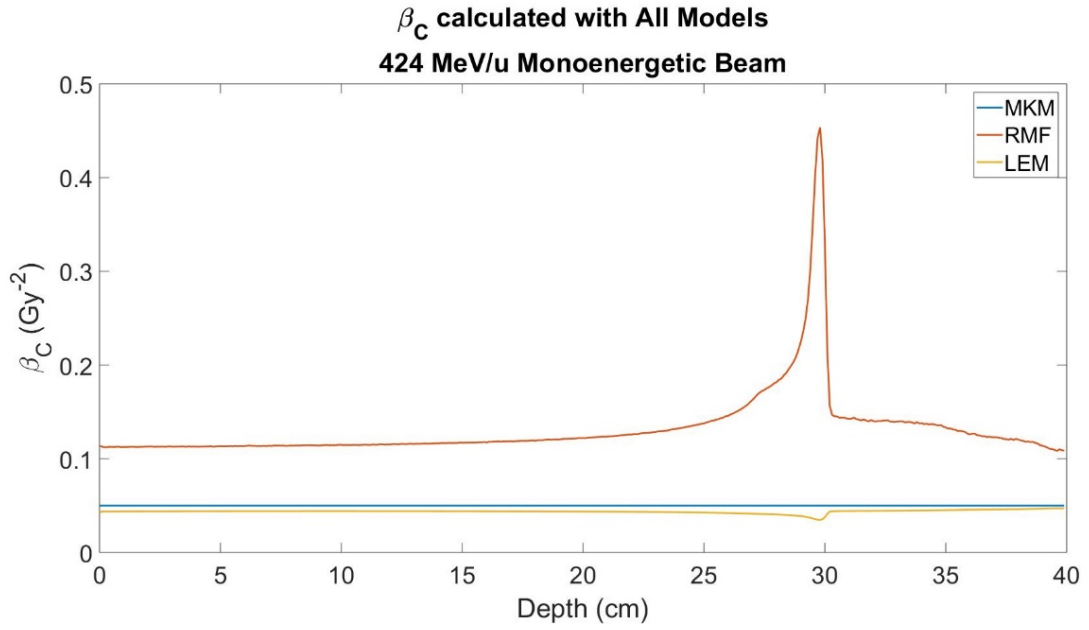


Figure 150. Beta calculated with all RBE models for 424 MeV/u monoenergetic beam.

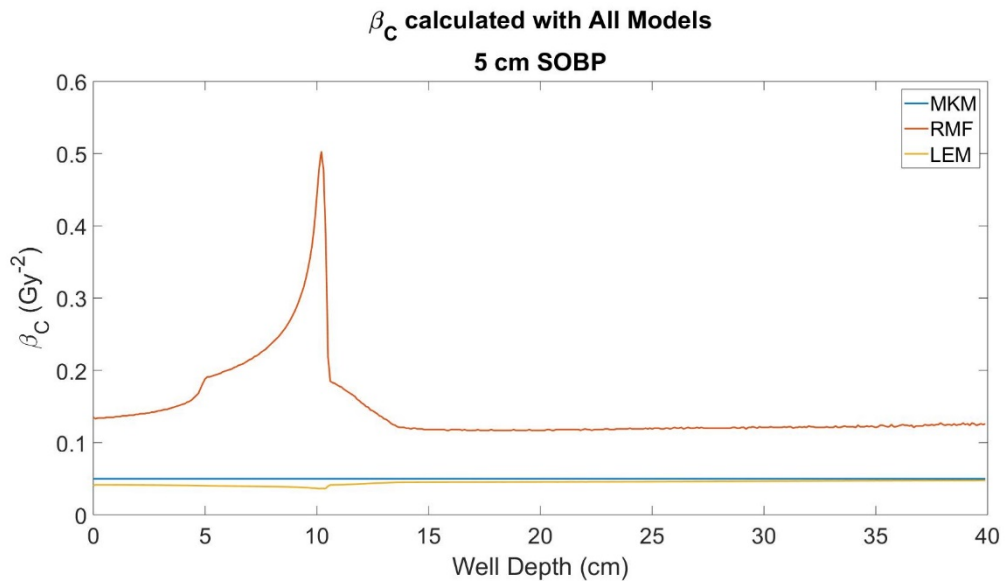


Figure 151. Beta calculated with all RBE models for 5 cm SOBP.

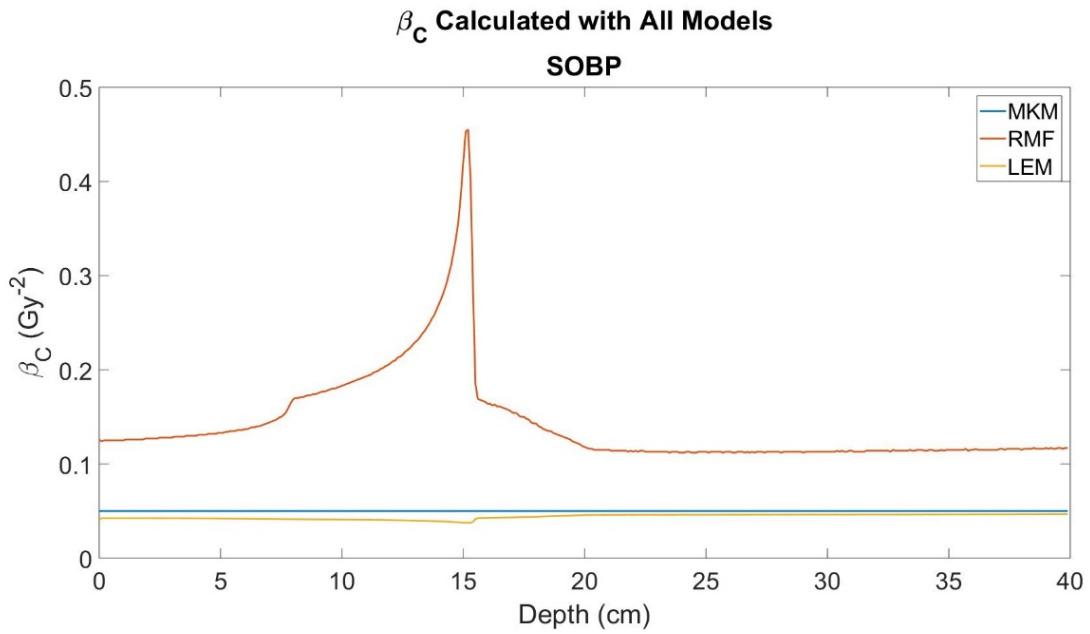


Figure 152. Beta calculated with all RBE models for a 7 cm SOBP.

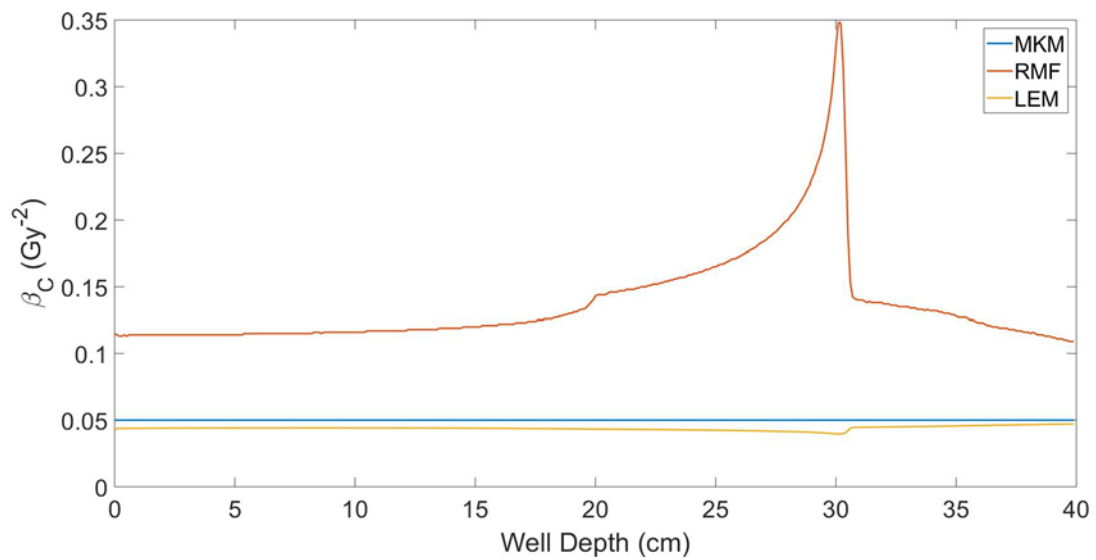


Figure 153. Beta calculated with all RBE models for a 10 cm SOBP.

5.3 RBE

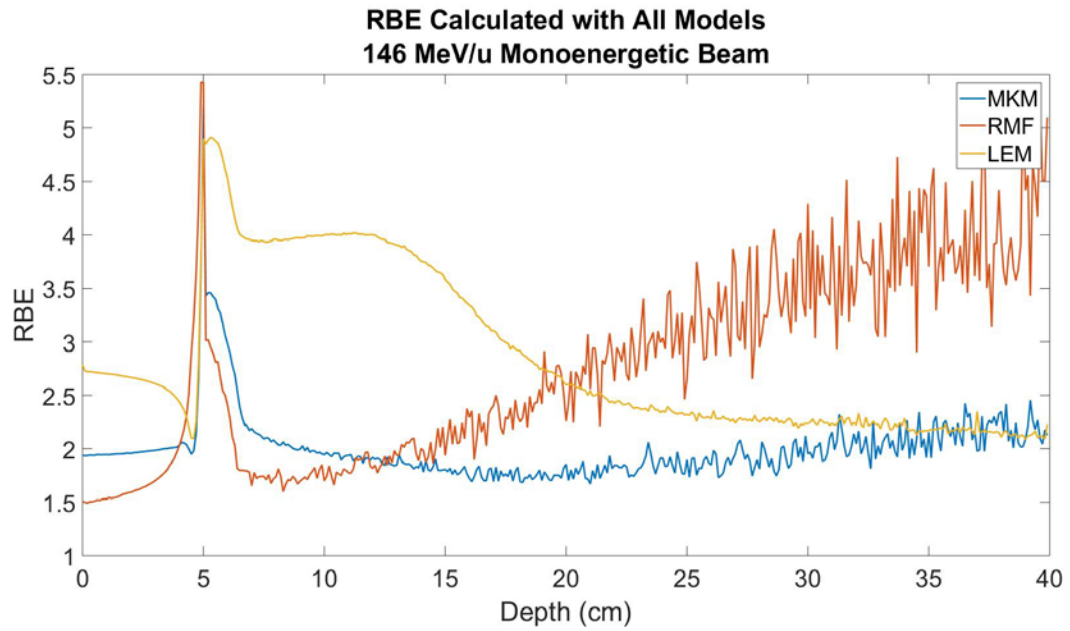


Figure 154. RBE calculated with each model for 146 MeV/u monoenergetic beam.

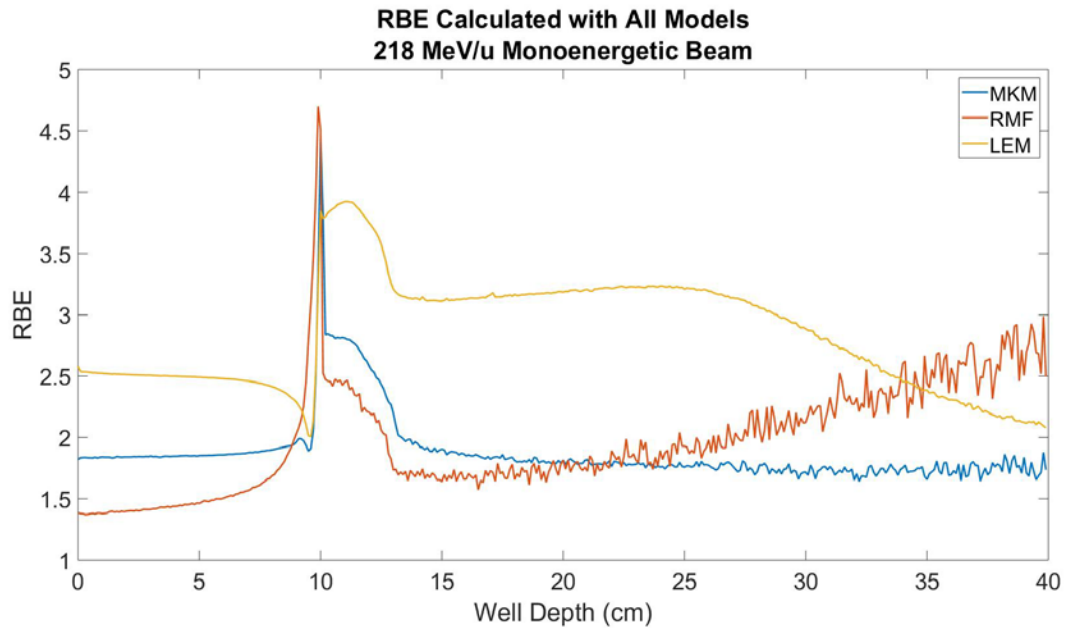


Figure 155. RBE calculated with each model for 218 MeV/u monoenergetic beam.

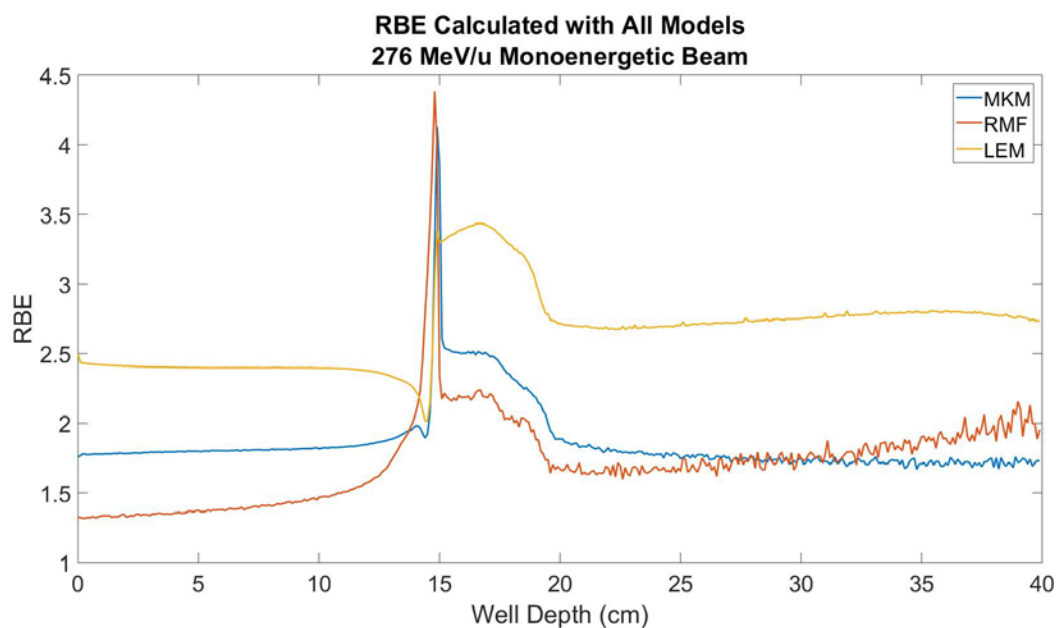


Figure 156. RBE calculated with each model for 276 MeV/u monoenergetic beam.

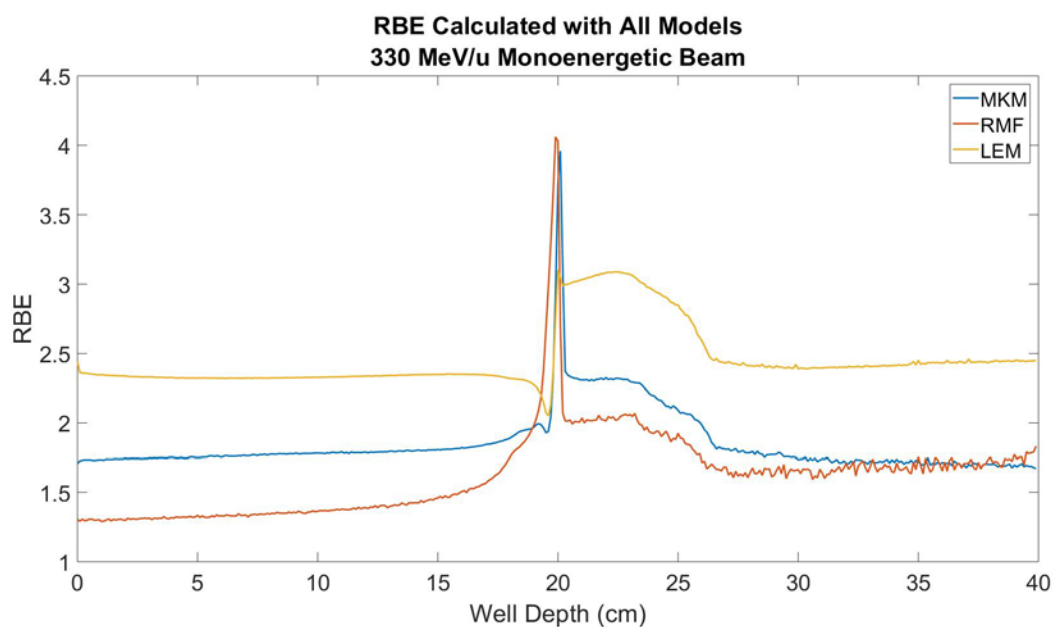


Figure 157. RBE calculated with each model for 330 MeV/u monoenergetic beam.

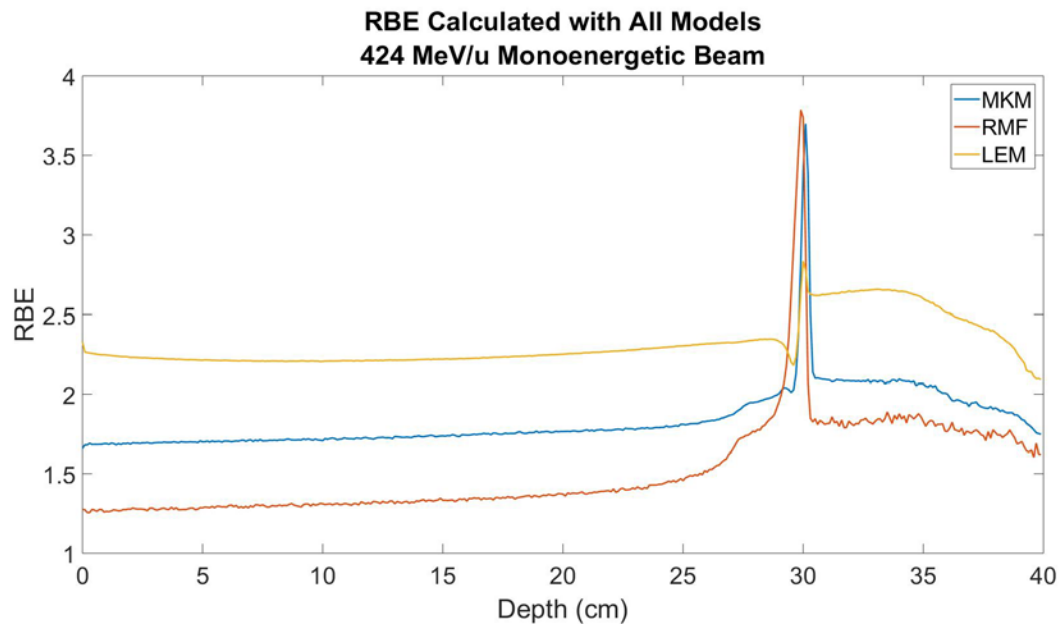


Figure 158. RBE calculated with each model for 424 MeV/u monoenergetic beam.

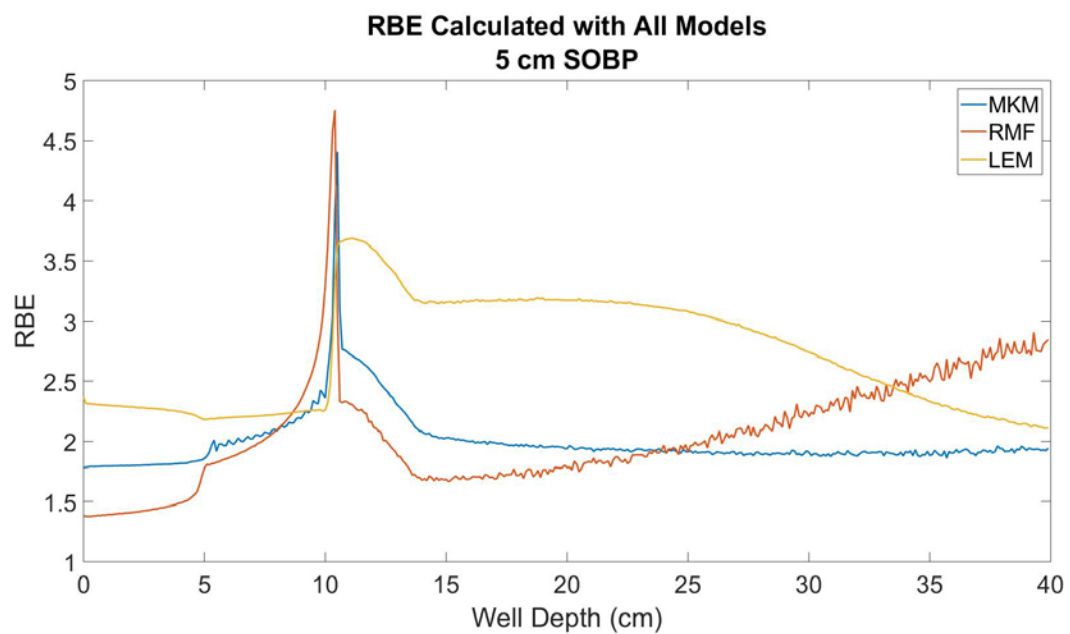


Figure 159. RBE calculated with each model for a 5 cm SOBP.

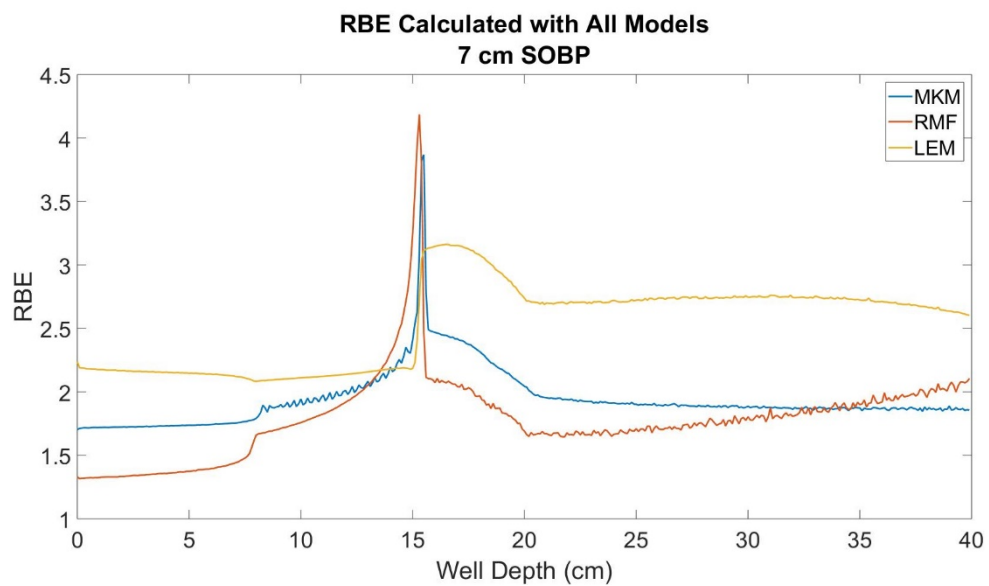


Figure 160. RBE calculated with each model for a 7 cm SOBP.

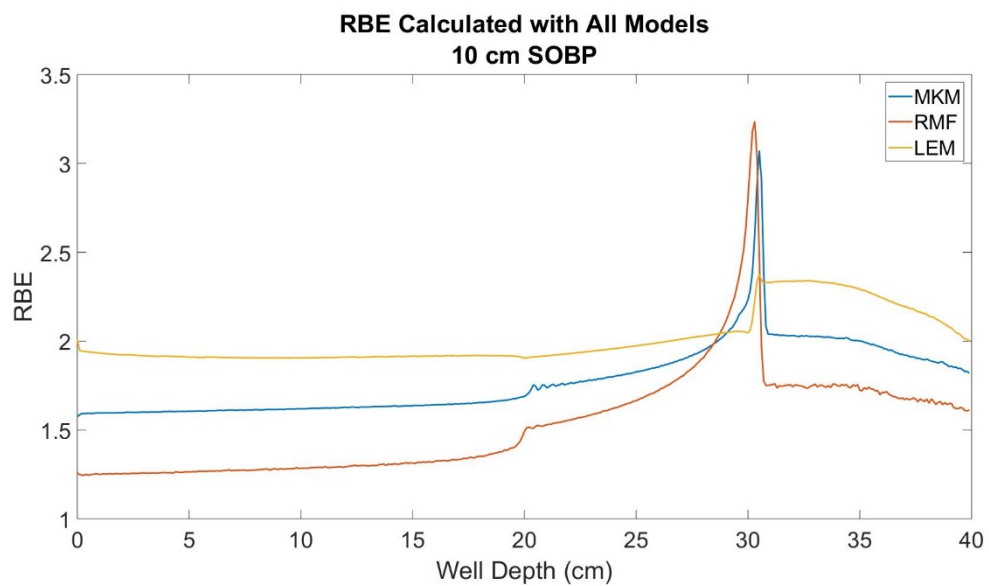


Figure 161. RBE calculated with each model for a 10 cm SOBP.

5.4 Biological Dose

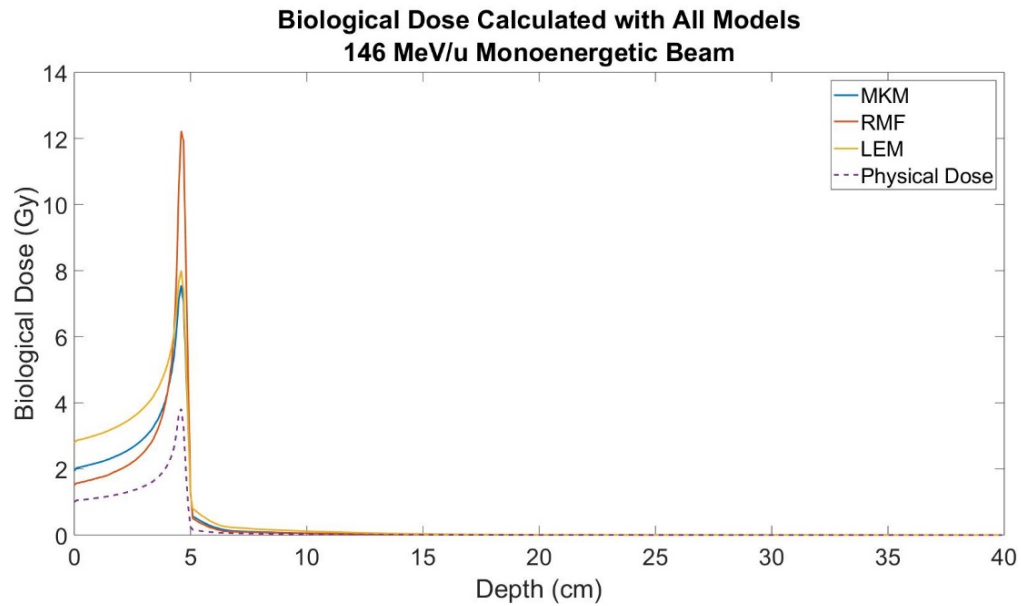


Figure 162. Biological dose calculated with each model for 146 MeV/u monoenergetic beam. Physical dose showed by the dotted line for reference.

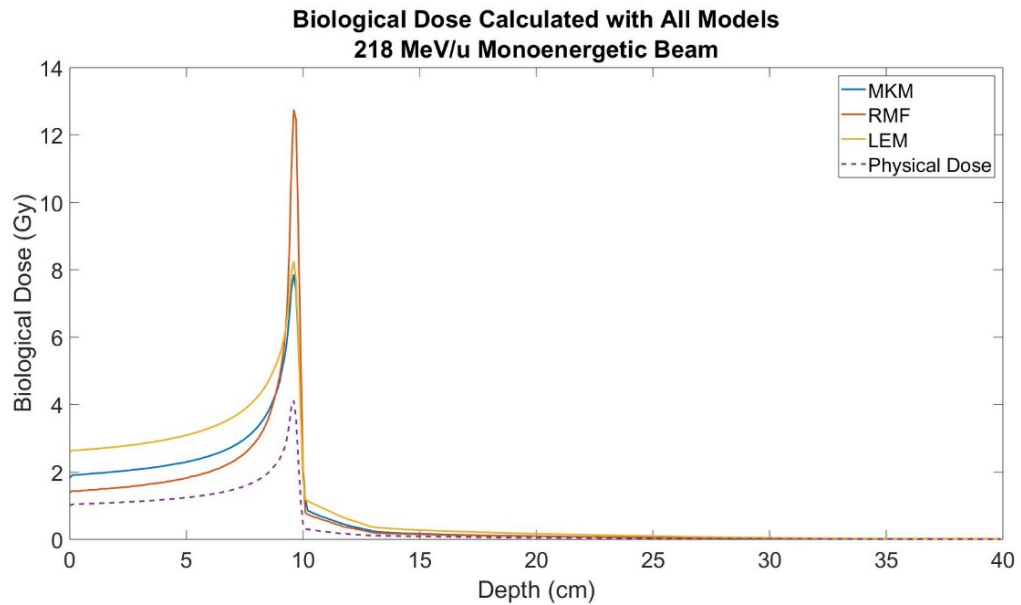


Figure 163. Biological dose calculated with each model for 218 MeV/u monoenergetic beam. Physical dose showed by the dotted line for reference.

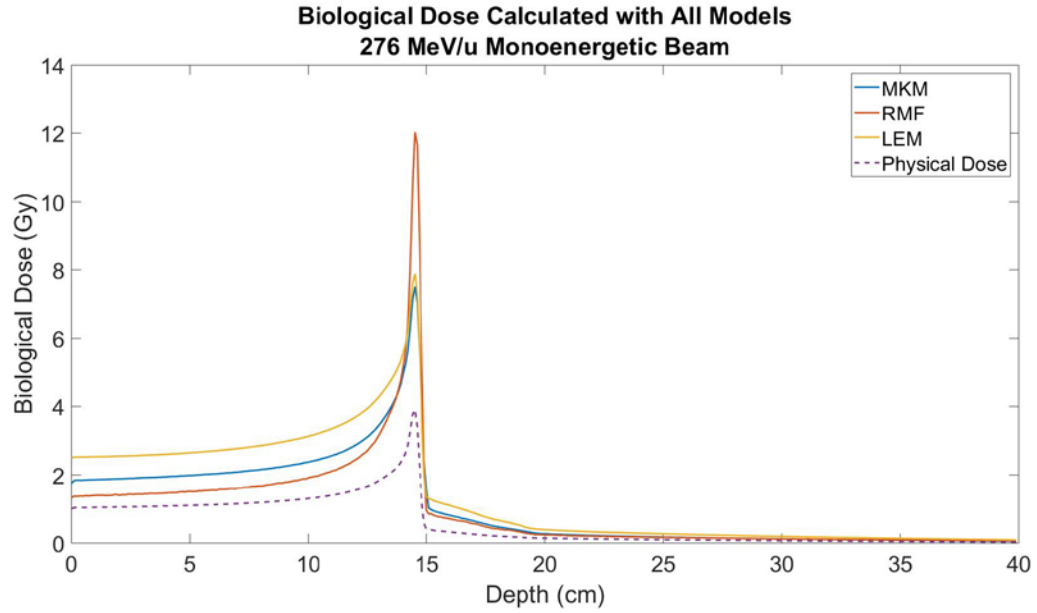


Figure 164. Biological dose calculated with each model for 276 MeV/u monoenergetic beam. Physical dose showed by the dotted line for reference.

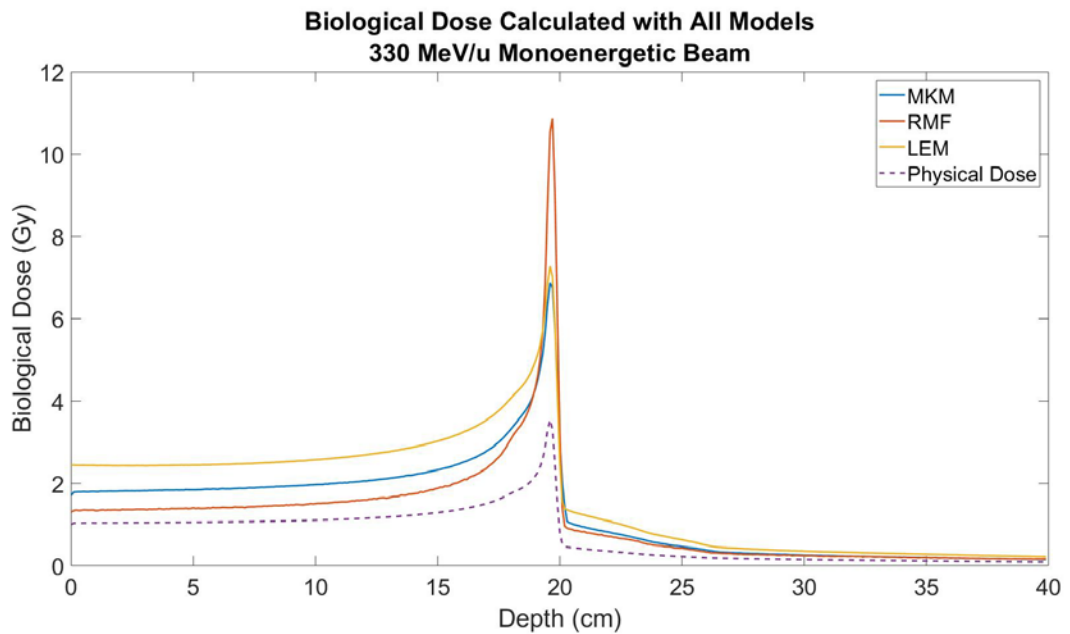


Figure 165. Biological dose calculated with each model for 330 MeV/u monoenergetic beam. Physical dose showed by the dotted line for reference.

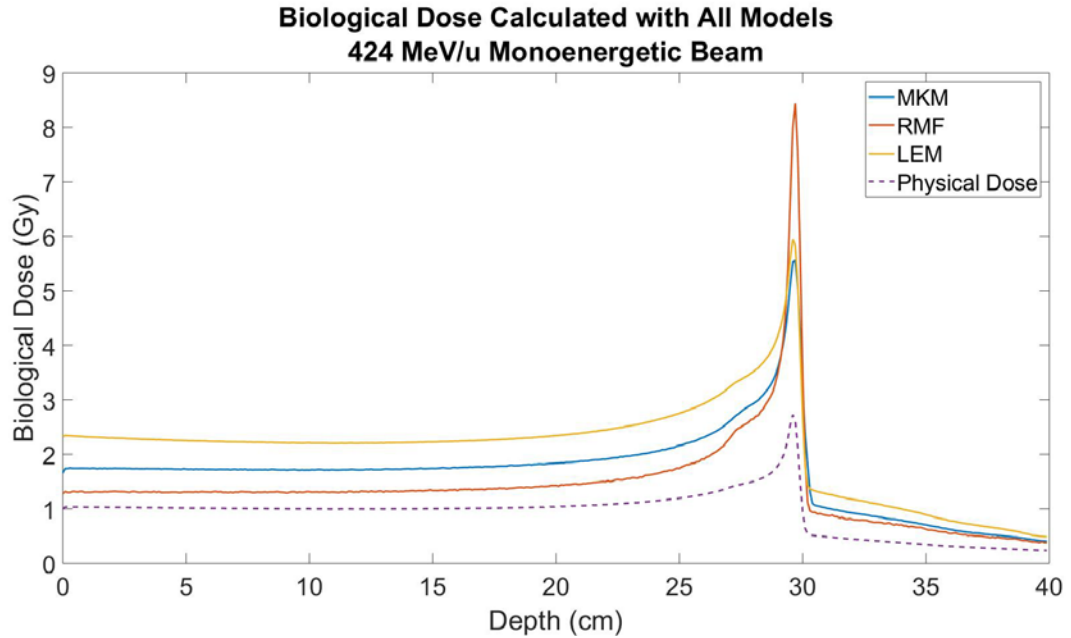


Figure 166. Biological dose calculated with each model for 424 MeV/u monoenergetic beam. Physical dose showed by the dotted line for reference.

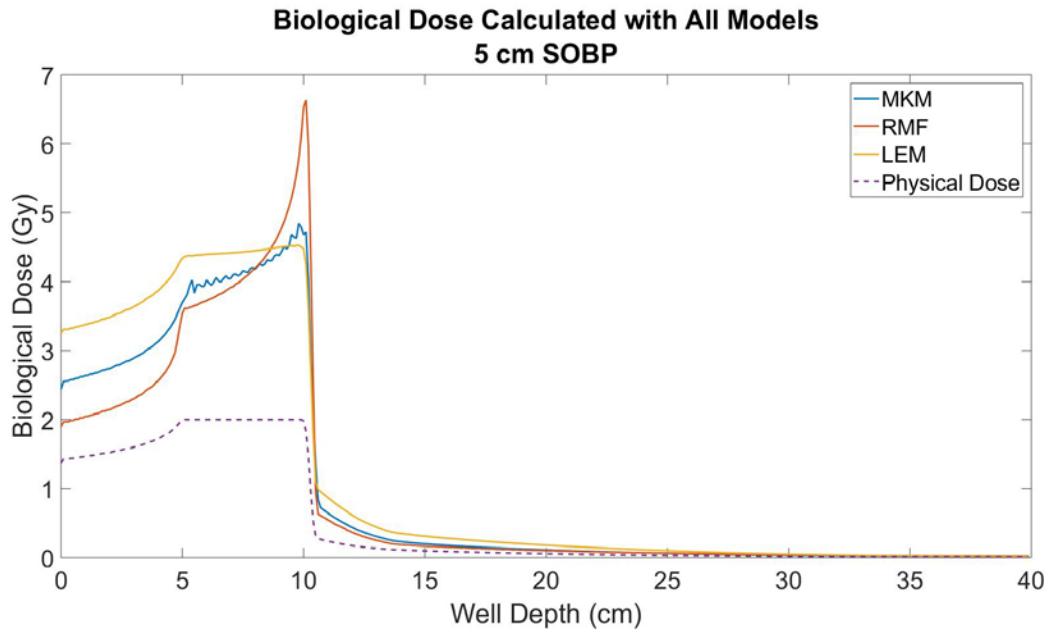


Figure 167. Biological dose calculated with each model for a 5 cm SOBP. Physical dose showed by the dotted line for reference.

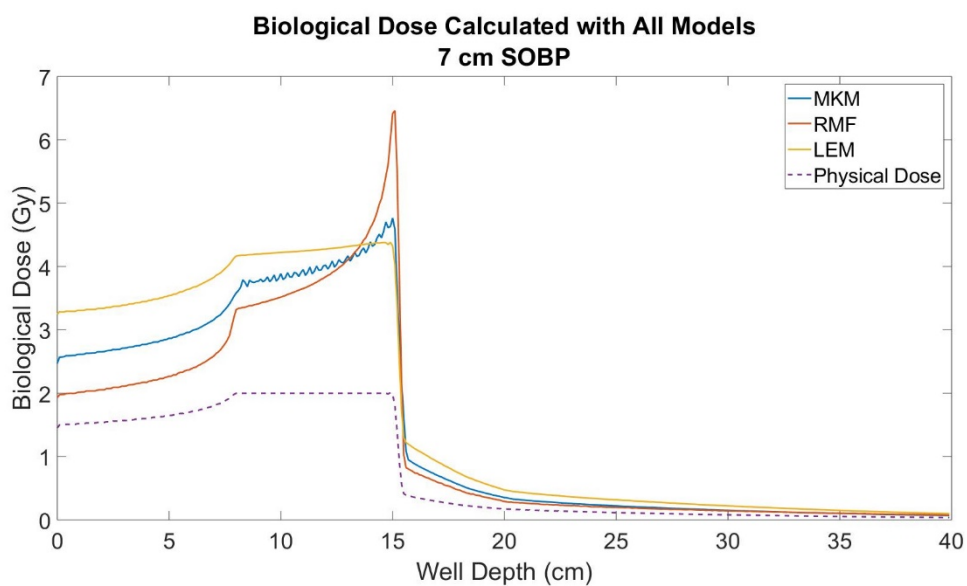


Figure 168. Biological dose calculated with each model for a 7 cm SOBP. Physical dose showed by the dotted line for reference.

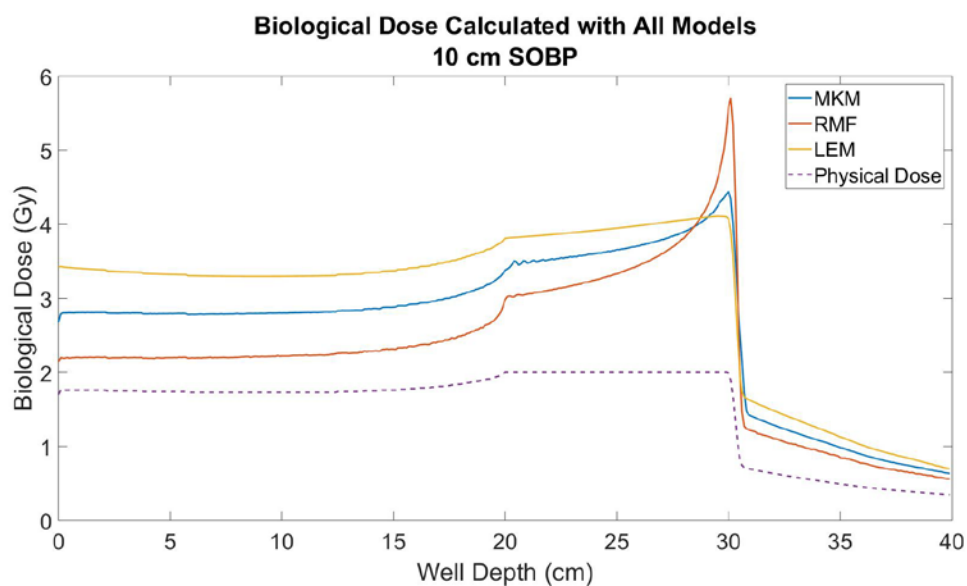


Figure 169. Biological dose calculated with each model for a 10 cm SOBP. Physical dose showed by the dotted line for reference.

5.5 Kinetic Energy

5.5.1 146 MeV/u

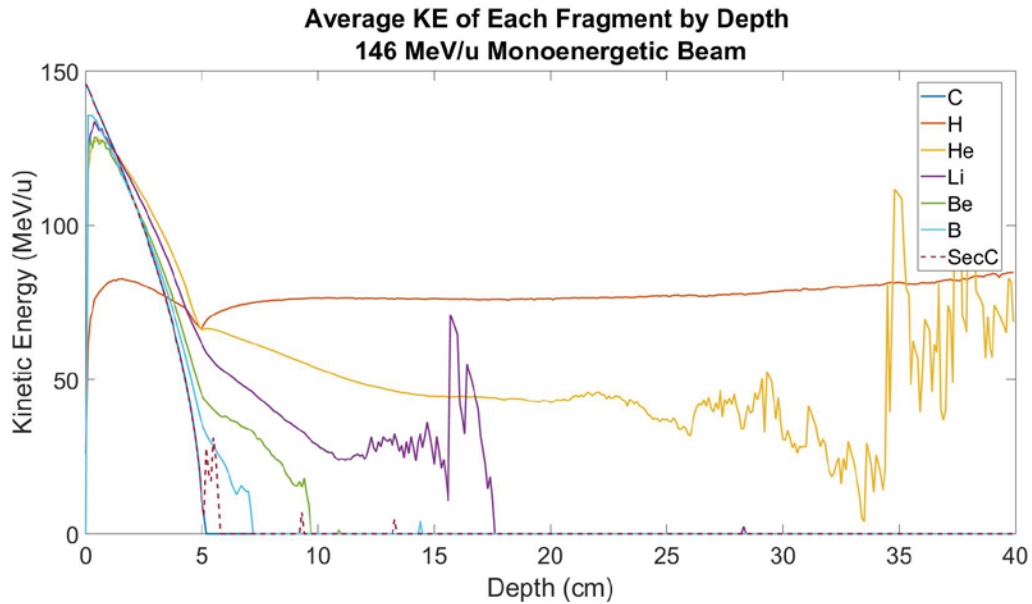


Figure 170. Average kinetic energy of each fragment for a 146 MeV/u monoenergetic beam.

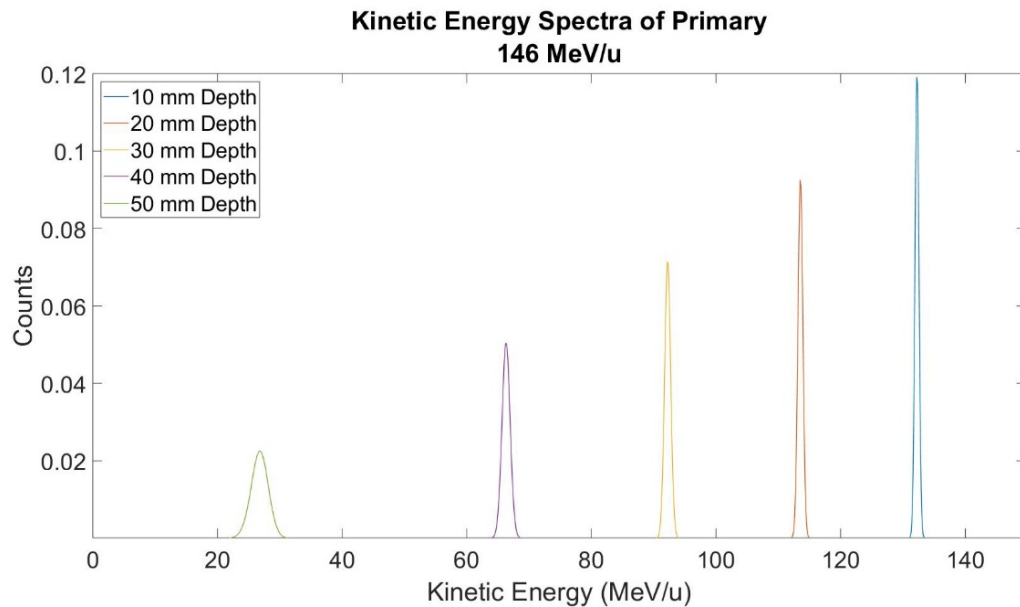


Figure 171. Kinetic energy distribution of primary carbons at the following depths for a 146 MeV/u monoenergetic beam: 10 mm, 20 mm, 30 mm, 40 mm, and 50 mm.

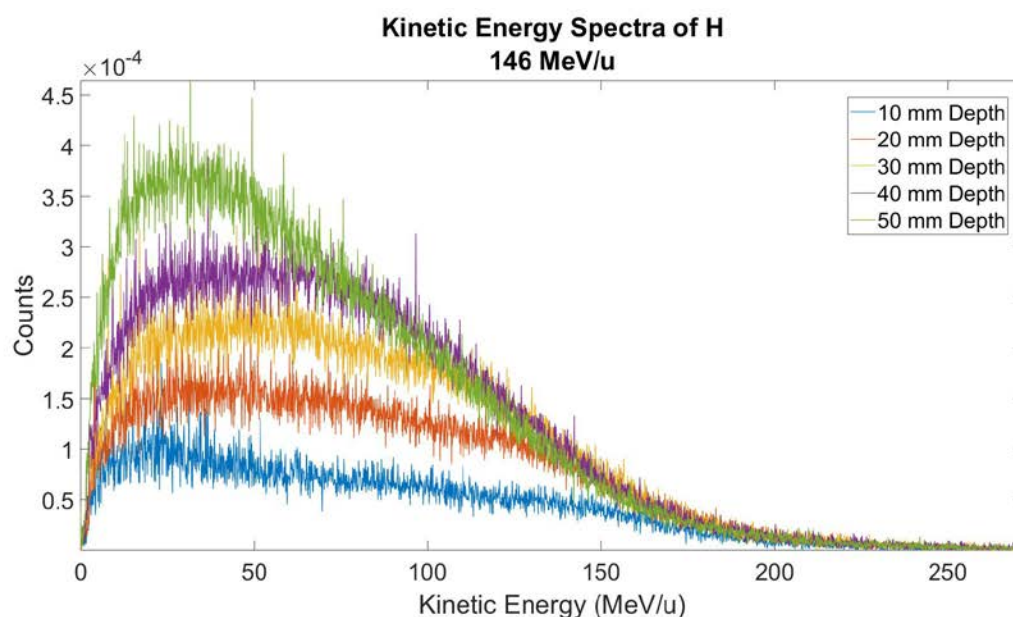


Figure 172. Kinetic energy distribution of secondary H at the following depths for a 146 MeV/u monoenergetic beam: 10 mm, 20 mm, 30 mm, 40 mm, and 50 mm.

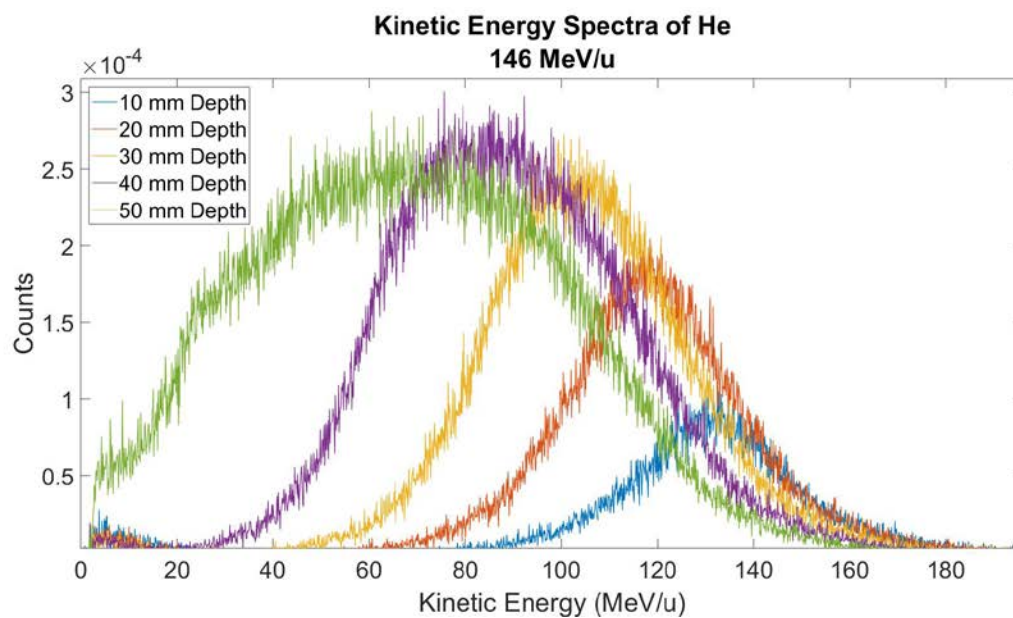


Figure 173. Kinetic energy distribution of secondary He at the following depths for a 146 MeV/u monoenergetic beam: 10 mm, 20 mm, 30 mm, 40 mm, and 50 mm.

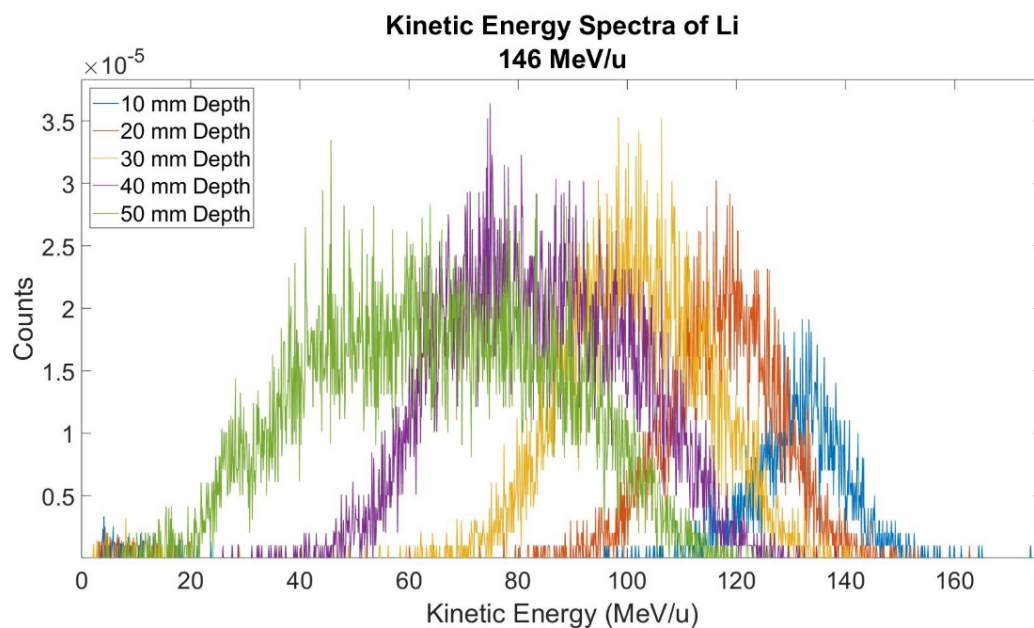


Figure 174. Kinetic energy distribution of secondary Li at the following depths for a 146 MeV/u monoenergetic beam: 10 mm, 20 mm, 30 mm, 40 mm, and 50 mm.

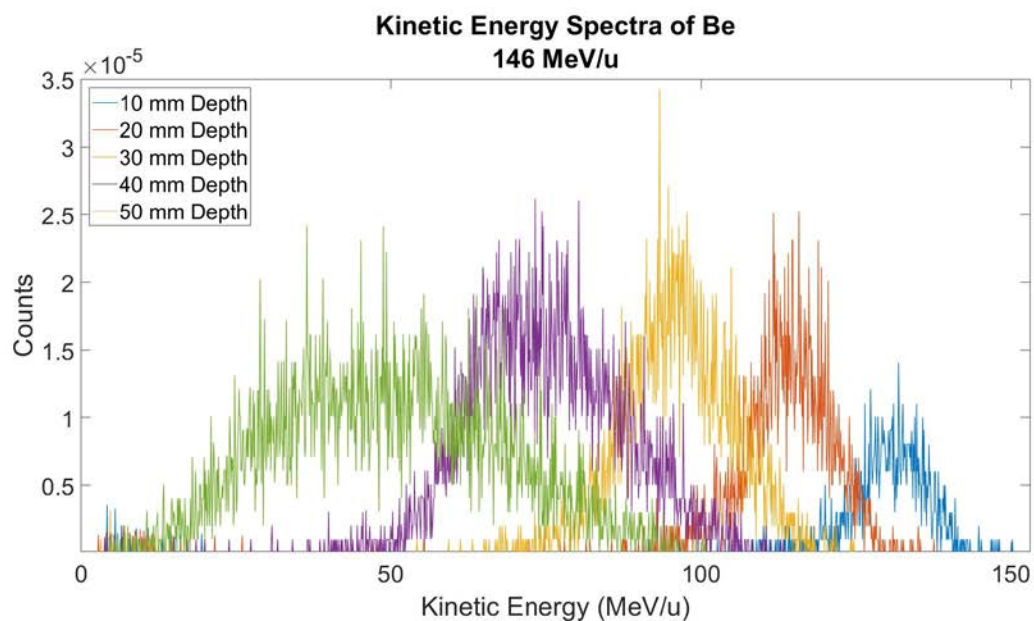


Figure 175. Kinetic energy distribution of secondary Be at the following depths for a 146 MeV/u monoenergetic beam: 10 mm, 20 mm, 30 mm, 40 mm, and 50 mm.

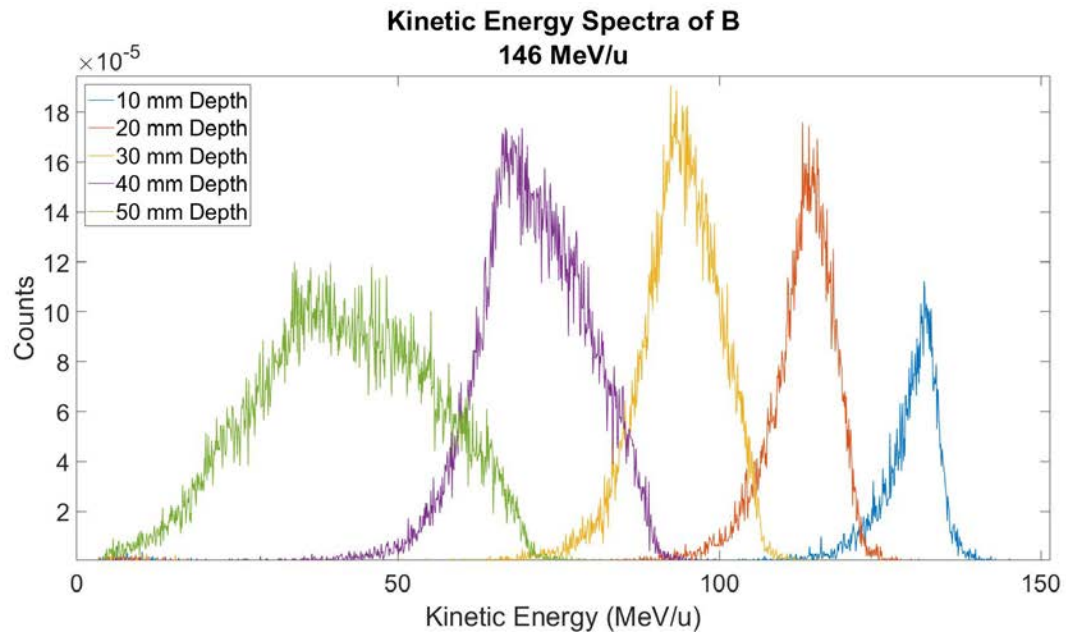


Figure 176. Kinetic energy distribution of secondary B at the following depths for a 146 MeV/u monoenergetic beam: 10 mm, 20 mm, 30 mm, 40 mm, and 50 mm.

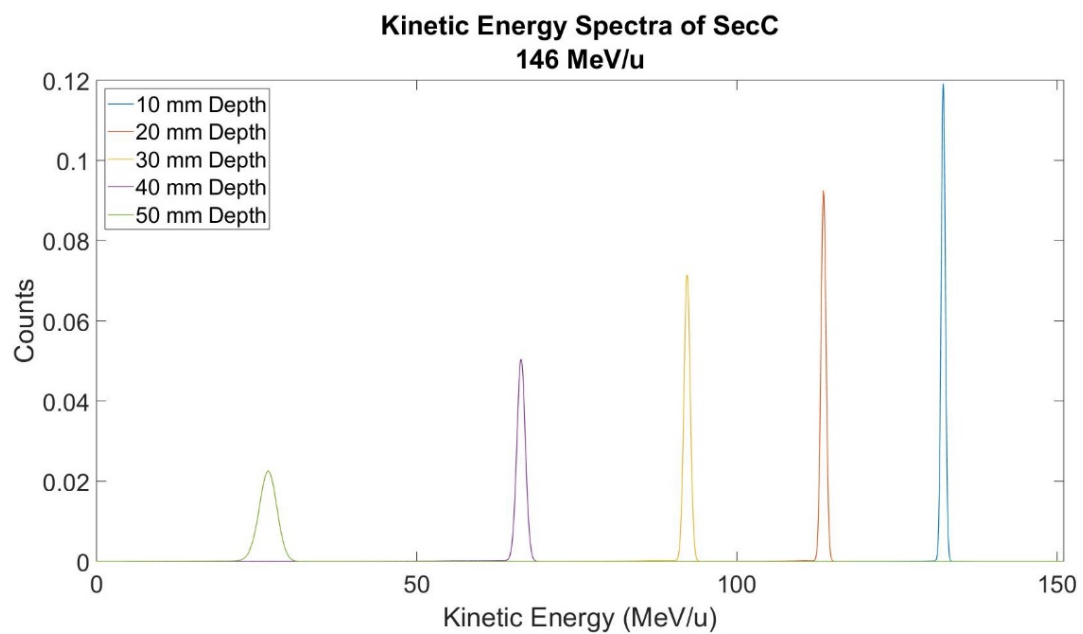


Figure 177. Kinetic energy distribution of secondary carbons at the following depths for a 146 MeV/u monoenergetic beam: 10 mm, 20 mm, 30 mm, 40 mm, and 50 mm.

5.5.2 424 MeV/u

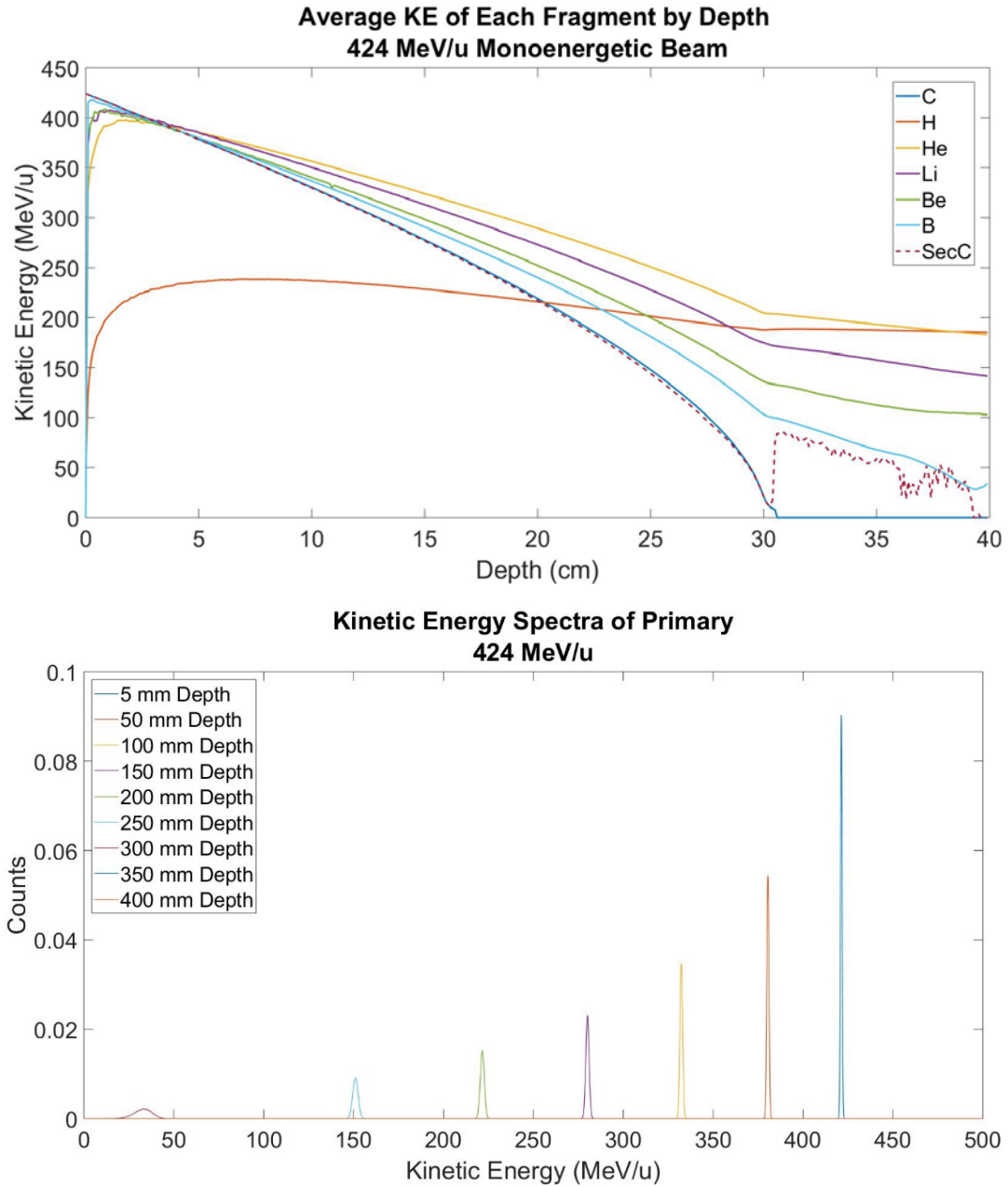


Figure 178. Kinetic energy distribution of primary carbons at the following depths for a 424 MeV/u monoenergetic beam: 5 mm, 50 mm, 100 mm, 150 mm, 200 mm, 250 mm, 300 mm, 350 mm, 400 mm.

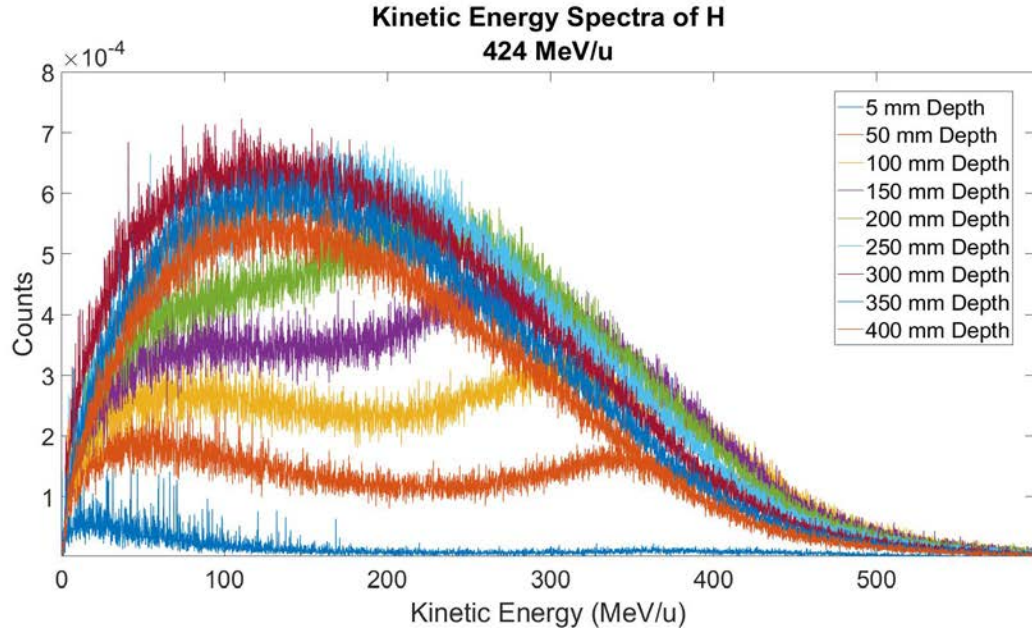


Figure 179. Kinetic energy distribution of secondary H at the following depths for a 424 MeV/u monoenergetic beam: 5 mm, 50 mm, 100 mm, 150 mm, 200 mm, 250 mm, 300 mm, 350 mm, 400 mm.

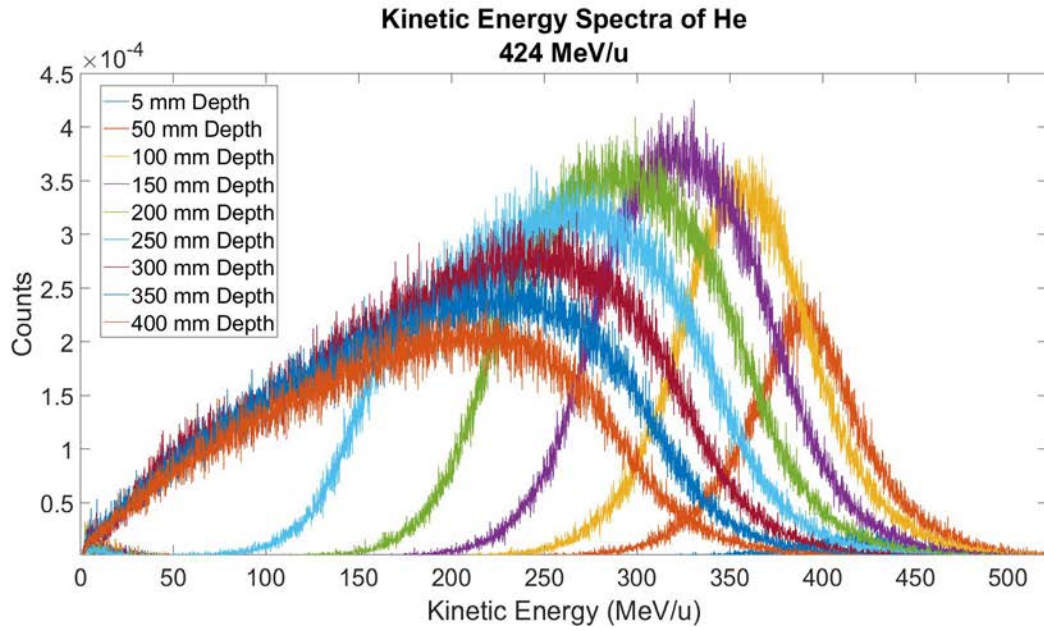


Figure 180. Kinetic energy distribution of secondary He at the following depths for a 424 MeV/u monoenergetic beam: 5 mm, 50 mm, 100 mm, 150 mm, 200 mm, 250 mm, 300 mm, 350 mm, 400 mm.

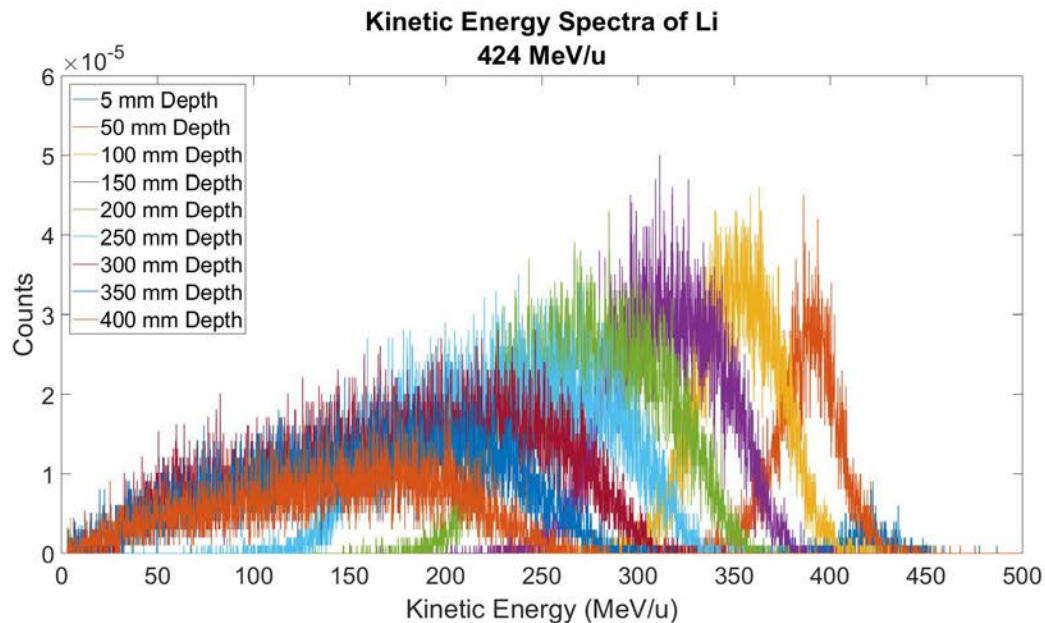


Figure 181. Kinetic energy distribution of secondary Li at the following depths for a 424 MeV/u monoenergetic beam: 5 mm, 50 mm, 100 mm, 150 mm, 200 mm, 250 mm, 300 mm, 350 mm, 400 mm.

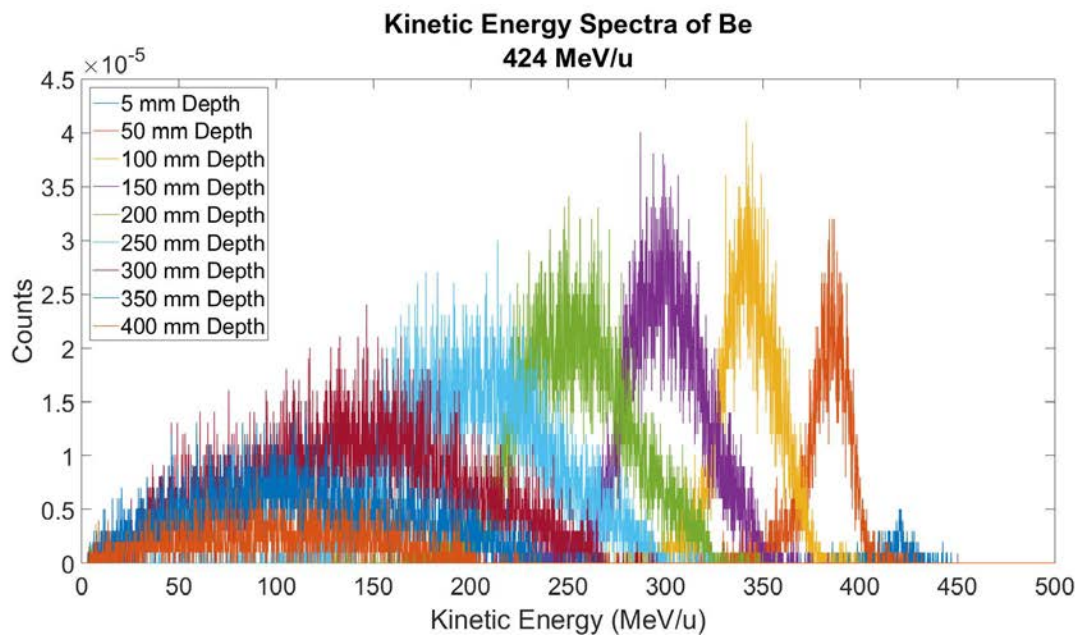


Figure 182. Kinetic energy distribution of secondary Be at the following depths for a 424 MeV/u monoenergetic beam: 5 mm, 50 mm, 100 mm, 150 mm, 200 mm, 250 mm, 300 mm, 350 mm, 400 mm.

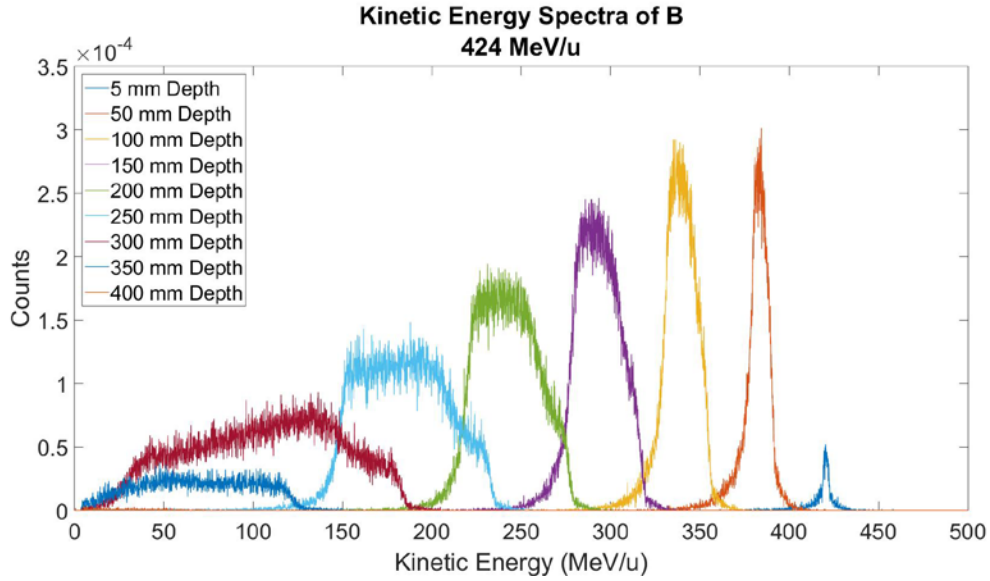


Figure 183. Kinetic energy distribution of secondary B at the following depths for a 424 MeV/u monoenergetic beam: 5 mm, 50 mm, 100 mm, 150 mm, 200 mm, 250 mm, 300 mm, 350 mm, 400 mm.

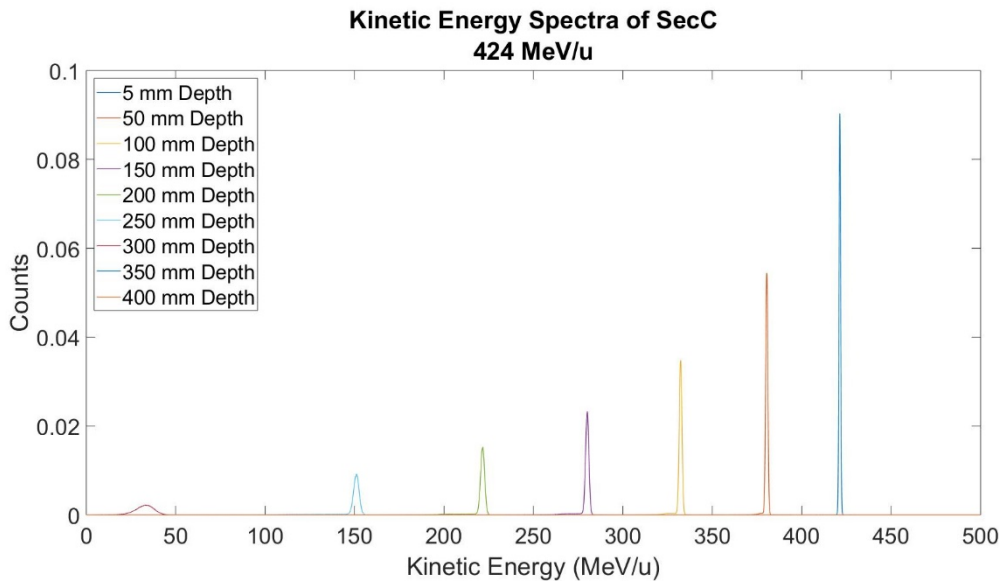


Figure 184. Kinetic energy distribution of secondary carbons at the following depths for a 424 MeV/u monoenergetic beam: 5 mm, 50 mm, 100 mm, 150 mm, 200 mm, 250 mm, 300 mm, 350 mm, 400 mm.

5.5.3 7 cm SOBP

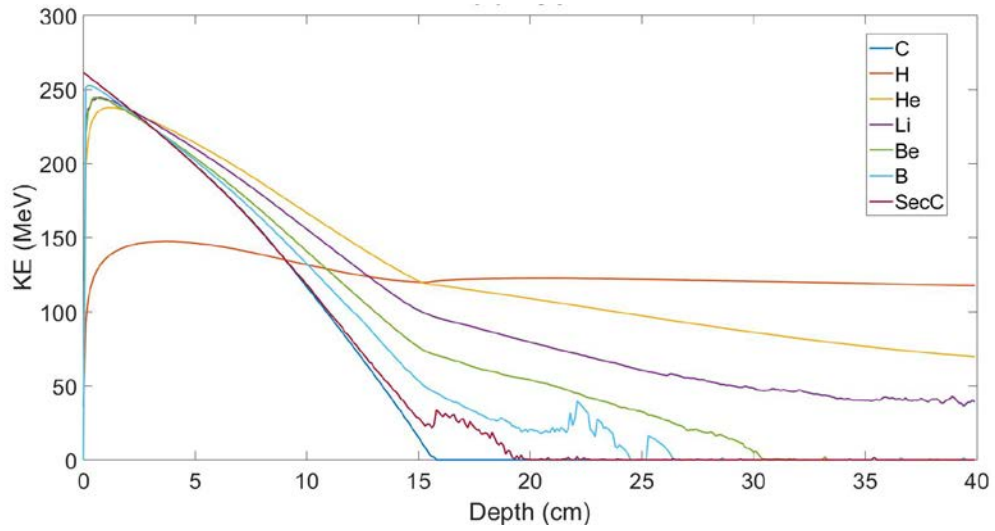


Figure 185. Average kinetic energy as a function of depth by each fragment in a 7 cm SOBP.

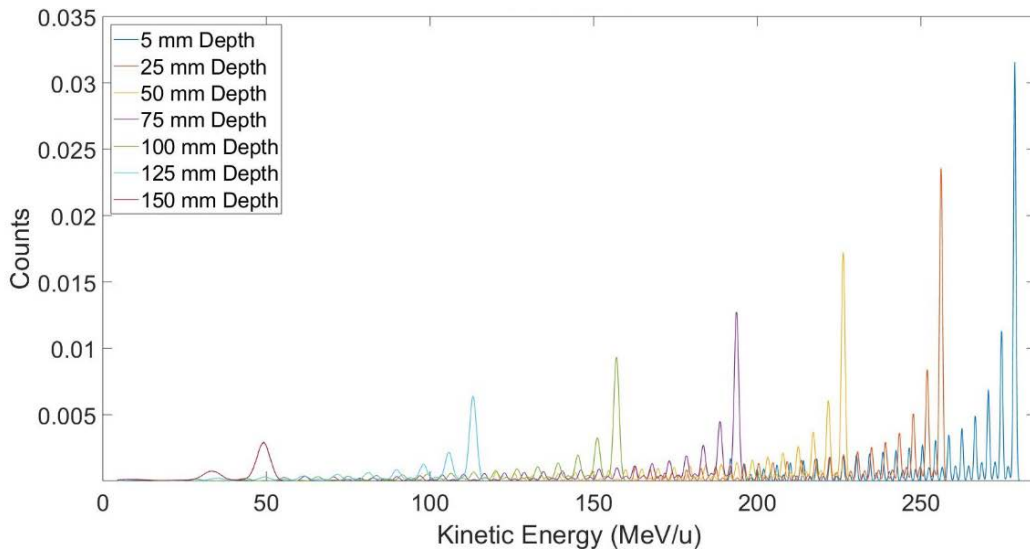


Figure 186. Kinetic energy distribution of primary carbons at the following depths for a 7 cm SOBP: 5 mm, 25 mm, 50 mm, 75 mm, 100 mm, 125 mm, 150 mm.

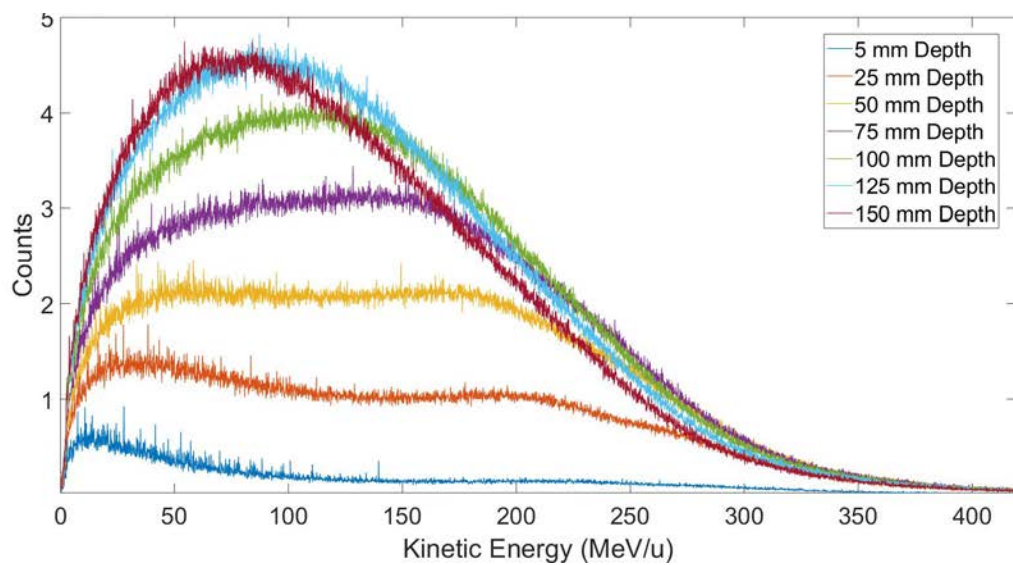


Figure 187. Kinetic energy distribution of secondary H at the following depths for a 7 cm SOBP: 5 mm, 25 mm, 50 mm, 75 mm, 100 mm, 125 mm, 150 mm.

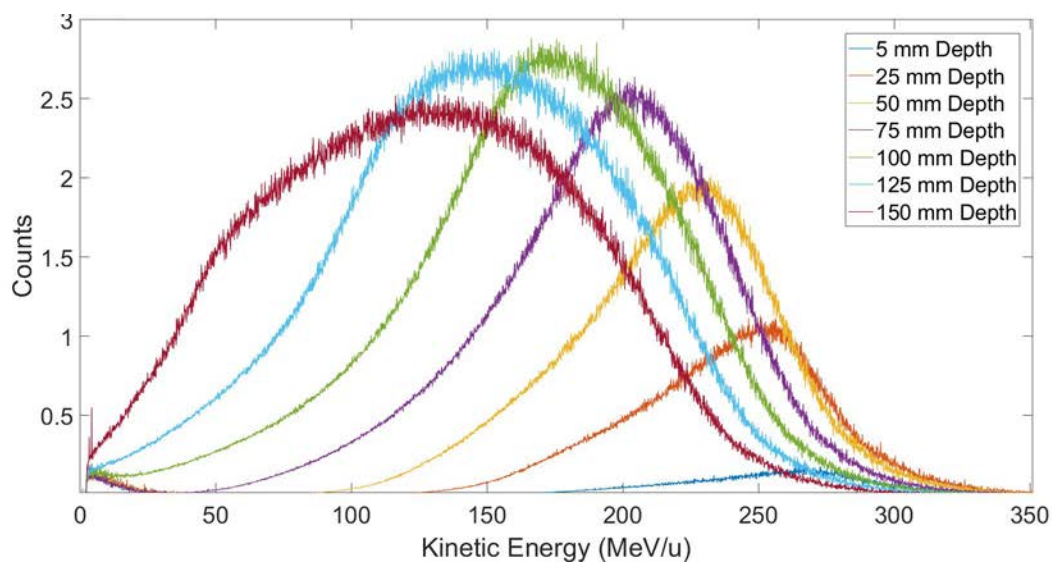


Figure 188. Kinetic energy distribution of secondary He at the following depths for a 7 cm SOBP: 5 mm, 25 mm, 50 mm, 75 mm, 100 mm, 125 mm, 150 mm.

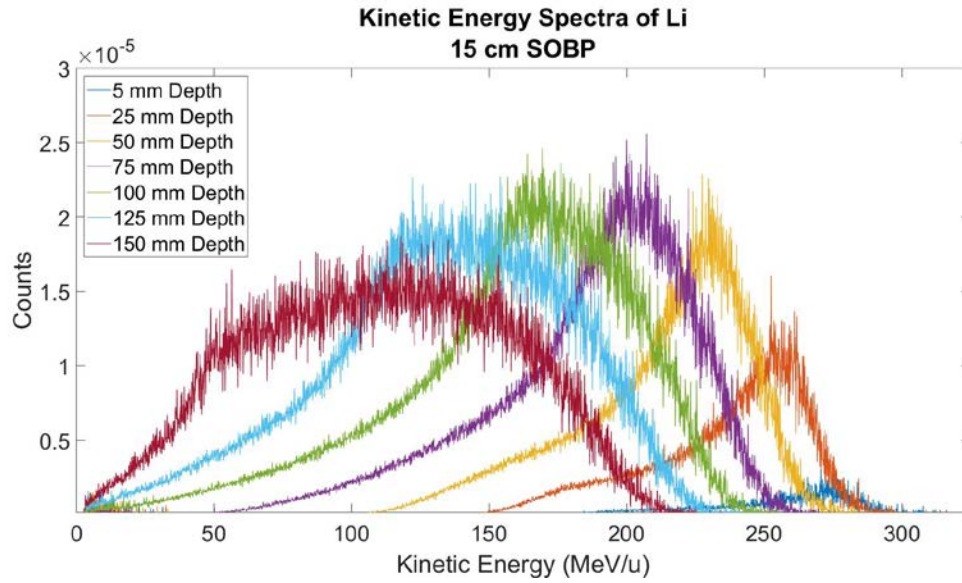


Figure 189. Kinetic energy distribution of secondary Li at the following depths for a 424 MeV/u monoenergetic beam: 5 mm, 25 mm, 50 mm, 75 mm, 100 mm, 125 mm, 150 mm.

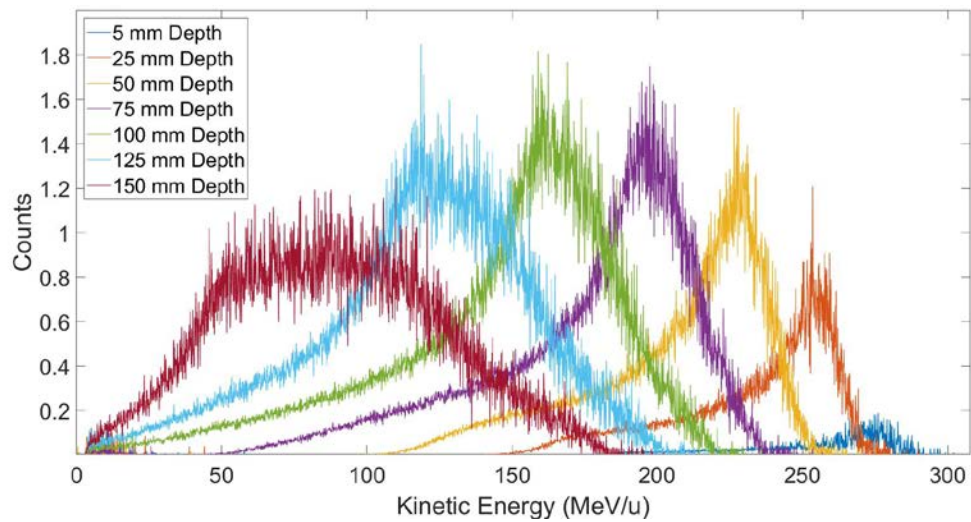


Figure 190. Kinetic energy distribution of secondary Be at the following depths for a 7 cm SOBP: 5 mm, 25 mm, 50 mm, 75 mm, 100 mm, 125 mm, 150 mm.

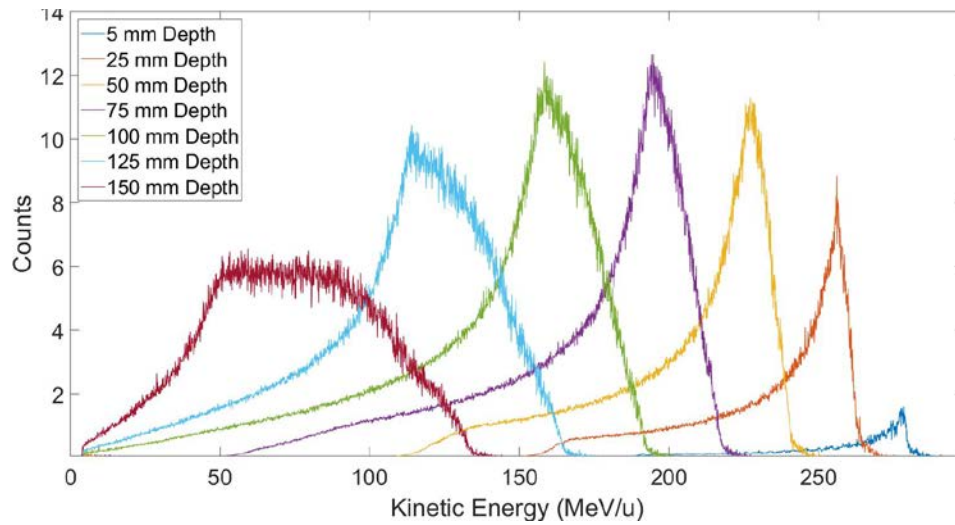


Figure 191. Kinetic energy distribution of secondary B at the following depths for a 7 cm SOBP: 5 mm, 25 mm, 50 mm, 75 mm, 100 mm, 125 mm, 150 mm.

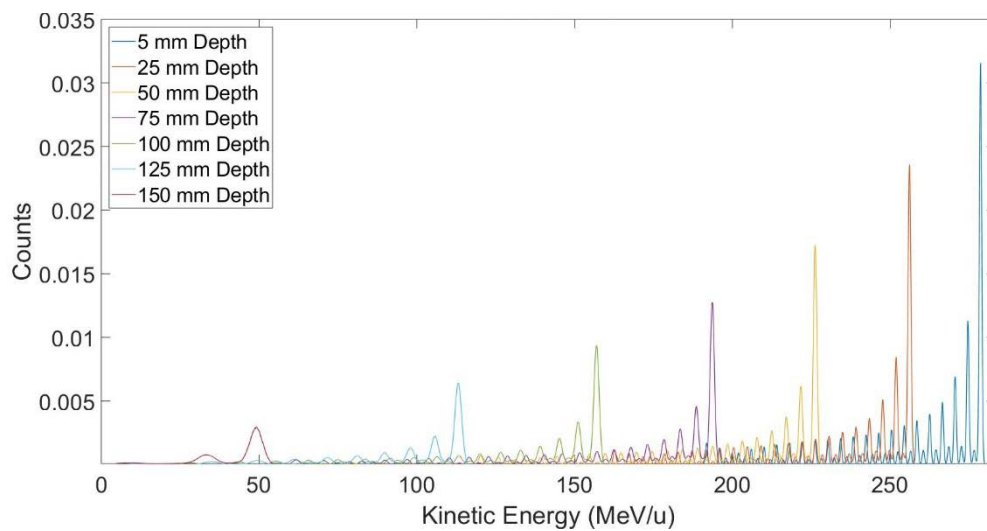


Figure 192. Kinetic energy distribution of secondary C at the following depths for a 7 cm SOBP: 5 mm, 25 mm, 50 mm, 75 mm, 100 mm, 125 mm, 150 mm.

5.6 Energy Deposition

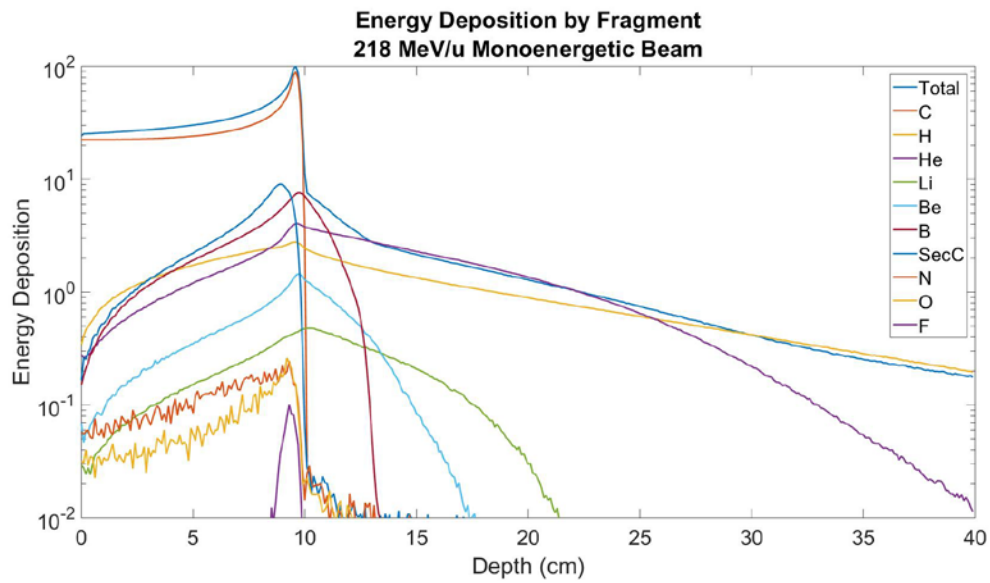


Figure 193. Energy deposition by fragment for a 218 MeV/u monoenergetic beam.

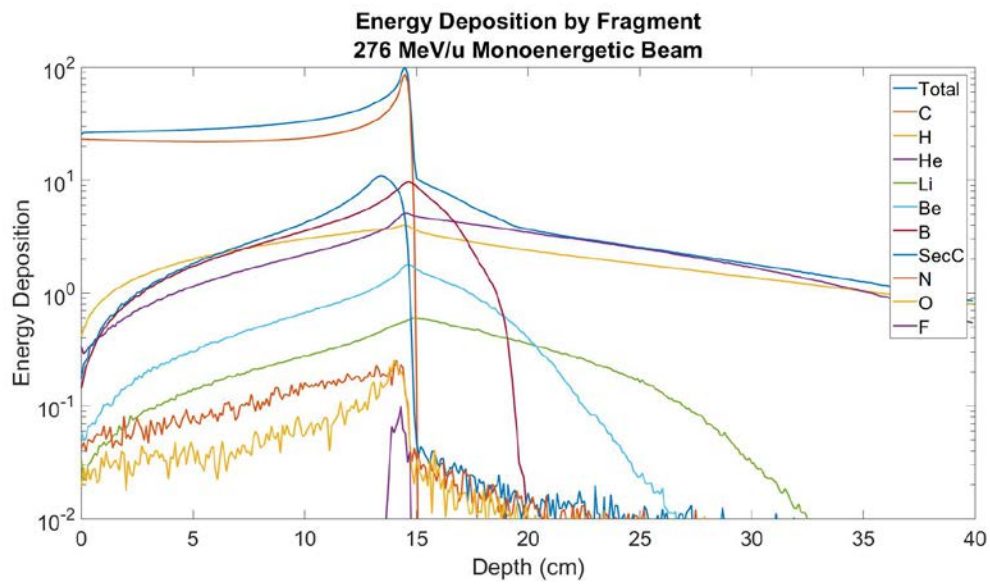


Figure 194. Energy deposition by fragment for a 276 MeV/u monoenergetic beam.

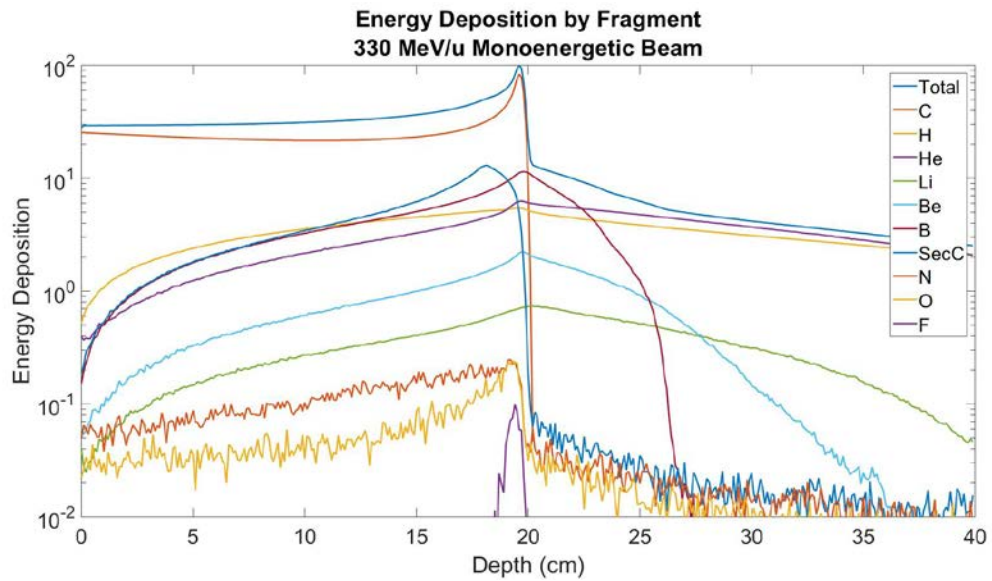


Figure 195. Energy deposition by fragment for a 330 MeV/u monoenergetic beam.

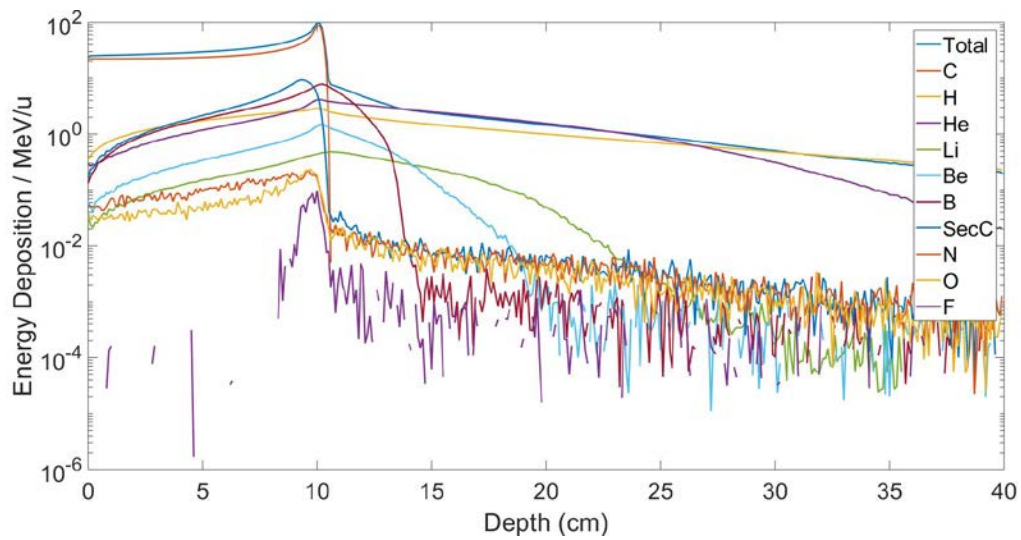


Figure 196. Energy deposition by fragment for a 5 cm SOB.

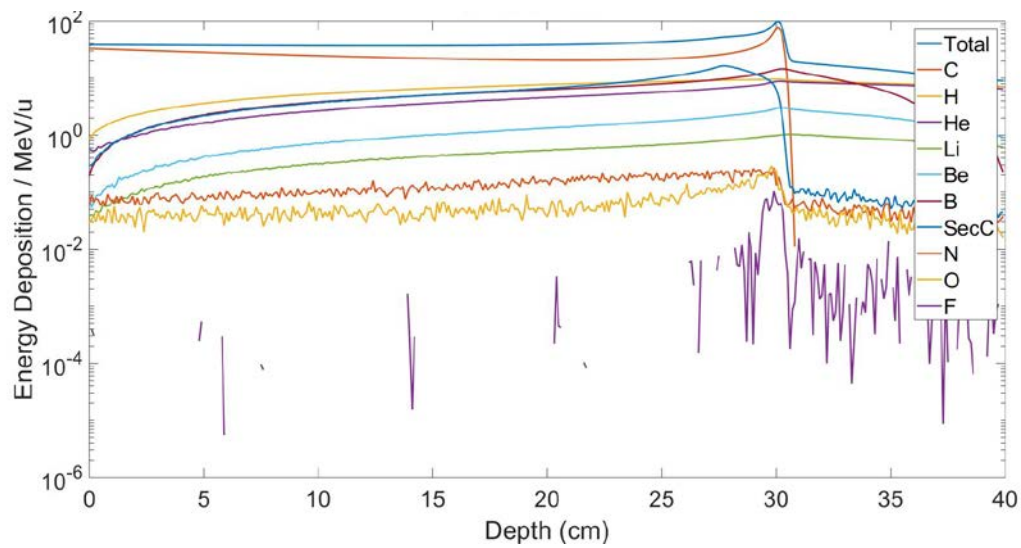


Figure 197. Energy deposition by fragment for a 10 cm SOBP.

6 References

- [1] PAPANIKOLAOU, N., BATTISTA, J. J., BOYER, A. L., KAPPAS, C., KLEIN, E., MACKIE, T. R., SHARPE, M. & DYK, J. V. 2004. Tissue Inhomogeneity Corrections for Megavoltage Photon Beams. *In: MEDICINE, T. G. N. I. T. R. T. C. O. T. A. A. O. P. I. (ed.) AAPM Report.* Madison, WI.
- [2] GUAN, F., GENG, C., CARLSON, D. J., MA, D. H., BRONK, L., GATES, D., WANG, X., KRY, S. F., GROSSHANS, D. & MOHAN, R. 2018. A mechanistic relative biological effectiveness model-based biological dose optimization for charged particle radiobiology studies. *Phys. Med. Biol.*, 64, 015008.
- [3] TSUJII, H., KAMADA, T., SHIRAI, T., NODA, K., TSUJI, H. & KARASAWA, K. 2014. *Carbon-Ion Radiotherapy | SpringerLink*, Springer, Tokyo.
- [4] TOMMASINO, F., SCIFONI, E. & DURANTE, M. 2016. New Ions for Therapy. *International Journal of Particle Therapy Online.*
- [5] SUIT, H., DELANEY, T., GOLDBERG, S., PAGANETTI, H., CLASIE, B., GERWECK, L., NIEMIERKO, A., HALL, E., FLANZ, J., HALLMAN, J. & TROFIMOV, A. 2010. Proton vs carbon ion beams in the definitive radiation treatment of cancer patients. *PubMed. comprises. more. than. 29 million. citations. for biomedical. literature. from. MEDLINE, life. science. journals., and online. books.,* 95, 3--22.
- [6] ALONSO, J. R. 2000. Review of Ion Beam Therapy: Present and Future. *In: ION-BEAM TECHNOLOGY PROGRAM, A. A. F. R. D., LAWRENCE*

- BERKELEY NATIONAL LABORATORY (ed.) *The 7th European Particle Accelerator Conference*. Vienna, Austria.
- [7] WEBER, U. & KRAFT, G. 1999. Design and construction of a ripple filter for a smoothed depth dose distribution in conformal particle therapy. *Phys. Med. Biol.*, 44, 2765--2775.
- [8] 1983. Microdosimetry. In: MEASUREMENTS, I. C. O. R. U. A. (ed.) *ICRU Report*. Bethesda, MD.
- [9] LINDBORG, L. & WALKER, A. 2017. *Microdosimetry: Experimental Methods and Applications*, Boca Raton, FL, CRC Press Taylor & Francis Group.
- [10] KASE, Y., KANAI, T., MATSUMOTO, Y., FURUSAWA, Y., OKAMOTO, H., ASABA, T., SAKAMA, M. & SHINODA, H. 2006. Microdosimetric Measurements and Estimation of Human Cell Survival for Heavy-Ion Beams. *Radiation Research*, 166, 629-638.
- [11] 2008. Model LET-1/2: Operation Manual. Goleta, CA: Far West Technology, Inc.
- [12] WATT, D. E. 1996. *Quantities for Dosimetry of Ionizing Radiations in Liquid Water*, Taylor&Francis Publishers since 1798.
- [13] FRIEDRICH, T., SCHOLZ, U., ELSÄSSER, T., DURANTE, M. & SCHOLZ, M. 2012. Systematic analysis of RBE and related quantities using a database of cell survival experiments with ion beam irradiation. *Journal of Radiation Research*, 54, 494-514.
- [14] KRAMER, M. & SCHOLZ, M. 2006. Rapid calculation of biological effects in ion radiotherapy. *Physics in Medicine and Biology*, 51, 1959-1969.

- [15] KASE, Y., KANAI, T., MATSUMOTO, Y., FURUSAWA, Y., OKAMOTO, H., ASABA, T., SAKAMAA, M. & SHINODAA, H. 2006. Microdosimetric Measurements and Estimation of Human Cell Survival for Heavy-Ion Beams. *Radiation Research*, 166, 629-638.
- [16] CARLSON, D. J., STEWART, R. D., SEMENENKO, V. A. & SANDISON, G. A. 2009. Combined Use of Monte Carlo DNA Damage Simulations and Deterministic Repair Models to Examine Putative Mechanisms of Cell Killing. *Radiation Research: Official Journal of the Radiation Research Society*.
- [17] BATTERMANN, J. J., BREUR, K., HART, G. A. M. & VAN PEPPERZEEL, H. A. 1981. Observations on Pulmonary Metastases in Patients After Single Doses and Multiple Fractions of Fast Neutrons and Cobalt-60 Gamma Rays. *Europ. J. Cancer*, 17, 539-548.
- [18] OHRI, N., SHEN, X., DICKER, A. P., DOYLE, L. A., HARRISON, A. S. & SHOWALTER, T. N. 2013. Radiotherapy protocol deviations and clinical outcomes: a meta-analysis of cooperative group clinical trials. *PubMed*. comprises. more. than. 29 million. citations. for. biomedical. literature. from. MEDLINE, life. science. journals., and. online. books., 105, 387--393.
- [19] PETERS, L. J., O'SULLIVAN, B., GIRALT, J., FITZGERALD, T. J., TROTTI, A., BERNIER, J., BOURHIS, J., YUEN, K., FISHER, R. & RISCHIN, D. 2010. Critical impact of radiotherapy protocol compliance and quality in the treatment of advanced head and neck cancer: results from TROG

- 02.02. *PubMed. comprises. more. than. 29 million. citations. for. biomedical. literature. from. MEDLINE, life. science. journals., and. online. books., 28, 2996--3001.*
- [20] PETTERSEN, M. N., AIRD, E. & OLSEN, D. R. 2008. Quality assurance of dosimetry and the impact on sample size in randomized clinical trials. *PubMed. comprises. more. than. 29 million. citations. for biomedical. literature. from. MEDLINE, life. science. journals., and online. books., 86, 195--199.*
- [21] 2016. Preamplifier Introduction. Oak Ridge, TN: Ortec Ametek.
- [22] ROSSI, H. H. & ZAIDER, M. 1996. *Microdosimetry and Its Applications*, Berlin, Springer-Verlag Berlin Heidelberg.
- [23] 1979. Average Energy Required to Produce an Ion Pair. *In: MEASUREMENTS, I. C. O. R. U. A. (ed.) ICRU Report. Washington, D.C.*
- [24] 2017. Easy-MCA-2K/8K. Oak Ridge, TN: Ortec Ametek.
- [25] UPP, D. L., KEYSER, R. M., GEDCKE, D. A., TWOMEY, T. R. & BINGHAM, R. D. 2001. An innovative method for dead time correction in nuclear spectroscopy. *Journal of Radioanalytical and Nuclear Chemistry*, 248, 377-383.
- [26] RADEMACHER, S. E., BORAK, T. B., ZEITLIN, C., HEILBRONN, L. & MILLER, J. 1998. Wall Effects Observed in Tissue-Equivalent Proportional Counters from 1.05 GeV/nucleon Iron-56 Particles. *Radiat. Res.*, 149, 387--395.

- [27] TSUDA, S., SATO, T., TAKAHASHI, F., SATOH, D., SASAKI, S., NAMITO, Y., IWASE, H., BAN, S. & TAKADA, M. 2012. Systematic measurement of lineal energy distributions for proton, He and Si ion beams over a wide energy range using a wall-less tissue equivalent proportional counter. *PubMed. comprises. more. than. 29 million. citations. for. biomedical. literature. from. MEDLINE, life. science. journals., and. online. books., Citations, include.*
- [28] TSUDA, S., SATO, T., OGAWA, T. & SASAKI, S. 2016. Review of the Microdosimetric Studies for High-Energy Charged Particle Beams Using a Tissue-Equivalent Proportional Counter. *JPS Conf. Proc.*, 11.
- [29] GUAN, F., PEELER, C., BRONK, L., GENG, C., TALEEI, R., RANDENIYA, S., GE, S., MIRKOVIC, D., GROSSHANS, D., MOHAN, R. & TITT, U. 2015. Analysis of the track- and dose-averaged LET and LET spectra in proton therapy using the geant4 Monte Carlo code. *Med. Phys.*, 42, 6234--6247.
- [30] BRUN, R. & RADEMAKERS, F. 1997. ROOT — An object oriented data analysis framework. *Nucl. Instrum. Methods Phys. Res., Sect. A*, 389, 81--86.
- [31] SCHUHMACHER, H. & KRAUSS, O. 1986. Area Monitoring of Photons and Neutrons from Medical Electron Accelerators Using Tissue-Equivalent Proportional Counters. *Radiat. Prot. Dosim.*, 14, 325--327.
- [32] BLEICHER, M., BURIGO, L., DURANTE, M., HERRLITZ, M., KRÄMER, M., MISHUSTIN, I., MÜLLER, I., NATALE, F., PSHENICHNOV, I.,

- SCHRAMM, S., TAUCHER-SCHOLZ, G. & WÄLZLEIN, C. 2012. Nanolesions induced by heavy ions in human tissues: Experimental and theoretical studies. *Beilstein Journal of Nanotechnology*, 3, 556-563.
- [33] TRAN, L. T., BOLST, D., GUATELLI, S., POGOSSOV, A., PETASECCA, M., LERCH, M. L. F., CHARTIER, L., PROKOPOVICH, D. A., REINHARD, M. I., POVOLI, M., KOK, A., PEREVERTAYLO, V. L., MATSUFUJI, N., KANAI, T., JACKSON, M. & ROSENFELD, A. B. 2018. The relative biological effectiveness for carbon, nitrogen, and oxygen ion beams using passive and scanning techniques evaluated with fully 3D silicon microdosimeters. *Med. Phys.*, 45, 2299--2308.
- [34] BOOZ, J., FIDORRA, J. & FEINENDEGEN, L. E. 1976. Quality Factor of Mixed-Radiation Neutron Gamma Rays: Comparison of the Radiation-Component Method and of the yD Method. *In*: BOOZ, J., EBERT, H. G. & SMITH, B. G. R., eds. Fifth Symposium on Microdosimetry, 1975 Verbania Pallanza. Luxembourg: Commission of the European Communities, 607-621.

7 Vita

Shannon Elise Hartzell was born in Maplewood, Minnesota on February 2nd, 1995, the daughter of Andrew Keith Hartzell and Karen Ann Hartzell. After completing her work at Hudson Senior High School in Hudson, Wisconsin in 2012 she entered Lafayette College in Easton, PA. She received the degree of Bachelor of Arts with a major in physics from Lafayette in 2016. She also received the degree of Bachelor of Science with a major in neuroscience in the same year. For the next year, she worked in project management at a clinical trial drug delivery company. In August of 2017, she entered the medical physics program at The University of Texas MD Anderson Cancer Center UTHealth Graduate School of Biomedical Sciences. She plans on continuing her education to pursue her PhD in medical physics.